CHARACTERIZATION AND ELECTROCATALYTIC APPLICATIONS OF METALLOPHTHALOCYANINE-SINGLE WALLED CARBON NANOTUBE CONJUGATES

A thesis submitted in fulfillment of the requirements for the degree of

DOCTOR OF PHILOSOPHY

OF

RHODES UNIVERSITY

BY

TAWANDA MUGADZA

DECEMBER 2010

DEDICATION

To my wife and children

“No mountain is too high if you climb with care and dedication”

ACKNOWLEDGEMENTS

My acknowledgements go to the following:

▪ The Almighty, I thank you for everything.

▪ My supervisor, Prof. Tebello Nyokong, I thank you for your visionary guidance and the new life that you have injected into me. ''This is the most treasured present in my life, for no one can snatch it from me''.

▪ Dr. Edith Antunes, I say thank you for all the assistance offered.

▪ Dr. Wadzanai Chidawanyika for the AFM pictures.

▪ EMU staff (Irvin and Shirley), I thank you so much for the good TEM pictures.

▪ My family, I say ''you are so dear and understanding'', you understood my resolve and marched on in my absence. You are wonderful.

▪ All the S22 comrades in arms, you are a marvelous bunch of Chemists.

▪ Rhodes Chemistry Department staff, for making Rhodes University my second home.

▪ Those who funded my studies: National Research Foundation (NRF) of South Africa and G. Goddard Scholarship.

ABSTRACT

Metallophthalocyanine-single walled carbon nanotube conjugates were successfully synthesized and applied in the electrochemical characterizations of pesticides (amitrole and diuron) and 2-mercaptoethanol (2-ME). The formation of conjugates was confirmed through the use of the following analytical techniques: UV-vis, FTIR, Raman and XRD spectroscopies, atomic force and transmission electron microscopies and voltammetry.

Chemically linking SWCNT to MPcs created platforms that offered efficient transfer of electrons and this was confirmed through electrochemical impedance studies (EIS) and voltammetry as shown by lower ΔEp values observed in conjugates. Carboxy carrying MPcs have very poor electron transfer kinetics (both tetrasubstituted and low symmetry), but the presence of SWCNTs activates their catalysis.

All electrochemical studies were done at pH 4. Cyclic voltammetry, rotating disk linear sweep voltammetry, chronoamperometry and EIS were used in the electrochemical characterization of 2-ME and the pesticides on *poly*-Ni(OH)TAPc and MPc-SWCNT modified glassy carbon electrodes (GCEs). High Tafel slopes were observed for the pesticides relative to 2-ME, an indication of the passivating nature of their oxidation products. However, conjugates showed very high resistances to passivation and were easily regenerated by shaking in methanol. Improved catalysis of the conjugates is also indicated by the high catalytic rate constants for the analytes, observed on these electrodes. Conjugates of low symmetry MPcs with SWCNTs gave the highest catalytic rate constants, confirming better catalysis on these electrode surfaces.

The nature of SWCNT functionalization also affected catalysis, with amine functionalized SWCNTs inducing better catalytic properties into the MPcs than carboxylic acid terminated CNTs. The presence of amine functionalized SWCNTs activates the catalysis of non-catalytic carboxy-carrying MPcs and this is more pronounced in conjugates of tetrasubstituted MPcs relative to those of low symmetry Pcs. Ethylene amine (EA) functionalized SWCNTs reduced redox overpotentials of the MPcs more than the phenyl-amine (PA) functionalized counterparts.

Poly-NiTAPc was successfully converted to *poly*-Ni(OH)TAPc through cyclisation in pH 4 buffer and showed very good catalytic properties towards diuron, relative to the former.

CONTENTS

LIST OF ABBREVIATIONS

AET- aminoethanethiol

AFM – atomic force microscopy

ATP – adenosine triphosphate

BDA – 1,4-benzene diamine

CA – chronoamperometry

CME - chemically modified electrode

CNP – carbon nanoparticle

CNT – carbon nanotube

CPE_{dl} – constant phase element (double layer capacitance)

CT - charge-transfer

CCVD – catalytic chemical vapour deposition

CV - cyclic voltammetry

- cyclic voltammogram

0 D – dimensionless

1 D – 1 dimensional

2 D – 2 dimensional

3 D – 3 dimensional

DC – direct current

DCM - dichloromethane

DMF - *N,N*-dimethylformamide

DMSO – dimethyl-sulphoxide

E - potential

EA – ethylene amine

EDA - ethylene diamine

E(CE)*n* - electrochemical-chemical-electrochemical

EIS – Electrochemical Impedance spectroscopy

f-SWCNT – functionalized SWCNT

f-SWCNT-COCl – acyl functionalized SWCNT

FT - IR – Fourier transform - infrared

GCE - glassy carbon electrode

HOMO - highest occupied molecular orbital

HOPG – highly oriented pyrolytic graphite

HPLC - high performance liquid chromatography

ICDD - International Center Diffraction Data

IR – infrared

K-L - Koutecky-Levich

LMCT - ligand-to-metal charge transfer

LOD – limit of detection

LUMO - lowest unoccupied molecular orbital

MAPc – monoamino-phthalocyanine

MCPc – monocarboxy-phthalocyanine

ME - mercaptoethanol

MLCT - metal-to-ligand charge transfer

MWCNT(s) – multi-walled carbon nanotube(s)

NDA – no data available

NIR - near infrared

OPG - ordinary pyrolytic graphite

PA – phenylene amine

- phenyl-amine

Pc - phthalocyanine

PDT - photodynamic therapy

PEG – poly(ethylene)glycol

RBM – radial breathing mode

RDE – rotating disk electrode

rpm - revolution per minute

TAPc - tetraaminophthalocyanine

$TBABF_4$ – tetrabutylammonium tetrafluoroborate

TGA – thermogravimetric analysis

THF – tetrahydrofuran

TEM – transmission electron microscopy

SAM(s) – self assembled monolayer(s)

SCE - saturated calomel electrode

$SOCl_2$ – thionyl chloride

SWCNT(s) – single-walled carbon nanotube(s)

SWCNT-COCl – methanoyl chloride functionalized SWCNTs

SWCNT-COOH – carboxylic acid functionalized single walled carbon nanotubes

EA-SWCNT– ethylene amine functionalized single walled carbon nanotubes

PA-SWCNT– phenylene amine functionalized single walled carbon nanotubes

UV-Vis – ultraviolet-visible

XRD – X-ray diffraction

LIST OF SYMBOLS

α - peripheral position

β – non-peripheral position

e^- - electron

Γ_{MPc} - surface coverage of metal phthalocyanine

n - number of electrons transferred

ν - scan rate

A - absorbance

- area of electrode

A_{eff} – effective electrode area

C – concentration

D - diffusion coefficient

ΔEp – peak to peak separation

Ep - peak potential

F - Faraday's constant

I - current

I_d – diffusion current

I_k – kinetic current

I_L – limiting current

I_p - peak current

K_{amp} - amperometric selectivity coefficient

M - molar concentration

Q - charge

R - universal gas constant

R_{et} – charge transfer resistance

R_s – solution resistance

T – temperature

ω – rotational speed

ω_{RBM} – frequency of the radial breathing mode

LIST OF FIGURES

LIST OF SCHEMES

LIST OF TABLES

CHAPTER 1

INTRODUCTION

This chapter gives an overview of the metallophthalocyanines (MPcs), single walled carbon nanotubes (SWCNTs) and the MPc-SWCNT conjugates used in this thesis. Included in this introduction are: a summary of synthetic approaches, microscopic, spectroscopic and voltammetric techniques used in this study.

1.1 Phthalocyanines

1.1.1 Discovery and general applications

The name phthalocyanine was coined by Linstead (1933) to describe both its origin from phthalic anhydride (*phthalo*) and its strikingly beautiful blue colour which was similar to *cyanine* dyes. Phthalocyanines (Pcs) are man's synthetic analogues of the porphyrins, such as chlorophyll, cyanocobalamine (vitamin B_{12}) and haemoglobin [1-3]. Pcs and their metallated forms (MPcs) are planar and highly conjugated 18л-electron systems [4]. The л-electron ring consists of alternating carbon and nitrogen atoms. The first metal-free phthalocyanine (H_2Pc) was reported in 1907 [5] and in 1927 de Diesbach and von der Weid made CuPc [6]. However, none of them characterized the products, so the discovery of Pcs is attributed to chemists at Scottish Dyes Ltd, who later made and characterized iron phthalocyanine (FePc), whose structure was elucidated by Linstead [7-12] at Imperial College and confirmed by Robertson [13-17] using X-ray diffraction (XRD). A patent describing the manufacturing process was filed in 1928 [18].

Pcs are brightly coloured, with high tinctorial strengths. They are the majority of the blue and green pigments used to make inks and car paints [1,19]. Pcs have found commercial applications in photocopying, laser printing, information storage, odour removal, oil sweetening, computer disk writing and infrared security devices, display devices (electrochromism and electroluminescence), organic catalysis, electrocatalysis, photocatalysis, photovoltaic devices, lithium batteries, gas sensors and fuel cells [1,20-27]. Today they are being developed for high technology applications such as photodynamic therapy of cancer and non-linear optical applications (e.g. optical limiting). MPcs whose accessible d-orbitals lie between the highest occupied molecular orbital (HOMO) and lowest unoccupied molecular orbital (LUMO) levels of the Pc^{2-} ligand, such as Cr, Mn, Fe and Co, play a role in the oxidation-reduction processes [28]. As such they have assumed an important role of being efficient electron transfer mediators in electrochemical reactions and electrocatalysis [25].

1.1.2 Syntheses of phthalocyanines

The Pc macrocycle has four iminoisoindoline units that are formed through cyclotetramerisation of the precursor units, under appropriate conditions. Scheme 1.1 shows the various precursors that can be used in the synthesis of Pcs.

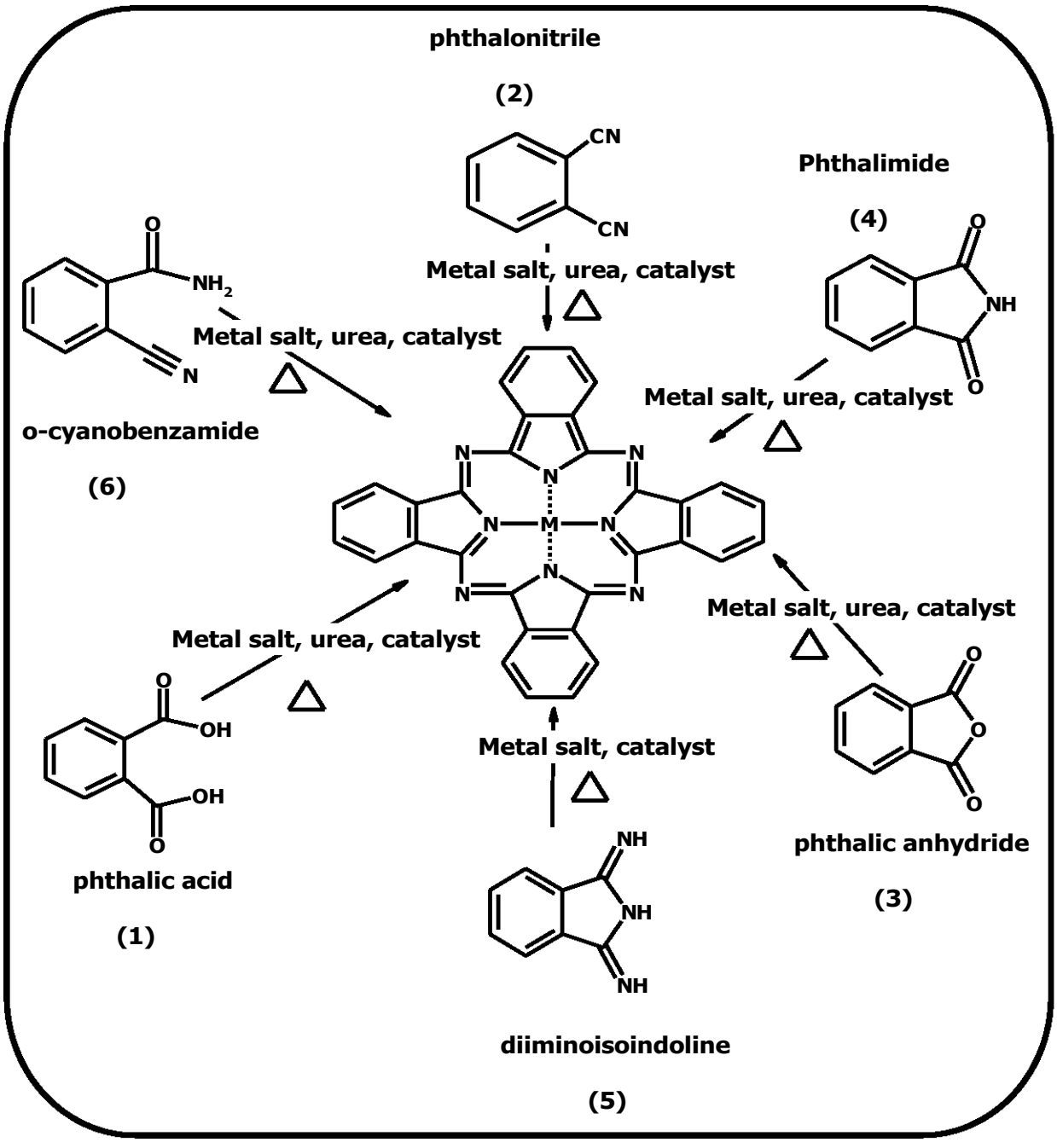

Scheme 1.1: Syntheses of MPcs from typical Pc precursors.

1.1.2.1 Unsubstituted phthalocyanines

Synthesis of unsubstituted MPcs involves a one-step condensation of the Pc precursors in the presence of a metal salt. The precursors include the following: phthalic acid **(1)** [29], phthalonitrile **(2)** [19,30], phthalic anhydride **(3)** [19], phthalimide **(4)** [31], diiminoisoindoline **(5)** [23] and o-cyanobenzamide **(6)**. Phthalic acid **(1)** can be used in the stepwise preparation of the phthalonitrile (**2**) precursors [32], via the formation of the phthalic anhydride **(3)** and phthalimide **(4)**. Two main routes are used today for the synthesis of Pcs, namely the phthalonitrile **(2)** and the phthalic anhydride/urea **(3)** [19]. The phthalic anhydride/urea route is used for the large-scale production of Pcs since it utilizes inexpensive starting materials. However, for laboratory and high purity Pc synthesis, the phthalonitrile route (Scheme 1.1) is used. Generally a finely ground mixture of the phthalonitrile precursor, ammonium chloride, urea, metal salt and a catalytic amount of ammonium molybdate is added to a high boiling point solvent like pentanol [33], nitrobenzene [29] or dimethyl-formamide (DMF) [34].

Metal free Pcs (H_2Pcs, Fig. 1.1) are synthesized by the cyclisation of phthalonitriles in the presence of lithium alkoxides [35] (normally of pentanol or octanol) in high boiling point solvents like chloronaphthalene or quinoline [36]. Alternatively H_2Pcs can be formed through the demetallation of MPcs [37-39]. The H_2Pcs serve as precursors for various MPcs, hence addition of a pure metal salt to the H_2Pc, leads to high yields of the MPcs.

The major limitation of unsubstituted Pcs is their poor solubility in common solvents because of the л-л interactions which keeps them together. This makes their purification a major obstacle, though repeated Soxhlet extractions and recrystallisation in sulphuric acid and water has yielded relatively pure Pcs. To enhance their solubility, Pcs have been substituted on their peripheral and non-peripheral positions, using a variety of groups. Tetra- and octa-substitutions have been done to improve their solubility.

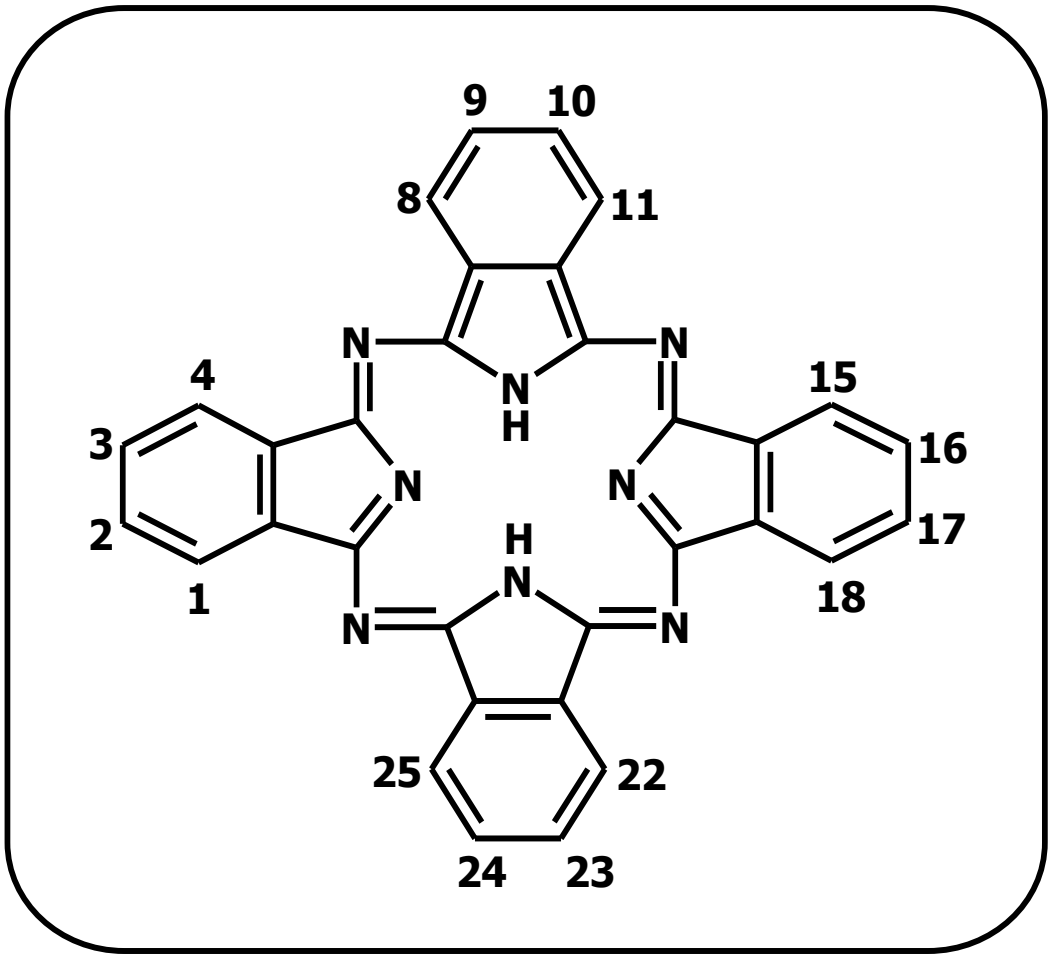

Figure 1.1: Metal free phthalocyanines (H_2Pcs).

1.1.2.2 Tetra-substituted Pcs

Substituents can be introduced directly onto the existing Pc ring, e.g. sulphonation [40] or by using monosubstituted Pc precursors. Pcs have 16 possible positions of substitution around the ring as shown in Fig. 1.1. Positions 1(4), 8(11), 15(18) and 22(25) describe the non-peripheral (α) positions, while positions 2(3), 9(10), 16(17) and 23(24) describe the peripheral (β) positions. Substitution on one α-position or one β-position on the four phenyl groups of the Pc ring produces isomeric tetra-substituted Pcs with reduced aggregation tendencies [41]. Polar substituents such as sodium salts of sulphonic acid, carboxylic acid or phosphonic acid groups provide water-soluble MPcs [42]. In this study, focus is on peripherally tetra-substituted MPcs (Fig. 1.2), using amino and carboxylic acid groups that can be

further derivatized with single walled carbon nanotubes (SWCNTs) for use in electrocatalysis.

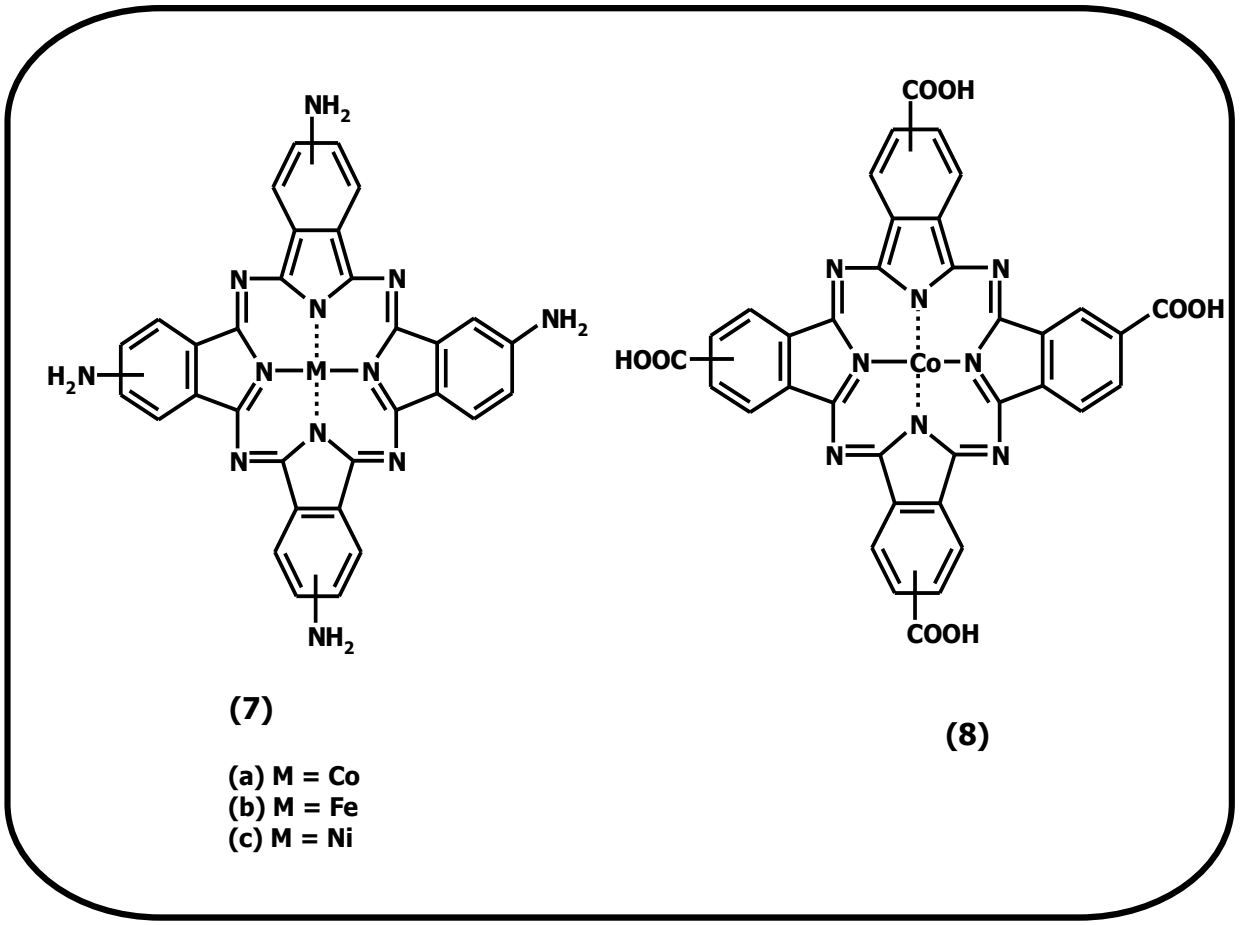

Figure 1.2: Tetraamino-substituted Pcs (TAPcs), CoTAPc (7a), FeTAPc (7b), NiTAPc (7c) and cobalt (II) tetracarboxy-Pc (CoTCPc, 8).

Tetraamino-Pcs **(7a-c)** may be prepared from the reduction of tetranitro-substituted Pcs using sodium sulphide nonahydrate ($Na_2S.9H_2O$) [29,30]. The tetranitro-Pcs may be synthesized from the tetracyclisation of 4-nitrophthalic acid or 4-nitrophthalonitrile in the presence of ammonium chloride, urea, a catalytic amount of ammonium molybdate and an appropriate salt [29,30,43]. Tetranitro-Pcs have also been prepared via microwave synthesis [44] followed by reduction with $Na_2S.9H_2O$ to give tetraamino-Pcs. Peripherally tetra-substituted MPcs were chosen in this thesis because of their higher solubilities in organic solvents relative to the

octasubstituted counterparts, due to the former having lower order in the solid state and higher dipole moments [42]. Metal tetraamino-phthalocyanines (MTAPcs) in particular, are very useful in the preparation of chemically modified electrodes (CMEs) for electrocatalytic reactions [44-48]. MTAPcs can be adsorbed or electropolymerized on glassy carbon electrodes [49]. The amino groups provide sites for chemically linking MTAPcs to acid derivatized SWCNTs [50].

Cobalt(II)-tetracarboxy-Pc (**8**) may be prepared using the phthalic anhydride **(3)** and urea as starting materials in the presence of a metal salt [51]. The carboxylic acid groups of the Pc molecule provide sites for the formation of chemical linkages with amino-functionalized SWCNTs [52].

Apart from their use in chemical bonding and improving solubility in aprotic solvents, the carboxylic acid and amino groups on the Pc ring change the electrochemical and physical behaviour of the MPcs. Their respective electron-donating and electron-withdrawing properties affect the redox chemistry of the central metal, with the electron-donating group i.e. $-NH_2$, reducing the oxidation overpotentials and vice-versa for the electron-withdrawing group [53].

Synthesis of MTAPcs (**7a-c**) and cobalt (II) tetracarboxy-Pc (CoTCPc (**8**)) is not new, but in this study focus is on how their electrocatalytic properties are influenced by the presence of SWCNTs that are chemically bound to them.

1.1.2.3 Low symmetry phthalocyanines

Monofunctional Pcs can be obtained through statistical condensation between two different substituted phthalonitriles or diiminoisoindolines [54,55]. This method produces of a mixture of products, which requires rigorous chromatographic isolation of the desired product. The second method involves the subphthalocyanine (SubPc) ring expansion [55-58]. SubPcs are Pc analogues having only three isoindole subunits. The third method involves the reaction of a polymer-bonded phthalonitrile with differently substituted dicarbonitriles in solution followed by cleavage of the formed Pc [59,60].

Monoamino-Pcs, just like tetraamino-Pcs, can also be prepared by hydrolysis of the appropriately protected amino groups (e.g. acetamido) or by reduction of the nitro

group in substituted Pcs [61-64]. The monoamino-substituted Pcs can be chemically linked to compounds carrying carboxylic acid, acid chloride or acid anhydride moieties to produce conjugates with improved solubilities. Functionalized Pcs can be chemically linked to SWCNTs for a variety of purposes including drug delivery [65-67] and electrocatalysis [68,69]. The presence of one -NH_2 group leads to a more defined bonding.

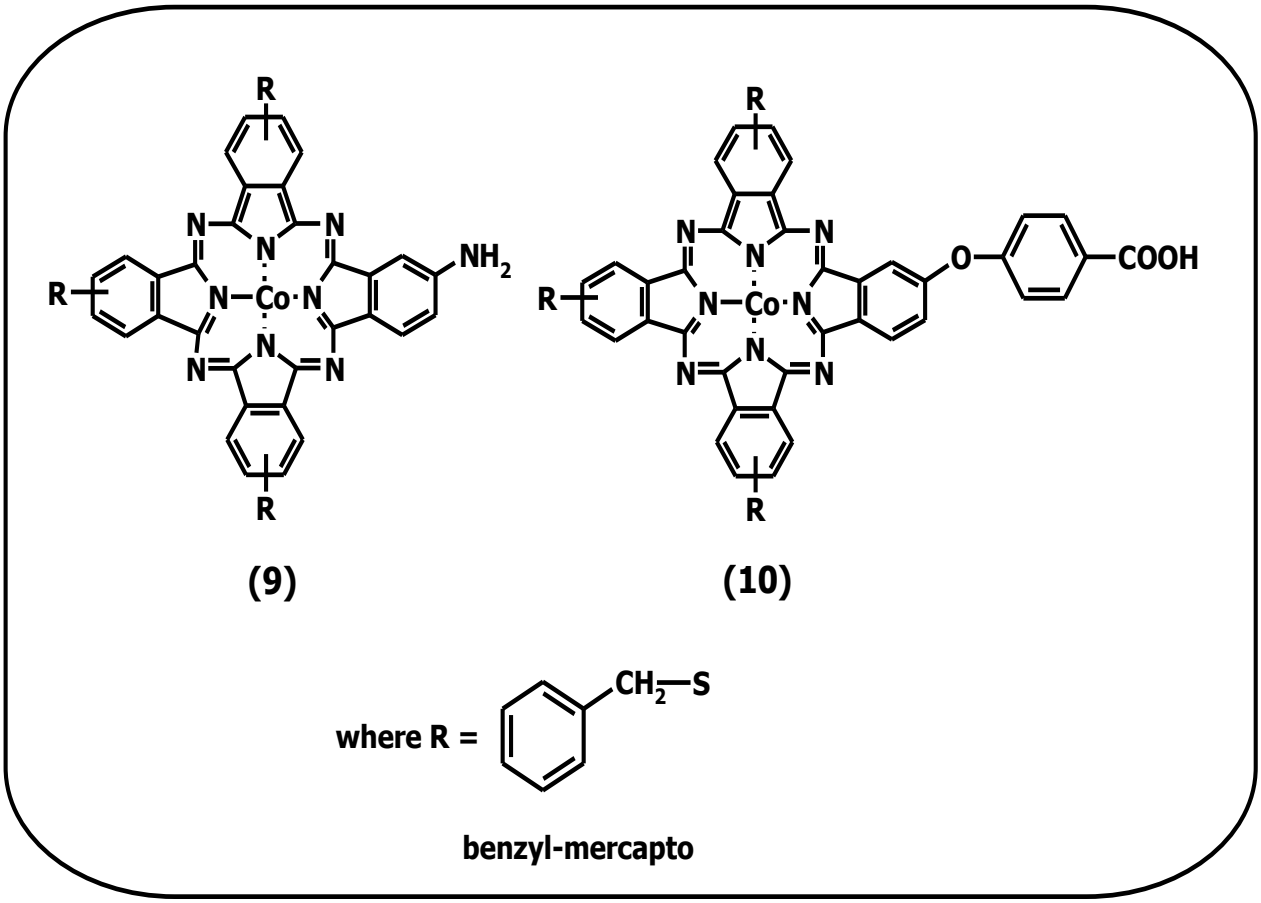

Figure 1.3: Synthesized low symmetry Pcs, (a) Cobalt (II)-tris(benzyl-mercapto)-monoaminophthalocyanine (CoMAPc, 9) and (b) Cobalt (II)-tris(benzyl-mercapto)-mono(carboxyphenoxy) phthalocyanine (CoMCPc, 10).

Cobalt (II)-tri(benzyl-mercapto)-monoaminophthalocyanine (**9**), (CoMAPc) and cobalt (II)-tri(benzyl-mercapto)-mono(carboxyphenoxy) phthalocyanine (**10**), (CoMCPc), are being reported here for the first time (Fig.1.3) and were chemically linked to SWCNTs and used in the electrocatalysis of amitrole, diuron and 2-

mercaptoethanol (2-ME). Low symmetry Pcs of this nature, containing carboxylic acid or amino groups, have an advantage of controlling the orientation and the number of the incoming groups, thereby giving rise to a well defined structure of limited size. The orientation of such derivatives on the electrode surface can be pre-determined and the electron transfer properties ascertained. The aryl thio groups were used in both CoMAPc **(9)** and CoMCPc **(10)** to improve solubility and reduce aggregation. Little or no aggregation is good for the effective transfer of electrons across the electrode|analyte interface. Due to their electron donating nature, the aryl thio groups lower the cobalt redox potentials, improving electrocatalytic behaviour.

1.1.3 UV-Vis electronic absorption spectra for phthalocyanines

The following bands are typical of MPcs and H_2Pcs UV-vis spectra, as shown in Figs. 1.4a and 1.4b respectively: (i) the Q-band (very intense absorption band, found in the region of 660 – 1000 nm), (ii) the vibronic bands (close to the foot and the blue end of the Q-band), (iii) the charge transfer band (a result of electron transfer between the ligand (L) and the metal (M) centre), can be either M → L or L → M and is blue shifted relative to the Q- and vibronic bands and (iv) the B- or Soret band (a result of the superimposition of two bands, B_1 and B_2, giving rise to the weak band around 350 nm). MPcs and H_2Pcs are characterized by single and split Q-bands as shown in Figs 1.4a and b, respectively.

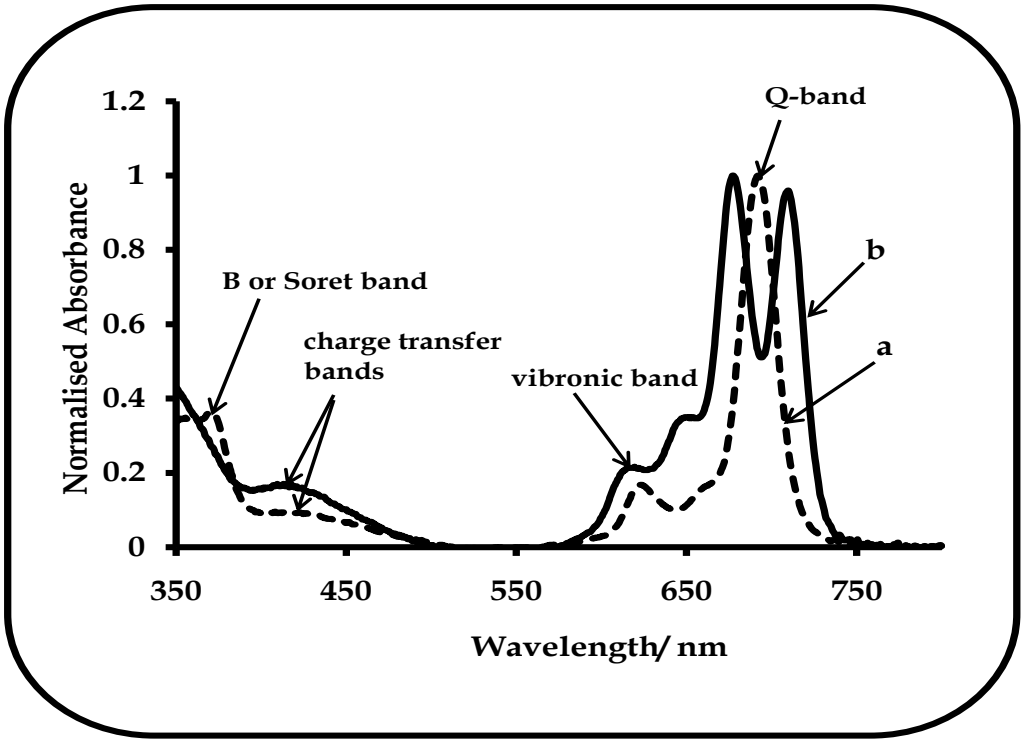

Figure 1.4: Typical electronic absorption spectra for (a) MPcs and (b) H_2Pcs.

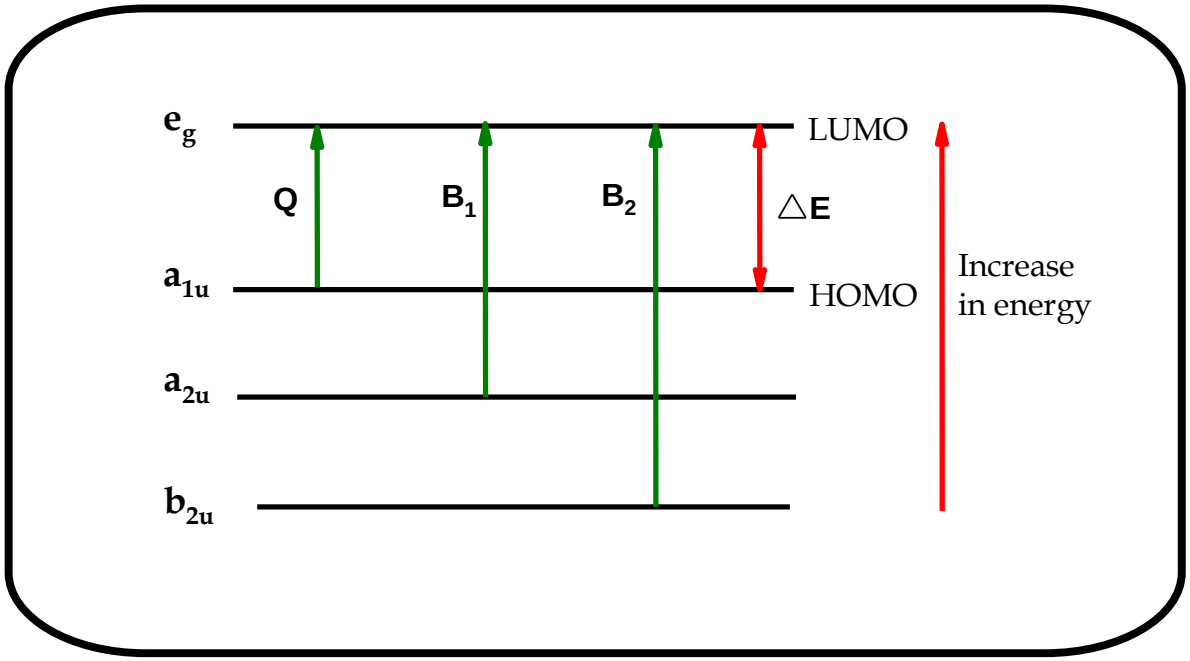

Figure 1.5: Diagrammatic representation of the origin of the Q and B-bands.

Fig.1.5 gives the diagrammatic representation of the electronic energy level transitions that are responsible for the formation of Q- and B-bands. The Q-band is due to the л-л electronic transitions from the HOMO to the LUMO of the Pc ring, Pc^{2-}, $a_{1u} \rightarrow e_g$. The B - bands are a result of electronic transitions from the deeper л-levels to the LUMO as shown in Fig. 1.5, B_1 ($a_{2u} \rightarrow e_g$) and B_2 ($b_{2u} \rightarrow e_g$). The position of the Q-band can be tuned through varying the following factors: central metal, symmetry and substituents (position, size and number of substituent groups) [41,70-73].

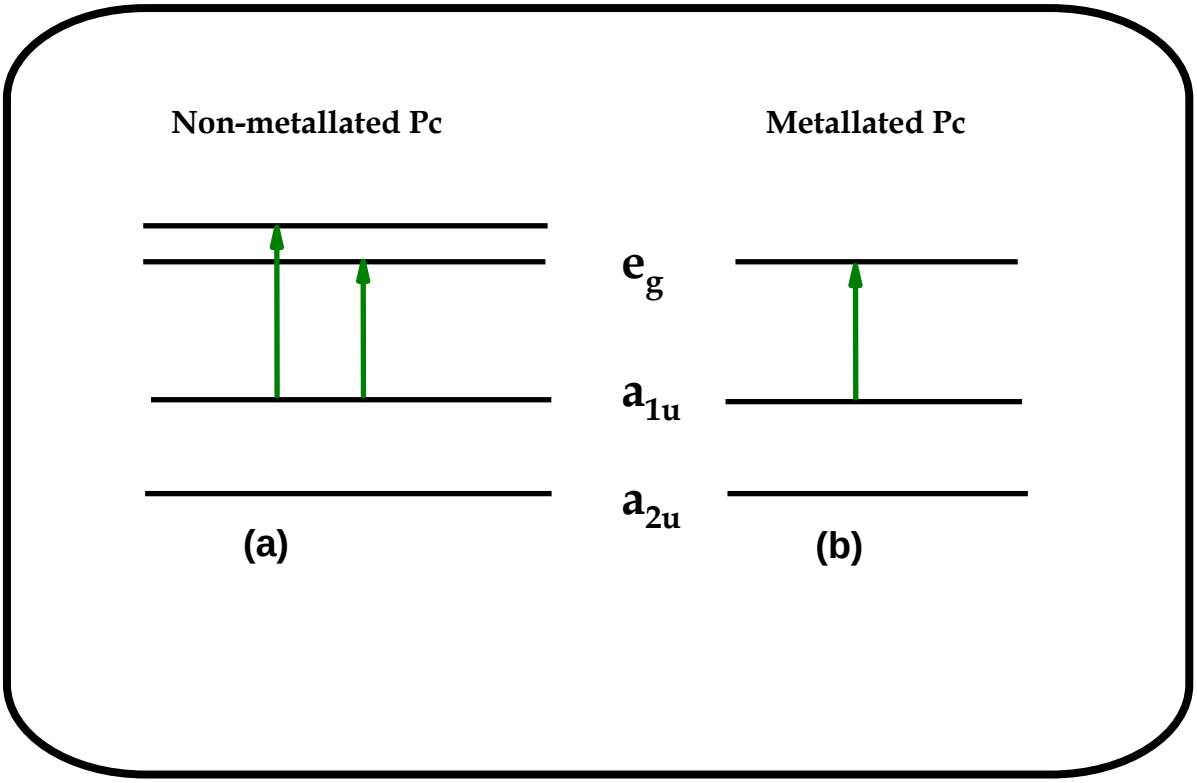

Figure 1.6: Diagrammatic representation of the origin of the split Q–band in H_2Pcs (a) and single Q-band in MPcs (b).

Fig. 1.6a and b show the diagrammatic representations of the energy levels for the H_2Pcs and MPcs respectively. The LUMO of the H_2Pc is non-degenerate (D_{2h} symmetry), as compared to the degenerate LUMO of the MPc (D_{4h} symmetry). As a result there are two allowed transitions from the HOMO level to the non-degenerate

LUMO levels, hence the appearance of a split Q-band in H_2Pcs, as shown in Fig. 1.4b. When the empty Pc core is occupied by the metal ion there is change in symmetry from D_{2h} to D_{4h} and this is responsible for the observed conversion from a split Q-band to a single Q-band.

1.1.4. Solution electrochemistry of MPcs

1.1.4.1. General behaviour

The MPc electrochemistry is characterized by multiple and often reversible redox processes that are localized on the metal center or the Pc ring [21,74-79], both in solution or when adsorbed on electrode surfaces. MPcs can be reduced or oxidized, but still retain their molecular structure and stability [21]. The Pc^{2-} ring can be oxidized ($Pc^{2-} \rightarrow Pc^{1-} \rightarrow Pc^{0}$) or can be successively reduced ($Pc^{2-} \rightarrow Pc^{3-} \rightarrow Pc^{4-} \rightarrow Pc^{5-} \rightarrow Pc^{6-}$). The electroactive transition-metal Pcs (Cr, Mn, Co and Fe) whose d-orbitals lie between HOMO and LUMO of the Pc ligand [80-82] have their metal oxidations or reductions occurring in between those corresponding to ligand reduction or oxidation [83-85], in the presence of coordinating species that would stabilize the metal center [80,82]. For MPcs containing non-redox metals such as Ni, Cu, Zn, Pd, the redox processes take place on the Pc ring. Their redox chemistry will be similar to those of MPcs containing a non-electroactive metal [86].

Changes in the nature of the peripheral substituents affects the electron density and consequently the redox chemistry of the Pc macrocycles [21,87,88]. Electron-donating substituents (e.g. amine, ether, thioether, methoxy) shift redox processes towards negative potentials while the presence of an electron-withdrawing group (e.g. fluoro, sulphonate, nitro, ester, carboxylic acid) shift redox processes towards positive potentials [89]. Since the electron transfer abilities of Pcs depend on the kind and the number of the substituents and also on the interaction between the Pc ring and the metal center [81,90-96], Pc redox chemistry can be easily tuned.

1.1.4.2 CoPc and FePc Electrochemistry

The redox behaviour of $Co^{II}Pc$ and $Fe^{II}Pc$ derivatives involves both the metal and the ring [97-100]. The metal based processes for $Co^{II}Pc$ may occur before or after ring processes, depending on the solvent and electrolyte [80,82]. In coordinating solvents such as dimethyl-formamide (DMF), Co^{III} is formed first [23] but in non-coordinating solvents such as dichloromethane (DCM) ring oxidation occurs first. Donor solvents strongly favours M(III) species therefore in their absence oxidation to M(III) is inhibited and the ring oxidation occurs first [80]. Other than the supporting electrolyte, the position of the Fe^{III}/Fe^{II} couple is also affected by pH [76,101].

1.1.4.3 NiPc Electrochemistry

Normally the redox processes for nickel are known to occur on the ring in solution [86]. The Ni^{III}/Ni^{II} processes are not known in solution. This couple has been reported when NiPcs are adsorbed on the electrode surface [44,102-106].

The aim of this work is to synthesize the following: (i) CoTAPc, FeTAPc and NiTAPc, (ii) CoTCPc, (iii) CoMAPc and (iv) CoMCPc for chemical linking to SWCNTs and (iv) convert NiTAPc into an oxo-bridged (O-Ni-O) complex. The SWCNTs used in this work were either synthesized or purchased.

1.2. Carbon nanotubes

1.2.1 Properties

Elemental carbon in sp^2 hybridization can form a variety of interesting structures, such as graphite (3D), graphene (2D), carbon nanotubes (CNTs, 1D) and fullerene (0D) [107]. CNTs were first produced by Iijima by a carbon-arc discharge method [108] and single walled carbon nanotubes (SWCNTs) can be described as a graphene sheet rolled up into a nanoscale-tube (Fig.1.7) [109]. CNTs can either be single-walled (SWCNTs) or multi-walled (MWCNTs, with additional graphene tubes around the core of SWCNTs). Their diameters are in the range between fractions of nanometers and tens of nanometers and lengths of up to several centimeters. Their ends are normally capped by half-fullerene-like structures. The metallic or semiconducting nature of SWCNTs depends on their chirality (i.e. the

chiral angle between carbon hexagons and the tube axis). Chemical synthesis of CNTs is complicated by the need to control the nanotube diameter, chirality and number of walls.

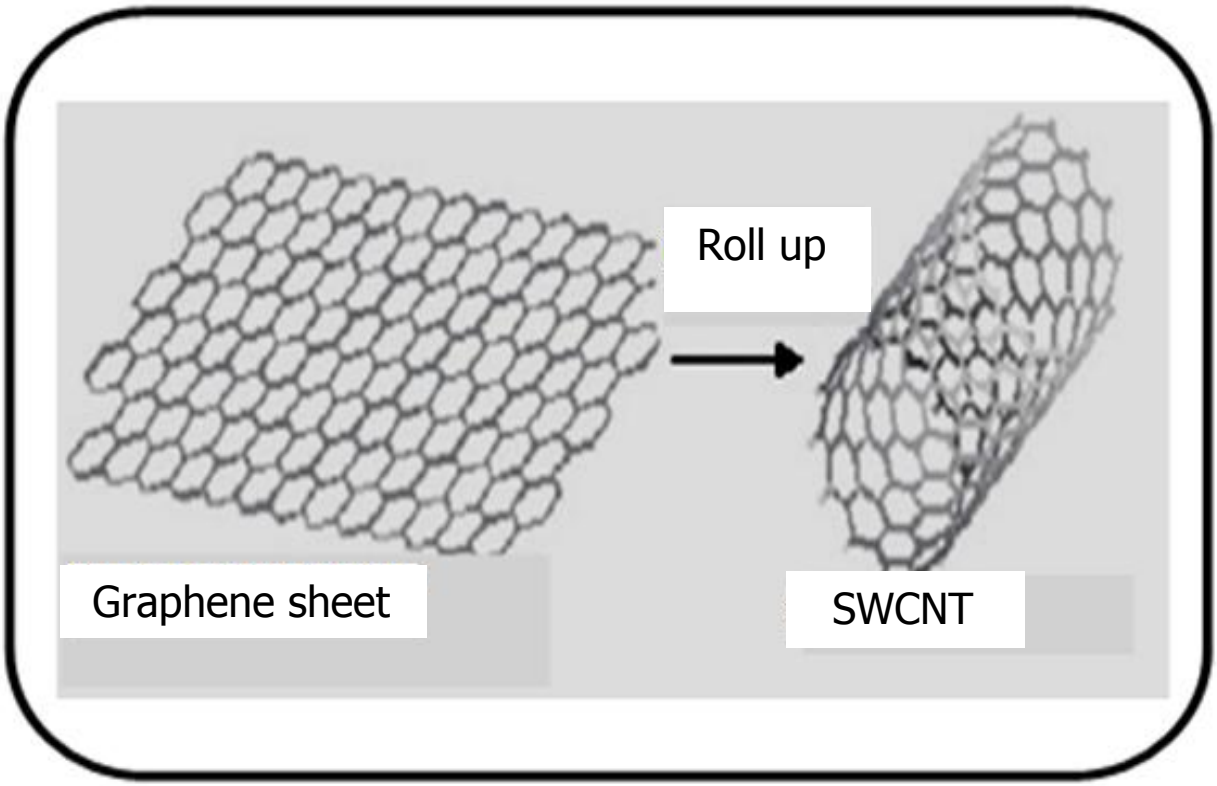

Figure 1.7: Diagrammatic representation of a graphene sheet being rolled into a SWCNT [109].

CNTs exhibit excellent properties, which include high chemical and thermal stability, high elasticity, high tensile strength and some tubes exhibiting metallic and semi-conducting behaviour, with low resistivities at 300 K of ~1.2×10^{-4} – 5.1×10^{-6} ohm cm [108,110]. They have very good conductivity along their tubular axis [111,112] and are earmarked as the key materials for use as molecular wires in molecular electronics [113]. Due to their small size and conductivity, they are also regarded as the smallest possible electrodes with diameters less than one nanometer [114,115]. CNTs can improve the reversibility of the electrode processes [116], hence their use in this study.

Based on their physical and chemical properties, the uses of CNTs include the following: (i) construction of gas sensors [117-119], (ii) electrocatalysts [120-124], (iii) construction of electrochemical biosensors [125,126].

1.2.2 Synthetic approaches

Synthetic approaches include: arc-discharge [108,127,128], laser ablation [129-131], pyrolysis of FePcs [132-143] and catalytic chemical vapor deposition (CCVD) [144]. The first three employ solid state carbon precursors, while CCVD methods use hydrocarbon gases as sources of carbon atoms and catalyst particles that serve as seeds to nucleate the growth of CNTs.

Pyrolysis of MPcs was employed in this work, hence it is discussed in more detail.

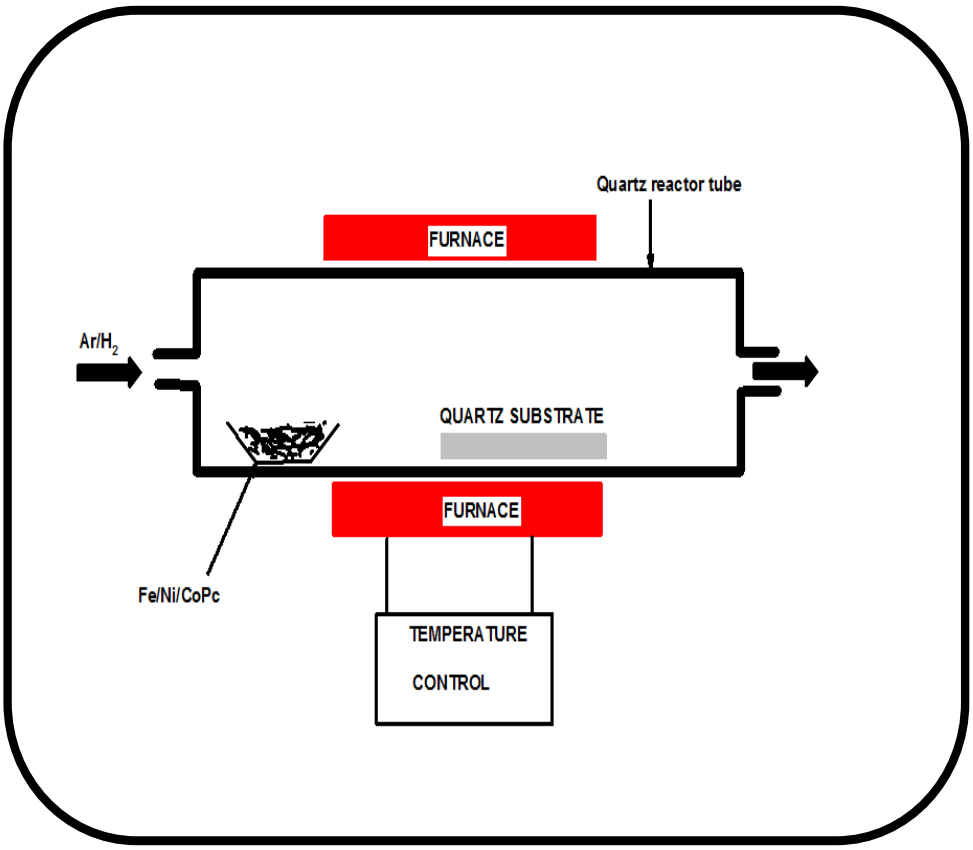

Figure 1.8: Experimental set-up for the synthesis of CNTs from MPcs.

This is a simple and cheap process involving the simultaneous supply of the catalyst source and the carbon source into a substrate or quartz tube to produce well

aligned CNTs [133,136-139], Fig. 1.8. The MPcs (M = Fe, Co, Ni; Pc = $C_{32}H_{16}N_8$) are the sources of carbon and metal catalyst. The major limitation in this synthesis is the lack of control of the CNT diameter size, which Harutyunyan et al tried to address by diluting FePc with various amounts of H_2Pc [140]. Chen et al produced highly disordered, activated FePc nanostructures through ball milling [141-143]. They used horizontal tubular furnaces and a mixture of Ar (95%)–H_2 (5%) carrier gas to produce both horizontal and vertical nanotubes, though their results showed a very slow growth rate accompanied by production of amorphous carbon.

This method was employed in this work for the synthesis of CNTs. For the first time ferric acetate was employed together with FePc and H_2Pc to form SWCNTs. It provides the Fe catalyst required for the initial growths of CNTs as well as inhibiting the formation of MWCNTs. Use of the press to activate MPcs has never been reported before. However for most of the studies, purchased SWCNTs were employed, since synthesis of SWCNTs was achieved towards the end of the PhD program.

1.2.3 Purification of raw CNTs

Purification methods for CNTs include: chemical, physical or a combination of both. The chemical method was employed in this work, hence is discussed in detail. Chemical purification involves oxidation by gases like air, O_2, Cl_2 H_2O, acid treatment and refluxing and electrochemical oxidation. It is based on the selective oxidation, where carbonaceous impurities due to their dangling bonds and structural defects are oxidized at a faster rate than CNTs [107]. In gas phase oxidative purification, CNTs are purified at temperatures ranging from 225 ^{0}C to 760 ^{0}C under a variety of oxidizing atmospheres [145-149] to remove carbonaceous impurities but eventually opening the caps of CNTs without vigorously introducing sidewall defects [107]. Oxidants like HNO_3 [150], H_2O_2 or a mixture of H_2O_2 and HCl [151], a mixture of H_2SO_4, HNO_3, $KMnO_4$ and NaOH [152] and $KMnO_4$ [153] have been used. Liu et al [154] developed a mixture of H_2SO_4/HNO_3 (3:1) compared to the use of HNO_3 alone [107]. Though the liquid phase method removes metal impurities and amorphous carbon, it however opens the CNTs ends and introduces structural

deformations due to the introduction of oxygenated terminals like hydroxyl and carboxylic groups. These groups can serve as points of further derivatization [150,155].

1.2.4 Chemical functionalization of CNTs

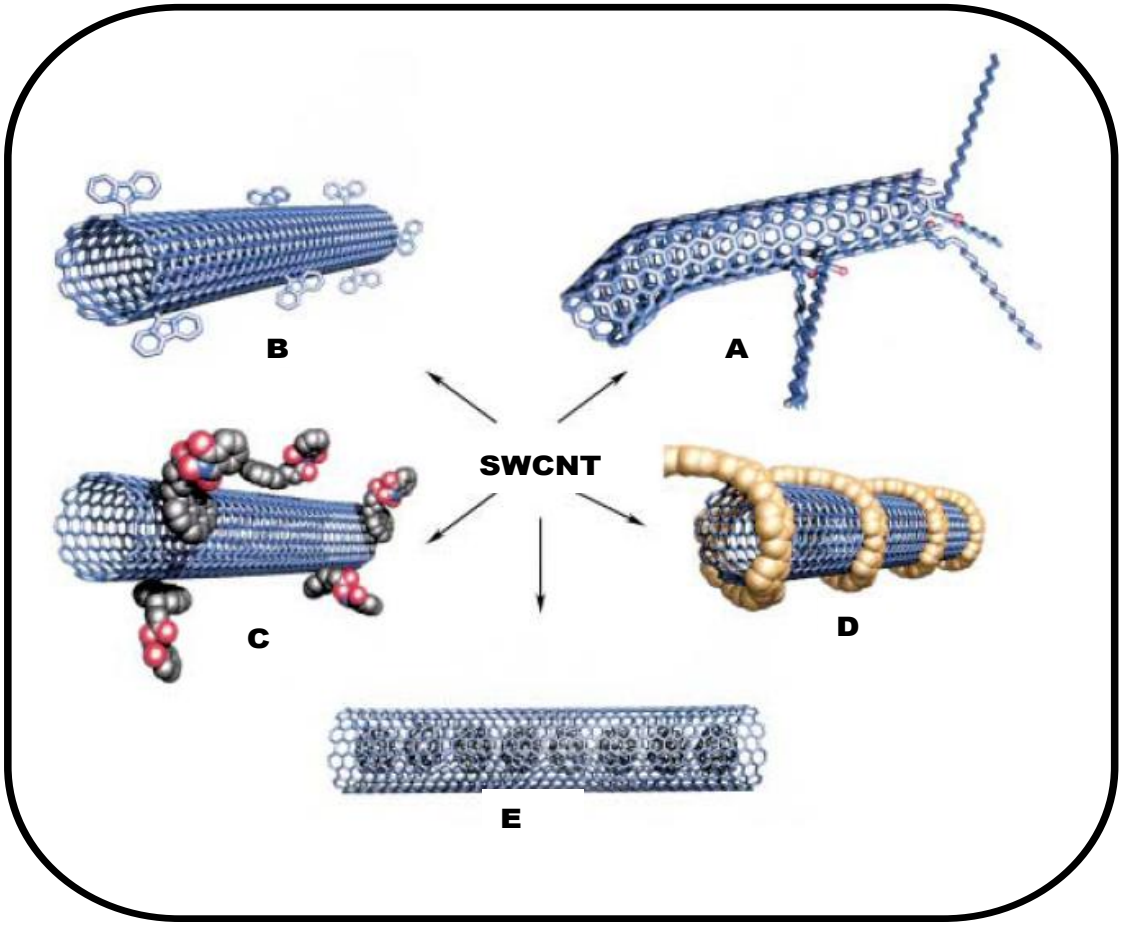

Figure 1.9: Functionalization possibilities for SWCNTs: (A) defect-group functionalization, (B) covalent sidewall functionalization, (C) non-covalent exohedral functionalization with surfactants, (D) non-covalent exohedral functionalization with polymers, and (E) endohedral functionalization with, for example, C_{60} [156] .

Functionalization of CNTs refers to the introduction of functional groups into/onto the CNTs. This can be through non-covalent or covalent bonding. Fig. 1.9 shows the various ways of functionalizing SWCNTs. A, represents defect-group on

the wall or the terminal end of the CNTs or rigorous chemical functionalization which breaks the CNT wall, B is covalent sidewall functionalization, C is the non-covalent exohedral functionalization with surfactants, D is the non-covalent exohedral functionalization with polymers and E is the endohedral functionalization with, for example, C_{60} [156]. CNT walls are generally not reactive, but their fullerene-like tips are known to be more reactive and are easily converted to carboxylic acid, hydroxyl or carbonyl groups [157]. However rigorous conditions can be employed to attach different functional groups onto the CNTs walls/ends [156,158]. This study focuses on covalent functionalization with amino and carboxylic acid groups for further derivatization with synthesized MPcs.

Covalent functionalization provides a higher degree of fine tuning for the chemical and physical properties of SWCNTs than non-covalent functionalization. It can introduce organic molecules and biomolecules that are suitable for biological and biomedical applications on CNTs [159-161]. Suitable covalent functionalization of SWCNTs can improve solubility in solvents including water, which is crucial for biological applications [156,162]. Higher solubility of CNTs requires attachment of relatively large functional groups. Since the first report by Haddon and co-workers [163] on the formation of amide bonds between nanotube-bound carboxylic acids with long-chain alkylamines (e.g. octadecylamine), a variety of oligomeric and polymeric compounds have been used in the functionalization of CNTs to improve their solubility in common organic solvents and/or water. The functionalization breaks the nanotube bundles, which is essential to their solubility. The following groups have been attached to different positions on the SWCNTs: nitrile imines [158], phthalocyanines [164], porphyrins [165], poly(ethylene glycol), PEG [166], amino [167,168] and carboxylic acids [168]. Prato and co-workers successfully applied the 1,3-dipolar cycloaddition of azomethine ylides for the organic functionalization of pristine SWCNTs and MWCNTs which resulted in high levels of solubility of the resulting products [169].

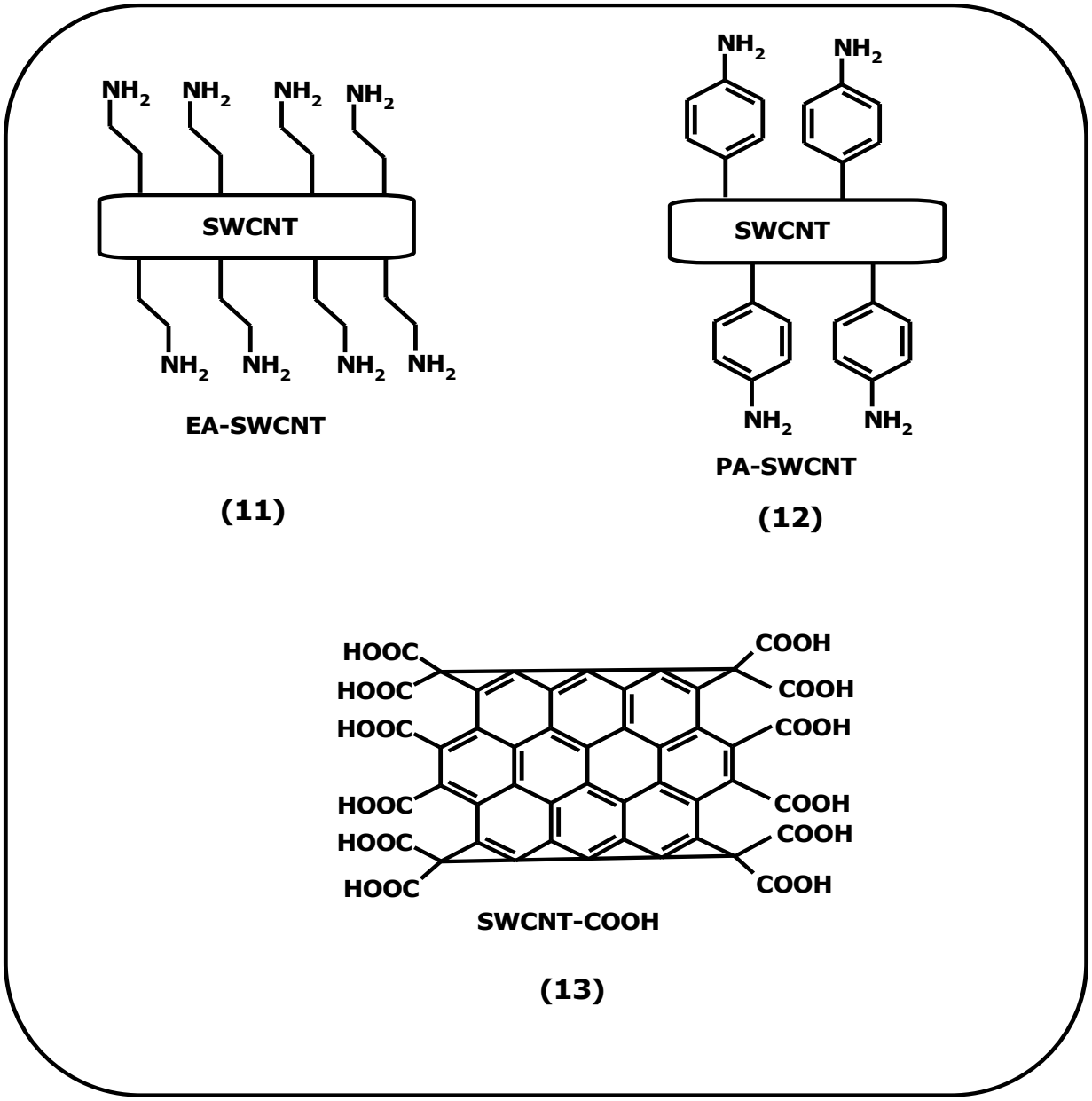

Figure 1.10: Side-wall (11 and 12) and terminally (13) functionalized SWCNTs.

Figure 1.10 shows representative structures for ethylene amine (**11**) and phenylamine (**12**) side-wall functionalized SWCNTs and carboxylic acid functionalized SWCNTs (**13**) that were chemically linked with MPcs in this thesis. Chemical functionalization should be done over shorter times to avoid the loss of CNTs desirable properties [170].

1.2.5 Characterization of synthesized CNTs

In this work, the methods discussed below will be employed for the characterization of SWCNTs in the absence and presence of MPcs (linked or mixed).

1.2.5.1 Transmission Electron Microscopy (TEM)

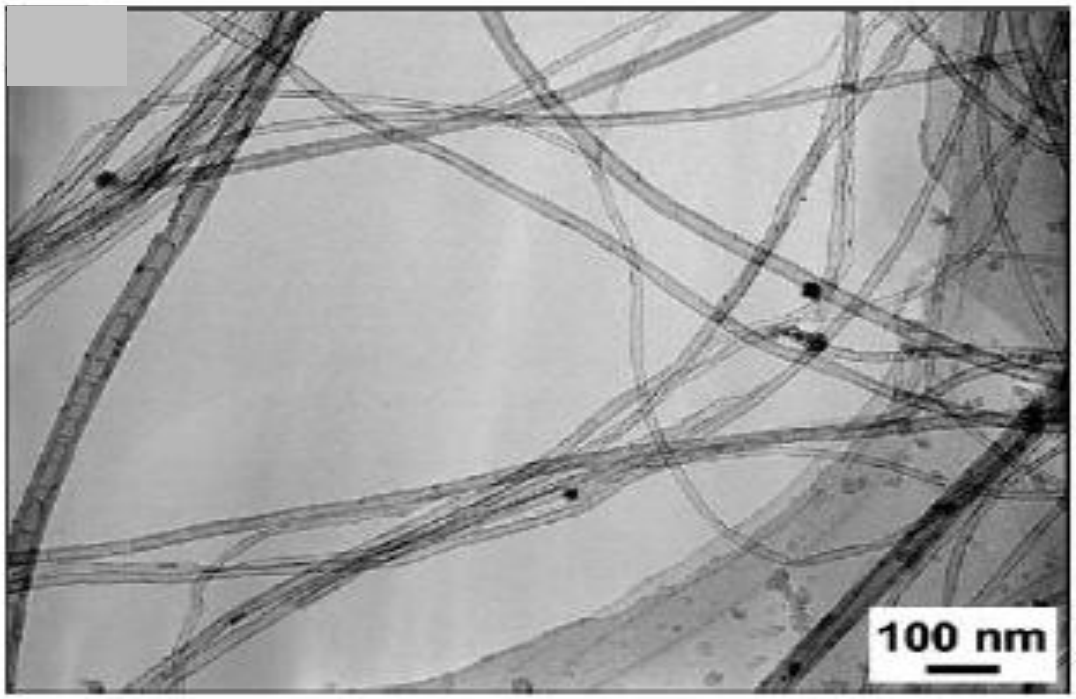

Fig. 1.11: Typical TEM image for CNTs [136].

TEM qualitatively assess the amount of defects, amorphous carbons, or fullerenes adhered on the wall of CNTs [107]. Its limitation is its failure to give quantitative information [171]. Fig. 1.11 shows the TEM images for CNTs [136], with the dark spots representing metallic clusters [164].

1.2.5.2 Thermogravimetric Analysis

Thermogravimetric analysis (TGA) is used for quantitative and qualitative characterization of CNTs. Homogeneity of the CNT samples is evaluated through checking the standard deviations of the oxidation temperature and metal content obtained in several separate TGA runs [172]. Figure 1.12 shows typical TGA traces of (a) raw SWCNTs, (b) amine-functionalized SWCNTs (H_2N-SWCNT), (c) ZnPc-

CONH–SWCNT(linked), (d) ZnPcCOOH:H_2N-SWCNT adsorbed and (e) complex, ZnPcCOOH [52]. The difference in the nature of the TGA profiles confirms the structural differences in these compounds. TGA profiles can be used to estimate the degree of functionalization, water and ash content of the CNTs and MPc-SWCNT conjugates [52].

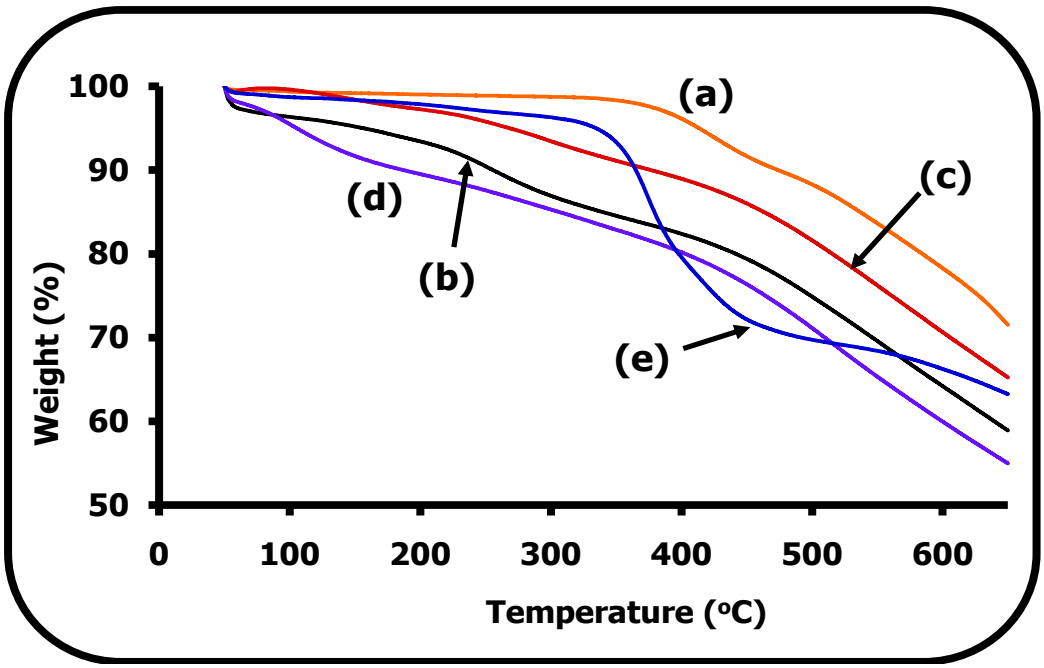

Figure 1.12: Typical TGA profiles of (a) raw SWCNTs, (b) H_2N-SWCNT, (c) ZnPc-CONH–SWCNT(linked), (d) ZnPcCOOH:H_2N-SWCNT(adsorbed) and (e) complex, ZnPcCOOH (10 ^{0}C min^{-1} under N_2) [52].

1.2.5.3 Raman Spectroscopy

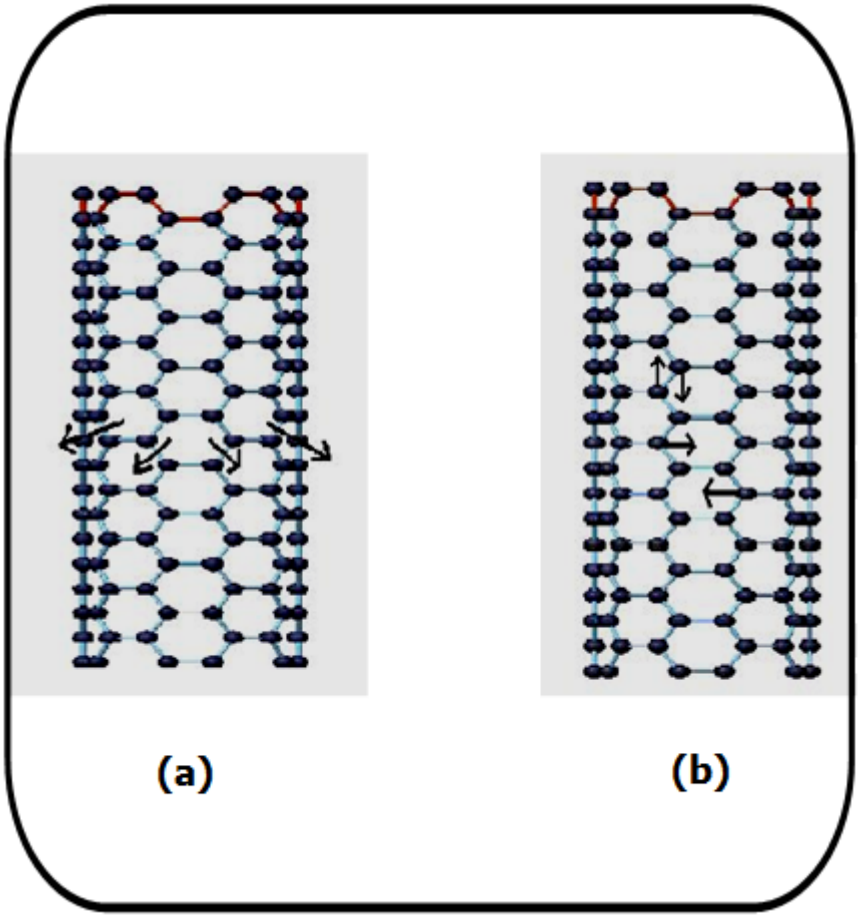

Figure 1.13: SWCNTs structures showing the origin of radial breathing modes (RBMs) and D bands (a) and G-bands (b) [173].

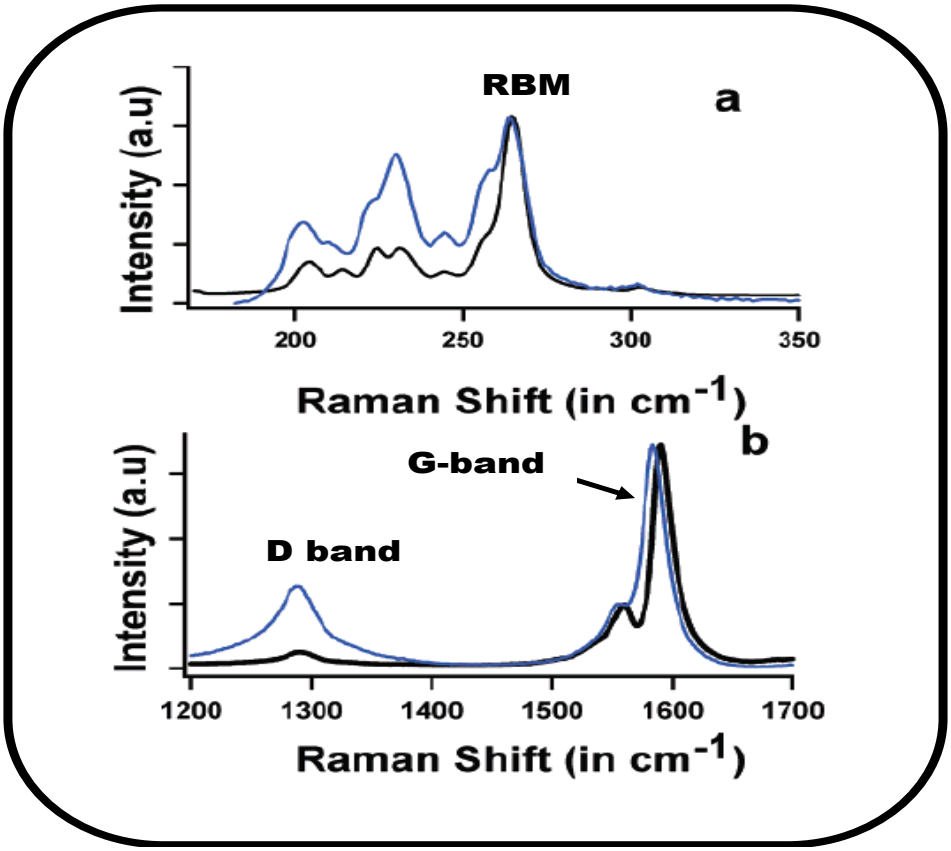

Figure 1.14: Raman spectra for raw (black) and functionalized (blue) SWCNTs. (a) The RBM feature at 264 cm^{-1}, (b) Tangential (G-band) and disorder (D-band) mode regions [174].

The main features of carbon containing compounds (graphite, metallic and semi-conducting nanotubes and amorphous carbons) are the D- and G-bands found at around 1280-1380 and 1560-1605 cm^{-1} respectively [136,164,173-177]. The D-bands are due to breathing modes of sp^2 atoms in rings [175,178,179], while the G-bands are due to bond stretching of all pairs of sp^2 atoms in both rings and chains [179,180], Figs. 1.13 and 1.14. CNTs have a dispersive double resonance G′-band around 2700 cm^{-1} and a non-dispersive phonon mode around 2500 cm^{-1} [177]. They are also characterized by the radial breathing mode (RBM), (100–400 cm^{-1}) [181-183]. The frequency of the RBM is inversely proportional to the tube diameter ($\omega_{RBM} = \alpha/d$, where α = 248 cm^{-1} nm for isolated SWCNTs) while the G-band is weakly depended on the nanotube diameter [177,184]. High peak intensity ratio of G:D bands indicate

that the as-grown CNTs have good crystallinity of graphite sheets [136,179]. 100% pure SWCNTs are characterized by one G-band with RBM and without D-band [107]. The main limitation of Raman spectroscopy is its inability to provide information on the nature of metal impurities and cannot be used on CNT samples with low amorphous carbon content [185].

1.2.5.4 UV-vis-NIR Spectroscopy

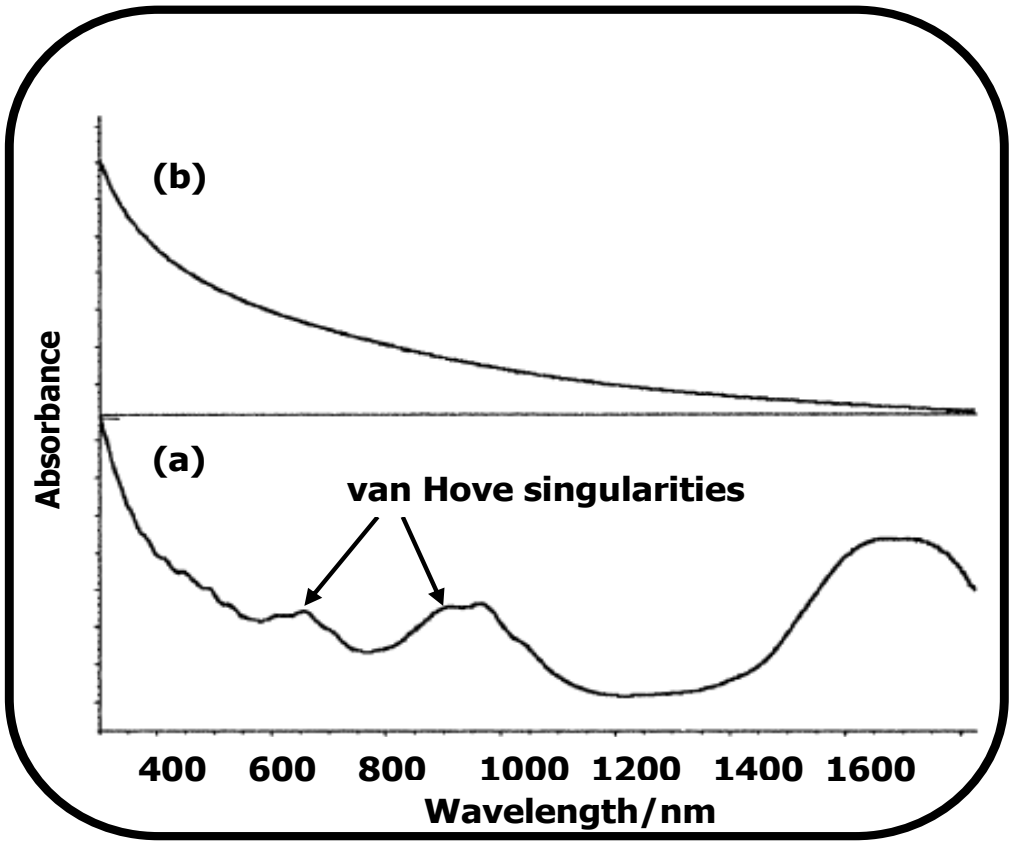

Figure 1.15: UV-vis-NIR spectra of raw SWCNTs (a) and functionalized SWCNTs (b) [186].

UV–vis-NIR spectroscopy is used to estimate the relative purity of bulk SWCNTs [171]. The irregularities in their spectra are due to the van Hove singularities (Fig. 1.15) of metallic and semiconducting nanotubes, whose width reflect the overlap of features from CNTs having different diameters and chiral

indices [186,187]. The van Hove singularities are absent in purified SWCNTs due to the conversion of sp^2 to sp^3 hybridized carbon atoms. Since the л- electrons in the HOMO have been used to form new bonds, the van Hove transitions vanish [167,176,186-188].

1.2.5.5 Infrared Spectroscopy

FT-IR is used to follow the CNTs surface structural changes by monitoring the appearance and disappearance of vibrational bands. Raw CNTs show weak vibrational bands which improve with functionalization [167]. In the presence of MPcs, the change in position of the carbonyl group in the carboxylic acid and in the amide (conjugate) is an important indicator of the formation of a linkage [189-191].

1.2.5.6 X-ray diffraction (XRD) analysis

The broadness and sharpness of the peaks in XRD is indicative of the amorphous and crystalline nature of the material respectively [44]. Phthalocyanines are characterized by a single broad peak in the region $2\theta = 26\text{-}27^0$ [192,193]. CNTs peaks due to the (002) [194-196], (111) [196] and (200) [196] reflections of carbon occur at 2θ values of $\sim 26.5^0$, $\sim 44.5^0$ and $\sim 52.0^0$ respectively. On chemically linking MPcs to the CNTs, both the degree of crystallization and the interplanar space change, implying a new crystal form or a new compound [189]. Changes in peak intensities can also confirm presence of chemical linkages.

1.3 MPc-SWCNT conjugates

1.3.1 Overview of literature

Substitution at the peripheral positions with amino and carboxylic acid groups provide sites for the further coordination of Pcs to CNTs. Chemically linking CNTs to MPcs [197,198] is known to improve electro-catalysis of MPcs, since SWCNTs can readily accept charges and in turn transport them along their tubular axis [199]. CNTs are good electro-catalysts for a variety of analytes [116, 200] and because of this they can enhance the performance of MPcs.

Very few MPcs have been chemically linked to SWCNTs, e.g. for the purpose of drug delivery [65-67] and electrocatalysis [68,201]. From literature search, the majority of the work done was focused on combining acid treated CNTs with MPcs, either as SAMs or mixed or MTAPc electro-polymerized on electrodes pre-modified with CNTs [68,69,75,77,202-207], using either iron or cobalt as metal centres. The use of SAMs [68,199,204] on Au surfaces increases the distance to be travelled by the electron during redox processes. On the other hand, the use of MPc/SWCNTs mixtures [69,75,202,205,208] does not give well defined nanostructures on the electrode surface and increases chances of aggregation on the electrode surface which reduces the sensitivity towards the analyte [68,205]. Ozoemena et al [68] attached CoTAPc linked to SWCNTs to pre-formed aminoethanethiol (AET) SAM on gold (Au) surface for the detection of dopamine. Because of the presence of the linker (AET), the explicit role played by the SWCNTs is not clearly defined. Similarly the individual role played by the MPc and SWCNTs in mixtures is not clear. The current study is therefore focused on directly linking SWCNTs decorated with either amino or carboxylic acid groups to MPcs in order to clearly evaluate the role played by the SWCNTs on the electrochemical performance of MPcs. The behaviour of these conjugates can then be evaluated against the bare electrode, the MPc, the SWCNT and the MPc/SWCNT(mixed) modified electrodes in the presence of an analyte.

The lower redox currents of SWCNTs and MPcs observed in SAMs may be a result of incomplete coupling [205,207]. In this study thionyl chloride ($SOCl_2$) was used to ensure exhaustive conversion of –COOH groups into the acid chloride derivatives (-COCl) which made chemical linking much easier and effective.

1.3.2 Synthetic approaches

Table 1.1: Selected synthesized MPc-CNTs conjugates from literature

Functional group on CNT	Functional group on MPc and Metal	Linkage formed (advantages)	Limitations	Ref
(i) Carboxylic acid	▪amino **Mn, Er (erbium)**	▪Amide (Improved solubility)	▪Hydrolysis of linkage; ▪CNT functionalization needs excess of reagent.	**189, 50**
(ii) Amino	▪Carboxylic acid **Zn, Zn**	▪Amide (Improved solubility)	▪As **(i)** above	**52, 199**
(iii) 4-(2-trimethyl) ethynyl-aniline	▪Azide **Zn**	▪C-C (C-C bond very stable; Improved solubility)	▪As **(i)** above	**209**
(iv) Pyrrolidine, carboxylic acid	▪Hydroxyl, ▪Aldehyde Zn	▪Ester (Improved solubility)	▪ Number of COOH moieties on the CNTs uncontrollable; ▪Hydrolysis of linkage;	**164**
(v) Carboxylic acid	▪Amino **Co**	▪Amide	▪As **(i)** above	**201**
(vi) Carboxylic acid	▪Amino **Co**	▪Amide	▪As **(i)** above	**198**
(vii) Carboxylic acid	▪alcohol **Fe**	▪Ester ▪Amide ▪Au-S	▪Hydrolysis of linkage; ▪CNT functionalization needs excess of reagent.	**207**
(viii) Carboxylic acid	▪Amino **Co**	▪Amide ▪Amide ▪Au-S	▪As **(i)** above	**68, 204**

Table 1.1 lists some selected soluble conjugates that have been synthesized. Most of them carry Zn as the central metal [50,52,74,164,189,199,209]. These conjugates are mainly used as photo-active donor-acceptor hetero-junction materials

for photo-detectors [50,189] and photo-sensitization [52]. Conjugates **(v)** and **(vi)** were used in the catalysis of sulfhydryl degradation products of V-type nerve agents [201] and decolourisation of rhodamine 6G [198], respectively. In this study, as stated before, conjugate **(v)** in Table 1 is being used for comparative purposes. Conjugates **(vii)** and **(viii)** are SAMs and contain Fe and Co metal centres respectively, with the SWCNTs sandwiched between the pre-formed Au-cysteamine platform and the MPc.

The electrochemistry of FeTAPc linked to SWCNTs only, without SAM formation has not been reported. It is therefore necessary to investigate the specific role played by the SWCNTs on the electrochemical behaviour of FeTAPc. So far no work has been reported on NiTAPc chemically attached to SWCNTs or as SAMs. Therefore it is worthwhile to explore the electrochemical behaviour of the NiTAPc-SWCNT conjugate, especially by looking at the role likely to be played by the Ni^{III}/Ni^{II} redox couple in electrocatalysis in the presence or absence of SWCNTs.

In this study SWCNTs and MPcs (M = Co, Fe and Ni, **7a-c, 8-10**, Figs. 1.2, 1.3) were chemically linked together in order to provide good platforms for the efficient transfer of electrons. The MPcs that were tetra- or mono-functionalized with amino and carboxylic acid groups, respectively, were chemically linked to SWCNTs that were terminated with carboxylic acid groups (**13,** Fig. 1.10) and side-wall functionalized with amino groups (**11**, **12,** Fig. 1.10) using ethane-1,2-diamine and benzene-1,4-diamine, respectively. These synthesized MPc-SWCNT conjugates (Figs. 1.16 - 1.20) are linked via an amide bond. This linkage is the bridge that facilitates the smooth flow of electrons from the MPc to the SWCNT and vice-versa, enhancing electrocatalysis. The presence of phenylene ($-C_6H_4-$), Fig. 1.17, and ethylene ($-CH_2CH_2-$), Fig. 1.18, groups enhances solubility of the conjugates as well as providing different electron transfer pathways. These modifiers provide a large surface area for electrocatalysis because of their large surface-to-volume ratio. Linking SWCNTs to unsymmetrically substituted MPc complexes is still relatively unexplored due to the difficulties in the synthesis of these complexes, as a result of a wide range of isomers that require extensive column purification, resulting in low yields. Covalently linking CoMAPc (**9**) and CoMCPc (**10**) to acid and amine

derivatized SWCNTs produces nanorods and nanomesh conjugates, respectively, which have well defined structures of limited size. The CoMAPc molecules terminate the ends of the SWCNTs while the CoMCPc is attached to the outside walls of the SWCNTs. Both can offer well defined structures on the surface of the electrode.

Even though they are connected by amide linkages, it is important to note that with the exception of CoTAPc-SWCNT complex, all the synthesized conjugates are unique and have not been reported before. As stated before the CoTAPc-SWCNT conjugates are being used in this study for comparative purposes. The application of mono- and tetra- substituted Pcs linked to SWCNTs in the detection of amitrole, diuron and 2-mercaptoethanol (2-ME) is new.

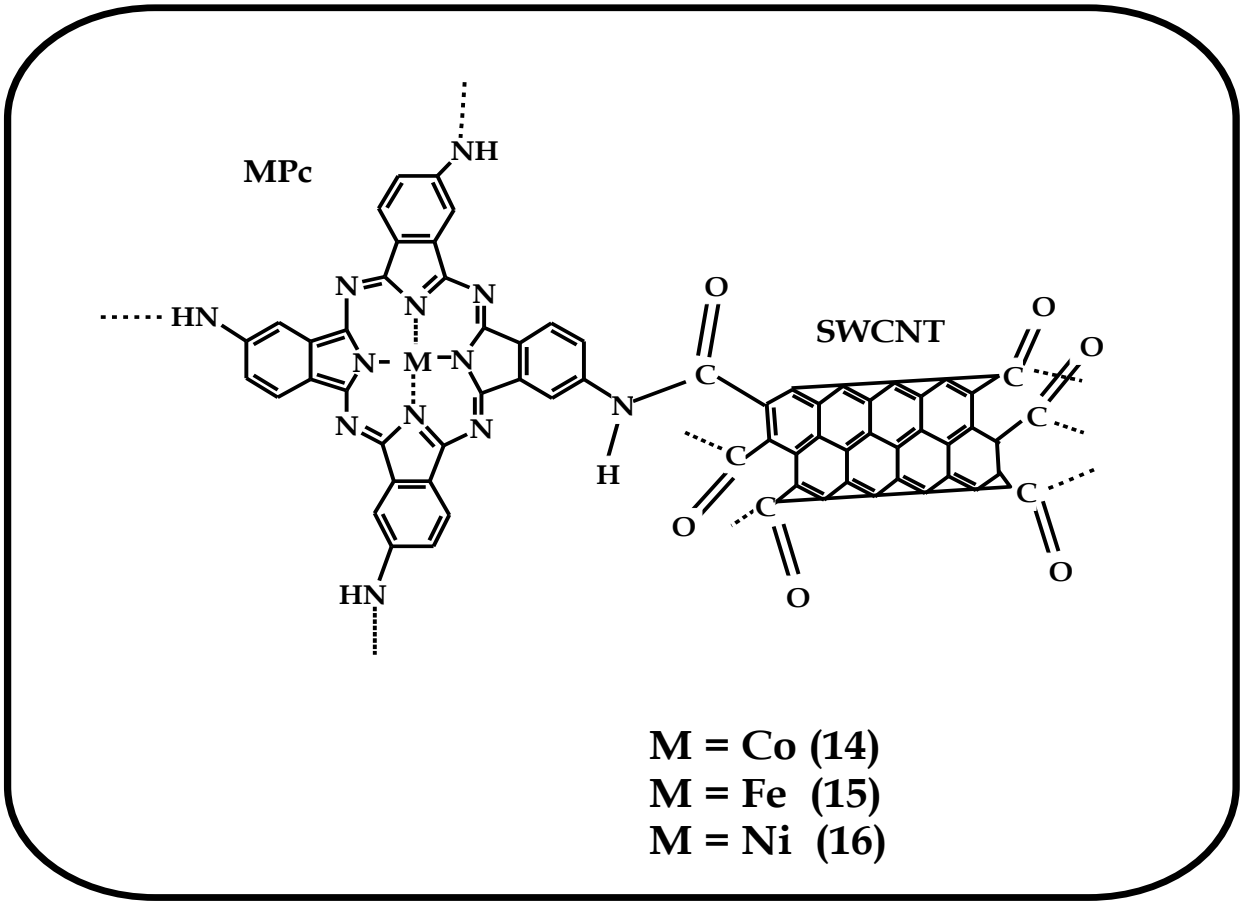

Fig.1.16: Representative structure of MTAPc-SWCNT conjugates, where M = Co (14), Fe (15) and Ni (16).

Fig. 1.16 shows the representative structure for the conjugates synthesized by chemically linking tetraamino-substituted MPcs (MTAPcs) with acid functionalized SWCNTs (SWCNT-COOH), where M represents Co, Fe and Ni for conjugates **14**, **15** and **16,** respectively. These conjugates were used in studying the effect of SWCNTs on the electrocatalysis of amitrole, diuron and 2-ME in the presence of different MPc derivatives.

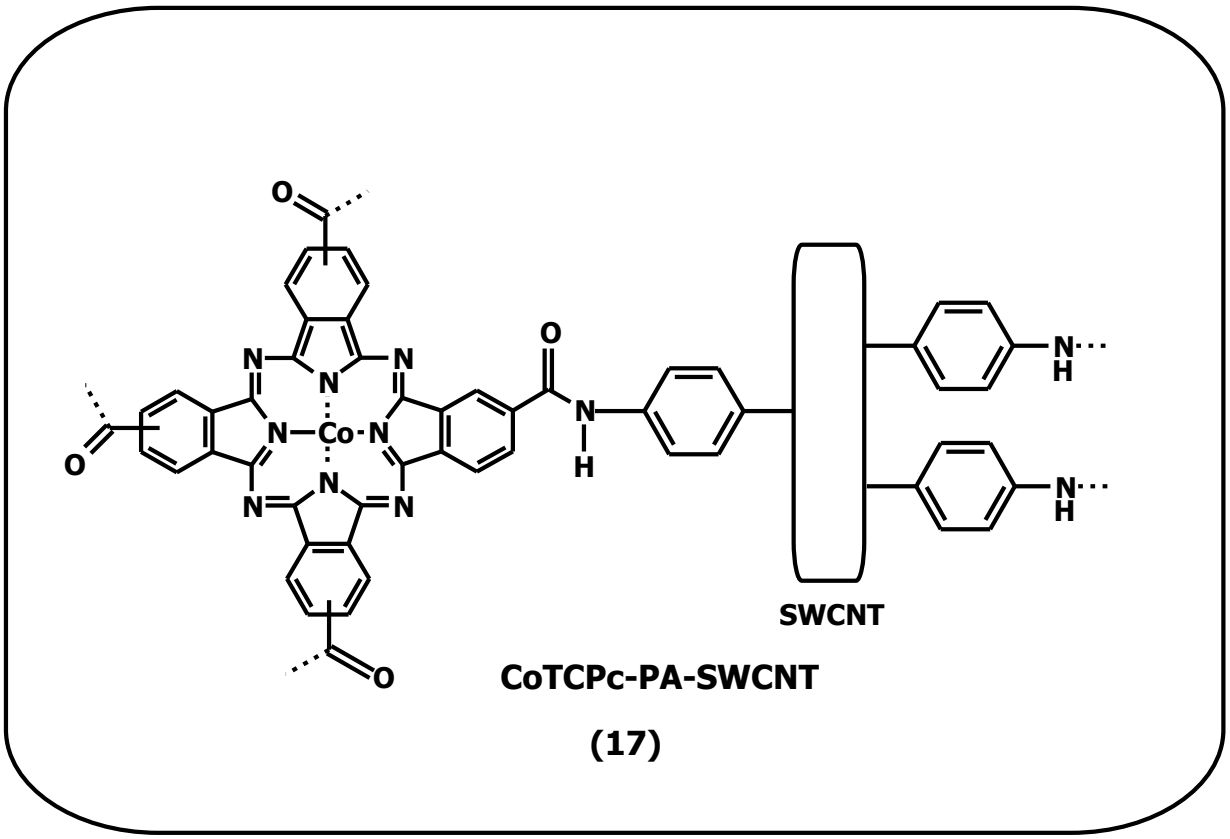

Fig.1.17: **Representative structure of CoTCPc-PA-SWCNT linked conjugates (17). PA = phenylamine.**

Fig. 1.17 shows the representative structure (**17**) for the conjugate formed between CoTCPc and phenylamine functionalized SWCNTs (PA-SWCNT). The phenylene (-C_6H_4-) group forms a bridge between the SWCNT and the CoTCPc. This conjugate is used to study the influence of the SWCNT amino groups on the electrocatalytic properties of the MPc, and how this compares with the behaviour of MTAPc-SWCNT conjugates, Fig. 1.16.

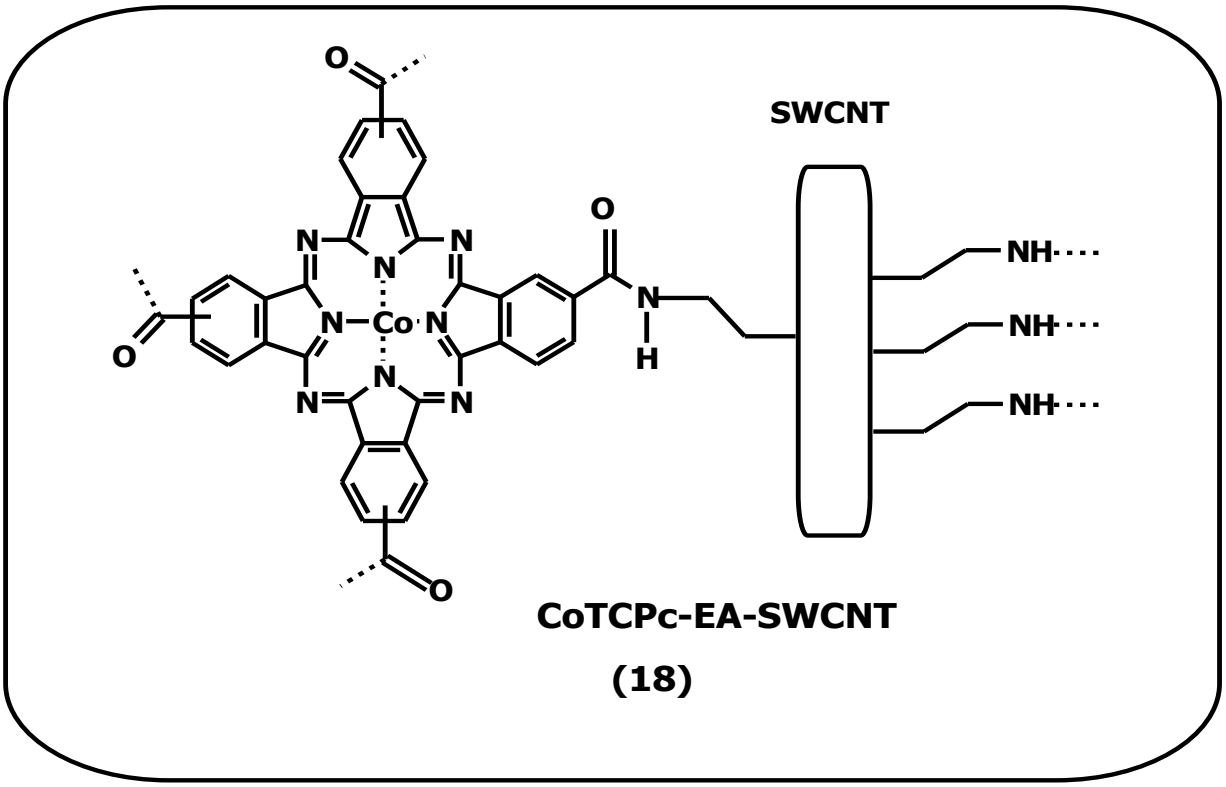

Fig.1.18: Representative structure of CoTCPc-EA-SWCNT linked conjugates (18). EA = ethylene amine.

Fig. 1.18 shows the representative structure (**18**) for conjugate formed between CoTCPc and ethylene amine functionalized SWCNTs (EA-SWCNT). The ethylene (-C_2H_4-) group forms a non-conjugated bridge between the SWCNT and the CoTCPc. This conjugate is used to compare the effect of the conjugated linker (phenylene) versus non-conjugated linker (ethylene) on electrocatalysis. The electrocatalytic properties of CoTCPc-EA-SWCNT and CoTCPc-PA-SWCNT conjugates are then compared with MTAPc-SWCNT conjugates in which the MPc is directly bonded to the SWCNT without any linkers.

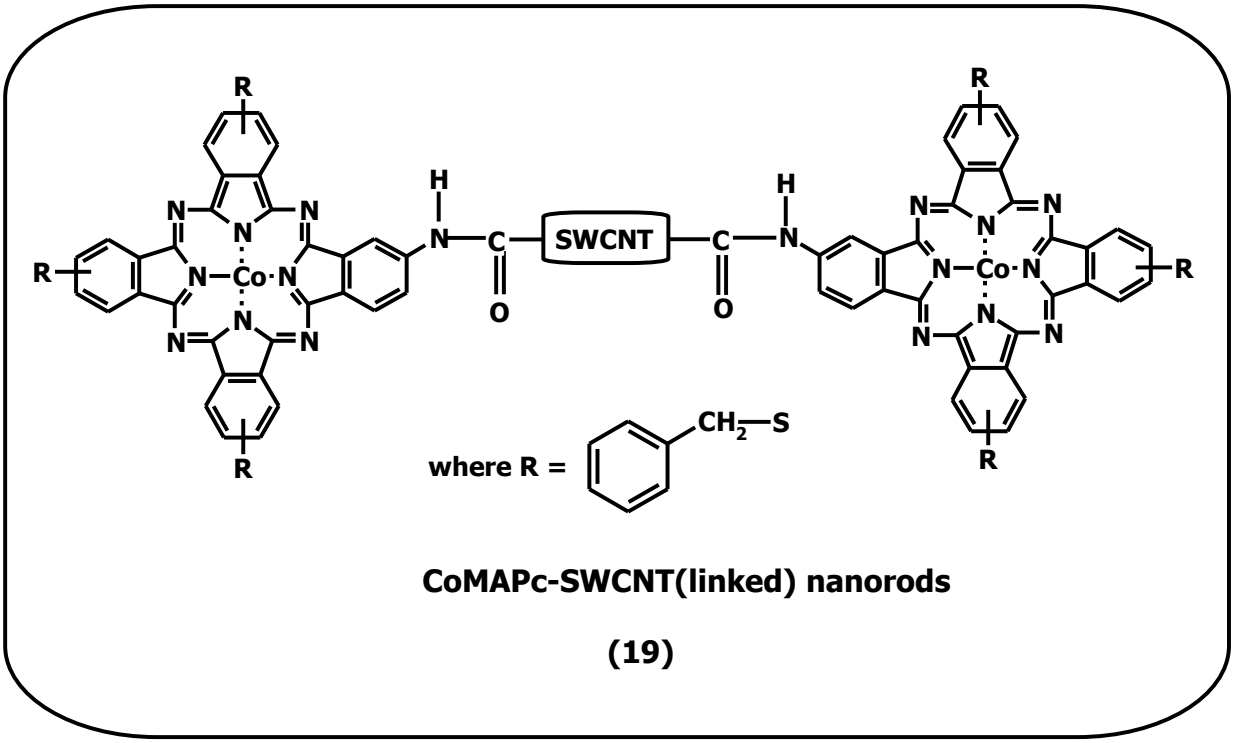

Fig.1.19: Representative structure of CoMAPc-SWCNT linked conjugates (19).

CoMAPc **(9),** Fig.1.19, is an unsymmetrical monoamino-substituted Pc (MAPc). The CoMAPc molecules terminate the ends of the acid functionalized SWCNTs (**19**). In the presence of a single amino group, well defined nanorod structures are easily formed. Since there are very high probabilities of having more than one carboxylic acid group at the SWCNT ends, more than one CoMAPc molecules can chemically attach at these ends.

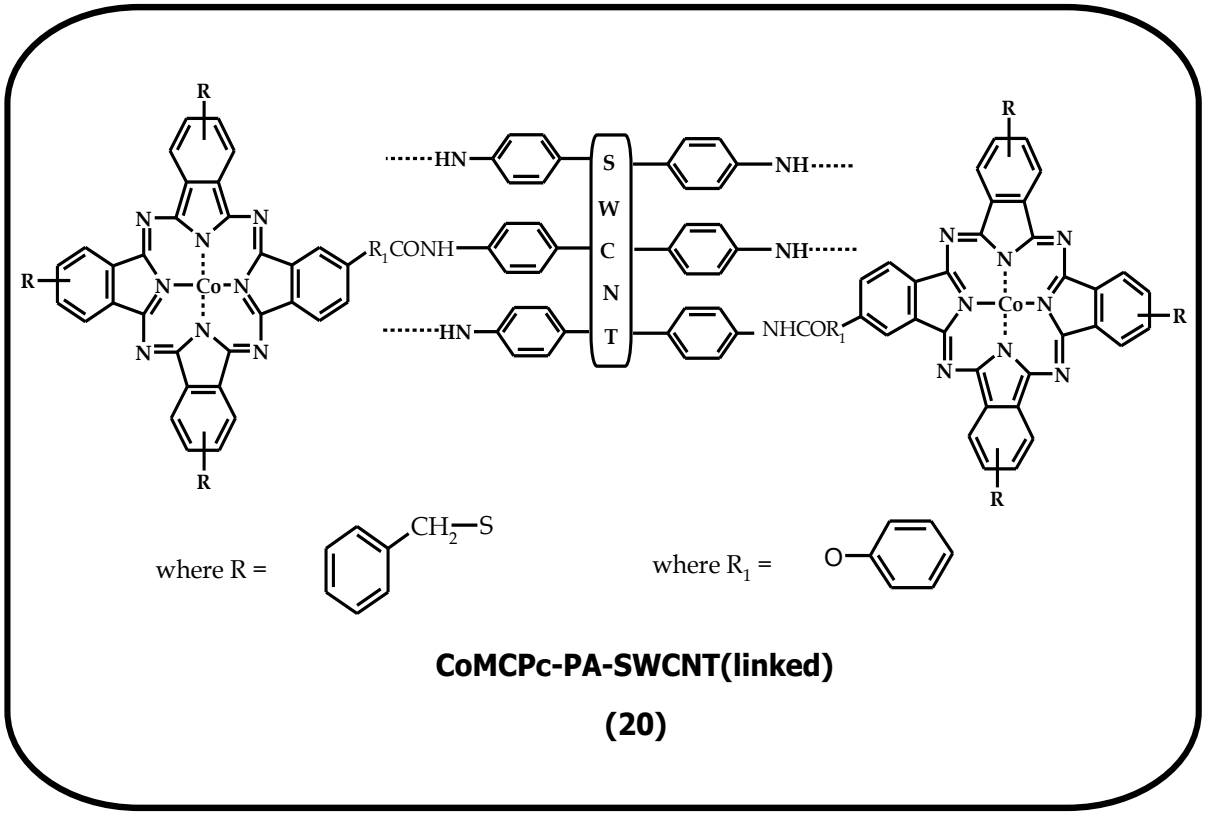

Fig.1.20: Representative structure of CoMCPc-PA-SWCNT linked conjugates (20).

The structure shown in Fig. 1.20 is representative of the conjugate formed between CoMCPc and PA-SWCNT. The CoMCPc is an unsymmetrical mono(carboxyphenoxy)-phthalocyanine (MCPc) and is bonded along the walls of the SWCNT, giving a nanomesh structure. The electrocatalytic properties of these conjugates will be compared with those of the nanorods (CoMAPc-SWCNT, **19**). The aryl thio group donates electrons to the Pc ring and ultimately the metal centre in both conjugates (**19** and **20**) and this influences the redox chemistry of cobalt.

1.4 Chemically Modified Electrodes (CMEs)

The following electrodes have been modified with MPcs and CNTs to give highly electrocatalytic chemically modified electrodes (CMEs): gold (Au), glassy carbon (GCE), ordinary pyrolytic graphite (OPG), highly oriented pyrolytic graphite (HOPG), indium titanium oxide (ITO) [21] and basal plane pyrolytic graphite (BPPG) [75]. Solid state redox processes can be observed when the Pc is immobilized

onto the electrode surface and then cyclized in an appropriate buffer, normally under aqueous conditions [21] where the electrode does not dissolve. Modified glassy carbon electrodes (GCE) were used in this study.

1.4.1 Methods of electrode modifications using MPcs

Methods of electrode modifications include direct deposition of MPc solution on the electrode through adsorption (dip-dry/drop-dry) [46], mixing of the MPc with carbon paste to make a conductive carbon cement [210], electropolymerization [96], electrodeposition [211], spin coating [212], vapour deposition [211] and by the formation of self assembled monolayers (SAMs) on metals such as gold and silver [2,29,94,95,213]. In this work, electropolymerization and the adsorption methods were employed and will be discussed in detail.

1.4.1.1 Electropolymerization

The process occurs through the immersion of an electrode into a solution of the monomer, followed by repetitive cycling between two predetermined potentials. Polymer formation is confirmed through differences in the nature of successive scans, as well as appearance of new peaks [214]. Electropolymerization is said to be complex and is believed to proceed via a general electrochemical-chemical-electrochemical, E(CE)*n*, mechanism [215] of substituents containing 'N' or 'S'. Frequently electropolymerized MPcs, carry amino-, pyrrole- or thiophene-appended complexes [53,216-219]. MPcs with such substituents are suitable in that coupling of their strong and well-defined electronic л-systems produce polymers of high stability and rigidity. Polymerization involves the formation of monomer free radicals that couple until the polymer becomes insoluble in the medium and precipitates onto the electrode surface [220]. Figure 1.21 shows a typical polymerization voltammogram evolved on a GCE for MnTAPc dissolved in DMF containing tetrabutylammonium tetrafluoroborate ($TBABF_4$) after continuous successive cyclisation [221].

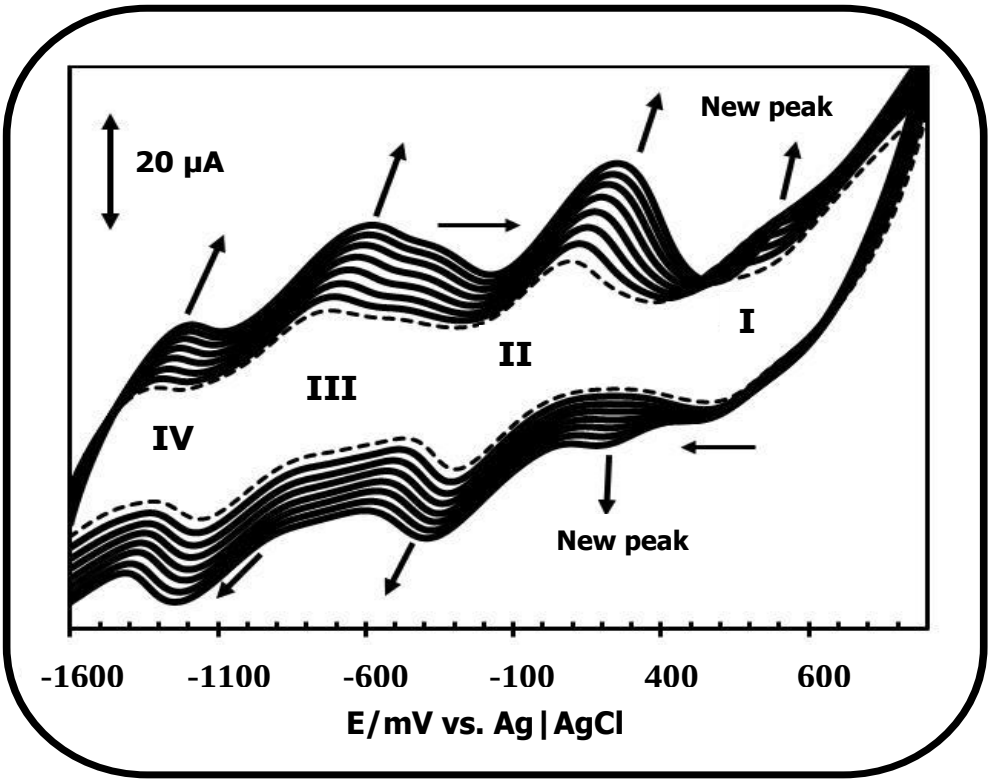

Figure 1.21: Typical polymerization voltammogram for MnTAPc (~3 × 10^{-4} M) on GCE in DMF containing 0.01 M $TBABF_4$ during repeated successive scans (only eight scans are shown). Scan rate: 200 mVs^{-1} (−1.8 to 1.2V vs. Ag|AgCl) [221].

Electropolymerization increases stability and electrocatalytic activity of these systems [46,221-223]. Relative to such techniques as ''dip-dry/drop-dry'' methods, it is largely elegant, attractive and easy [224]. It is reproducible and the thickness of the modifier on the electrode can be accurately controlled [225]. Thermal and chemical stability is enhanced without compromising the catalytic activity. A three-dimensional reaction zone is formed, hence increased sensitivity and reaction rates. Electrochemical polymerization can occur in both aqueous and organic media [224]. The disadvantage of polymerization is that monolayer surface coverage is difficult to achieve and control at times.

1.4.1.2 Adsorption (dip-dry/drop-dry)

The catalyst (MPc) is dissolved in a solvent where maximum solubility is achieved. In dip-dry method, the electrode is dipped into the MPc solution and then allowed to dry, while for drop-dry, the MPc solution is dropped onto the electrode surface and then allowed to dry. The CNTs are pre-sonicated in solvents like DMF [125,226] and dimethyl-sulphoxide (DMSO) [227] and then adsorbed onto the electrode surface using the drop-dry method [121,227]. Alternatively the CNTs can be abrasively immobilized onto the electrode surface [228]. Immobilization of CNTs is encouraged by the л-л interactions that occur between them and the GCE. The advantage of this modification process is that it is fast and depending on the nature of the electrode used, a relatively stable Pc/SWCNT layer can be formed on e.g. carbon based electrodes where л-л interactions can occur between the MPc and SWCNTs, and the substrate surface. The disadvantages are that the electrode surfaces are not reproducible and unstable over long periods of time.

Both electropolymerization and adsorption were employed in this work. The dip-dry/drop-dry method was used to immobilize MPcs onto the electrode surface in the presence of SWCNTs. As stated above SWCNTs have been coordinated to tetra-substituted Pcs [68,201] since these Pc complexes are commercially available and their synthesis is relatively simple. Coordination to monosubstituted Pcs is relatively new.

1.4.2 Characterization of CMEs

1.4.2.1 Cyclic Voltammetry (CV)

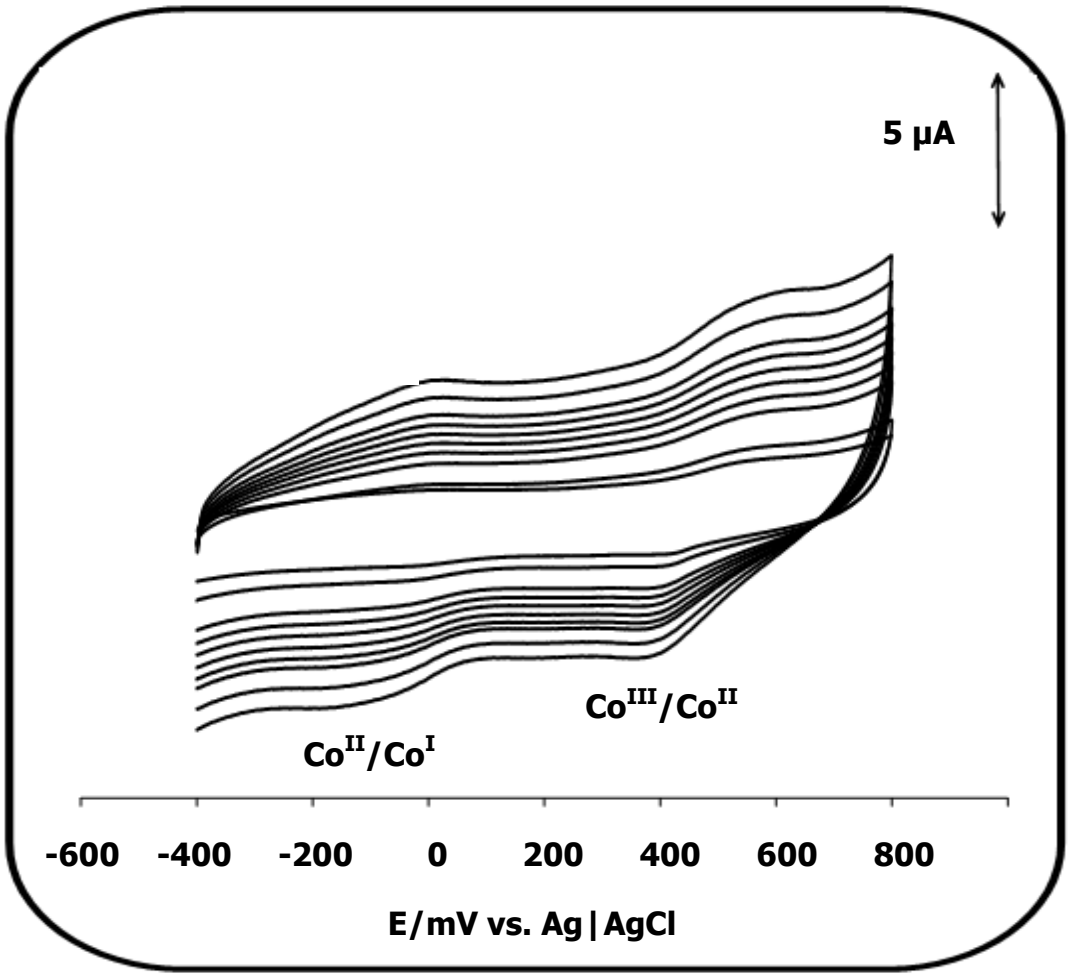

Figure 1.22: Typical cyclic voltammograms (CVs) of CoPc-GCE recorded in pH 4 buffer showing the dependence of peak currents on scan rates [**229**].

Fig. 1.22 shows the typical voltammogram for a CoPc modified electrode cyclized in pH 4 buffer [229]. The Co^{II}/Co^{I} and Co^{III}/Co^{II} redox couples are well defined. This shows that when an electrode has been modified, on cyclising it in an appropriate buffer solution, a voltammogram typical of the surface immobilized species is produced. Fe^{II}/Fe^{I} and Fe^{III}/Fe^{II} redox couples have also been observed for both adsorbed and polymerized FeTAPc [76]. These redox processes can also be observed in the presence of SWCNTs [230].

Fig.1.22 shows an increase in peak current with scan rate, which is typical of surface confined species [229,230]. For both electropolymerization and adsorption processes, a linear relationship exists between the background corrected peak current (I_p) for the surface-immobilized species and the scan rate (v) and from the slope of the linear plot and using Eq. 1.1 [231], the surface coverage can be estimated.

$$I_p = \frac{n^2F^2}{4RT} \upsilon A \Gamma_{\mathrm{MPc}} \quad (1.1)$$

where I_p is the background corrected peak current, n is the number of transferred electrons, F is the Faraday constant, Γ_{MPc} is the film surface coverage, A, is the effective electrode area, υ is the scan rate, R is the gas constant and T is the temperature.

Alternatively, the surface coverage can be estimated through the charge under the redox peaks of the MPc or MPc-SWCNT conjugates, produced in a buffer solution, using Eq. 1.2, Fig. 1.22.

$$\Gamma_{MPc} = \frac{Q}{nFA} \quad (1.2)$$

where Q is the charge under the oxidation or reduction peak and all other symbols are as described above.

Cyclic voltammetry (CV) provide a rapid and simple way of acquiring information about the rate of electron transfer, redox processes, the stability of the analyte, the stability of the electrode modifier, the adsorption processes as well as electrode kinetics and mechanisms [229,232-235].

1.4.2.2 Electrochemical impedance spectroscopy (EIS)

1.4.2.2.1 Nyquist Plots

Electrochemical impedance spectroscopy (EIS) is used to probe the redox and structural features of a surface confined species [201].

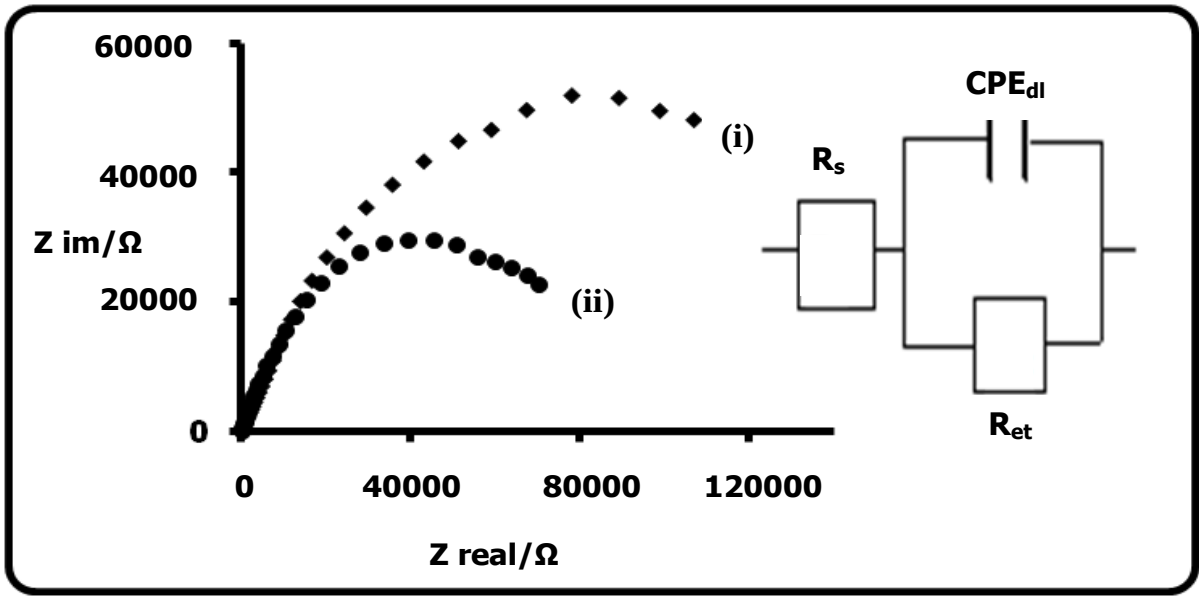

Figure 1.23: Typical Nyquist plots obtained on (i) bare GCE and (ii) CoPc modified electrode. Inset: Equivalent Randles' circuit model.

Fig. 1.23(i) and (ii) show the Nyquist plots for the bare and CoPc modified electrode, respectively. The semi-circles represent a combination of charge transfer resistance and the double layer capacitance of the electrodes [236] and are in agreement with kinetically controlled movement of electrons [68]. The origin of the semi-circles in Nyquist plots is attributed to microscopic roughness, which brings heterogeneity in solution resistance and the double layer capacitance [237]. The diameter of the semi-circle is proportional to charge-transfer resistance (R_{et}) and the decrease in the value of R_{et} proves that the films can form high electron conduction pathways between the electrode and electrolyte/analyte [238]. Fig. 1.23, inset, shows the circuit that is compatible with the given Nyquist plots in Fig. 1.23. R_s, CPE_{dl} and R_{et} represent solution resistance, a constant phase element (corresponding to the double layer capacitance) and the charge transfer resistance, respectively. The nature of circuit is variable and depends on whether the electrode processes are controlled by kinetics or diffusion [201].

The apparent electron - transfer rate constants, k_{app}, which indicates how fast the charge transfer occurs on the electrode surface are calculated using Eq. 1.3 [239].

$$k_{app} = RT/F^2 R_{et} C \quad (1.3)$$

where C, R, T and F represent the concentration (mol cm^{-3}), the universal gas constant, the temperature in Kelvins and the Faraday constant, respectively.

1.4.2.2.2 Bode Plots

The nature of the Bode plots confirms the structural differences between the bare electrode and modified electrodes. Bode plots ((phase angle versus log f), Fig. 1.24a), shows a well-defined symmetrical peak for the bare electrode at a particular angle and corresponding frequency, representing the relaxation process at the electrode|solution interface. This relaxation process shifts to different phase angles and frequencies on modification of the electrode. These shifts indicate that the reactions are now occurring at a modified surface rather than the bare electrode. The slopes in Fig.1.24b should be ~ -1 for ideal capacitors.

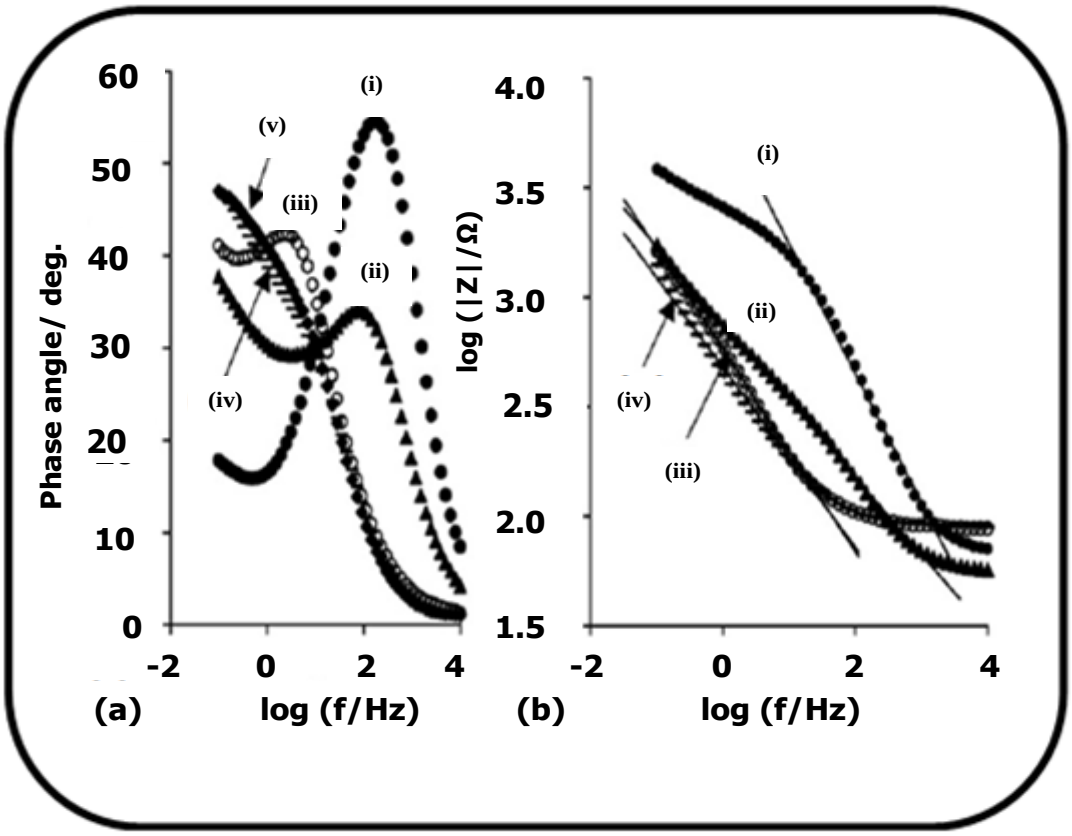

Fig. 1.24: Typical Bode plots of (a) phase angle vs. logarithm of frequency and (b) logarithm of complex impedance vs. logarithm of frequency for the following electrodes (i) bare, (ii) CoTAPc, (iii) SWCNT-CoTAPc(linked), (iv) SWCNT/CoTAPc(mix) and (v) SWCNT in 0.1M KCl containing 1 mM $[Fe(CN)_6]^{3-/4-}$ solution [201].

1.4.2.3: Raman spectroscopy

Raman spectroscopy can prove the presence of a modifier on the electrode surface. When a clean GCE is subjected to Raman analysis, a single G-band in the region 1560-1600 cm^{-1} [107,136,164,175-178] should be observed. A modified electrode would show more peaks that are characteristic of the adsorbed species. Raman analysis of zinc phthalocyanine [240] and SWCNTs [241] adsorbed on glassy carbon has been done.

1.4.2.4 Atomic force microscopy (AFM)

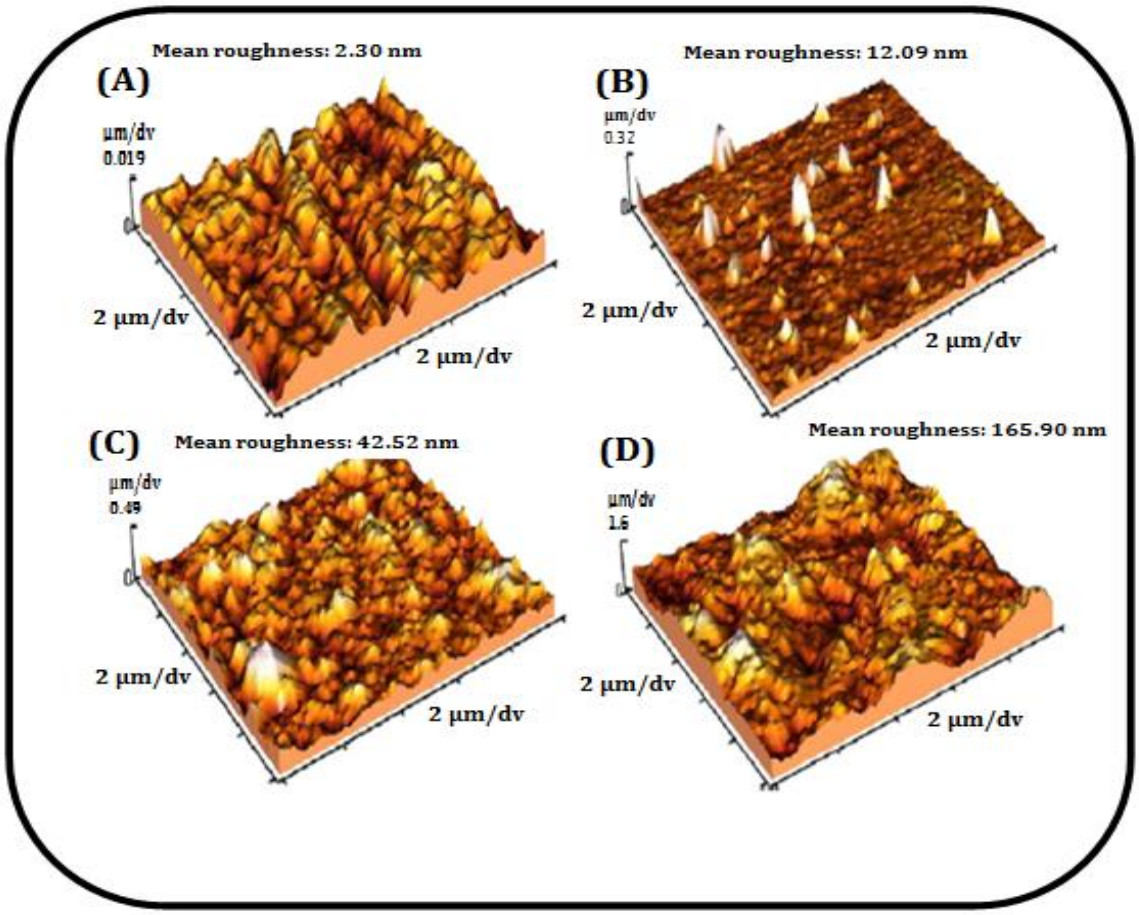

Figure 1.25: Typical AFM images of the surface of: bare GC electrode (A), GC/CoPc$_{ads}$ (B), GC/SWCNT (C) and GC/SWCNT + CoPc (D) [230].

Atomic force microscopy (AFM) shows changes in the surface morphologies of the GCE modified surfaces. Fig. 1.25 shows the AFM images of bare GCE (A), GCE/CoPc (B), GCE/SWCNT (C) and GCE/SWCNT + CoPc (D). Different surface roughness values confirm the different compositions of the hybrid electrodes used in this study. The roughness values of 2.30 nm, 12.09 nm, 42.52 nm and 165.90 nm for Figs.1 A, B, C and D respectively shows the different extents of modification by the various surface modifiers [230].

1.4.2.5 Transmission electron microscopy (TEM)

TEM has been used for the characterization of carbon nanotubes and MPc-CNT conjugates that are used in electrode modifications. The SWCNTs, MPc-SWCNTs and MPc/SWCNTs mixtures can be used to modify electrodes and the extent of surface coverage can be monitored using TEM.

1.4.2.6 Chronoamperometry (CA)

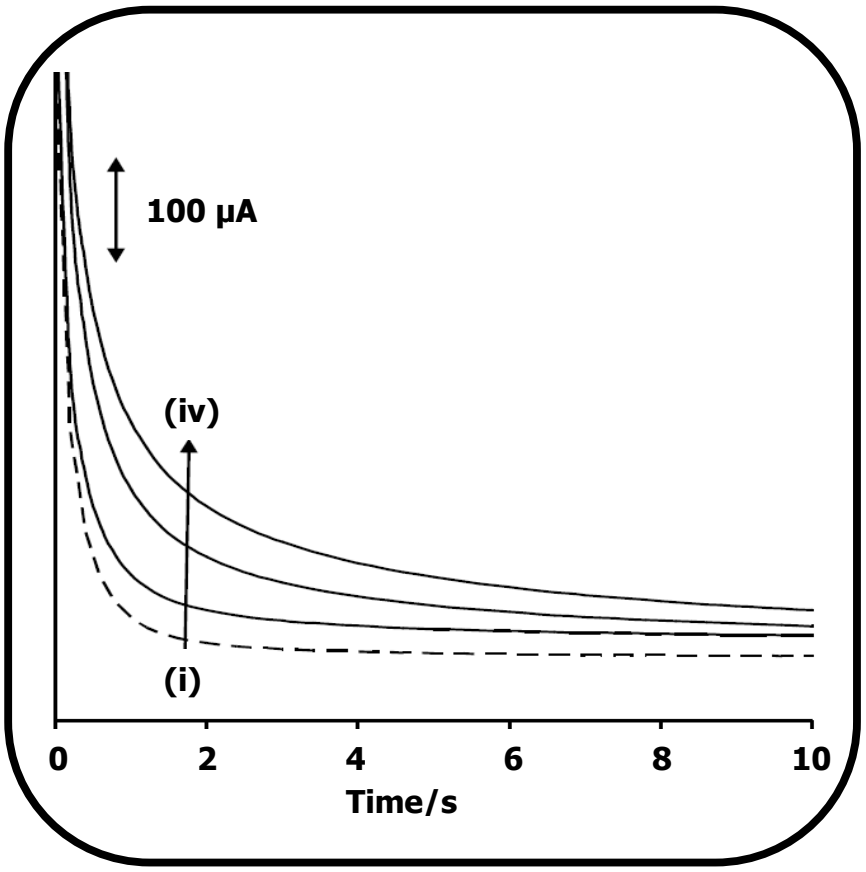

Fig.1.26: Typical chronoamperometric evolutions of the BPPGE-MWCNT-poly-FeTAPc obtained in 0.1 M phosphate buffer (pH 12) containing different concentrations of amitrole (0.0, 3.0, 4.0 and 5.0 nM (from (i) to (iv)) at fixed potential of 0.4 V versus Ag|AgCl. Inset is a typical plot of current response versus concentration of amitrole [69].

CA is a transient technique in which the applied potential leads to the immediate oxidation or reduction of the analyte on the electrode surface, to give a current signal that rapidly decays [69,77,242-244]. Fig. 1.26 shows the typical chronoamperograms obtained on a modified basal plane pyrolytic graphite electrode (BPPGE) in buffer (i) and in different concentrations of analyte (ii to iv).

CA can be used to determine the sensitivity of an electrode modifier towards an analyte as well as its limit of detection (LOD). The rate of oxidation on the electrode surface should be faster than the rate of analyte diffusion onto the electrode surface. Current is monitored as a function of time and analyses of data is according to the Cottrell relationship, Eq. 1.4 [245].

$$I = nFD^{1/2}AC_0\pi^{-1/2}t^{-1/2} \quad (1.4)$$

where D, A, C and t are the diffusion coefficient ($cm^2\ s^{-1}$), the electrode area (cm^2), the bulk concentration (mol cm^{-3}) and time (s), respectively. The D value for the analyte or the area (A) of the modified electrode can be calculated [246].

CA can also be used in the evaluation of the catalytic rate constant for the electrochemical reaction occurring at the electrode surface by applying Eq. 1.5 [247].

$$\frac{I_{cat}}{I_{buf}} = \gamma^{1/2}[\pi^{\frac{1}{2}}\,\mathrm{erf}\left(\gamma^{\frac{1}{2}}\right) + \frac{\exp(-\gamma)}{\gamma^{\frac{1}{2}}}] \quad (1.5)$$

where I_{cat} and I_{buf} are the currents of the electrode modifier in the presence and absence of analyte and $\gamma = kC_0t$ (C_0 is the bulk concentrations of analyte) and erf is the argument of the error function. In the cases where γ exceeds 2, the error function is almost equal to 1; Eq. 1.5 reduces to Eq. 1.6.

$$\frac{I_{cat}}{I_{buf}} = \gamma^{1/2}\pi^{1/2} = \pi^{1/2}(kC_0t)^{1/2} \quad (1.6)$$

where k, C_0 and t are the catalytic rate constant ($M^{-1}\ s^{-1}$), the bulk concentration (M) and the time elapsed (s). From the plot of I_{cat}/I_{buf} versus $t^{1/2}$ at intermediate times and at a given concentration, the value of k can be obtained. The magnitude of k is a measure of how fast redox processes take place at the electrode|analyte interface.

Chronoamperometry can also be used in selectivity and interference studies. The mixed solution method [248] is used to confirm the selectivity of an electrode modifier for an analyte in the presence of an interferent. The value of K_{amp} (where K_{amp} is the amperometric selectivity coefficient) is determined from Eq. 1.7:

$$K_{amp} = \left(\frac{\Delta I_{mixture}}{\Delta I_{analyte}} - 1\right)\frac{[analyte\ ]}{[interferent\ ]} \quad (1.7)$$

where $\Delta I_{mixture}$ and $\Delta I_{analyte}$ are the changes in chronoamperometric current for the mixture (containing the analyte and the interferent) and the analyte alone respectively, relative to the signal of the buffer at a particular time. A K_{amp} value of less than 10^{-3} indicates non-interference while one which falls within the order of 10^{-3} suggests that the species is an interferent but not a strong one.

1.4.2.7 Rotating Disk electrode (RDE) studies

In rotating disk electrode (RDE) voltammetry the mode of transfer of the analyte to the electrode|solution interface is by convection and the observed currents are strongly dependant on the electrode rotational speed. RDE can be used to determine the sensitivity of an electrode towards an analyte and ultimately the LOD. The redox process occurring at the RDE surface for the analyte are purely controlled by the mass transfer process in the solution. Fig. 1.27 shows a typical RDE voltammogram evolved on a modified GCE. From the voltammograms, the limiting current and rotation speed should obey the Levich equation, Eq. 1.8 [245]. On the basis of Eq. 1.8, a plot of limiting current, I_{lim}, versus $\omega^{1/2}$ should give a straight line to confirm the mass transfer process.

$$I_{lim} = 0.62nFAD^{2/3}\upsilon^{-1/6}\omega^{1/2}C_0 \quad (1.8)$$

where D, υ, ω, C_0, n, A and F are the diffusion coefficient, the kinematic viscosity, the electrode angular rotational speed, the bulk concentration of the reactant in the solution, the total number of electrons involved, the electrode surface area and the Faraday constant, respectively. The values of D or n can be obtained from the slope of the Levich plot [243].

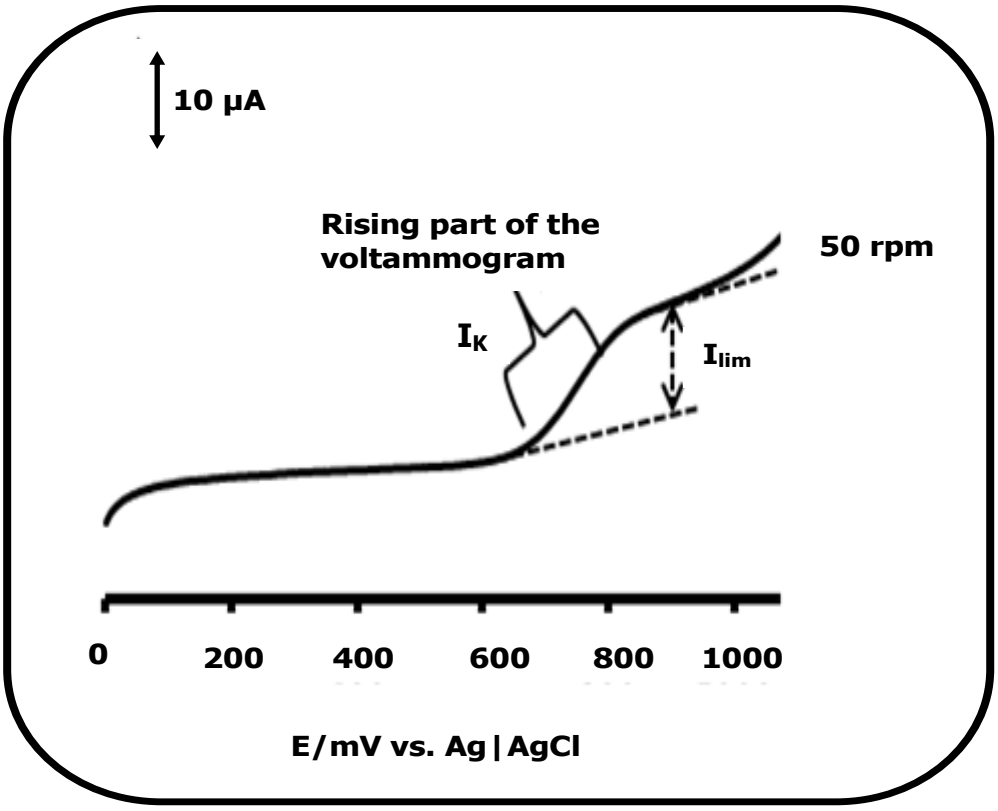

Fig. 1.27: Typical RDE voltammogram generated on a modified electrode rotating at 50 rpm.

The catalytic rate constant, *k,* can be calculated from the Koutecky-Levich theory [245], represented by Eq. 1.9.

$$\frac{1}{I_{lim}} = \frac{1}{nFAC_o k} + \frac{1}{0.62nFAD^{2/3}\upsilon^{-1/6}C_0\omega^{1/2}} \quad (1.9)$$

$$Intercept = \frac{1}{nFAk\,C_0} \quad (1.10)$$

where I_{lim} is the measured limiting current, C_o is the bulk concentration and v is the kinematic viscosity of the solution. A plot of $1/I_{lim}$ versus $1/\omega^{1/2}$ (from Eq. 1.9) gives a linear relationship with a positive intercept, indicating that the electrode reactions are controlled by both kinetics and the mass transport of the analyte at the electrode

surfaces. The value of *k* is calculated from the intercept of the Koutecky-Levich plot using Eq. 1.10.

Plots of potential (from the rising part of the RDE voltammogram) versus log I_k at different rotational speeds allow for the determination of the Tafel slopes. I_k is obtained from the rising part of the voltammogram at different potentials, as shown in Fig. 1.27.

The following techniques were employed in this work to characterize the modified electrodes: IR, XRD, UV-vis and Raman spectroscopies, TEM, AFM and EIS. CV, CA and RDE were used in both characterization of the modified electrodes and the electrochemical detection of amitrole, diuron and 2-mercaptoethanol (2-ME).

1.4.3 Electrocatalytic behaviour of SWCNTs

The electrocatalytic behaviour of the CNT modifier can be evaluated against the bare electrode. The first study on the use of CNTs in electroanalysis was by Britto, who applied a MWCNT paste in the analysis of dopamine [116] and observed a nearly reversible two electron redox process for a normally irreversible system. The oxidation of dopamine was observed at lower potentials than expected and at a faster rate than what was observed on graphite electrodes [116]. Use of CNTs improves reversibility of redox processes [116,246] through the provision of many active sites [246]. The electrochemical area of CNT based electrodes has been evaluated using chronoamperometry in ferrocene monocarboxylic acid solution [246]. Improved electro-activity of CNT based electrodes result in sharper voltammograms, lower ΔEp (peak to peak separation) and higher peak currents [246,249, 250].

1.4.4 Electrocatalytic behaviour of MPc-SWCNT hybrids

Table 1.2: Selected literature applications of MPc-CNT modified electrodes

MPc-CNT modified electrodes	**Analyte: Ep/V (vs.Ag|AgCl)**	**Linear Range: Sensitivity: Detection Limit[b]**	**Ref**
GCE/CoPc/MWCNT (mixed)-Adsorbed	Carbaryl: 0.8[a]	0.33–6.61 μM : NDA: 1.09±0.02 μgL^{-1}	**203**
Au-Cys-SWCNT-CoTAPc (linked)-SAM	Epinephrine: 0.2	(<130 μM) : 9.4×10^{-3} AM^{-1}: 6 μM	**205**
Au-AET-SWCNT-CoTAPc (linked)-SAM	Dopamine: 0.17	NDA : NDA : NDA	**68**
GCE-MWCNT-CoTSPc (mixed)-drop-dry + electrodeposition	Epinephrine: 0.28	0.25 - 3.5 μM: (0.132±0.003) A M^{-1}: ~0.45 μM	**206**
Au-DMAET-SWCNT-PABS-nanoFePc(linked)-SAM + adsorption	Hydrogen peroxide: -	NDA : 0.00087 AM^{-1}: 0.55 mM	**204**
GCE-MWCNT-FeTAPc (mixed)-Abrasion + dip-dry.	Amitrole: ~0.35	1 – 5 nM: 8.80±0.44 A/mM: 0.5 nM	**69**
BPPGE-MWCNT–CoTAPc (mixed)–Abrasion + polymerization.	Asulum: 0.65	4.5 – 20 μM: 241×10^{-3} A/M: 1.15 μM	**75**

[a]Ep/V vs. Standard Calomel Electrode (SCE), [b]NDA = No Data Available.

Table 1.2 shows the selected MPc-SWCNT conjugates and mixtures that have been applied in electrocatalysis. The MPc-SWCNT conjugates are mainly limited to

SAMs on Au electrodes [68, 204,205] using Co [68,205] and Fe [204] as the electroactive metals. Nickel metal has never been used in these studies. However Ozoemena et al [68] used dopamine to only show the catalytic nature of the Au-AET-SWCNT-CoTAPc (linked)-SAM relative to the other electrodes used, hence the absence of sensitivity and detection limit values in Table 1.2. Literature shows that MPcs/CNTs mixtures [69,74,75,203,206] constitute the majority of electrocatalysts that are being used today. This may partly be due to simple methods that are employed to produce such hybrids, when compared to the rigorous steps and time spent in producing chemically linked conjugates.

This research was motivated by the realization of the good electron transfer efficiencies of both the Pcs (especially those carrying electroactive metals) and the SWCNTs. Chemically linking the two could provide an efficient platform for the transfer of electrons in electrochemical reactions, by providing shorter distances to be travelled by the electrons (compared to MPc-SWCNT-SAMs) to and from the surface of the modified electrode and improved communication between the MPc and the SWCNT. Compared to SAMs, MPcs directly linked to SWCNTs offer less resistance to charge transfer, especially in nanorod and nanomesh conjugates.

Electrocatalysis is characterized by an increase in current and a shift in peak potentials to lower values with respect to unmodified electrode [229]. The MPc metal center or ring is involved in the oxidation-reduction processes of an analyte and this depends on the solvent system [80,82] and the nature and the number of substituents. In conjugates the SWCNTs should facilitate the smooth transfer of electrons to and from the MPc. Electrocatalysis of thiols on CoPcs is known to involve the Co^{III}/Co^{II} couple in acidic media [251]. Studies have shown that the electrocatalysis of 2-ME on FePcs is only encouraged by electron donating groups [252]. For the NiPcs, the ring is normally involved in electrocatalysis because of the absence of orbitals that lie between the HOMO and the LUMO of the Pc ring [86]. This work therefore is focused on the effects of the differently functionalized SWCNTs on the catalysis of MPcs towards amitrole, diuron and 2-ME.

1.5 Analytes studied in this work

1.5.1 Amitrole

(a) (b)

amitrole (3-amino-1,2,4-triazole) diuron (3-(3,4-dichlorophenyl)-1,1-dimethylurea))

Figure 1.28: Structures of amitrole (a) and diuron (b).

Amitrole (3-amino-1,2,4-triazole), Fig. 1.28a, belongs to a class of non-selective systemic herbicides known as triazoles. It is used in weed control to inhibit the carotenoid biosynthesis. It has carcinogenic effects in animals [253,254] and interferes with lymphoblast transformation as well as inhibiting cell growth [255]. It has very low volatility and high solubility in water making it a potential toxin [256]. Therefore levels of amitrole should be monitored so that they do not exceed the regulatory level of 0.1 μg L^{-1} in drinking water, set by the European Economic Commission (EEC) [256]. Detection of amitrole through reversed-phase high performance liquid chromatography (RP-HPLC) and gas chromatography (GC) has been explored, but has been hindered by the poor resolution [78]. MWCNTs paste electrodes [78], combined MWCNT/FeTAPc electrodes [69] and nafion/lead-ruthenium oxide pyrochlore chemically modified electrodes [257] have been used in the electrochemical detection of amitrole. Its electrochemical detection has been done in both alkaline (pH =12) [69] and acidic media (pH =4.5) [240]. Chicharro et al showed that amitrole peak currents dropped dramatically as the pH decreased and increased from 4 to 1 and 5 to 12, respectively [258]. They obtained 0.6 μM as the

detection limit on MWCNTs at potentials around 0.85 V at pH = 4.5 [258]. Siswana et al got detection limit of 0.305 mg/L, with a sensitivity of 3.44 mA/nM (at 0.42 V vs. Ag|AgCl under basic conditions) on FePc nanoparticles modified electrode [259]. Due to the high detection limits obtained using the above methods, the use of MPc-SWCNT conjugates was investigated in this work with the aim of improving the detection limits.

1.5.2 Diuron

Diuron (3-(3,4-dichlorophenyl)-1,1-dimethylurea) is a non-selective systemic substituted phenyl-urea herbicide (Fig. 1.28b), which is easily taken up by the root system of plants and quickly trans-located through the xylem vessels into stems and leaves. Diuron inhibits the Hill reaction in photosynthesis, thus limiting the production of high energy compounds such as adenosine triphosphate (ATP) which are used for various metabolic processes [260]. Relative to other pesticides of the same type, diuron is considered highly mobile and persistent [260,261]. The Environmental Protection Agency, EPA, of the USA has classified diuron as "known/likely" human carcinogen [262]. Electrochemical methods have been employed for the detection of diuron [263,264], however passivation of the electrode surface due to the deposition of polymeric products has been observed [263,265]. The oxidation route for diuron is thought to involve the hydrogen ion and an electron, giving rise to a free radical which in turn dimerises [265]. MPc-SWCNT conjugates are being used in this work in order to improve the detection limits.

1.5.3 2-Mercaptoethanol (2-ME)

Sulfur-containing compounds, such as mercaptans are by-products of industrial processes and are water pollutants [266]. They are widely distributed in petroleum products and they cause foul odors and the deterioration of food products. In addition, because of their acidity, they are corrosive to metals, therefore they are harmful to store and use.

Thiols also undergo electrochemical oxidation in both acidic [98,267] and alkaline [268] conditions. The oxidation of thiols to disulphides strongly depends on

the nature of the central metal [224]. Of all the transition metal Pcs, cobalt as a central metal has been observed to enhance the catalytic oxidation of thiols because its orbital energies closely match those of sulphur, enabling easy transfer of electrons from the sulphur orbital to the d_{z^2} and d_{xz} orbitals of the metal [25]. Electron donating groups also enhance the catalysis of thiols [269]. Different chemically modified electrodes have been designed for the detection of 2-ME [25,224,270]. Oxidations of thiols are known to proceed via an inner sphere mechanism [25] where bonding between the sulphur atom and the active metal centre occurs before or during electron transfer [25].

1.6 Summary of the aims of the thesis

Since both MPcs and SWCNTs have good electron transfer properties, chemically linking them together could produce very good electron transfer mediators for electrocatalysis. Also, MPcs carrying electroactive metals like Co and Fe have excellent redox properties and if chemically coupled to SWCNTs, very efficient electrochemical sensors could be produced. From literature, the use of MPcs and SWCNTs conjugates in electrocatalysis is limited, especially when it comes to the detections of 2-ME, amitrole and diuron. Coupling of low symmetry MPc molecules with SWCNTs is quite novel and the use of such conjugates as electrochemical sensors is new. The role played by the SWCNTs when coupled with MPcs needs to be investigated. As a result of the above arguments, the following constitute the aims of this research:

(a) Synthesis of (i) Co-, Fe- and Ni-tetraamino-phthalocyanines,
(ii) Co-tetracarboxy-phthalocyanine,
(iii) Co-monoamino-substituted phthalocyanine,
(iv) Co-monocarboxy-substituted phthalocyanine.

(b) Synthesize SWCNTs from the pyrolysis of FePc.

(c) Conversion of *poly*-NiTAPc into an oxo-bridged complex (O-Ni-O).

(d) Functionalize SWCNTs with:
(i) Carboxylic acid groups,

(ii) Ethylene amine (EA) groups,

(iii) Phenylamine (PA) groups.

(e) Characterize the MPcs and functionalized SWCNTs.

(f) Synthesize chemically linked conjugates, using various possible combinations of MPcs and SWCNTs from (a) and (d) above.

(g) Characterize the MPc-SWCNT conjugates.

(h) Use the conjugates in the electrochemical detections of 2-ME, amitrole and diuron.

2. EXPERIMENTAL

This chapter reports on all the synthetic procedures and characterization methods i.e. spectroscopic, microscopic and electrochemical techniques that were used in this study.

2.1 Materials

Dimethylformamide (DMF), dimethyl sulfoxide (DMSO), ethanol, absolute methanol, tetrahydrofuran (THF), hydrochloric acid (32%), nitric acid (55%), cobalt (II) acetate, 4-nitrophthalic acid, cobalt sulphate, nitrobenzene, phthalic anhydride, potassium carbonate, sodium carbonate, sodium chloride, sodium acetate, acetic acid, sodium hydroxide, sodium nitrite, sodium sulphide nonahydrate, sulphuric acid (98%), tetrabutylammonium tetrafluoroborate ($TBABF_4$), thionyl chloride, potassium bromide, potassium ferricyanide, urea, diethyl-ether, chloroform, diuron, amitrole, 2-mercaptoethanol (2-ME), 1,4-benzene diamine, ethane-1,2-diamine (ethylene amine, EA), benzyl-mercaptan, ammonium chloride, ammonium molybdate, iron (II) acetate, nickel (II) acetate, 4-hydroxybenzoic acid, single walled carbon nanotubes (SWCNTs, 0.7 – 1.2 nm in diameter and 2 – 20 μm in length) and pH 4 buffer tablets, were either purchased from Sigma-Aldrich, Fluka or Merck. DMF, DMSO and THF were freshly distilled and dried before use. 4-Nitrophthalonitrile **(21)**, 4-(benzyl-mercapto)-phthalonitrile **(22)** and 4-(3,4-dicyanophenoxy)benzoic acid **(24)** were prepared following literature methods [271-274]. CoTAPc **(7a)**, FeTAPc **(7b)** and NiTAPc **(7c)** were prepared according to a procedure by Somashekarappa and co-workers [29]. CoTCPc **(8)** was prepared according to a procedure reported elsewhere [51,275]. Aqueous solutions were prepared using Millipore water from Milli-Q Water Systems (Millipore Corp., Bedford, MA, USA, conductivity range = 0.055 – 0.294 μS/cm). All other chemicals and reagents were of analytical grade and were used as received. Silica gel C_{60} was used to prepare chromatographic columns.

2.2 Equipment

1. Voltammetric and chronoamperometric data were recorded using a Princeton Applied Research potentiostat/galvanostat Model 264 equipped with Electrochemistry PowerSuite software.

2.Transmission electron microscope (TEM) pictures were obtained using a JEOL JEM 1210 transmission electron microscope at 100 kV accelerating voltage. Sample suspensions were prepared in DMF through ultra-sonication for 1 h.

3. Shimadzu UV - 2550 spectrophotometer was used to collect UV-Vis spectral data. The UV-vis spectra were obtained after ultra-sonication of the SWCNTs, MPc/SWCNT mixtures and MPc-SWCNT conjugates for 1 h.

4. The Perkin–Elmer FTIR spectrometer and Bruker Vertex 70 - Ram II spectrometer (equipped with a 1064 nm Nd:YAG laser and a liquid nitrogen cooled germanium detector) were used to collect Infrared and Raman data, respectively. FTIR spectral data (using KBr pellets) for the raw SWCNTs, the functionalized SWCNTs (f-SWCNTs), the MPcs, the MPc-SWCNT–linked (conjugates) and the MPc/f-SWCNTs mixtures were obtained in their solid forms. The Raman spectral data for the SWCNTs (raw and functionalized), the Pcs and the MPc-SWCNT-linked were obtained in their powder forms and some from their suspensions after sonicating their respective powdered samples in DMF for 1 h [276].

5. X-ray powder diffraction (XRD) patterns were recorded on a Bruker D8 Discover, equipped with a PSD LynxEye detector, using Cu-K_α radiation (λ = 1.5405 Å, nickel filter). Samples were placed on a zero background (511) silicon wafer embedded in a generic sample holder and data recorded within the range $2\theta = 15^o$ to 60^o, scanning at 1^o min^{-1} with a filter time-constant of 2.0 s per step at room temperature. A slit width of 6.0 mm was used in the measurements. X-ray diffraction data were fitted using Eva (evaluation curve fitting) software, while analysis of data was done using International Center Diffraction Data (ICDD) database. The XRD spectral data for the raw SWCNTs, the f-SWCNTs, the MPcs, the conjugates and the MPc/f-SWCNTs mixtures were also obtained in their solid forms.

6. Rotating disk electrode (RDE) voltammetry data was acquired using BAS 100W electrochemical workstation version 2.0.

7. Electrochemical impedance spectroscopy (EIS) data were obtained using the Autolab potentiostat PGSTAT 302 equipped with GPES software version 4.9.

8. Thermal gravimetric analysis (TGA) was carried out using a Perkin–Elmer TGA 7 thermogravimetric analyzer at a heating rate of 10 ^{0}C min^{-1} in a high-purity nitrogen and air atmosphere. The resultant data was analyzed with Pyris Version 4.01 software.

9. Elemental analyses were done using a Vario Elementary EL111 Series.

10. Mass spectra were collected with a Bruker Autoflex III Smartbeam TOF/TOF mass spectrometer. The instrument was operated in the positive ion mode using an m/z range of 400-3000. The voltage of the ion sources were set at 19 and 16.7 kV for 1 and 2, respectively, while the lens was set at 21 and 9.7, respectively. The spectra were acquired using dithranol as the MALDI matrix, using a 354 nitrogen laser.

11. Atomic force microscopy (AFM) images were recorded in the non-contact mode in air with a CP-11 Scanning Probe Microscope from Veeco Instruments (Carl Zeiss, South Africa) at a scan rate of 1 Hz.

2.3 Synthesis

2.3.1 Functionalization of SWCNTs

2.3.1.1 Ethylene amine functionalization (11), Scheme 3.1 route I (EA-SWCNT)

Functionalization with EA was done according to literature [168] but with slight modifications as follows: SWCNTs (30 mg) were mixed with 40 mg (0.60 mmol) of $NaNO_2$ and 60 mg (0.60 mmol) of ethylene diamine (EDA). Concentrated H_2SO_4 (0.026 mL, 0.5 mmol) was added, and the mixture was heated and stirred at 60 °C for 1 h. The mixture was allowed to cool to room temperature, dissolved in DMF and centrifuged. DMF was decanted, fresh one added and centrifugation repeated several times until DMF remained colourless. This treatment removed excess unreacted EDA and carbon ash. The residue was further washed several times

with Millipore water to remove H_2SO_4 and metal salts. The pH of the washings was tested to ensure no acid remained. The product is represented as EA-SWCNT **(11)**.
EA-SWCNT: **IR [(KBr)** υ_{max}**/cm^{-1}]**: 3430-3470 (NH doublet), 1640 (N-H). **[Raman** υ_{max}**/cm^{-1}]**: 2542 (G*), 1590 (G), 1270 (D).

2.3.1.2 Phenylamine (PA) functionalization (12), Scheme 3.1 route II (PA-SWCNT)

Phenylamine functionalized SWCNTs, represented as PA-SWCNT **(12)**, were synthesized as for EA-SWCNT (route **II)**, using 1,4-benzene diamine (BDA) as a precursor, instead of EDA. Other reagents and reaction conditions are the same as for EA-SWCNT functionalization.
PA-SWCNT: **IR [(KBr)** υ_{max}**/cm^{-1}]**: 3428-3490 (NH doublet), 1644 (N-H).

2.3.1.3 Carboxylic acid functionalization (13), Scheme 3.1 route III (SWCNT-COOH)

Carboxylic acid functionalized SWCNTs represented as SWCNT-COOH, were synthesized according to Scheme 3.1 (route **III**). SWCNTs ((60 mg), 0.7 – 1.2 nm in diameter and 2 – 20 μm long)) were suspended in a 3:1 mixture of concentrated H_2SO_4 and concentrated HNO_3 and stirred for 2 h at 70 ^{0}C. The resulting mixture was centrifuged and washed with Millipore water several times until a pH of 5 was attained. The SWCNT–COOH **(13)** were oven dried at 110 ^{0}C for 12 h [154].
SWCNT-COOH: **IR [(KBr)** υ_{max}**/cm^{-1}]**: 3400 (O-H), 1620 (C=O). **[Raman** υ_{max}**/cm^{-1}]**: 1595 (G), 1326 (D).

2.3.2 Synthesis of MPcs

The synthesis of MTAPcs (M = Co, Fe, Ni) and CoTCPc have been reported, see section 2.1.

2.3.2.1 Synthesis of CoMAPc (9), Scheme 3.2

To 40 mL of dry DMF, 4-nitrophthalonitrile (**21**, 0.29 g, 1.67 mmol), 4-(benzyl-mercapto)-phthalonitrile (**22**, 1.26 g, 5 mmol) and $Co(CH_3COO)_2.4H_2O$ (0.14 g, 0.56 mmol) were added and the mixture heated under reflux for 5 h at 180 ^{0}C under

nitrogen atmosphere. The mixture was allowed to cool to room temperature and excess methanol was added to precipitate cobalt(II)-tris(benzyl-mercapto)-mononitrophthalocyanine **(23).** The precipitate **(23)** was further washed with methanol, dried at 110 ^{0}C overnight and then reduced to CoMAPc **(9)** by adding $Na_2S.9H_2O$ and heating at 50 ^{0}C for 5h under aqueous conditions. CoMAPc **(9)** was then purified according to literature methods [29]. Dry CoMAPc **(9)** was dissolved in a minimum amount of DMF and chromatographed on a Si_{60} column with diethyl ether/DMF (9:1) solvent mixture as eluant, with the solvent polarity gradually increased to 100 % DMF, to obtain the desired second fraction. Further chromatographic purification of **9** was done using a 9:1 mixture of chloroform and methanol as eluant. **Yield:** 0.35 g (22.0 %). **[UV/vis (DMF)]**: λ_{max} nm (log ε); 677 (4.81), 617 (4.47). **[IR (KBr)**: ν_{max}/cm^{-1}]: 3447 (ν_{NH}), 1601 (ν_{NH}), 746 (ν_{C-S}). Calcd. for $C_{53}H_{35}N_9S_3Co$: C; 56.21, H; 2.73, N; 8.82, S; 8.50; Found: C; 55.95, H; 2.85, N; 8.54, S; 8.17. **[MALDI-TOF MS *m/z*]**: Calcd: (M^+) 952. Found: (M^+) 952.

2.3.2.2 Synthesis of CoMCPc (10), Scheme 3.3

The synthesis of CoMCPc (**10)** was according to Scheme 3.3. To 50 mL of dry DMF, 4-(benzyl-mercapto)-phthalonitrile (**22**, 1.88 g, 7.5 mmol), 4-(3,4-dicyanophenoxy)benzoic acid (**24**, 0.66 g, 2.5 mmol) and $Co(CH_3COO)_2.4H_2O$ (0.21 g, 0.84 mmol) were added and the mixture was refluxed at 180 ^{0}C for 5 h under a nitrogen atmosphere. The resultant reaction mixture was allowed to cool to room temperature and excess methanol was added to precipitate an impure cobalt(II)-tris(benzyl-mercapto)-mono(carboxyphenoxy)-phthalocyanine, CoMCPc **(10).** The product, CoMCPc **(10),** was dissolved in minimum amount of DMF and chromatographed on a Si_{60} column with diethyl ether/DMF (9:1) solvent mixture as eluant and gradually increasing the solvent polarity to 100 % DMF, to obtain the desired second fraction. Further chromatographic purification was done using a chloroform:methanol (9:1) mixture as eluant to give CoMCPc **(10)**. **Yield:** 0.40 g (26.0 %). **[UV/vis (DMF)]**: λ_{max} nm (log ε); 672 (4.94), 608 (4.30), 462 (3.82). **[IR (KBr)**: ν_{max}/cm^{-1}]: 3266 (ν_{O-H}), 2921 ((ν_{C-H}), 1720 ($\nu_{C=O}$), 748 (ν_{C-S}). Calcd. for

$C_{60}H_{40}N_8S_3O_3Co$: C; 66.01, H; 3.26, N; 10.22, S; 9.80; Found: C; 65.85, H; 3.45, N; 9.94, S; 9.67. **[MALDI-TOF MS *m/z*]**: Calcd: (M^+) 1075. Found: (M^+) 1075.

2.3.3 Synthesis of MPc-SWCNT conjugates

2.3.3.1 Synthesis of MTAPc-SWCNT(linked), Scheme 3.4

SWCNT-COOH (1 mg) were treated with 5 mL of $SOCl_2$ and 12 drops of anhydrous DMF at 70 ^{0}C for 24 h to give acid chloride derivatives (**SWCNT-COCl, 25**) [163,201]. The mixture was centrifuged for 20 min, DMF decanted and the solid washed with anhydrous THF. Centrifugation was repeated with the THF layer being decanted. The solid SWCNT-COCl **(25)** was dried under vacuum in a desiccator. The SWCNT-COCl **(25)** was refluxed with 0.1 g of MTAPc **(7a-7c)** in 15 mL of DMF for 96 h and the resulting solids were centrifuged for 20 min, DMF decanted and the solid washed with ethanol. The solid products (MTAPc-SWCNT(linked) were dried at room temperature under vacuum [163].

CoTAPc-SWCNT(linked) (14): IR [(KBr) υ_{max}/cm^{-1}]: 3457 (N-H, amide), 1608 (C=O, amide). **[Raman υ_{max}/cm^{-1}]**: 1593 (G), 1330 (D), 1541 (Co ion marker band).

FeTAPc-SWCNT(linked) (15): IR [(KBr) υ_{max}/cm^{-1}]: 3395 (N-H, amide), 1610 (C=O, amide). **[Raman υ_{max}/cm^{-1}]**: 1593 (G), 1330 (D), 1536 (Fe ion marker band), 1666 (amide I), 1477 (amide II), 1277 (amide III).

NiTAPc-SWCNT(linked) (16): IR [(KBr) υ_{max}/cm^{-1}]: 3395 (N-H, amide), 1610 (C=O, amide). **[Raman υ_{max}/cm^{-1}]**: 1593 (G), 1330 (D), 1545 (Ni ion marker band), 1665 (amide I), 1500 (amide II), 1266 (amide III).

2.3.3.2 Synthesis of CoTCPc-PA-SWCNT(linked) (17) and CoTCPc-EA-SWCNT(linked) (18), Scheme 3.5

CoTCPc-PA-SWCNT(linked) **(17)** was synthesized according to Scheme 3.5 as follows: CoTCPc (**8**, 0.2 g) was treated with 5 mL of $SOCl_2$ and 10 mL of anhydrous DMF and heated at 70 ◦C for 24 h [277] to give a blue-green cobalt phthalocyanine acid chloride derivative (CoTCOClPc, **26**). To the mixture, 5 mg of PA-SWCNT **(12)** was added and the mixture continuously stirred at 70 °C for 96 h. After cooling to room temperature the mixture was centrifuged for 20 min and the solution containing unreacted CoTCOClPc **(26)** decanted. The solid was washed with

anhydrous THF. Centrifugation was repeated with the THF layer being decanted. Finally the solid was washed with ethanol to remove THF. The resultant black solid (CoTCPc-PA-SWCNT(linked) **(17)**) was dried under vacuum in a desiccator [163]. CoTCPc-EA-SWCNT(linked) **(18)** (Scheme 3.5) was synthesized following similar steps to those of CoTCPc-PA-SWCNT(linked) **(17)**, but replacing PA-SWCNT **(12)** with EA-SWCNT **(11)**.

CoTCPc-PA-SWCNT(linked) (17): IR [(KBr) υ_{max}**/cm^{-1}]**: 3431 (N-H, amide), 1714 (C=O, amide).

CoTCPc-EA-SWCNT(linked) (18): IR [(KBr) υ_{max}**/cm^{-1}]**: 3425 (N-H, amide), 1650 (C=O, amide). **[Raman** υ_{max}**/cm^{-1}]**: 1598 (G), 1279 (D), 2715 (G'), 2547 (non-dispersive phonon mode).

2.3.3.3 Synthesis of CoMAPc-SWCNT(linked) (19), Scheme 3.6

CoMAPc-SWCNT conjugates were synthesized according to Scheme 3.6 as follows: 1 mg of SWCNT-COOH **(13)** was treated with 5 mL of $SOCl_2$ and 12 drops of anhydrous DMF and the mixture heated at 70 ^{0}C for 24 h [278] giving an acid chloride derivative (SWCNT-COCl, **25**). The mixture was centrifuged for 20 min and $SOCl_2$ decanted and the solid washed with anhydrous THF. Centrifugation was repeated with the THF layer being decanted. The solid SWCNT-COCl **(25)** was dried under vacuum in a desiccator. The SWCNT-COCl was refluxed with 50 mg of CoMAPc in 10 mL of DMF for 96 h and the resulting solid was centrifuged for 20 min, DMF decanted and the solid washed with ethanol. The solid product (CoMAPc-SWCNT(linked), **19**) was dried at room temperature under vacuum [163].

CoMAPc- SWCNT(linked) (19): IR [(KBr) υ_{max}**/cm^{-1}]**: 3372 (N-H, amide), 1640 (C=O, amide), 2927 (C-H).

2.3.3.4 Synthesis of CoMCPc-PA-SWCNT(linked) (20), Scheme 3.7

CoMCPc-PA-SWCNT conjugate was synthesized according to Scheme 3.7 as follows: 50 mg of CoMCPc were dissolved in 10 mL DMF and 5 mL of $SOCl_2$ added to the solution. The mixture was heated at 70 ◦C for 24 h [278] to give cobalt (II)-tris(benzyl-mercapto)-monomethanoyl-phthalocyanine, CoMCOClPc **(27)**. To the

mixture, 1 mg of PA-SWCNT **(12)** was added and this mixture was heated for a further 96 h at the same temperature. The resultant mixture was allowed to cool to room temperature, centrifuged for 20 min and the resultant solid was washed with anhydrous THF. Centrifugation was repeated with the THF layer being decanted. The solid CoMCPc-PA-SWCNT(linked) **(20)** was further washed with ethanol and dried under vacuum in a desiccator [163].

CoMCPc-PA-SWCNT(linked) (20): IR [(KBr) υ_{max}/cm^{-1}]: 3200 (N-H, amide), 1700 (C=O, amide), 1598 (N-H).

2.4 Electrochemical Methods

Cyclic voltammetry (CV), chronoamperometry (CA), rotating disk electrode (RDE) voltammetry and electrochemical impedance spectroscopy (EIS) were performed on a three electrode electrochemical cell comprising of glassy carbon electrode (GCE) as the working electrode (area = 0.071 cm^2), platinum wire (Pt) as a counter electrode and a silver|silver chloride wire (Ag|AgCl) as a pseudo-reference electrode. Before use, the GCE was polished on a Buehler-felt pad using alumina (0.05 μm), and then washed with Millipore water, sonicated for 5 min in Millipore water, washed again with Millipore water and then with pH 4 buffer solution. The potential response of Ag|AgCl pseudo-reference electrode in aqueous conditions was less than the Ag|AgCl (3 M KCl) electrode by 0.015 ± 0.003 V. For electrochemical reactions done in DMF, tetrabutylammonium tetrafluoroborate ($TBABF_4$) was used as a supporting electrolyte. For aqueous studies, voltammetric solutions were prepared in pH 4 buffer using Millipore water. Prior to the analyses, all the solutions were purged with argon/nitrogen gas to drive out oxygen and this argon/nitrogen atmosphere was maintained throughout the analyses.

Electropolymerization of the complexes on GCE were performed by repetitive scanning (CV) of the complex solutions (1 mM) in DMF containing $TBABF_4$. After polymerization, the GCE modified with the film was removed from the electrolytic cell, rinsed with DMF and finally with pH 4 buffer. The modified electrodes were conditioned by continuous cyclisation in pH 4 buffer solution until stable voltammetric currents were obtained. These electrodes are represented as *poly-*

MTAPc-GCE. *Poly*-NiTAPc **(7c)** was converted to *poly*-Ni(OH)TAPc by continuous cyclisation of the former in 0.1 M NaOH.

For adsorption, a solution of SWCNTs, MPcs, MPc-SWCNT(linked) or MPc/SWCNT(mixed) was introduced onto the GCE through the drop/dip-dry methods, where a drop of the solution is placed on the electrode or the electrode was dipped in solution. The electrodes were then dried under an atmosphere of argon/nitrogen, rinsed and cyclized in pH 4 buffer. Regeneration of the modified electrode after use was achieved by either shaking it in pH 4 buffer solution or in methanol, followed by repetitive scanning in pH 4 buffer until stable voltammetric currents were obtained.

RESULTS & DISCUSSION

▪ Publications

▪Chapter 3

Synthesis, spectroscopic and microscopic characterizations

▪Chapter 4

Electrochemical characterizations

▪Chapter 5

Electrocatalysis

▪Chapter 6

Synthesis of single walled carbon nanotubes and their characterization

Publications

The results discussed in the following chapters have been presented in the articles listed below, that have been published or submitted for publication in peer-reviewed journals. These articles have not been referenced in this thesis:

1. Synthesis and characterization of electrocatalytic conjugates of tetraamino cobalt (II) phthalocyanine and single wall carbon nanotubes, **Tawanda Mugadza** and Tebello Nyokong, *Electrochim. Acta* **54** (2009) 6347.

2. Facile electrocatalytic oxidation of diuron on polymerized nickel hydroxo-tetraamino-phthalocyanine modified glassy carbon electrodes, **Tawanda Mugadza** and Tebello Nyokong, *Talanta* **81** (2010) 1373.

3. Electrocatalytic oxidation of amitrole and diuron on iron(II) tetraamino phthalocyanine-single walled carbon nanotube dendrimer, **Tawanda Mugadza** and Tebello Nyokong, *Electrochim. Acta* **55** (2010) 2606.

4. Synthesis, characterization and the electrocatalytic behaviour of nickel (II) tetraamino-phthalocyanine chemically linked to single walled carbon nanotubes, **Tawanda Mugadza** and Tebello Nyokong, *Electrochim. Acta* **55** (2010) 6049.

5. Covalent linking of ethylene amine functionalized single-walled carbon nanotubes to cobalt (II) tetracarboxyl-phthalocyanines for use in electrocatalysis, **Tawanda Mugadza** and Tebello Nyokong, *Synthetic Metals* **160** (2010) 2089.

6. Electrochemical, microscopic and spectroscopic characterization of benzene diamine functionalized single walled carbon nanotube-cobalt (II) tetracarboxy-phthalocyanine conjugates, **Tawanda Mugadza** and Tebello Nyokong, ***J. Colloid and Interface Science*** **(in press).**

7. Electrocatalytic behaviour of cobalt (II)-tris(benzyl-mercapto)-monoaminophthalocyanine-single walled carbon nanotube nanorods, **Tawanda Mugadza** and Tebello Nyokong , *Electrochim. Acta* (**in press**).

8. Rapid and simple activation of metal free and iron (II) phthalocyanines in the presence of ferric acetate for the synthesis of single-walled carbon nanotubes, **Tawanda Mugadza**, Edith Antunes and Tebello Nyokong, (**submitted**).

9. Synthesis, characterization and application of monocarboxy-phthalocyanine-single walled carbon nanotube conjugates in electrocatalysis, **Tawanda Mugadza** and Tebello Nyokong (in preparation).

CHAPTER 3

Synthesis, spectroscopic and microscopic characterizations

This chapter deals with the syntheses, spectroscopic and microscopic characterization of the MPcs, SWCNTs, MPc/SWCNT mixtures and MPc-SWCNT conjugates.

Table 3.1 List of synthesized MPcs, functionalized SWCNTs and MPc-SWCNT conjugates, their abbreviations and numbers in this thesis

1. MPc complexes	Abbreviation	No
Cobalt (II) tetraamino phthalocyanine	CoTAPc	7a
Iron (II) tetraamino phthalocyanine	FeTAPc	7b
Nickel (II) tetraamino phthalocyanine	NiTAPc	7c
Cobalt tetracarboxy-phthalocyanine	CoTCPc	8
Cobalt (II) tris(benzyl-mercapto)-monoamino phthalocyanine	CoMAPc	9
Cobalt (II) tris(benzyl-mercapto)-mono(carboxyphenoxy) phthalocyanine	CoMCPc	10
2. Functionalized SWCNTs		
Ethylene amine functionalized	EA-SWCNT	11
Phenylamine functionalized	PA-SWCNT	12
Carboxylic acid functionalized	SWCNT-COOH	13
3. MPc-SWCNT conjugates		
Cobalt (II) tetraamino phthalocyanine-single walled carbon nanotubes	CoTAPc-SWCNT	14
Iron (II) tetraamino phthalocyanine-single walled carbon nanotubes	FeTAPc-SWCNT	15
Nickel (II) tetraamino phthalocyanine-single walled carbon nanotubes	NiTAPc-SWCNT	16
Cobalt (II) tetracarboxy-phthalocyanine-phenylamine-single walled carbon nanotubes	CoTCPc-PA-SWCNT	17
Cobalt (II) tetracarboxy-phthalocyanine-ethylene amine-single walled carbon nanotubes	CoTCPc-EA-SWCNT	18
Cobalt (II)-tris(benzyl-mercapto)-monoaminophthalocyanine-single walled carbon nanotubes	CoMAPc-SWCNT	19
Cobalt (II)-tris(benzyl-mercapto)-mono(carboxyphenoxy) phthalocyanine-single walled carbon nanotubes	CoMCPc-PA-SWCNT	20

3.1 Functionalization of SWCNTs

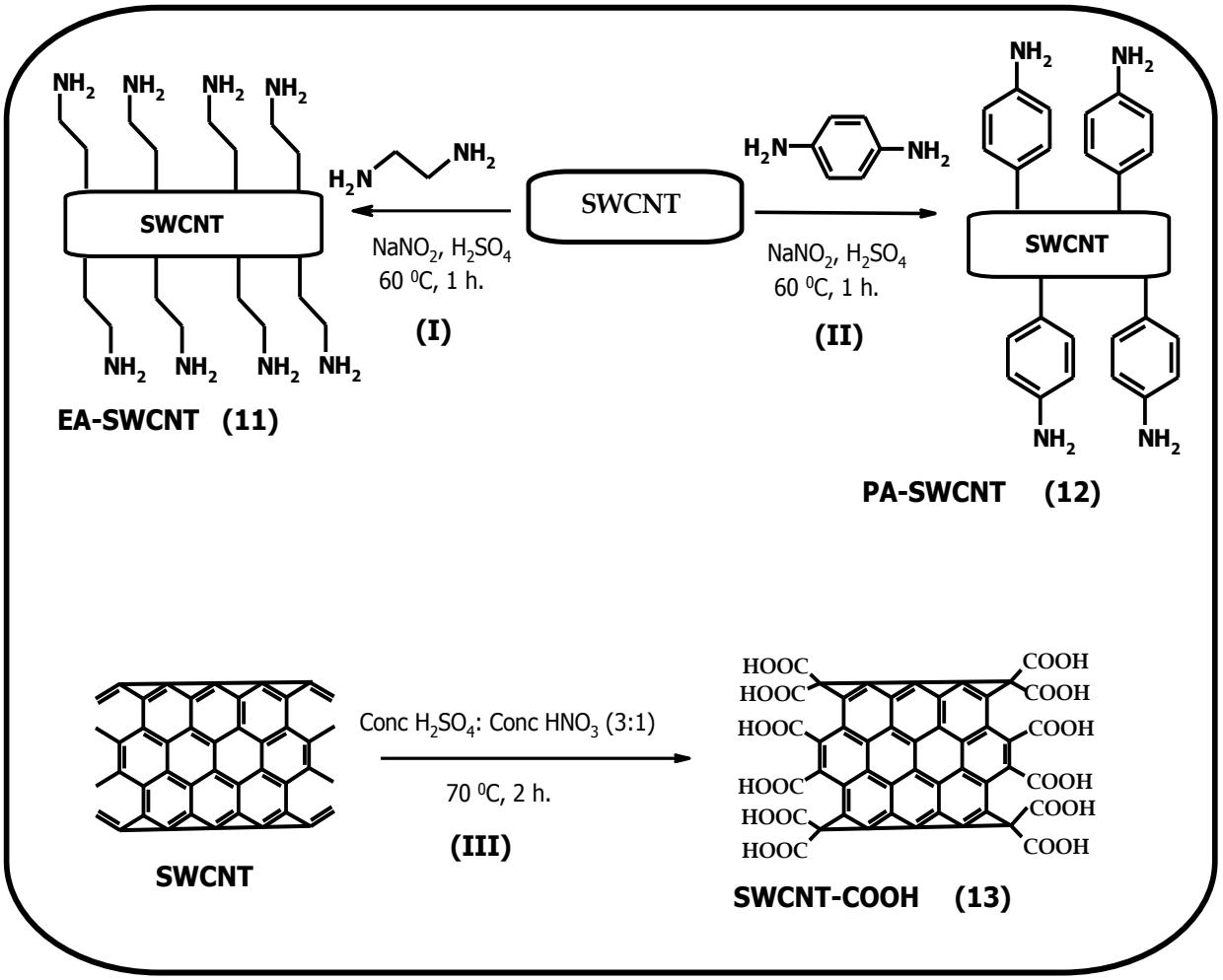

Scheme 3.1: Functionalization of SWCNTs to EA-SWCNT (11), PA-SWCNT (12) and SWCNT-COOH (13).

Although the electronic properties of nanotubes can be compromised via functionalization, it is however a necessary step in order to unbundle them [154,180] and enable derivatization. SWCNTs were ethylene amine and phenylamine functionalized via the diazonium ion formation according to literature [168,180,279]. SWCNTs were amine functionalized with ethylene amine (EA) and phenyl-amine (PA) according to Schemes 3.1 (route **I**) and (route **II**) to give products EA-SWCNT **(11)** and PA-SWCNT **(12)**, respectively. The amine groups are attached on the walls of the SWCNTs, Scheme 3.1. A mixture of conc. H_2SO_4 and conc. HNO_3 in the ratio of 3:1 was used to cut and terminate SWCNTs with carboxylic acid groups, SWCNT-COOH **(13),** Scheme 3.1 (route **III**).

3.1.1 Characterization of functionalized SWCNTs

3.1.1.1 FTIR and Raman spectroscopies

Figure 3.1a shows the FTIR spectra for the various forms of SWCNTs. The IR spectra for the functionalized SWCNTs showed enhanced bands, Figs. 3.1a(ii)-a(iv), compared with the raw (Fig. 3.1a(i)). The $-NH_2$ bands for the EA-SWCNT (Fig. 3.1a(iv)) were observed in the region 3430-3470 cm^{-1} (doublet) [168] and 1390-1640 cm^{-1} for the scissoring modes [168,178,190]. PA-SWCNT (Fig. 3.1a(iii)) showed an $-NH_2$ doublet in the region of 3428-3490 cm^{-1} [168] and a scissoring mode around 1644 cm^{-1} [168,178,190].

SWCNT-COOH (Fig. 3.1a(ii)) showed O-H and C=O bands at the following wave numbers: 3400-3500 cm^{-1} and 1620-1720 cm^{-1}, respectively [68,163,176,191].

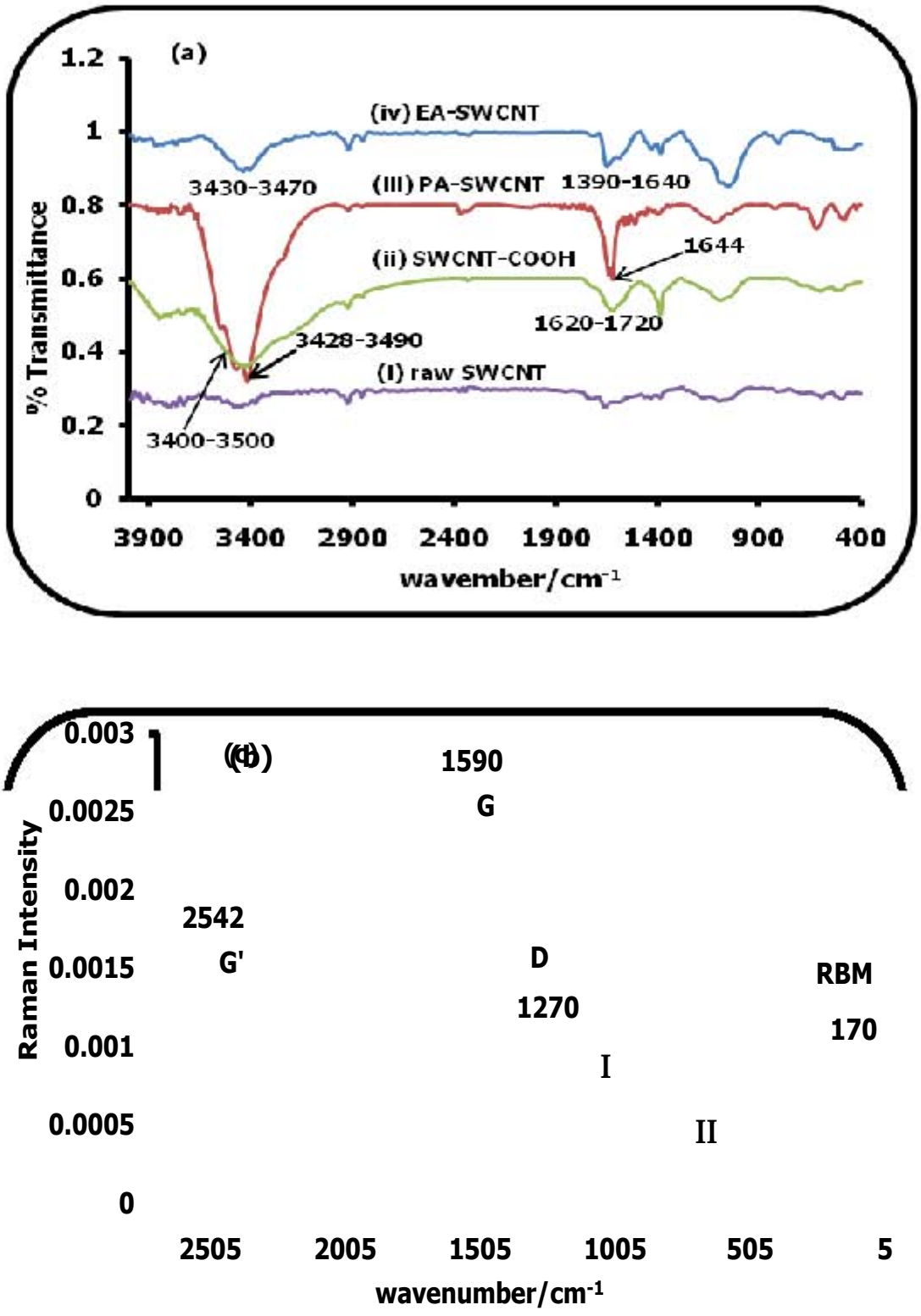

Figure 3.1: (a) FTIR spectra for (i) raw SWCNTs, (ii) SWCNT-COOH, (iii) PA-SWCNT and (iv) EA-SWCNT and (b) Raman spectra for (I, dashed line) raw SWCNTs and (II, solid line) EA-SWCNT in powder form.

Figure 3.1b (I and II**)** shows the Raman spectra for the raw SWCNTs and EA-SWCNT, respectively. The G band was observed at 1590 cm^{-1} as in other studies [164,175,176,178], while the D band was found around 1270 cm^{-1} and is close to what has been observed elsewhere [136,176]. The significant increase in the D band intensity (relative to the G band) is an indication of sidewall functionalization [168]. The non-dispersive G'-band at 2542 cm^{-1} and the radial breathing mode (RBM) at 170 cm^{-1} are in agreement with other studies [177]. The G- and the D-bands were observed at 1593 cm^{-1} and 1326 cm^{-1}, respectively (for the SWCNT-COOH), in agreement with literature [164,175,178]. Increase in intensity of the D-band relative to the raw is due to the conversion of sp^2 bonding into sp^3 and this confirms successful functionalization [164]. Raman spectral studies for PA-SWCNT **(12)** were not done because of instrumental problems, but the spectrum is expected to be similar to that of EA-SWCNT **(11)**.

3.1.1.2 Transmission electron microscopy (TEM)

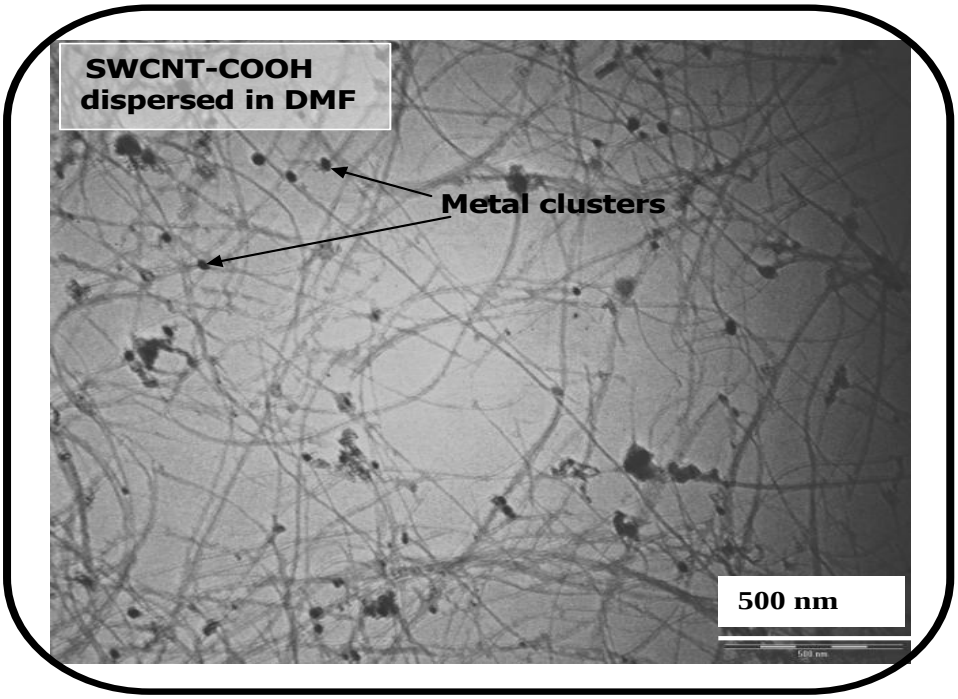

Figure 3.2: TEM image of SWCNT-COOH (13). Magnification: x10 000.

Figure 3.2 shows the transmission electron microscopy (TEM) picture of SWCNT-COOH **(13)** that were initially dispersed in DMF. The dark spots in between the SWCNTs could be metallic clusters from the catalyst used in their synthesis [164,280,281].

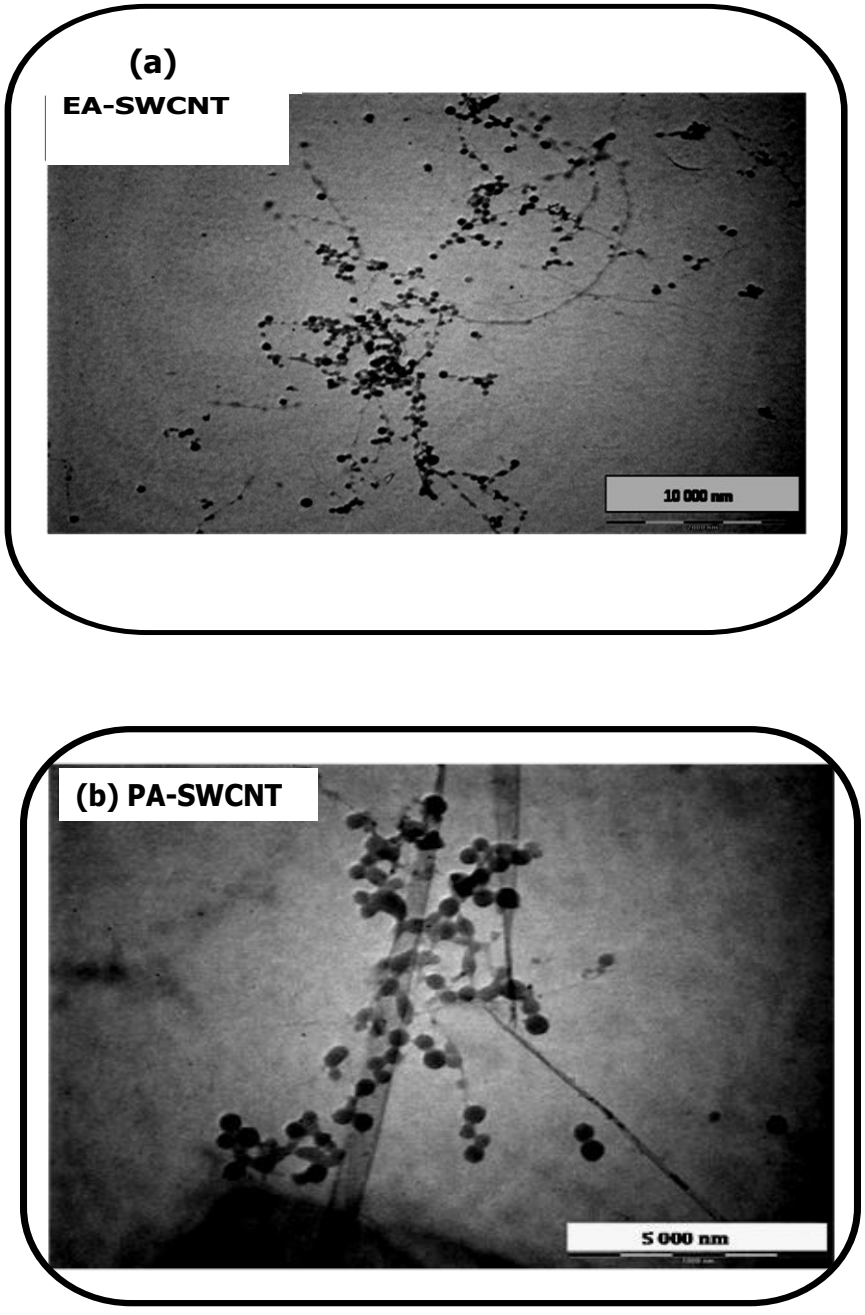

Figure 3.3: TEM image of side walled functionalized SWCNT: (a) EA-SWCNT (11) and (b) PA-SWCNT (12).

TEM was successfully used to show modification of SWCNTs (Figs. 3.2 and 3.3). The TEM pictures shown in Fig. 3.3(a and b) were taken after sonication of EA-SWCNT **(11)** and PA-SWCNT **(12)** in DMF for 1 h and then drying the solvent. The pictures show well dispersed beaded SWCNT rods, an indication of successful functionalization with ethylene diamine (EDA) and 1,4-benzene diamine (BDA). The nice dispersion of EA-SWCNT (Fig. 3.3a) and PA-SWCNT (Fig. 3.3b) shows the good exfoliating properties of DMF. The beads along the sides of the SWCNTs confirm that the amine groups are attached on the walls. The beads observed in EA-SWCNT (Fig. 3.3a) appear smaller than those shown for PA-SWCNT (Fig. 3.3b), possibly due to the differences in the sizes of EA and PA. The nature of the TEM images for SWCNT-COOH **(13)**, EA-SWCNT **(11)** and PA-SWCNT **(12)** indicate the different modes of functionalization.

3.1.1.3 XRD spectroscopy

Table 3.2: XRD parameters for the raw and functionalized SWCNTs.

Type of SWCNT	**2θ (in degrees)**	**d – spacing (Å)**
Raw SWCNTs	17.5; 20.5; 25.5; **26.5**; 44.5; 51.5	5.00; 4.29; 3.36; **3.32**; 2.04; 1.77
SWCNT-COOH **(13)**	17.5; 20.5; 25.5; **26.5**; 44.5; 52.0	5.06; 4.28; 3.43; **3.36**; 2.04; 1.76
EA-SWCNT **(11)**	10.6; 17.5; 20.6; **26.6**; 44.3; 51.6	8.31; 5.05; 4.32; **3.35**; 2.04; 1.77
PA-SWCNT **(12)**	10.8; 17.6; 20. 6; **26.6**; 44.5; 51.5	8.17; 5.04; 4.31; **3.35**; 2.03; 1.76

Changes in 2θ angles and d-spacings confirm a new crystal form [189]. The (002) d-spacing for the functionalized SWCNTs (at ~26.6^0, Table 3.2 **in bold**) have significantly increased and this could confirm the formation of a new crystal.

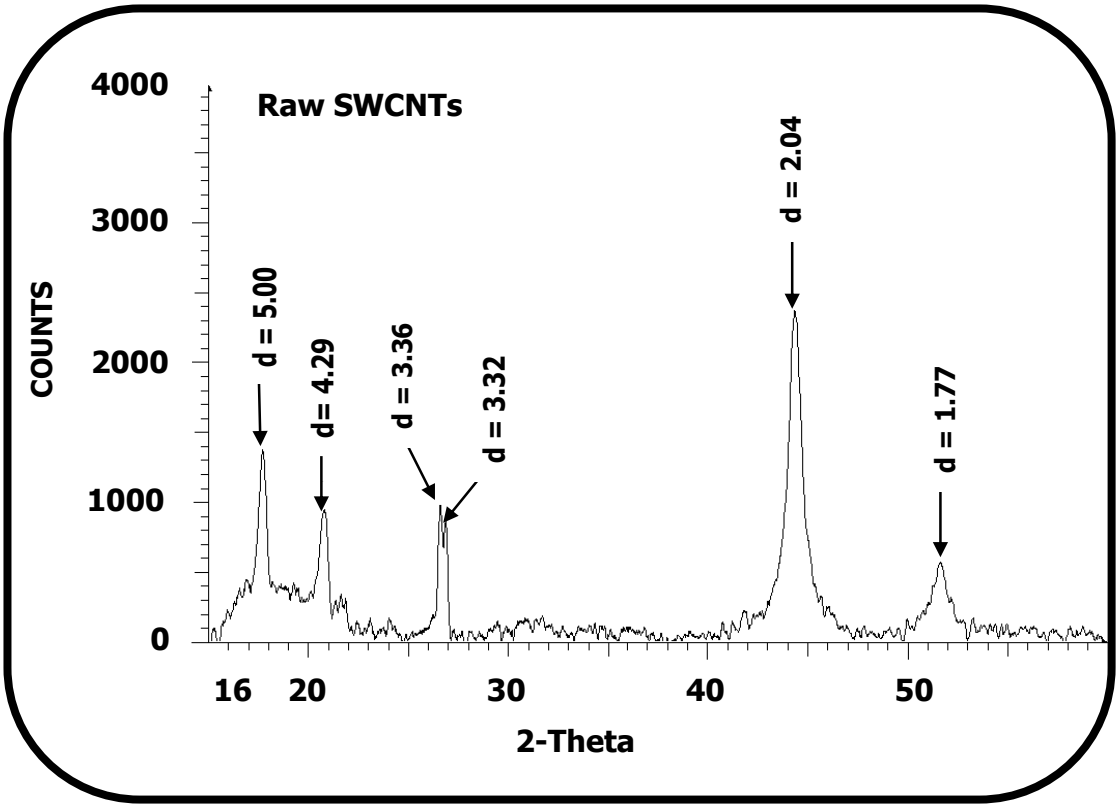

Figure 3.4: XRD spectrum for raw SWCNTs.

The powder X-ray diffraction study of raw SWCNTs and SWCNT-COOH were done over the range of $2\theta = 15–60^0$ on a silicon wafer. XRD data were fitted using Eva (evaluation curve fitting) software. Alternatively the d-spacings can be estimated using the Scherrer Eq. 3.1 [282].

$$d(\text{Å}) = \frac{k\lambda}{\beta \text{Cos}\theta} \tag{3.1}$$

where k is an empirical constant equal to 0.9, λ is the wavelength of the X-ray source, (1.5405 Å), β is the full width at half maximum of the diffraction peak and θ is the angular position of the peak.

Raw SWCNTs (Fig. 3.4) show peaks at 2θ angles of 17.5^0 (singlet), 20.5^0 (singlet), 26.0^0 (doublet average value), 44.5^0 (singlet) and 51.5^0 (singlet) corresponding to d-spacing values of 5.00 Å, 4.29 Å, 3.36 Å and 3.32 Å, 2.04 Å and 1.77 Å, respectively, Table 3.2.

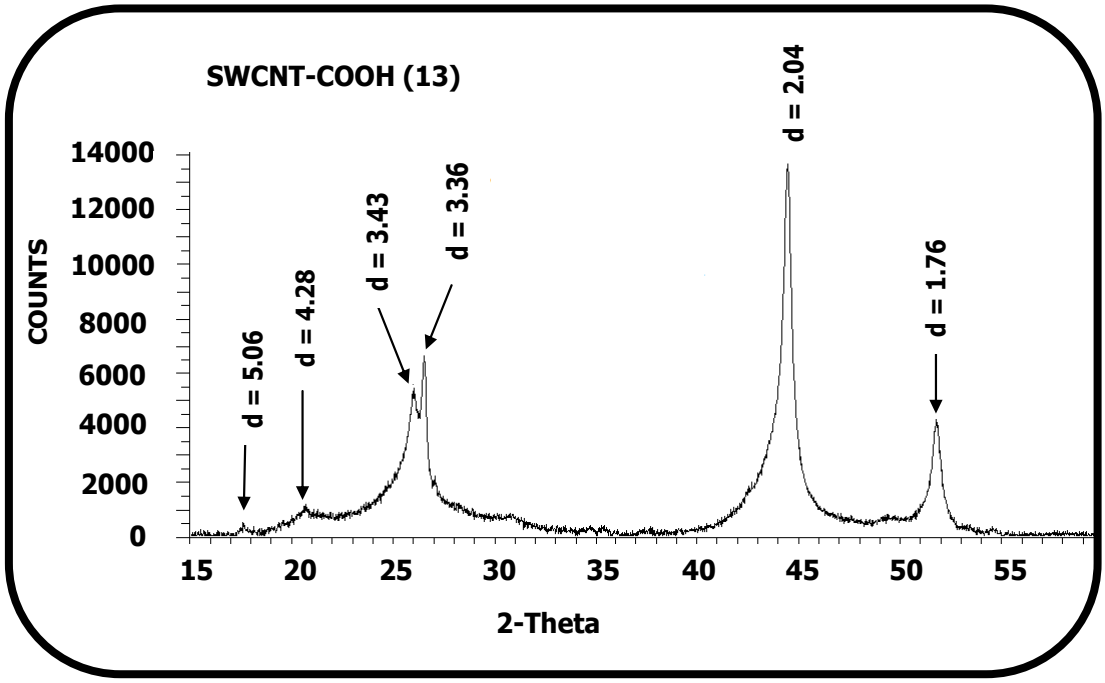

Figure 3.5: XRD spectrum for SWCNT-COOH (13).

The SWCNT-COOH (Fig. 3.5) peaks at $2\theta = 17.5^0$ (d = 5.06 Å) and 20.5^0 (d = 4.28 Å) dropped drastically in intensity upon COOH functionalization and these could have resulted from the removal of impurities in the raw SWCNTs. All other peaks increased in intensities with the doublet peak appearing at an average value of 26.0^0 ($(25.5^0 + 26.5^0)/2$). This doublet corresponds to the graphite (002) d-spacing of the SWCNTs [194-196]. The d_{002} values derived from the doublet (SWCNT-COOH = 3.43 Å and 3.36 Å) are higher than that of the perfect graphite (d_{002} = 3.35 A^0) as observed in other studies [195]. The two peaks at 2θ values of 44.5^0 and 52^0 correspond to the (111) and (200) planes of carbon [196] (Fig. 3.5), Table 3.2. The difference in the nature of the XRD spectra (i.e. 2θ angles and d-spacings) for the raw SWCNTs (Fig. 3.4) and SWCNT-COOH (Fig. 3.5) is an indication of formation of new crystal [189], hence successful functionalization. All the peaks for SWCNT XRDs are very sharp, an indication of their crystalline form [44].

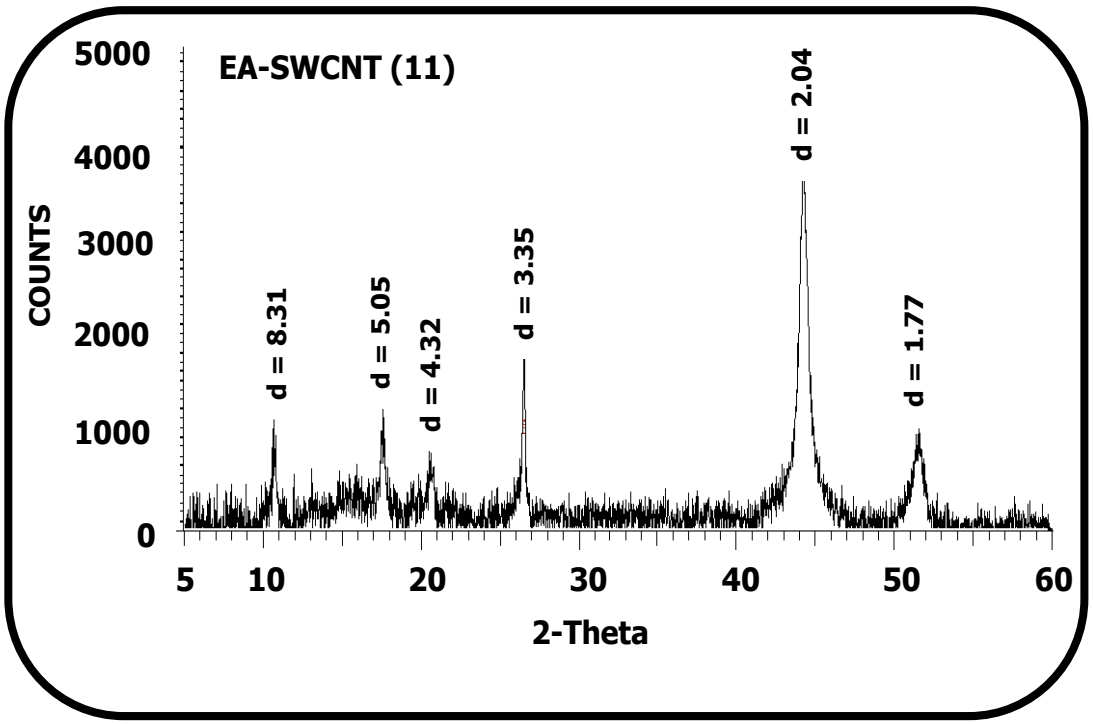

Figure 3.6: XRD spectrum for EA-SWCNT (11).

The EA-SWCNT **(11)** spectrum (Fig. 3.6) shows a number of peaks at 2θ angles of 10.6^0, 17.5^0, 20.6^0, 26.6^0, 44.3^0 and 51.6^0 (Table 3.2). The peaks at 2θ angles of 26.6^0, 44.3^0 and 51.6^0 corresponds to the graphite (002) d-spacing of the SWCNTs [194-196], the (111) and (200) reflections of carbon [196], respectively. The sources of the peaks at 2θ angles of 10.6^0, 17.5^0 and 20.6^0 are not yet clearly understood.

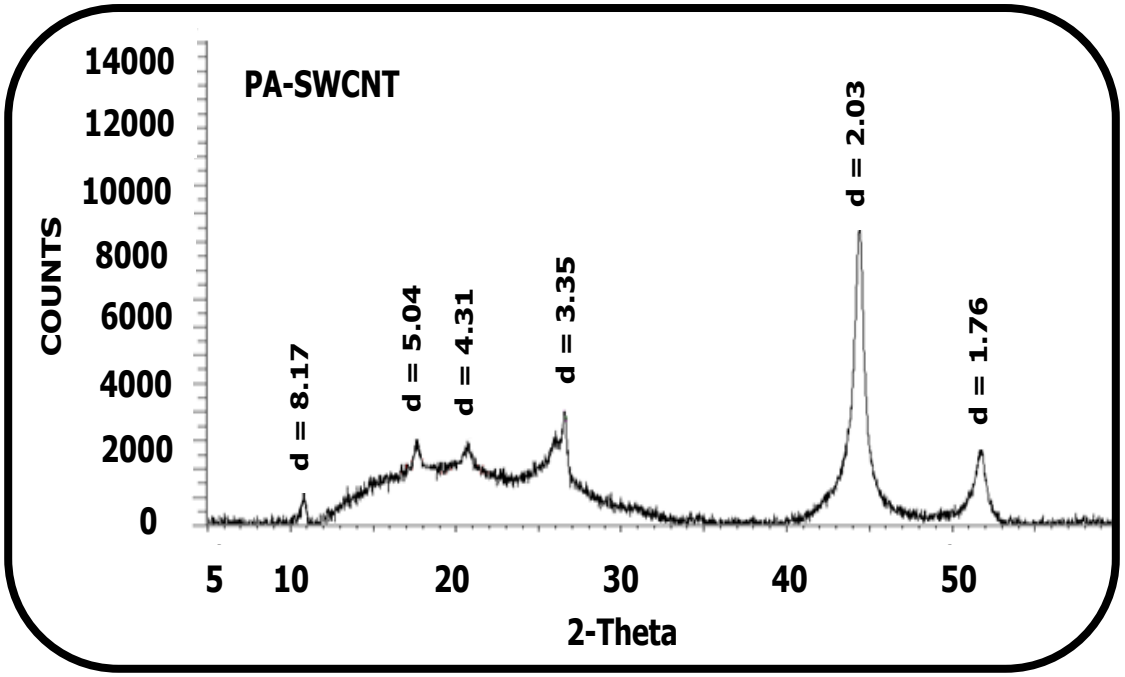

Figure 3.7: XRD spectrum for PA-SWCNT (12).

The PA-SWCNT **(12)** spectrum (Fig. 3.7) shows six peaks at 2θ angles of 10.8^0, 17.6^0, 20.6^0, 26.6^0, 44.5^0 and 51.5^0 (Table 3.2), with the peaks at 2θ angles of 26.6^0, 44.5^0 and 51.5^0 corresponding to the graphite (002) d-spacing of the SWCNTs [194-196], the (111) and (200) reflections of carbon [196]. 1,4-Benzene diamine (BDA) alone showed peaks at 17.8^0 and 20.5^0 which are close to the 2θ values that are observed in the PA-SWCNT **(12)** spectra. However peaks close to these (17.8^0 and 20.5^0) have also been observed in the EA-SWCNT spectrum and it therefore becomes difficult to conclude the source of their origin at this point. The source of the peak at 2θ angles of 10.8^0 is not yet clearly understood. The changes in 2θ values and d-spacings could confirm crystallographic rearrangements that occur when the phenylamine group is attached to the walls of the SWCNTs.

3.1.1.4 Thermogravimetric analyses

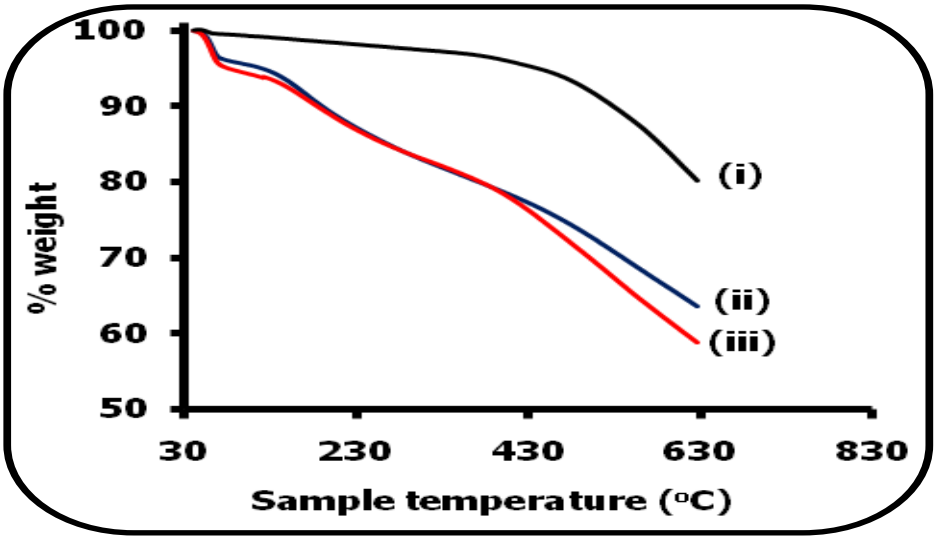

Figure 3.8: Thermogravimetric analysis (TGA) of (i) raw SWCNT, (ii) EA-SWCNT (11) and (iii) SWCNT-COOH (13) obtained at a heating rate of 10 ^{0}C/min under nitrogen.

Structural differences (Fig. 3.8, **i – iii**) between the raw SWCNT **(i)**, EA-SWCNT **(ii)** and SWCNT-COOH **(iii)** were confirmed using thermal gravimetric analysis (TGA). Different thermal decay profiles, (Fig. 3.8, **i - iii**), point to structurally different materials. Weight loss observed for the raw SWCNT may be due to the destruction of the residual amorphous carbon present in the carbon nanotubes. TGA showed weight loss of 19.8 %, 36.4 % and 40.4% for the raw SWCNT, EA-SWCNT and SWCNT-COOH, respectively, at 625 °C. The extent of functionalization is expressed as the number of substituents per SWCNT carbon atoms. The estimated weight losses due to the functionalization on EA-SWCNT and SWCNT-COOH are 16.6 % and 20.6 %, respectively. Using the formula reported in the literature [209], this gave about one EA functional group per 25 carbon atoms for EA-SWCNT and is close enough to what has been observed in other studies [52]. The ratio of COOH groups to carbon atoms was found to be 1:15.

3.2 Synthesis and characterization of symmetrical Pcs (MTAPcs (7a, 7b, 7c) and CoTCPc (8))

The synthesis of CoTAPc **(7a)**, FeTAPc **(7b),** NiTAPc **(7c)** and CoTCPc **(8)** has been reported before [29,43,44, 51,275]. The IR spectra of MTAPcs showed bands in the region 3400-3500 cm^{-1} and 1500-1600 cm^{-1} (due $-NH_2$ stretching and bending vibrations) [68,176,190] and around 2900 cm^{-1} (due to C-H vibrations) [283,284]. The IR spectrum of CoTCPc **(8)** gave vibrational bands at 3475, 1710 and 1090 cm^{-1}, representing the O-H, C=O and the C-O stretching bands, respectively.

The UV-vis spectra for CoTAPc **(7a)**, FeTAPc **(7b)**, NiTAPc **(7c)** and CoTCPc **(8)** showed a symmetrical peaks at 680, 700, 708 and 666 nm, respectively (all in DMF), Table 3.3.

Table 3.3: UV-vis absorption maxima for complexes and mixtures

Complex	Q-band/nm
CoTAPc **(7a)**	680
CoTAPc-SWCNT(linked) **(14)**	635
CoTAPc/SWCNT-COOH(mix)	635
FeTAPc **(7b)**	700
FeTAPc-SWCNT(linked) **(15)**	681 (shoulder); 684
FeTAPc/SWCNT-COOH(mix)	688
NiTAPc **(7c)**	708
NiTAPc-SWCNT(linked) **(16)**	703
NiTAPc/SWCNT-COOH(mix)	705
CoTCPc **(8)**	666
CoTCOClPc	675
CoTCPc-PA-SWCNT(linked) **(17)**	680
CoTCPc/PA-SWCNT(mix)	678
CoTCPc **(8)**	666
CoTCOClPc	675
CoTCPc-EA-SWCNT(linked) **(18)**	675
CoTCPc/EA-SWCNT(mix)	666
CoMAPc **(9)**	677
CoMAPc-SWCNT(linked) **(19)**	686
CoMAPc/SWCNT-COOH(mix)	686
CoMCPc **(10)**	672
CoMCOClPc	672
CoMCPc-PA-SWCNT(linked) **(20)**	686
CoMCPc/EA-SWCNT(mix)	686

3.3 Synthesis and characterization of CoMAPc (9)

CoMAPc **(9)** is a low symmetry Pc carrying a single amino group. It was synthesized according to Scheme 3.2. The statistical approach was employed and the Pc was synthesized via the formation of its corresponding mononitro-Pc **(23)** in DMF, followed by the reduction of the nitro-Pc **(23)** in aqueous $Na_2S.9H_2O$ to give CoMAPc **(9)**. CoMAPc **(9)** was then purified according to literature methods for amino Pcs [29]. Further purification was by chromatography on a Si_{60} column and dried over P_2O_5.

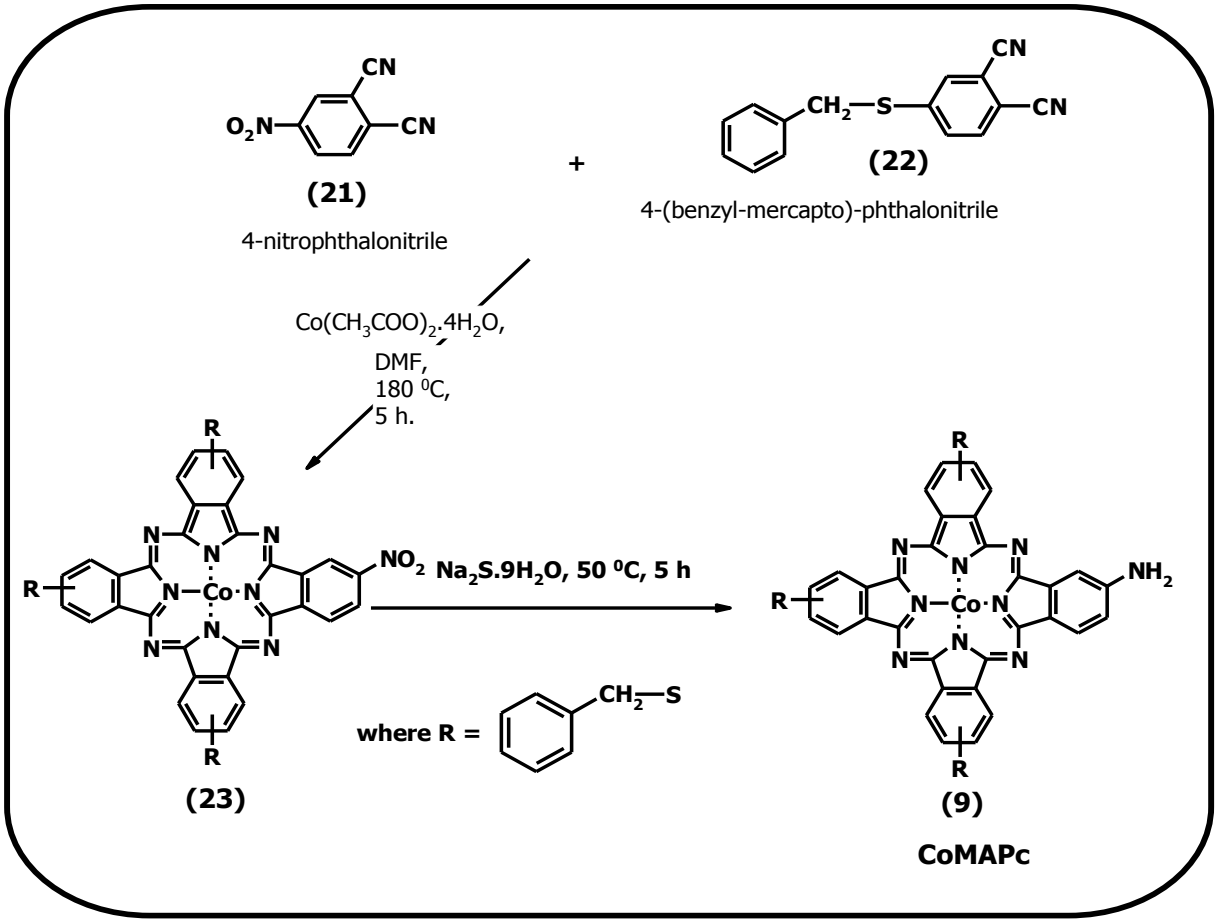

Scheme 3.2: Synthetic route to CoMAPc (9).

Elemental analysis results and the calculated values showed good agreement. Mass spectral results gave the same molecular mass as the one calculated from the molecular formula at 952 atomic mass units. Splitting of the Q-band which is typical of low symmetry phthalocyanines is not very clear in Fig. 3.9, however, there is

broadening which could either be due to low symmetry or aggregation. The Beer-Lambert law was obeyed for the complex in the concentration range 1×10^{-6} to 1×10^{-5} M (in DMF), hence the broadening could be due to unresolved splitting due to low symmetry nature of the molecule. The IR spectrum for the CoMAPc showed a peak at 1601 cm^{-1} as well as a broad (and weak) feature at ~3300 cm^{-1} for the -NH_2 stretching [168] and scissoring modes [168,178,190], respectively.

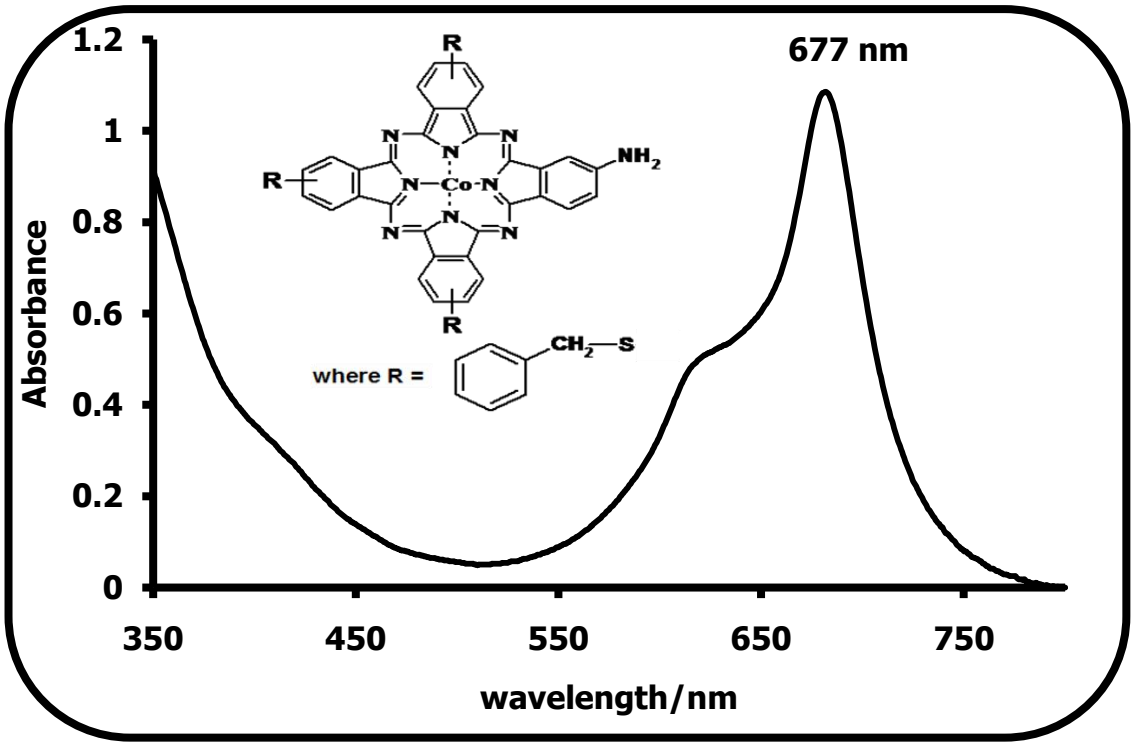

Figure 3.9: UV-vis spectrum for 1 x 10^{-5} M CoMAPc (9) in DMF. Inset: Molecular structure of 9.

3.4 Synthesis and characterization of CoMCPc (10)

CoMCPc **(10)** is a low symmetry Pc carrying a single carboxylic acid group. It was synthesized according to Scheme 3.3, using the statistical approach as was for CoMAPc **(9)**.

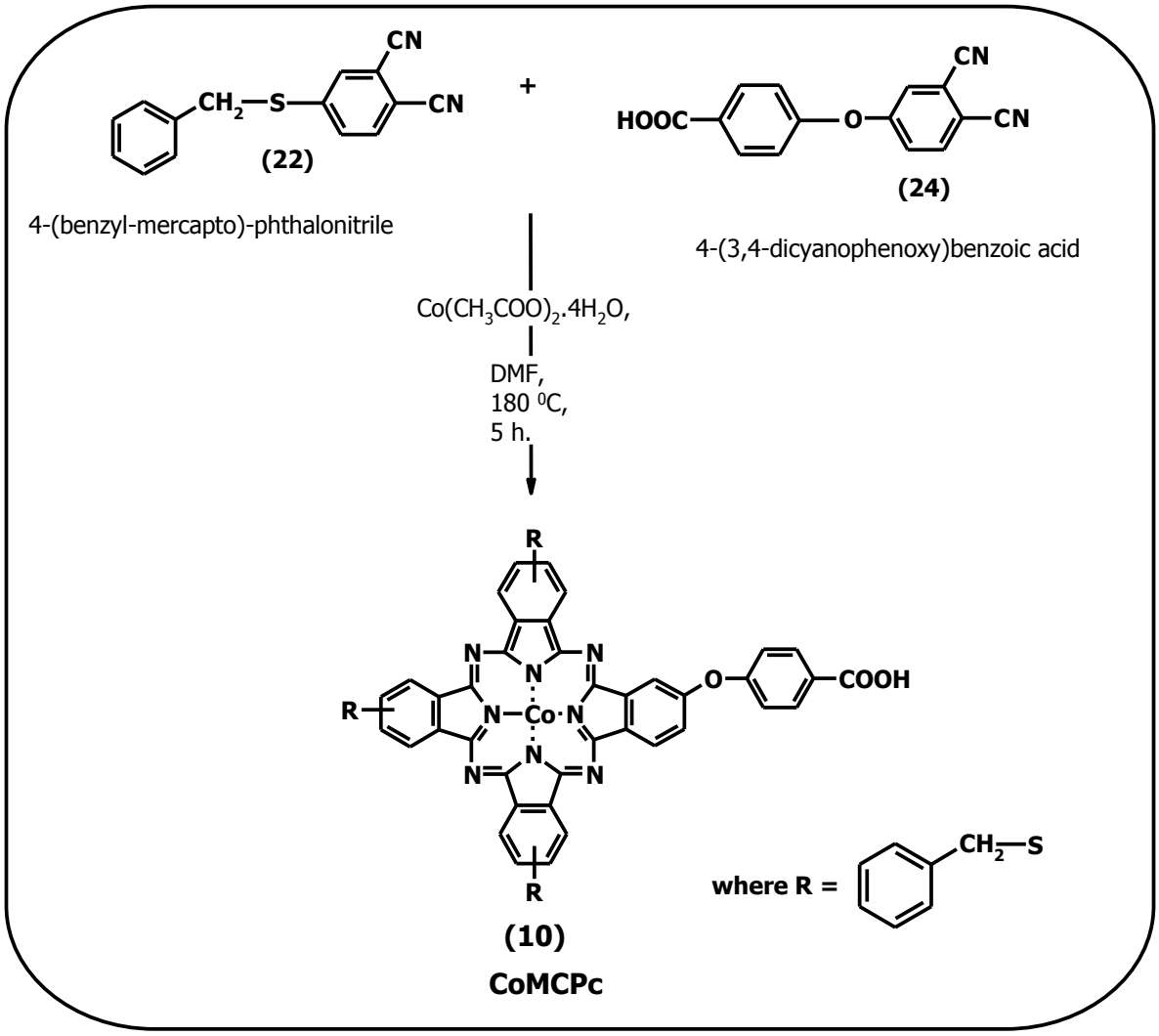

Scheme 3.3: Synthetic route to CoMCPc (10).

Elemental analysis confirmed the synthesis of CoMCPc **(10).** Mass spectral analysis results were in good agreement with the calculated molecular ion mass at M^+ = 1075. The IR spectrum showed bands at 3266 cm^{-1}, 2921 cm^{-1}, 1720 cm^{-1} and 748 cm^{-1} wave numbers, corresponding to the O-H, C-H, C=O and C-S vibrational bands, respectively.

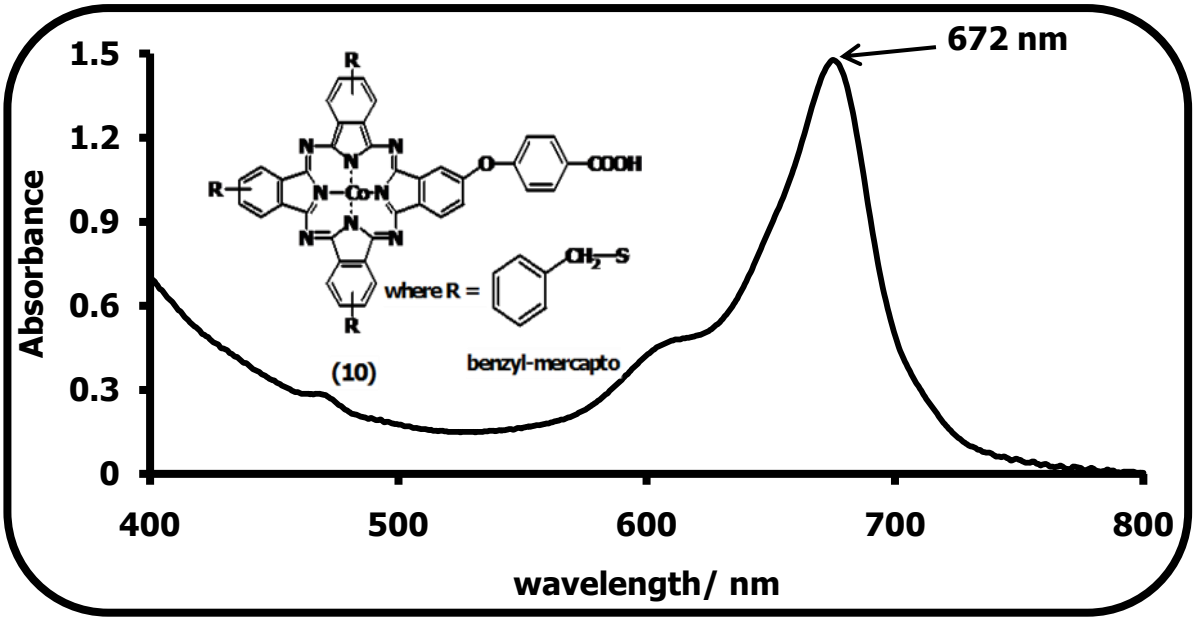

Figure 3.10: UV-vis spectrum for 1 x 10^{-5} M CoMCPc (10) in DMF. Inset: Molecular structure of 10.

UV-Vis spectrum for **10** is shown in Fig. 3.10. The splitting of the Q-band expected of low symmetry Pcs is not very clear (Fig. 3.10), as was with CoMAPc, although there is broadening which could either be due to low symmetry incomplete splitting of the Q-band (at 672 nm, Table 3.3) or aggregation. However, CoMCPc **(10)** obeyed the Beer-Lambert law in the concentration range 1 × 10^{-7} to 1 × 10^{-5} M (in DMF), hence the broadening can be attributed to the unresolved splitting of this molecule, due to its low symmetry nature. A charge transfer band was observed at around 460 nm.

3.5 Synthesis and characterization of MTAPc-SWCNT conjugates (14,15,16)

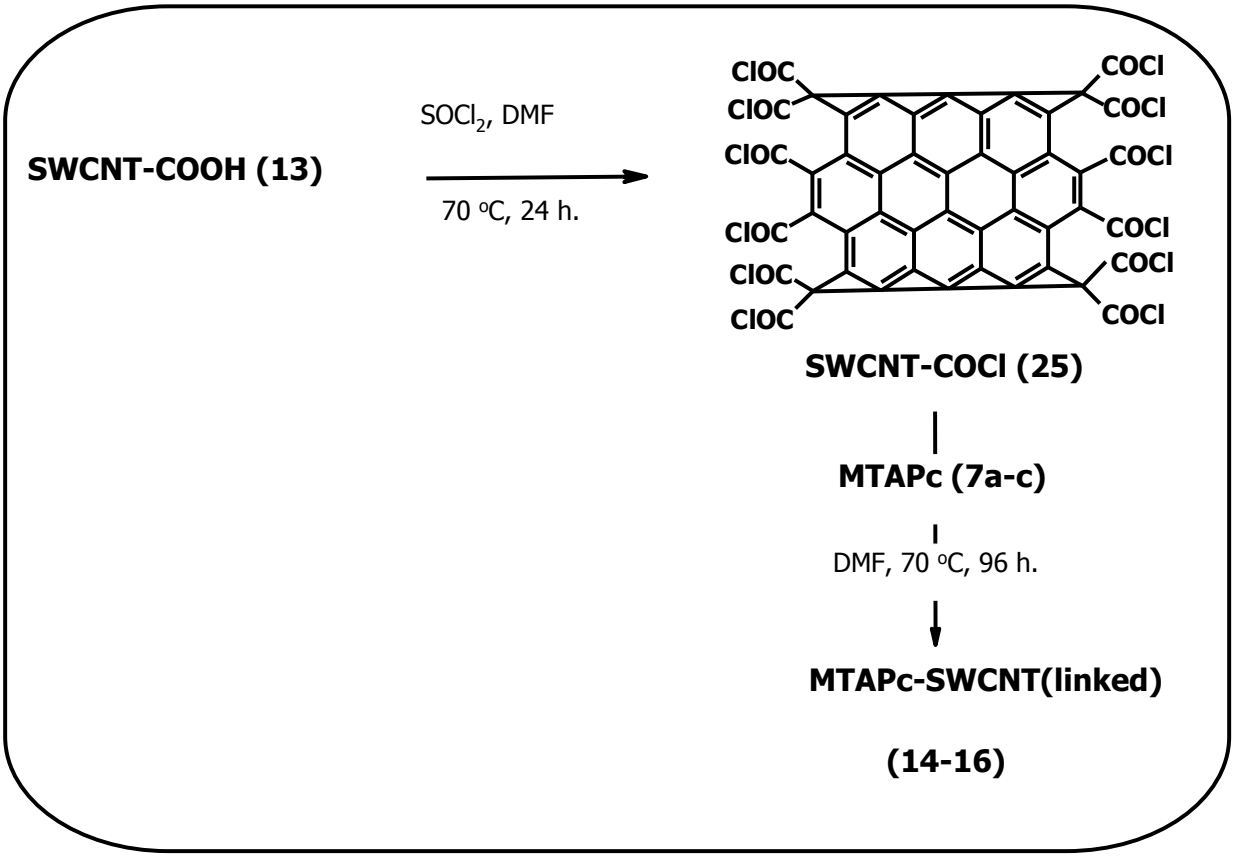

Scheme 3.4: Synthetic route to MTAPc-SWCNT (14-16).

The syntheses of MTAPc-SWCNT(linked), are shown in Scheme 3.4. SWCNT-COOH (**13**) (1 mg) were converted into the acid chloride derivative (SWCNT-COCl**, 25**) [163,201] through the use of $SOCl_2$ and a few drops of anhydrous DMF catalyst. Solid SWCNT-COCl **(25)** was refluxed with MTAPc in DMF (96 h at 70 ^{0}C). The product (MTAPc-SWCNT(linked)) was exhaustively washed with DMF to remove most the MTAPc adsorbed on the SWCNT walls. The solid products were dried at room temperature under vacuum.

3.5.1 Characterization of CoTAPc-SWCNT(linked) (14)

3.5.1.1 UV-vis spectroscopy

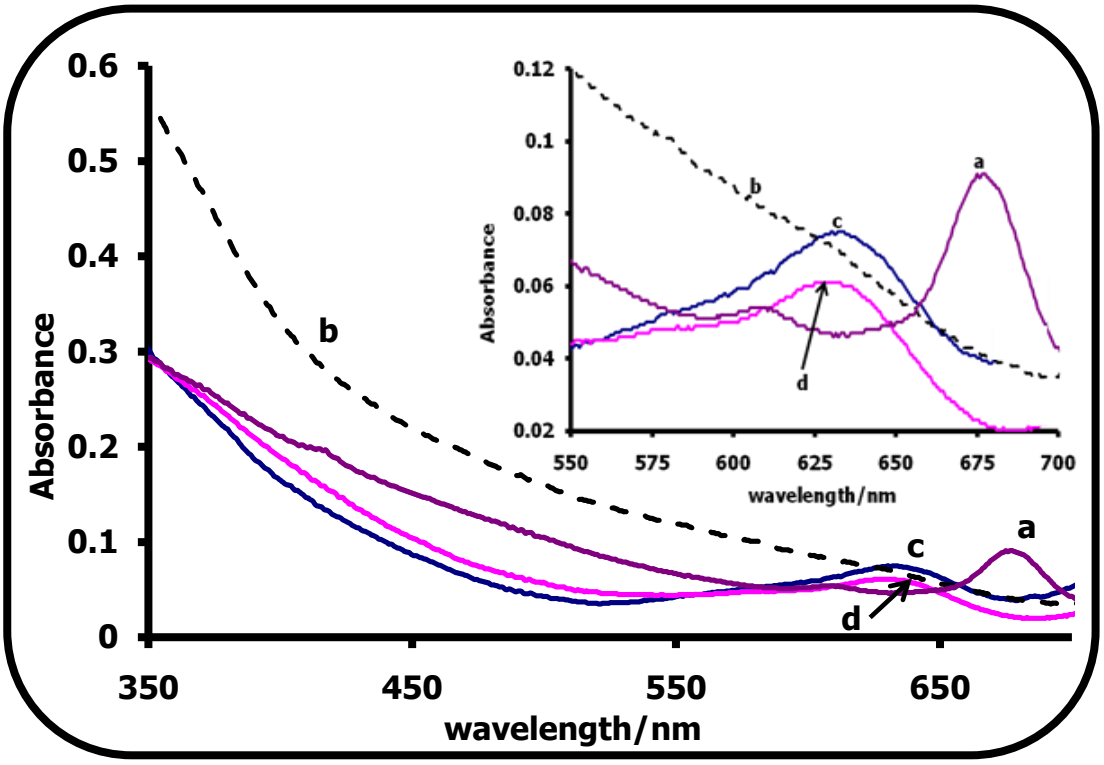

Figure 3.11: UV-Vis spectra of (a) CoTAPc, (b) SWCNT-COOH (13), (c) 1 µM CoTAPc-SWCNT(linked) (14) and (d) CoTAPc/SWCNT-COOH(mix). Inset: Expanded view from 550-700 nm. Solvent DMF.

The UV-Vis spectra of SWCNT-COOH **(13)**, CoTAPc **(7a)**, CoTAPc-SWCNT(mix) and CoTAPc-SWCNT(linked) (**14)** were recorded in DMF (after 1 h of sonication). The absorption spectral bands for SWCNT-COOH **(13)**, Fig. 3.11b, are very weak and this has been observed in other studies [180]. The Q-band (λ = 635 nm) of CoTAPc-SWCNT(linked), (Fig. 3.11c), is shifted from CoTAPc **(7a)** (λ = 680 nm), Fig. 3.11a, but it is the same as that of CoTAPc/SWCNT-COOH(mix) (λ = 635 nm, Fig. 3.11d). In this case, the UV-Vis spectra do not give clear evidence of chemical bonding since both CoTAPc-SWCNT(linked) and CoTAPc/SWCNT-COOH(mix) have Q-bands at the same wavelength. The blue shifting in the spectrum in the presence of SWCNT-COOH **(13)** is typical of aggregation in MPc complexes [285]. However in this type of aggregation, both the monomer and dimer

will normally be present, which is not the case in Fig. 3.11. Therefore this blue shift could be due to the SWCNT-COOH which withdraws electrons from the $-NH_2$ groups of CoTAPc following coordination. This electron withdrawal increases the HOMO-LUMO gap, resulting in this blue shift. However mixing CoTAPc and SWCNT-COOH also result in blue shifting, suggesting that there could some interactions which distort the Pc л-conjugation.

3.5.1.2 IR spectroscopy

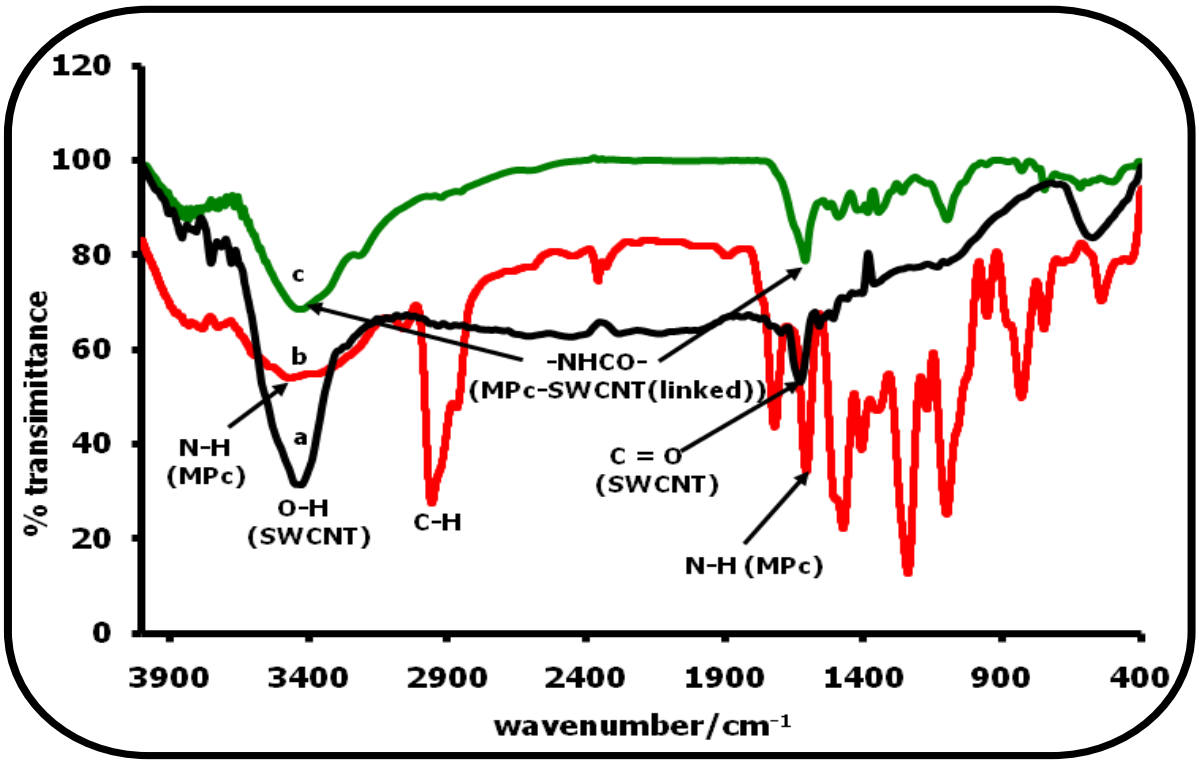

Figure 3.12: FTIR spectra of (a) SWCNT-COOH (13), (b) CoTAPc (7a), (c) CoTAPc-SWCNT(linked), 14.

Fig. 3.12 shows the FTIR spectra of SWCNT-COOH **(13)**, CoTAPc **(7a)** and CoTAPc-SWCNT(linked). The IR spectrum of the CoTAPc-SWCNT(linked) showed a band at 1608 cm^{-1} due to the C=O stretch of the amide bond (-NHCO-) and lies in between 1600 cm^{-1} ($-NH_2$) and 1620 cm^{-1} (C=O) for the CoTAPc **(7a)** and SWCNT-COOH, respectively, confirming the presence of a chemical bond between SWCNT-COOH and CoTAPc.

3.5.1.3 Raman spectroscopy (on modified GCE)

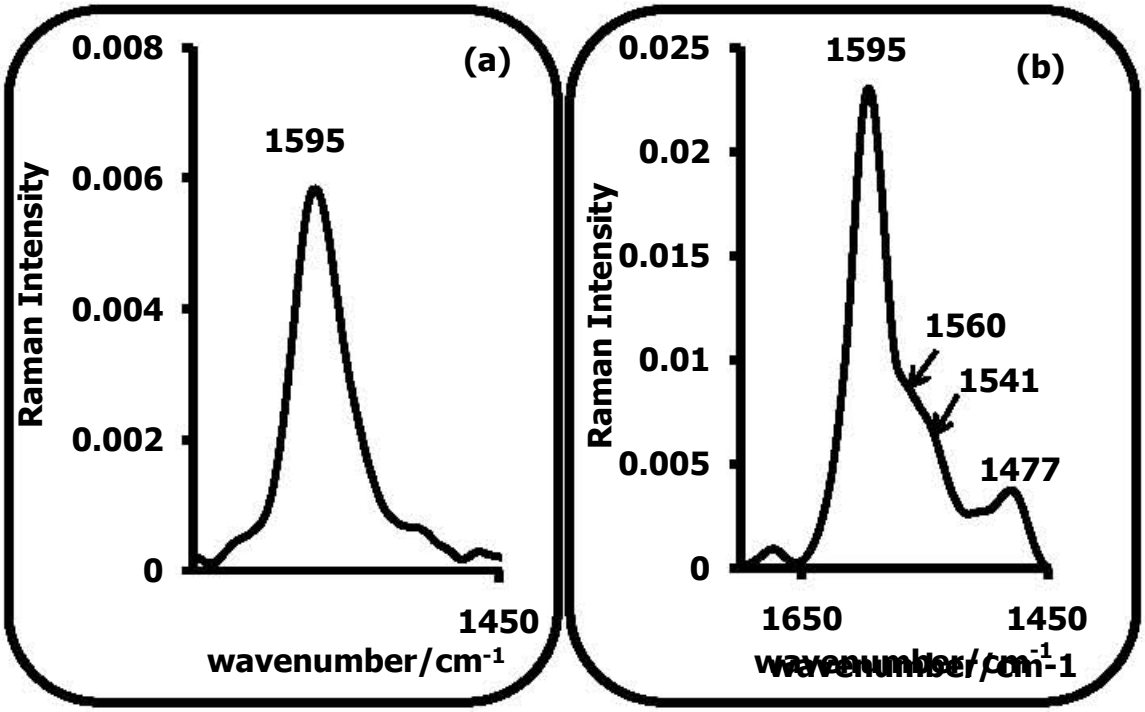

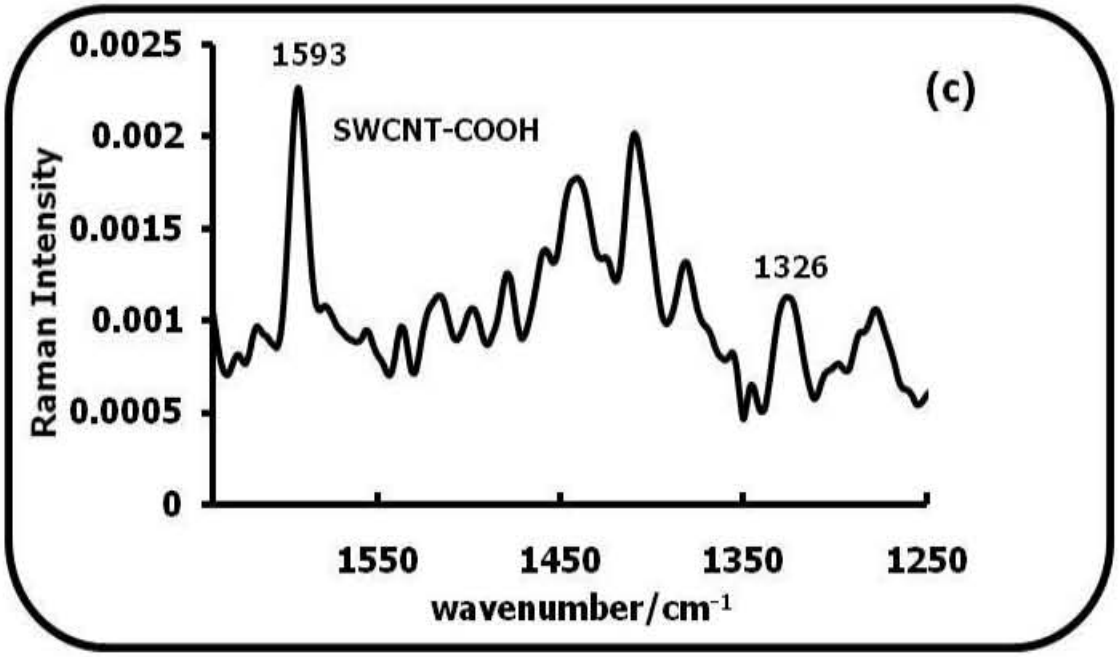

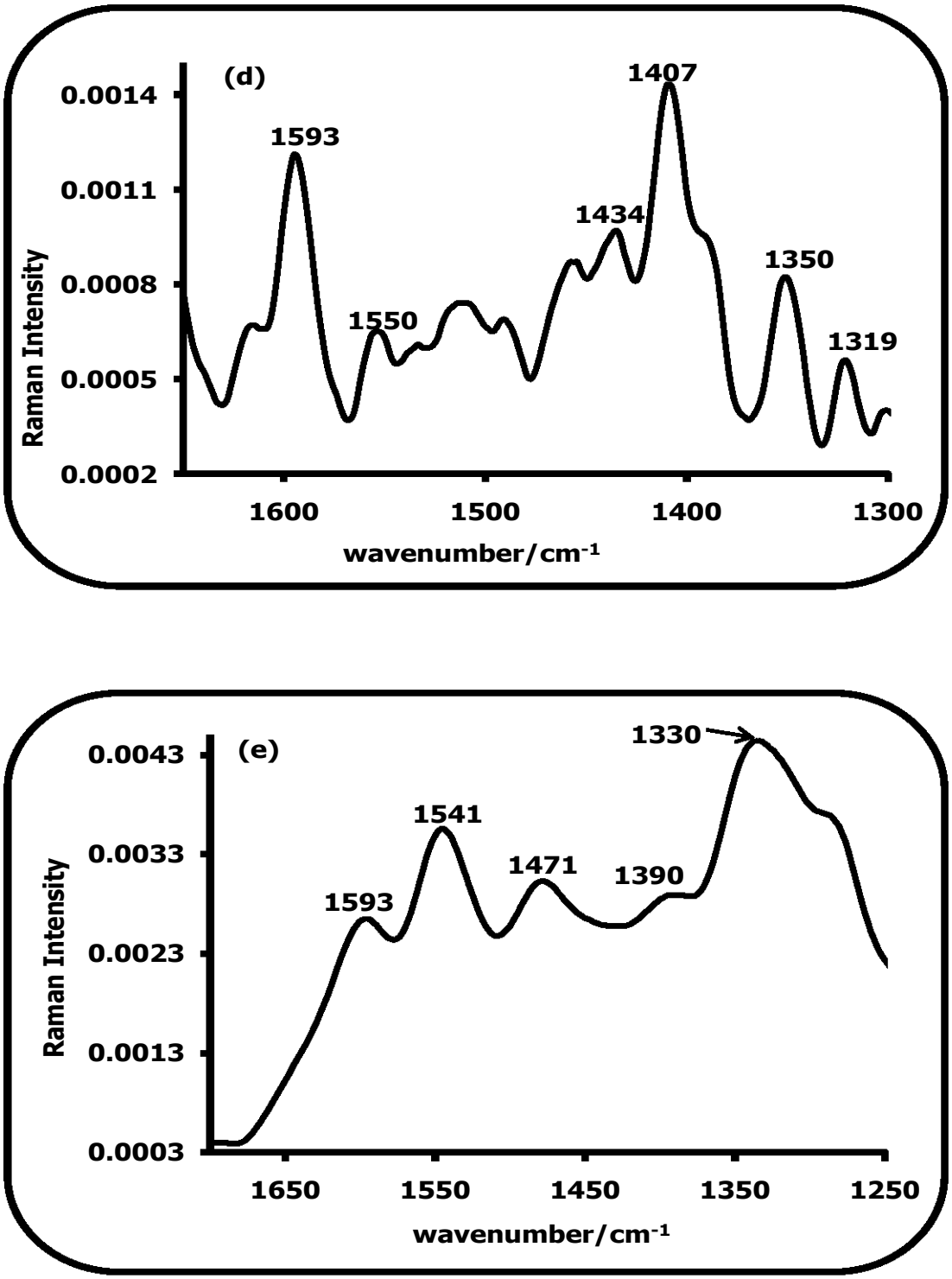

Figure 3.13: Raman spectra (a) GCE, (b) CoTAPc-GCE, (c) raw SWCNT-GCE and SWCNT-COOH-GCE, (d) CoTAPc/SWCNT-COOH(mix)-GCE and (e) CoTAPc-SWCNT(linked)-GCE. In DMF suspension.

The Raman bands have been reported at 1340 (D band) and 1610 cm^{-1} (G band) for a bare GCE [286]. The latter (G band) was observed at 1595 cm^{-1} for GCE (Fig. 3.13a), which shifted to 1593 cm^{-1} for SWCNT-COOH-GCE, CoTAPc/SWCNT-COOH(mix)–GCE and CoTAPc-SWCNT(linked)-GCE, Figs. 3.13c-e (Table 3.4). There is a decrease in intensity of the G band at 1593 cm^{-1} on formation of the CoTAPc-SWCNT(linked)-GCE (Fig. 3.13e) compared with CoTAPc/SWCNT-COOH(mix)-GCE (Fig. 3.13d) and these differences are associated with chemical linking in the former. The enhancement of the D bands with functionalization is a clear proof of the conversion of sp^2 bonding into sp^3 [164]. The D band for SWCNT-COOH **(13)** is observed at 1326 cm^{-1} (Fig. 3.13c), at 1330 cm^{-1} for CoTAPc-SWCNT(linked)-GCE (Fig. 3.13e) and at 1319 cm^{-1} for CoTAPc/SWCNT-COOH(mix)-GCE (Fig. 3.13d). The observed G- and D-bands are close to those reported in literature [166,176,191]. The Raman band at 1541 cm^{-1} (Fig. 3.13e) is due to the cobalt metal ion [287] in the CoTAPc **(7a)**, this band is observed at 1541 cm^{-1}, 1550 cm^{-1} and 1541 cm^{-1} for CoTAPc-GCE, CoTAPc/SWCNT-COOH(mix)-GCE and CoTAPc-SWCNT(linked)-GCE, respectively (Table 3.4), again showing the difference between the linked and mixed SWCNT-COOH and CoTAPc. The ion marker band in CoTAPc-GCE is not well resolved.

The prosposed structure of all MTAPc-SWCNT conjugates is shown in Fig. 3.14. In Fig. 3.14a some of the amino groups are not attached to the MTAPc, while in Fig. 3.14b, all the amino groups are linked to form conjugates.

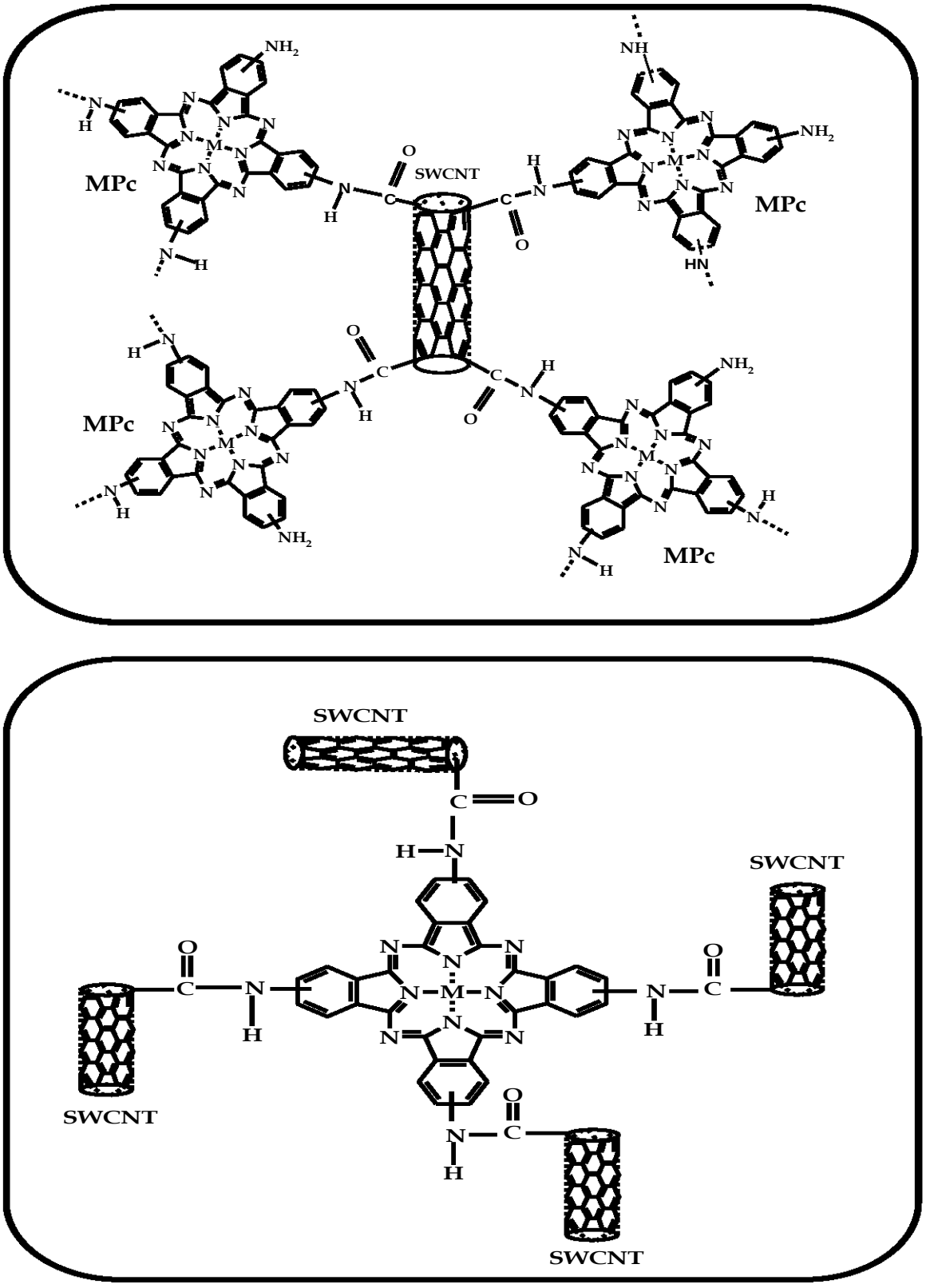

Figure 3.14: Representation of conjugates formed between SWCNT-COOH (13) and MTAPc using (a) some of the amino substituents and (b) all the amino substituents on the MTAPc.

Table 3.4: Raman bands

Complex	D-band/cm^{-1}	G-band/cm^{-1}	Ion marker band/cm^{-1}
GCE	1315	1595	-
SWCNT-COOH **(13)**	1326	1593	-
CoTAPc **(7a)**	1320	1595	1541
CoTAPc-SWCNT(linked) **(14)**	1330	1593	1541
CoTAPc/SWCNT-COOH(mix)	1319	1593	1550
FeTAPc **(7b)**	1330	1590	1536
FeTAPc-SWCNT(linked) **(15)**	1325	1585	1536
FeTAPc/SWCNT-COOH(mix)	-	-	Not clear
NiTAPc **(7c)**	1326	1593	1547
NiTAPc-SWCNT(linked) **(16)**	1320	1600	1545
NiTAPc/SWCNT-COOH(mix)	-		Not clear
EA-SWCNT **(11)**	1270	1590	-
CoTCPc **(8)**	1348	1551	Not clear
CoTCPc-EA-SWCNT(linked) **(18)**	1279	1598	Not clear
CoTCPc/EA-SWCNT(mix)	1278	1600	Not clear

3.5.2 Characterization of FeTAPc-SWCNT(linked) (15)

3.5.2.1 UV-Vis Spectroscopy

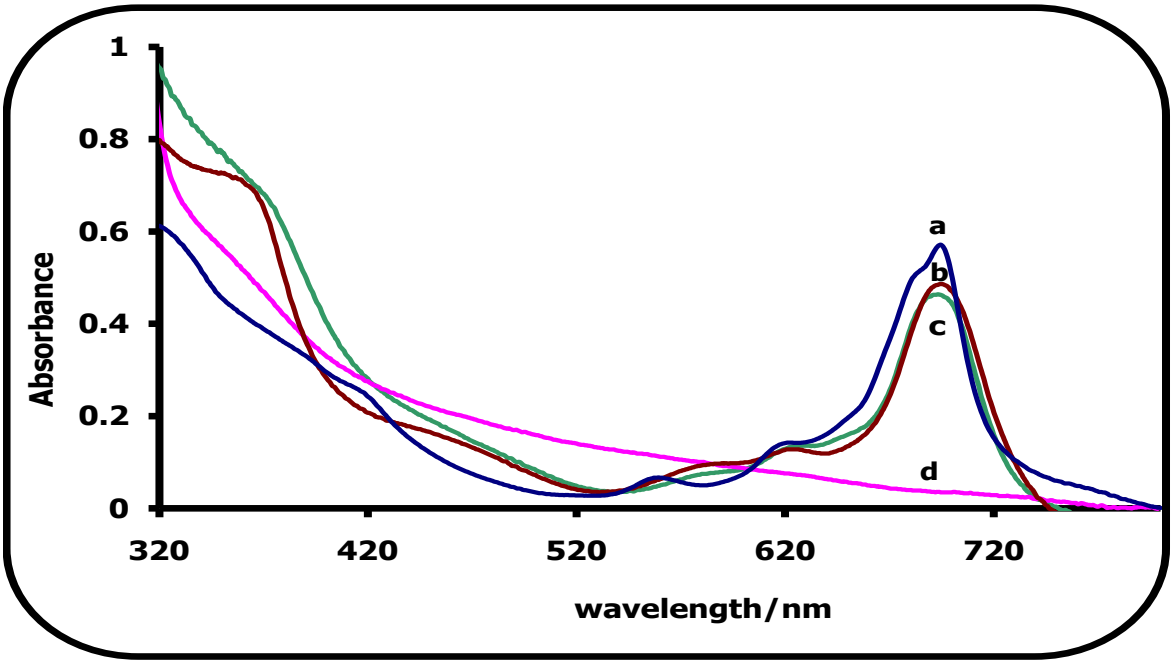

Figure 3.15: UV-vis spectra of (a) FeTAPc-SWCNT(linked) (15), (b) 1 µM FeTAPc (7b), (c) FeTAPc/SWCNT-COOH(mix) and (d) SWCNT-COOH (13). Solvent: DMF.

Figure 3.15, a – d, shows the UV–vis spectra of FeTAPc-SWCNT(linked) (λ = 684, with a shoulder at 681 nm), FeTAPc (λ = 700 nm), FeTAPc/SWCNT-COOH(mix) (λ = 688 nm) and SWCNT-COOH **(13)**, whose absorption maxima is undefined. The absorption maximum (Fig. 3.15a) for FeTAPc-SWCNT(linked) **(15)** shows a split Q band which is not evident in FeTAPc (Fig. 3.15b) and FeTAPc/SWCNT-COOH(mix), Fig. 3.15c. The explanation for the blue shifting observed for FeTAPc-SWCNT(linked) and FeTAPc/SWCNT-COOH(mix) is the same as for CoTAPc-SWCNT(linked) **(14)**. The splitting in the Q band may confirm a loss of symmetry [285], probably due to unsymmetrical substitution of the MTAPc forming conjugates of the type shown in Fig. 3.14a, where not all of the amino groups are coordinating to the SWCNT-COOH as opposed to Fig. 3.14b. This may suggest that all MTAPc form this type of conjugates though Q-band splitting is not evident in CoTAPc or NiTAPc (discussed later). In Fig. 3.15, it is also possible that there are two Q bands

one belonging to the coordinated FeTAPc and the other to FeTAPc complexes which were not coordinated at all since the Q band is at the same position as that of FeTAPc without SWCNT-COOH in solution. However, in all syntheses excess unreacted MTAPc was removed by continuously washing the reaction mixture with DMF. Thus it is more likely that the split in the Q band (Fig. 3.15a) is due to loss of symmetry with some of the amino groups not being coordinated to SWCNTs, Fig. 3.14a.

3.5.2.2 FTIR Spectroscopy

FTIR was also used to ascertain the presence of the amide linkage between FeTAPc **(7b)** and SWCNT-COOH **(13)**. Fig. 3.16 shows the IR spectra for FeTAPc **(7b)**, FeTAPc–SWCNT(linked) and SWCNT-COOH. The doublet peak for FeTAPc at around 3400 – 3500 cm^{-1} is typical of the $-NH_2$ stretching mode and the $-NH_2$ scissoring mode is associated with the peak at 1618 cm^{-1} [176]. The doublet peak between 3400 and 3500 cm^{-1} for FeTAPc becomes a single peak and shifts towards lower wavenumber (3395 cm^{-1}) on formation of FeTAPc–SWCNT(linked) **(15)**. The $-NH_2$ scissoring mode shifts to 1610 cm^{-1} compared to 1618 cm^{-1} for FeTAPc without SWCNT-COOH. The band at 1710 cm^{-1} for FeTAPc could be attributed to deformations of different types of N-H bond or attributed to carbon–nitrogen double bonds as observed in other studies [288].

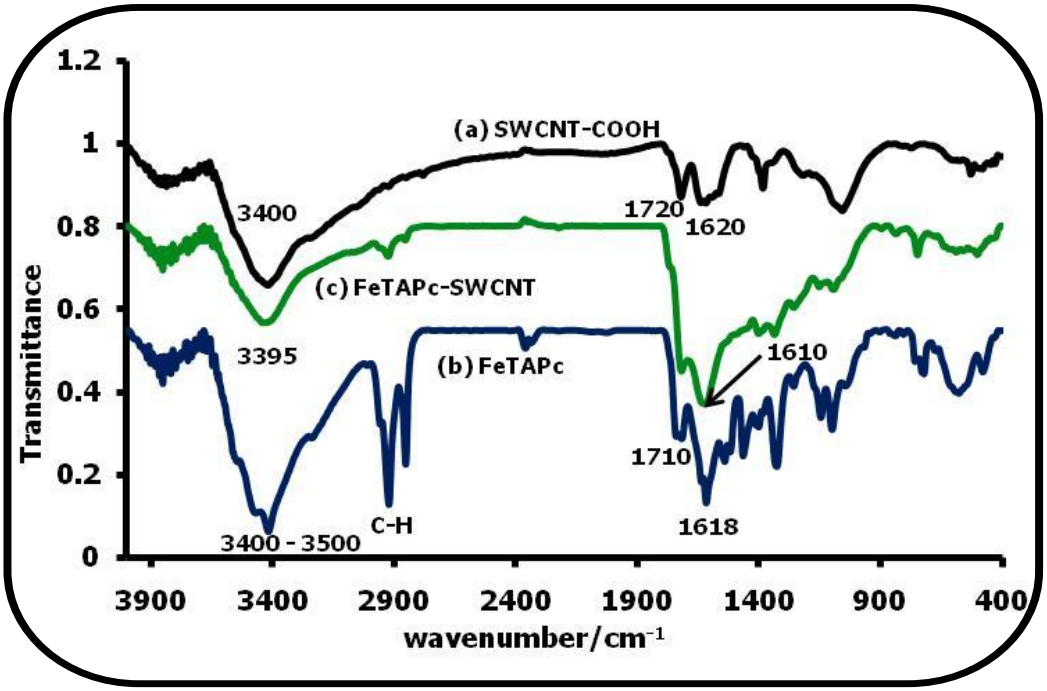

Figure 3. 16: FTIR spectra of (a) SWCNT-COOH (13), (b) FeTAPc (7b), (concentration ~ 1 x 10^{-5} M) and (c) FeTAPc-SWCNT(linked) (15).

3.5.2.3 Raman Spectroscopy

The amide I, amide II and amide III bands are at 1666, 1496 and 1277 cm^{-1}(low intensity), respectively, confirming the linkage between the SWCNT-COOH and FeTAPc (Fig. 3.17). This is in agreement with what has been observed elsewhere [289,290] for amides. Table 3.4 shows that all other bands occur at totally different wavenumbers (for SWCNT-COOH, FeTAPc and FeTAPc-SWCNT(linked)), with the exception of the iron ion marker bands which appear at the same position, indicating that coordination between FeTAPc and SWCNT-COOH has occurred. The iron ion marker peak is at 1536 cm^{-1} for both FeTAPc and FeTAPc-SWCNT(linked), a value that is close to 1530 cm^{-1} reported in literature [287]. The G-bands for FeTAPc and FeTAPc-SWCNT(linked) are at 1590 and 1585 cm^{-1}, while the D-bands appear at 1330 and 1325 cm^{-1}, respectively, Table 3.4.

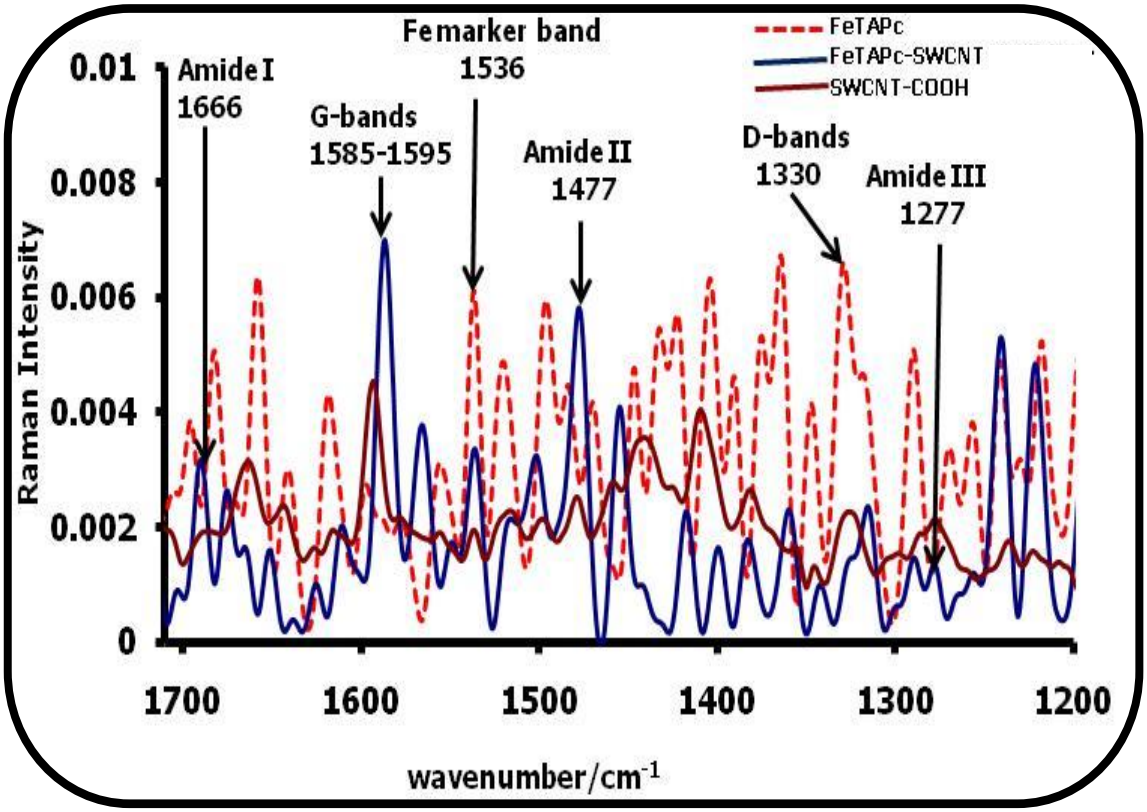

Figure 3.17: Raman spectra of SWCNT-COOH (13), FeTAPc (7b) and FeTAPc-SWCNT(linked) (15).

3.5.3 Characterization of NiTAPc-SWCNT (linked) (16)

For NiTAPc, XRD spectral studies were done since the equipment arrived after the CoTAPc and FeTAPc had been concluded. It was also decided to make a more comprehensive characterization for NiTAPc conjugates using Raman spectroscopy and transmission electron microscopy (TEM).

3.5.3.1 UV-vis spectroscopy

The UV-Vis spectra (Fig. 3.18) of SWCNT-COOH **(13)**, NiTAPc **(7c)**, NiTAPc/SWCNT-COOH(mix) and NiTAPc-SWCNT(linked), **16**, were recorded in DMF (after 1 h of sonication). As has been stated before, the absorption spectrum for SWCNT-COOH (Fig. 3.18d) is featureless. The Q band of NiTAPc-SWCNT(linked) (λ = 703 nm) and NiTAPc/SWCNT-COOH(mix) (λ = 705 nm), Figs. 3.18b and 3.18c, respectively, are blue shifted from NiTAPc whose Q-band is at λ = 708 nm, (Fig.

3.18a), for the same reasons given before for the shifts observed for both CoTAPc-SWCNT(linked) and CoTAPc/SWCNT-COOH(mix). However, the large blue-shifting for CoTAPc-SWCNT(linked), Fig. 3.11, relative to that observed for FeTAPc-SWCNT(linked) (Fig. 3.15) and NiTAPc-SWCNT(linked), Fig. 3.18, is still unexplained.

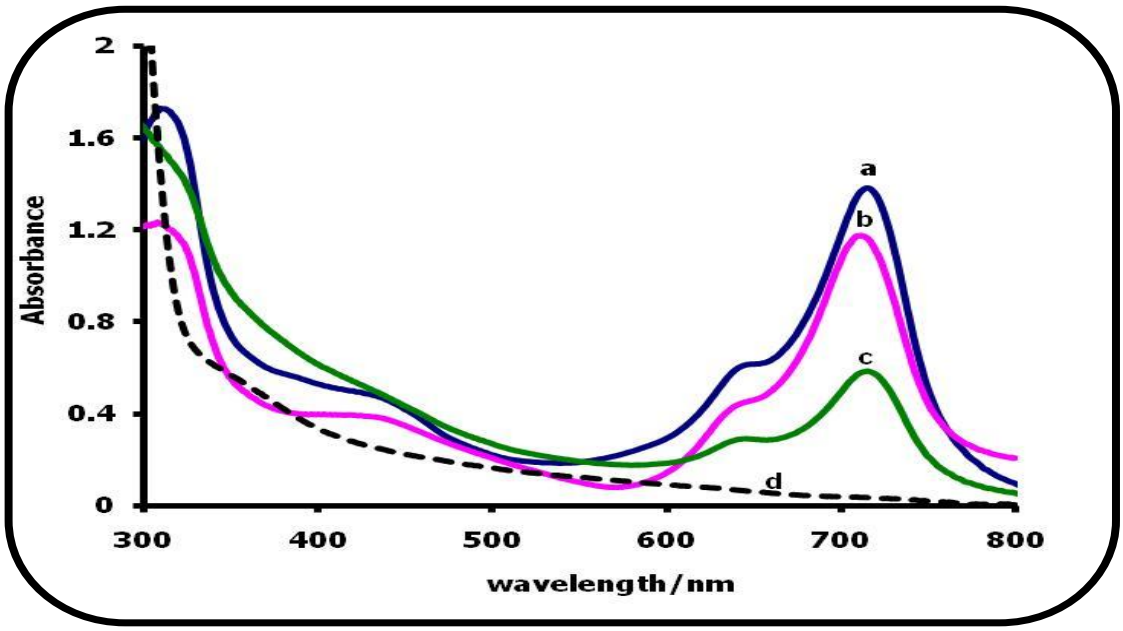

Figure 3.18: UV–vis spectra of (a) NiTAPc (7c), (b) NiTAPc-SWCNT(linked), (16), (c) NiTAPc/SWCNT-COOH(mix) and (d) SWCNT-COOH (13). Solvent = DMF. [NiTAPc] ~ 1 μM.

3.5.3.2 FTIR spectroscopy

Figure 3.19a-c shows the FTIR spectra of SWCNT-COOH (a), NiTAPc-SWCNT(linked) (b) and NiTAPc (c), respectively. The NiTAPc (Fig. 3.19c) spectrum shows a typical doublet between 3228 and 3457 cm^{-1} and a sharp peak at around 1613 cm^{-1} due to stretching mode of the -NH_2 [176] and –NH_2 vibration mode, respectively [190]. The peaks below 1600 cm^{-1} are the phthalocyanines fingerprints. NiTAPc-SWCNT(linked) has broad peak at around 3457 cm^{-1} with a small shoulder at around 3200 cm^{-1}. An amide peak at around 1618 cm^{-1} (in-between the –NH_2

vibration mode and the C=O stretching peak) is a clear indication of coordination between NiTAPc **(7c)** and SWCNT-COOH **(13)**.

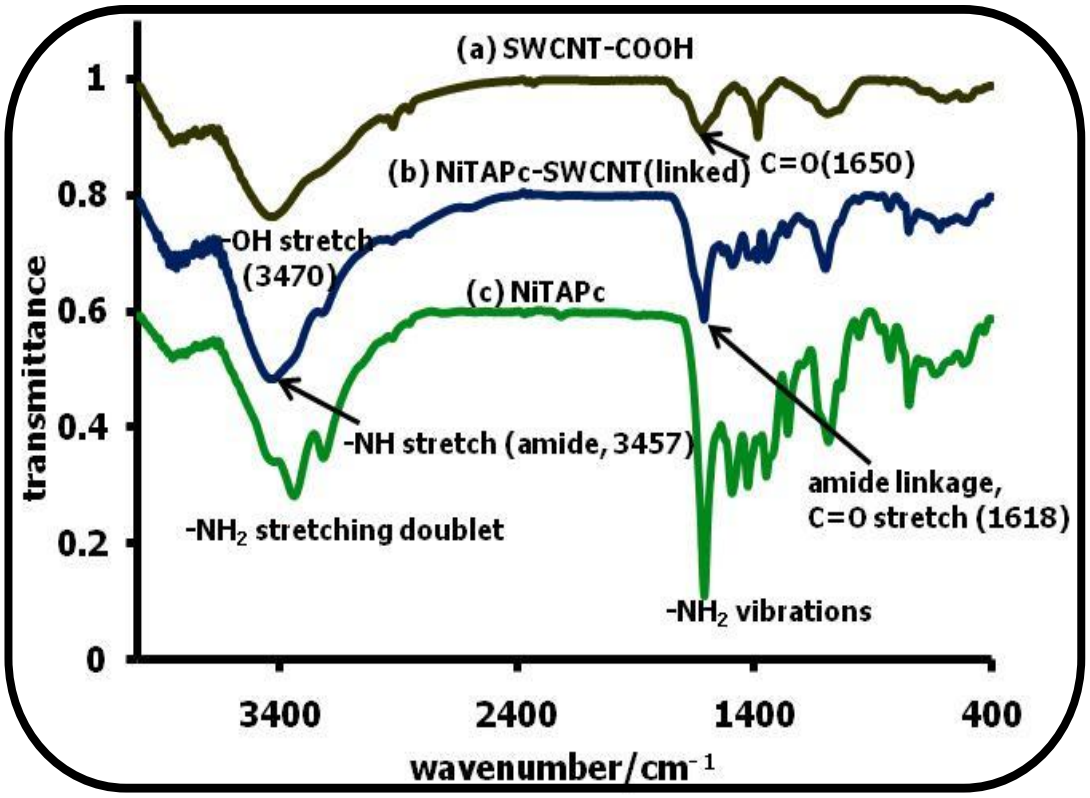

Figure 3.19: FTIR spectra of (a) SWCNT-COOH (13), (b) NiTAPc-SWCNT(linked) (16) and (c) NiTAPc (7c).

3.5.3.3 Raman Spectroscopy

The amide I, II and III bands for NiTAPc-SWCNT(linked) were at 1665, 1500 and 1267 cm^{-1}, respectively, as observed elsewhere [289,290]. The D-bands were at 1326 and 1320 cm^{-1} and the G-bands at 1593 and 1600 cm^{-1} for the NiTAPc and NiTAPc-SWCNT(linked), respectively. The nickel ion marker band was observed at 1547 cm^{-1} and 1545 cm^{-1} in NiTAPc **(7c)** and NiTAPc-SWCNT complex **(16)**, respectively, which is in close agreement with 1545 cm^{-1} that was observed in other studies [287,291]. These D- and G-band values compare well with those obtained for CoTAPc and FeTAPc, Table 3.4.

3.5.3.4 XRD spectroscopy

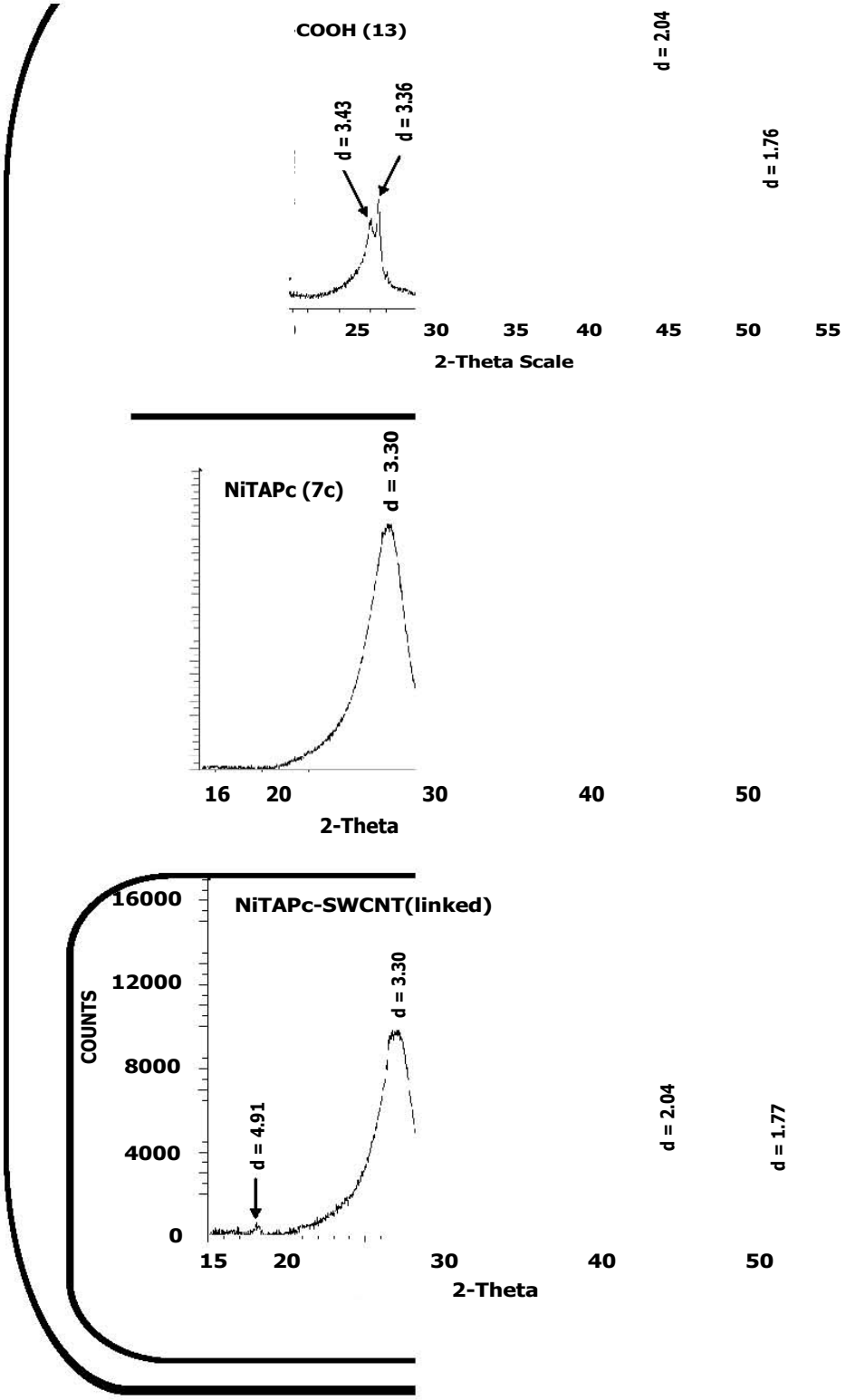

Figure 3.20: XRD spectra for SWCNT-COOH (13), NiTAPc (7c) and NiTAPc-SWCNT(linked) (16).

Table 3.5: XRD parameters for raw SWCNTs, SWCNT-COOH (13), NiTAPc (7c) and NiTAPc-SWCNT(linked) (16).

Electrode modifier	2θ (in degrees)	d – spacing (Å)
Raw SWCNTs	17.5; 20.5; 25.5; **26.5**; 44.5; 51.5	5.00; 4.29; 3.36; **3.32**; 2.04; 1.77
SWCNT-COOH **(13)**	17.5; 20.5; 25.5; **26.5**; 44.5; 52.0	5.06; 4.28; 3.43; **3.36**; 2.04; 1.76
NiTAPc **(7c)**	27	3.30
NiTAPc-SWCNT(linked) **(16)**	17.8; **26.5**; 44.5; 51.5	4.91; **3.30**; 2.04; 1.77

Figure 3.20 shows comparative XRD spectra for NiTAPc **(7c)**, SWCNT-COOH **(13)** and NiTAPc-SWCNT(linked) **(16)**. The interplanar spacing for the broad peak in NiTAPc-SWCNT(linked) is 3.30 Å ($2\theta = 27^0$), Fig. 3.20, Table 3.5. This d-spacing value is close to 3.3-3.4 Å that has been reported elsewhere [192,193]. The broadness of the XRD peak for NiTAPc-SWCNT(linked), Fig. 3.20, suggests that it is in semi-crystalline form [44]. Apart from the Pc peak at $2\theta = 27^0$, that overlapped with the SWCNT peak at ~26^0, the XRD for NiTAPc-SWCNT(linked) show three additional peaks which could be attributed to SWCNTs. This shows that NiTAPc has been incorporated into the SWCNTs. Peak shifts, for example d-spacings at ~26.5^0 (**in bold**), shows that NiTAPc-SWCNT conjugate is in a different crystal form, relative to NiTAPc and SWCNT-COOH and this confirms chemical linking.

3.5.3.5 Transmission electron microscopy (TEM) images

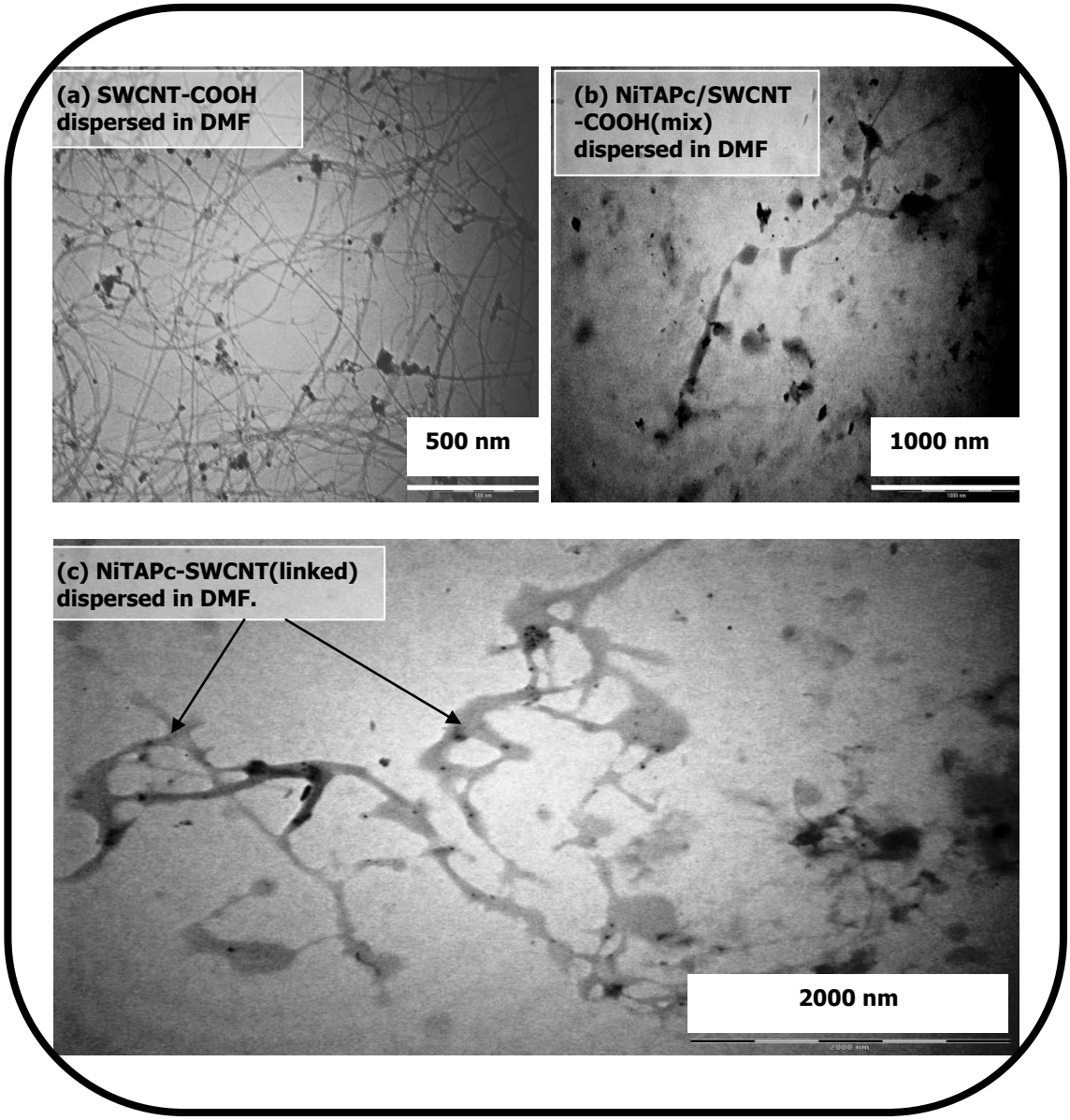

Figure 3.21: Comparative TEM images for (a) SWCNT-COOH (13), (b) NiTAPc/SWCNT-COOH(mix) and (c) NiTAPc-SWCNT(linked) (16).

Figure 3.21 shows the TEM images of SWCNT-COOH **(13)**, NiTAPc-SWCNT(linked) **(16)** and NiTAPc/SWCNT-COOH(mix) dispersed through ultrasonication in DMF. In the absence of NiTAPc **(7c)**, the SWCNT-COOH **(13)** show well dispersed rods (Fig. 3.21a). The TEM image of NiTAPc/SWCNT-COOH(mix) (Fig. 3.21b) shows aggregates of NiTAPc between the rods. The TEM for

the mixture also shows clusters of NiTAPc adsorbed onto the walls of the SWCNT rods. The TEM for NiTAPc-SWCNT(linked) shows the linkages between NiTAPc and SWCNT-COOH as confirmed through a number of nodal points (Fig. 3.21c). The nodal points represent the NiTAPc molecule, from which the SWCNTs are attached according to Fig. 3.14 (where M = Ni). The observed discontinuities in coordination could be attributed to the breaking of linkages due to sonication (Fig. 3.21).

3.6 Synthesis and characterization of CoTCPc-PA-SWCNT(linked) (17) and CoTCPc-EA-SWCNT(linked) (18)

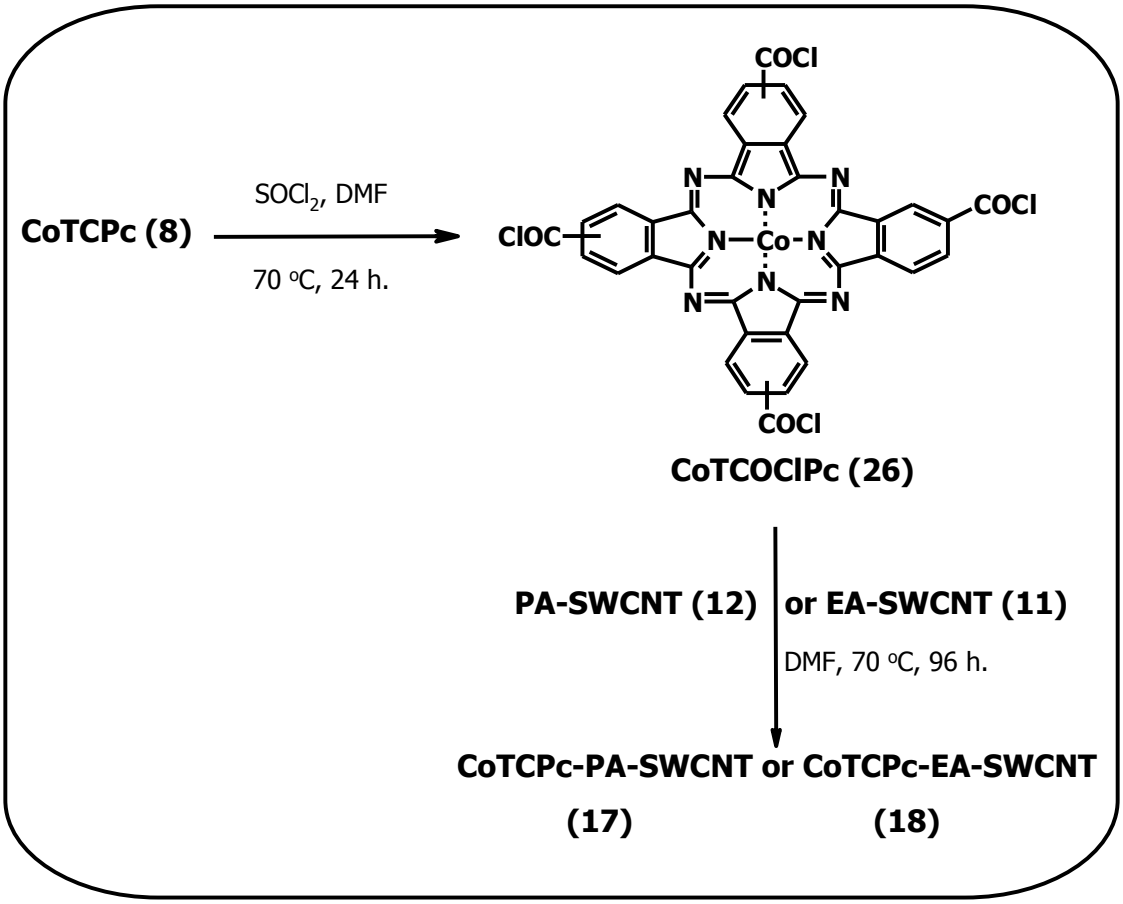

Scheme 3.5: Synthetic route to CoTCPc-PA-SWCNT(linked) (17) and CoTCPc-EA-SWCNT(linked) (18)

Conjugates **(17)** and **(18)** were synthesized according to Scheme 3.5 following literature methods [168,279,292]. For both conjugates (**17** and **18**), as explained in the

experimental section, $SOCl_2$ was initially used to exhaustively convert the COOH groups of CoTCPc **(8)** into the acid chloride derivatives (COCl) before mixing with limiting quantities of PA-SWCNTs **(12)** or EA-SWCNT **(11)** in DMF. The mixtures were continuously stirred at 70 ^{0}C for 96 h to give products **17** and **18**.

3.6.1 Transmission electron microscopy (TEM)

Figure 3.22 shows the TEM images of PA-SWCNT, CoTCPc/PA-SWCNT(mix) and CoTCPc-PA-SWCNT(linked) initially dispersed in DMF through ultra-sonication followed by evaporation of the solvent. PA-SWCNT (Fig. 3.22a) show large beads along SWCNT axis, representing the phenyl-amine groups that are attached to the SWCNT walls. The TEM image of CoTCPc/PA-SWCNT(mix) (Fig. 3.22b) shows aggregates of CoTCPc between and on top the beaded PA-SWCNT rods. The TEM image (Fig. 3.22c) for CoTCPc-PA-SWCNT(linked) is different from that of CoTCPc/PA-SWCNT(mix) and shows sideway linkages between adjacent SWCNTs. The nature of linkages does suggest that the phenyl-amine groups are located at the walls of the CNTs.

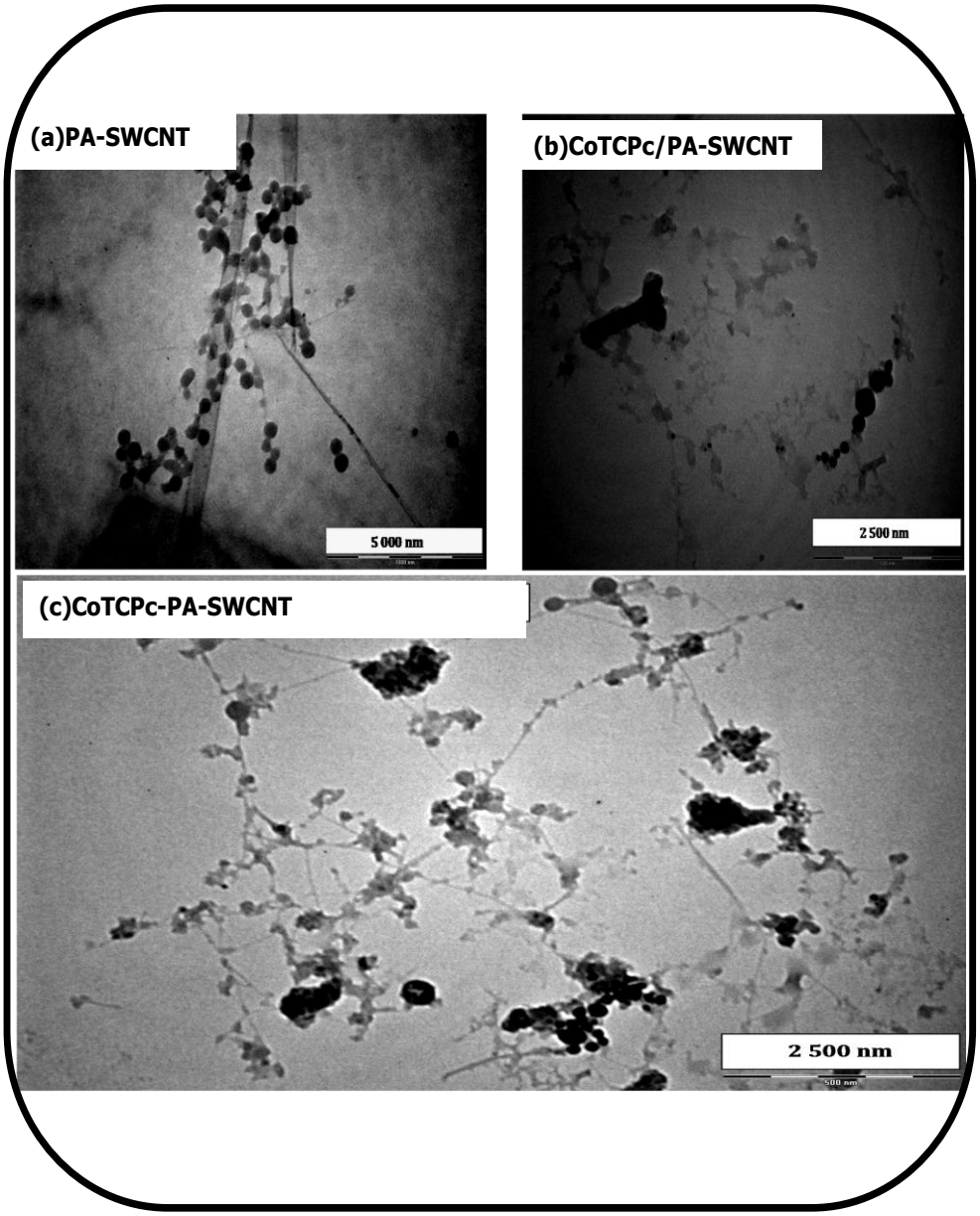

Figure 3.22: TEM images of (a) PA-SWCNT (12), (b) CoTCPc/PA-SWCNT(mix) and (c) CoTCPc-PA-SWCNT(linked) (17).

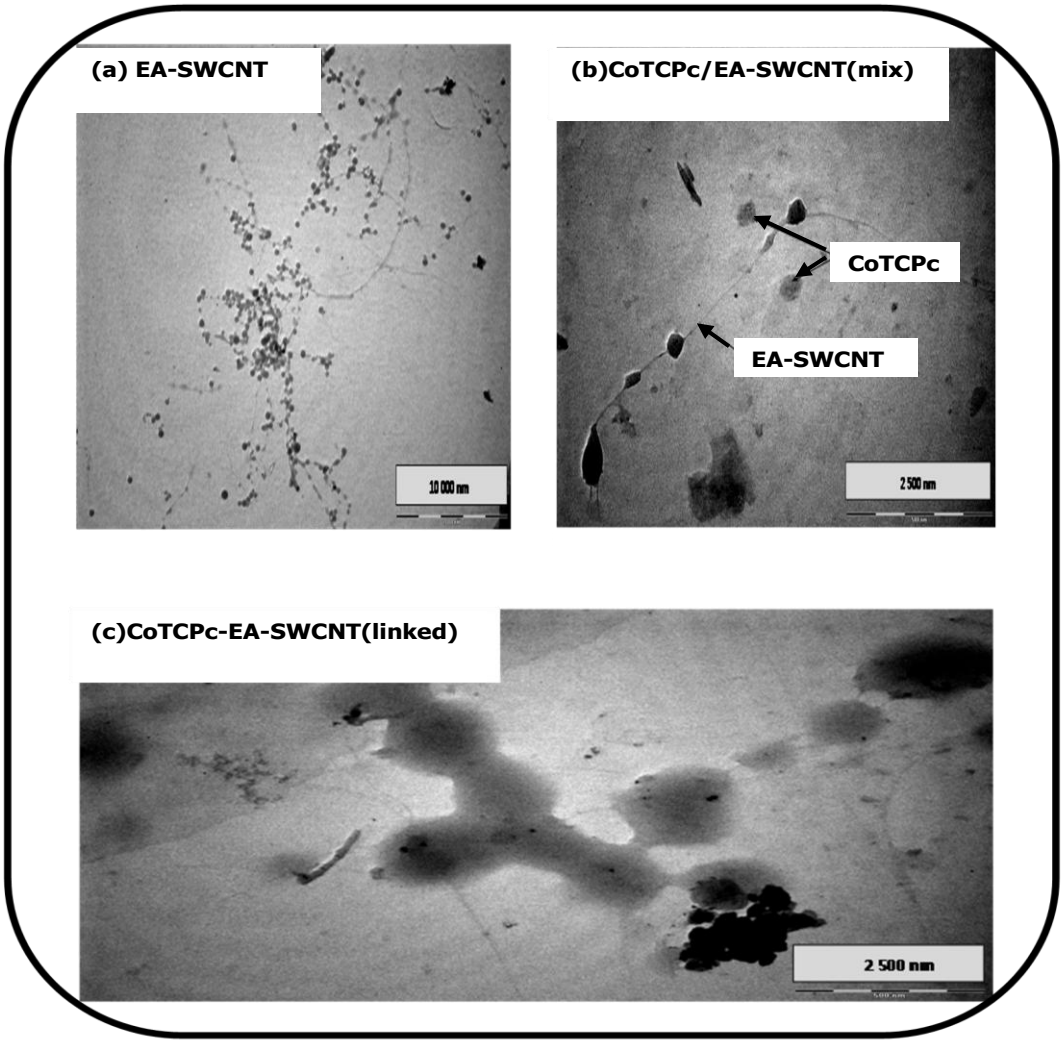

Figure 3.23: TEM images of (a) EA-SWCNT (11), (b) CoTCPc/EA-SWCNT(mix) and (c) CoTCPc-EA-SWCNT(linked) (18).

Figure 3.23a-c shows the TEM images of EA-SWCNT **(11)**, CoTCPc/EA-SWCNT(mix) and CoTCPc-EA-SWCNT(linked) **(18)** initially dispersed through ultra-sonication in DMF. EA-SWCNT pictures in Fig. 3.23a are similar to those observed in Fig. 3.22a. The TEM image of CoTCPc/EA-SWCNT(mix) (Fig. 3.23b) shows aggregates of CoTCPc **(8)** between the beaded SWCNT rods. The TEM for CoTCPc-EA-SWCNT(linked) shows CoTCPc directly linked and sitting on top, around and along the SWCNT rod, as evidenced by a number of nodal points, Fig. 3.23c, hence confirming the linking of CoTCPc to SWCNT. TEM confirms that there

are no significant differences in coordination of CoTCPc to EA-SWCNT or PA-SWCNT.

3.6.2 UV-vis spectroscopy

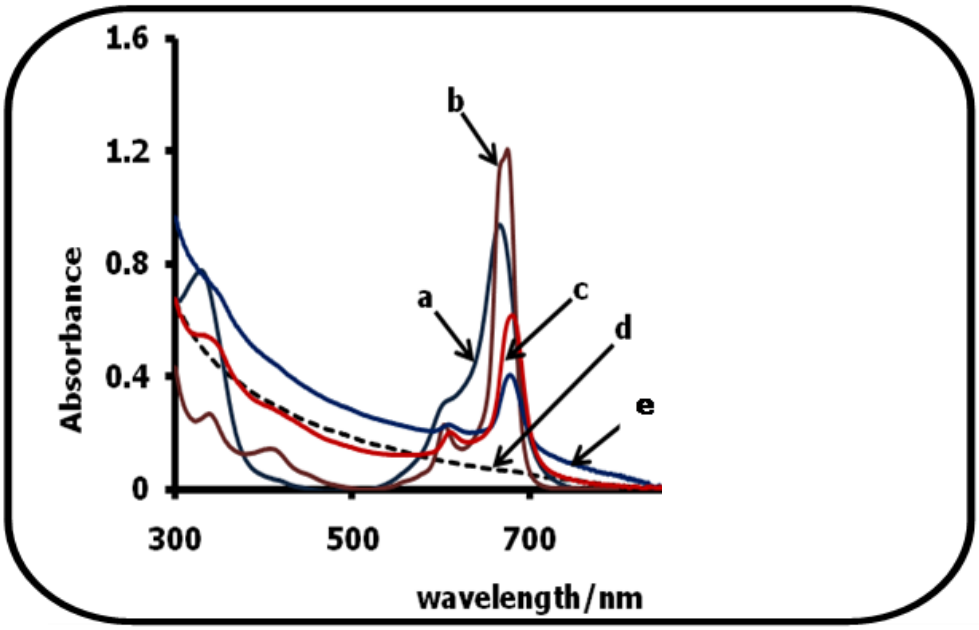

Figure 3.24: UV-vis spectra for (a) 1 µM CoTCPc (8), (b) CoCOClPc, (c) CoTCPc-PA-SWCNT(linked) (17), (d) PA-SWCNT (12) and (e) CoTCPc/PA-SWCNT(mix). Solvent = DMF.

Figure 3.24a-e shows the UV-vis spectra for CoTCPc **(8)**, CoTCOClPc, CoTCPc-PA-SWCNT(linked) **(17)**, PA-SWCNT **(12)** and CoTCPc/PA-SWCNT(mix), respectively, in DMF. The Q-bands for CoTCOClPc (Fig. 3.24b), CoTCPc/PA-SWCNT(mix)(Fig. 3.24e) and CoTCPc-PA-SWCNT(linked), Fig. 3.24c, are red-shifted at 675 nm, 678 nm and 680 nm, respectively, relative to CoTCPc **(8)** whose absorption maxima is at 666 nm, Fig. 3.3. The shift of 4 nm between CoTCOClPc and CoTCPc-PA-SWCNT **(17)** could indicate coordination of SWCNT to CoTCOClPc. The observed red shifting indicate that the phenyl-amine groups on the SWCNTs are donating electrons into the Pc ring which result in the reduction of the HOMO-LUMO gap. The Q band for CoTCOClPc indicate some form of asymmetry as judged by a split Q band, and this may be due to incomplete transformation of COOH

groups to COCl in CoTCOClPc. This asymmetry is however no longer observed in CoTCPc-PA-SWCNT and CoTCPc/PA-SWCNT(mix). The UV-Vis spectrum for PA-SWCNT has no noticeable absorption bands, which is typical of functionalized SWCNTs [176].

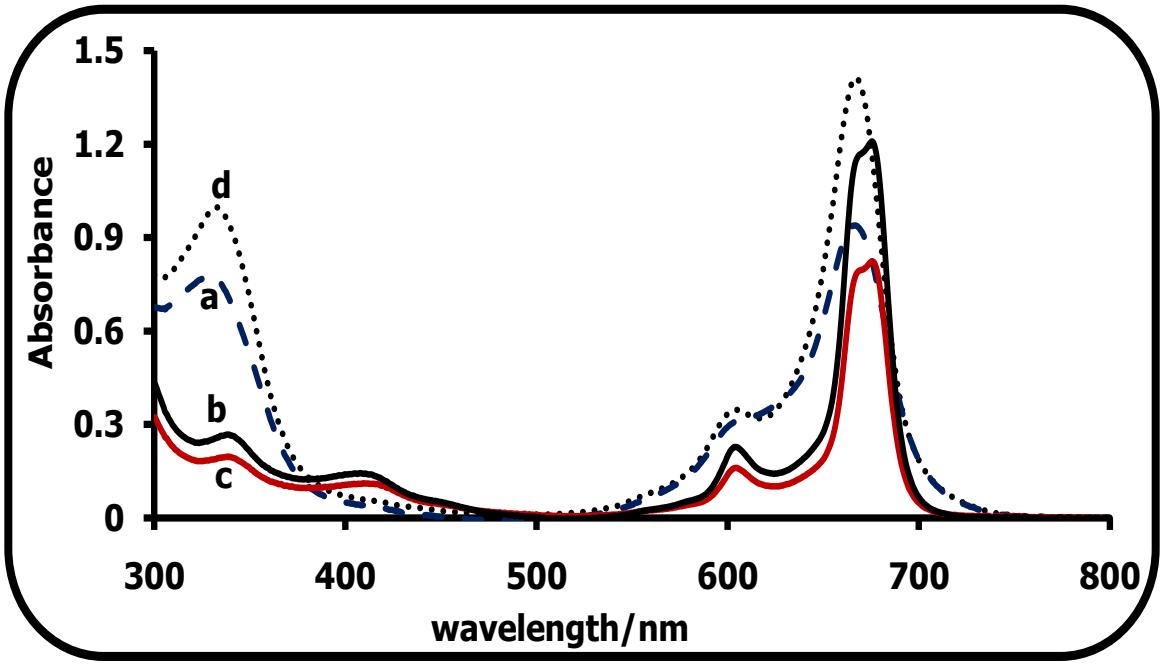

Figure 3.25: UV-Vis spectra of (a) 1 µM CoTCPc (8), (b) CoTCOClPc, (c) CoTCPc-EA-SWCNT(linked) (18) and (d) CoTCPc/EA-SWCNT(mix). Solvent = DMF.

Figure 3.25a-d shows the UV-vis spectra for CoTCPc **(8)**, CoTCOClPc, CoTCPc-EA-SWCNT(linked) **(18)** and CoTCPc/EA-SWCNT(mix), respectively, in DMF. The Q-bands for both CoTCOClPc and CoTCPc-EA-SWCNT(linked) are red-shifted at 675 nm, relative to CoTCPc **(18)** and CoTCPc/EA-SWCNT(mix) whose absorption maxima is at 666 nm. As observed with CoTCPc-PA-SWCNT(linked), the CoTCPc-EA-SWCNT(linked) red shifting indicate that the EA-SWCNT molecules are donating electrons into the Pc ring, lowering the HOMO-LUMO energy gap. While EA and PA groups are electron donating, the COOH group in SWCNT is electron withdrawing and therefore increases the HOMO-LUMO gap, resulting in the blue shifting observed for the MTAPc-SWCNT conjugates **(14-16)**. For the CoTCOClPc and CoTCPc-EA-SWCNT(linked) **(18)**, the Q band shows splitting probably due to asymmetry as a result of incomplete transformation of COOH to COCl (Fig. 3.25b) or

incomplete coordination between EA-SWCNT and CoTCPc (Fig. 3.25c). There is also appearance of the charge transfer bands (around 405 nm) for both CoTCOClPc and CoTCPc-EA-SWCNT(linked) **(18)**.

3.6.3 FTIR spectroscopy

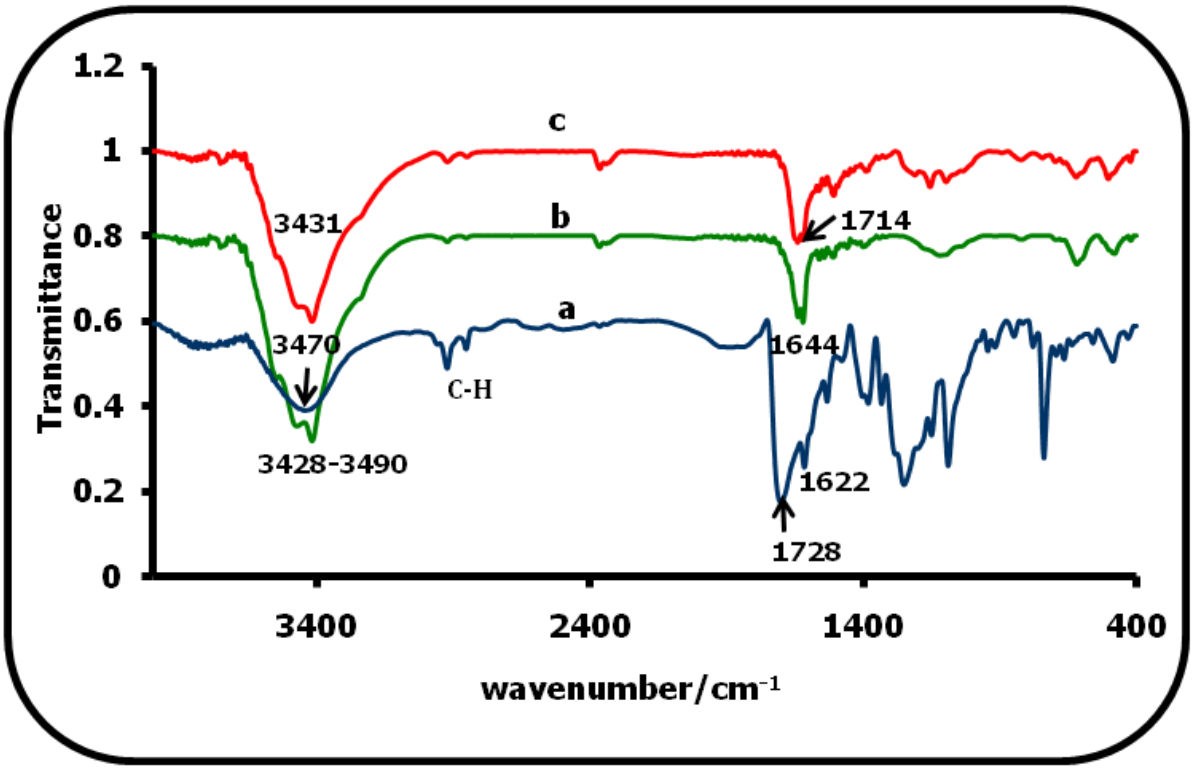

Figure 3.26: FTIR spectra of (a) CoTCPc (8) , (b) PA-SWCNT (12) and (c) CoTCPc-PA-SWCNT(linked) (17).

Figure 3.26 shows the FTIR spectra for CoTCPc (a), PA-SWCNT (b) and CoTCPc-PA-SWCNT(linked) (c). Figure 3.26c shows the spectrum for the amide linked CoTCPc-PA-SWCNT conjugate. It has the –NH stretch of the amide at 3431 cm^{-1}, the C=O stretch of the amide at 1714 cm^{-1}, this is in between the C=O (1728 cm^{-1}) stretch of the carboxylic acid of CoTCPc (Fig. 3.26a) and the $-NH_2$ stretch of the functionalized SWCNT (1644 cm^{-1}), Fig. 3.26b. The CoTCPc (Fig. 3.26a) shows the broad O-H stretch at around 3470 cm^{-1}, the C=O stretch for the carbonyl group at 1728 cm^{-1} and the C-O stretch at 1095 cm^{-1} as observed elsewhere [176]. The shift of

C=O stretch for CoTCPc (1728 cm^{-1}) to 1714 cm^{-1} for CoTCPc-PA-SWCNT(linked) confirms linking between CoTCPc and PA-SWCNT.

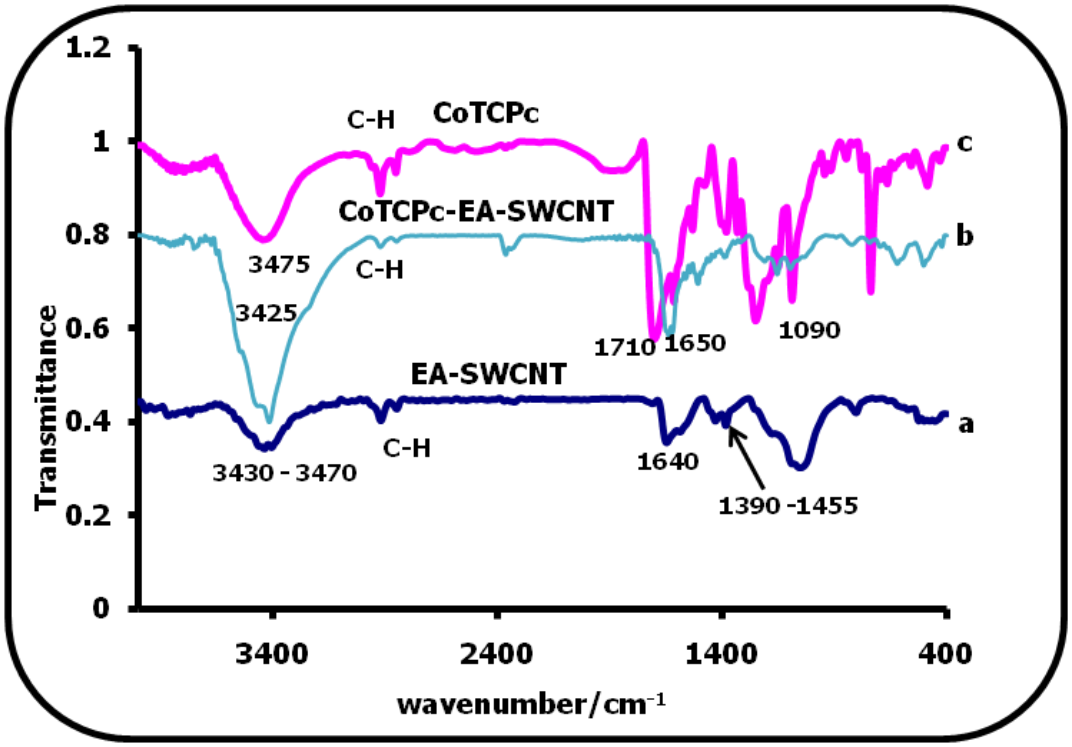

Figure 3.27: FTIR spectra for (a) raw SWCNTs, (b) EA-SWCNT (11), (c) CoTCPc-EA-SWCNT(linked), 18, and (d) CoTCPc (8).

Fig. 3.27b shows the spectrum for the amide linked CoTCPc-EA-SWCNT complex **(18)**. It has the –NH stretch of the amide at 3425 cm^{-1}, the C=O strecth of the amide at 1650 cm^{-1}, this is in between the C=O (1710 cm^{-1}) stretch of the carboxylic acid of CoTCPc (Fig. 3.27c) and the $-NH_2$ stretch of EA- SWCNT (1640 cm^{-1}) (Fig. 3.27a). The CoTCPc (Fig. 3.27c) shows the following carboxylic acid stretching bands: broad O-H stretch at around 3475 cm^{-1}, the C=O stretch for the carbonyl group at 1710 cm^{-1} and the C-O stretch at 1090 cm^{-1} as has been reported before [176]. The shift of C=O stretch for CoTCPc (1710 cm^{-1}) to 1650 cm^{-1} for the linked confirms bonding, as also confirmed for CoTCPc-PA-SWCNT conjugate above.

3.6.4 XRD spectroscopy

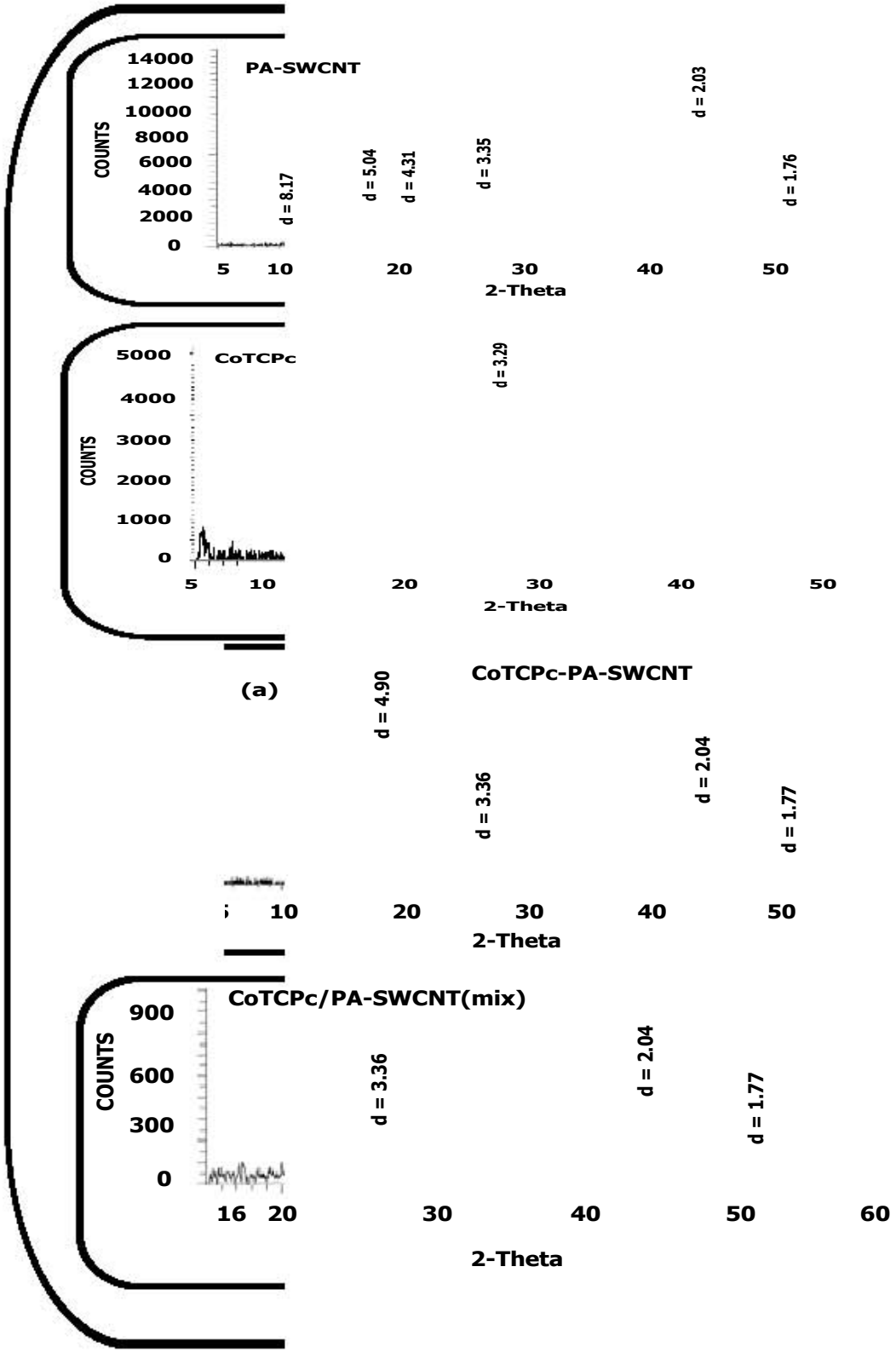

Figure 3.28: XRD spectra for PA-SWCNT (12), CoTCPc (8), CoTCPc-PA-SWCNT(linked) (17) and CoTCPc/PA-SWCNT(mix).

Table 3.6: XRD parameters for EA-SWCNT (11), PA-SWCNT (12), CoTCPc (8), CoTCPc-PA-SWCNT(linked) (17), CoTCPc-EA-SWCNT(linked) (18), CoTCPc/PA-SWCNT(mix) and CoTCPc/EA-SWCNT(mix).

ELECTRODE	**2θ (in degrees)**	**d– spacing (Å)**	**Intensity**
CoTCPc **(8)**	27.1	3.29	4209
PA-SWCNT **(12)**	10.8; 17.6; 20. 6; 26.6; 44.5; 51.5	8.17; 5.04; 4.31; 3.35; 2.03; 1.76	1290; 3140; 3225; 4430; 10739; 2850
CoTCPc/PA-SWCNT(mix)	26.5; 44.3; 51.6	3.36; 2.04; 1.77	231; 321; 122
CoTCPc-PA-SWCNT(linked) **(17)**	18.1; 26.6; 44.5; 51.8	4.90; 3.36; 2.04; 1.77	7425; 2006; 3919; 990
EA-SWCNT **(11)**	10.6; 17.5; 20.6; 26.6; 44.3; 51.6	8.31; 5.05; 4.32; 3.35; 2.04; 1.77	1385; 1453; 853; 1964; 4092; 1200
CoTCPc/EA-SWCNT(mix)	26.6; 44.3; 51.6	3.35; 2.04; 1.77	389; 634; 240
CoTCPc-EA-SWCNT(linked) **(18)**	18.1; 20.8; 26.7; 44.4; 51.7	4.91; 4.29; 3.34; 2.04; 1.77	11099; 8996; 9290; 12076; 4578

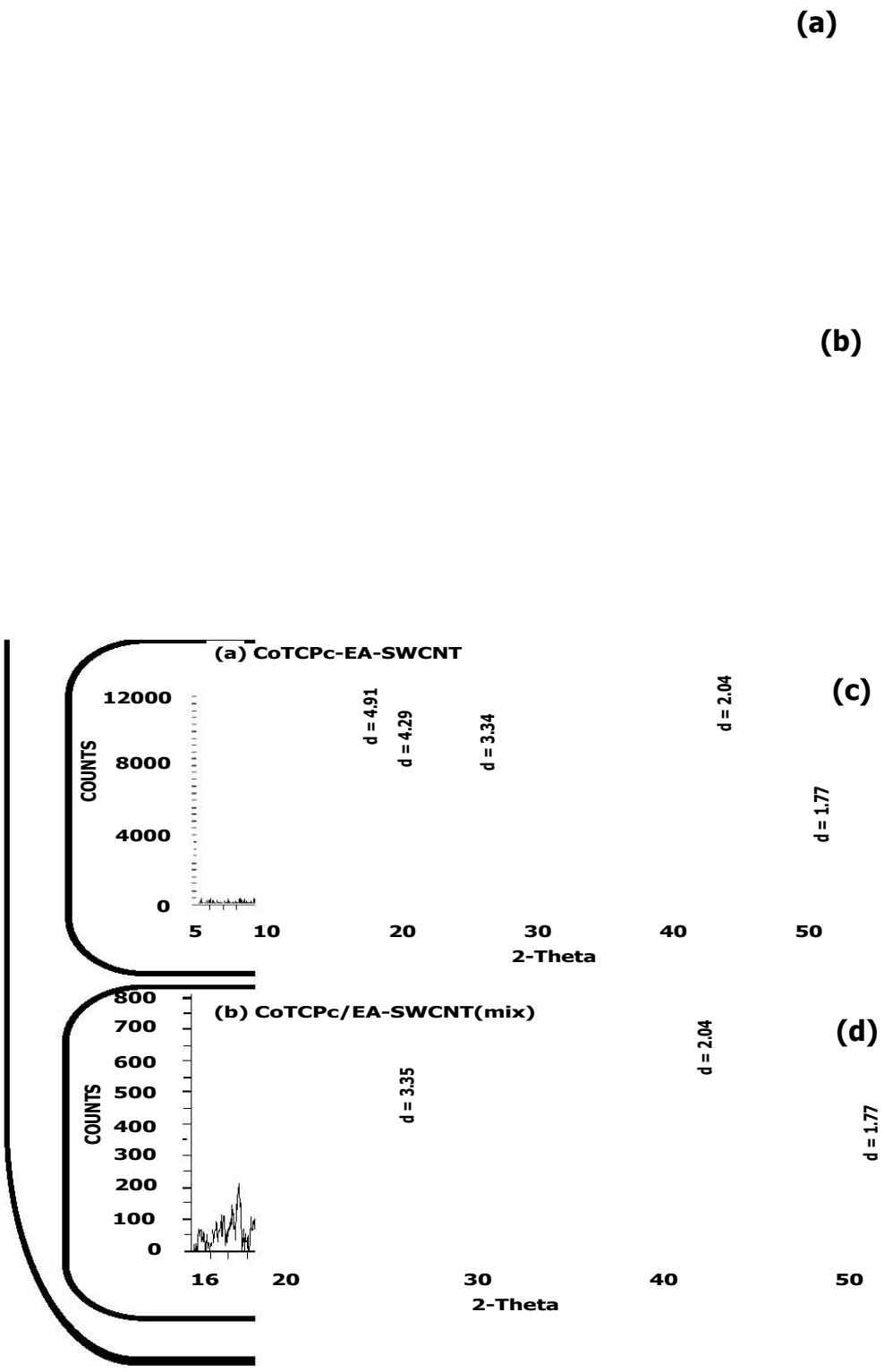

Figure 3.29: XRD spectra for EA-SWCNT (11), CoTCPc (8), CoTCPc-EA-SWCNT(linked) (18) and CoTCPc/EA-SWCNT(mix).

Figures 3.28 shows comparative XRD spectra for PA-SWCNT **(12)**, CoTCPc **(8)**, CoTCPc-PA-SWCNT(linked) **(17)** and CoTCPc/PA-SWCNT(mix). The d-spacings, 2θ values and the peak intensities for CoTCPc **(8)**, PA-SWCNT **(12)**, CoTCPc-PA-SWCNT(linked) and CoTCPc/PA-SWCNT(mix) are given in Table 3.6. Figure 3.29 shows the XRD spectra for EA-SWCNT **(11)**, CoTCPc, CoTCPc-EA-SWCNT(linked) **(18)** and CoTCPc/EA-SWCNT(mix), respectively. Table 3.6 lists the 2θ-values, d-spacings and the peak intensities for compounds CoTCPc, EA-SWCNT**,** CoTCPc/EA-SWCNT(mix) and CoTCPc-EA-SWCNT(linked). Fig. 3.29c shows the spectrum for the CoTCPc-EA-SWCNT(linked) with all the peaks that have been identified in the EA-SWCNT being conspicuously present.

The spectrum for CoTCPc-PA-SWCNT(linked) **(17)** shows four peaks at 2θ values of 18.1^0; 26.6^0; 44.5^0 and 51.8^0. The peaks for CoTCPc-PA-SWCNT coincide with those observed in the spectrum for PA-SWCNT (Fig. 3.28), though there is a noticeable shift in 2θ value for the peak at 18.1^0 and a slight shift for the peak at 51.8^0 for the conjugate (Table 3.6). The Pc peak overlapped with the PA-SWCNT peak at $2\theta = 26.6^0$ (Fig. 3.28). The d-spacing for the peaks at 17.6^0 for PA-SWCNT and at 18.1^0 for CoTCPc-PA-SWCNT **(17)** are 5.04 Å and 4.9 Å, an indication that the sources of these two reflections could be totally different. Relative to PA-SWCNT, the d-spacings for CoTCPc/PA-SWCNT(mix) and CoTCPc-PA-SWCNT(linked) have increased slightly in some cases, although the peak intensities for CoTCPc/PA-SWCNT(mix) are very low relative to the conjugate (Table 3.6). The XRD for CoTCPc/PA-SWCNT(mix) has three distinct peaks at $2\theta = 26.6^0$, 44.3^0 and 51.6^0. These peaks are at 2θ values that are at least 0.1^0 less than those of CoTCPc-PA-SWCNT. Peaks at 17.6^0 and 18.1^0 for the PA-SWCNT and CoTCPc-PA-SWCNT, respectively, are no longer visible in CoTCPc/PA-SWCNT(mix), possibly due to the destruction of crystallographic planes of PA-SWCNT during mixing. Peak shifts could indirectly confirm linkage between CoTCPc and PA-SWCNT. The crystalline nature of CoTCPc-PA-SWCNT(linked) **(17)** is confirmed by the sharp peaks, while the amorphous nature of CoTCPc/PA-SWCNT(mix) is shown by the broadness of its peaks (Fig. 3.28) [44]. Shifts in 2θ and changes in peak intensities for both

CoTCPc-PA-SWCNT(linked) and CoTCPc-EA-SWCNT(linked) from those of PA-SWCNT and EA-SWCNT respectively, confirm conjugation.

3.6.5 Raman Spectroscopy

This technique is only discussed for EA-SWCNT conjugates since the sources of the spectral bands are similar to those of PA-SWCNT.

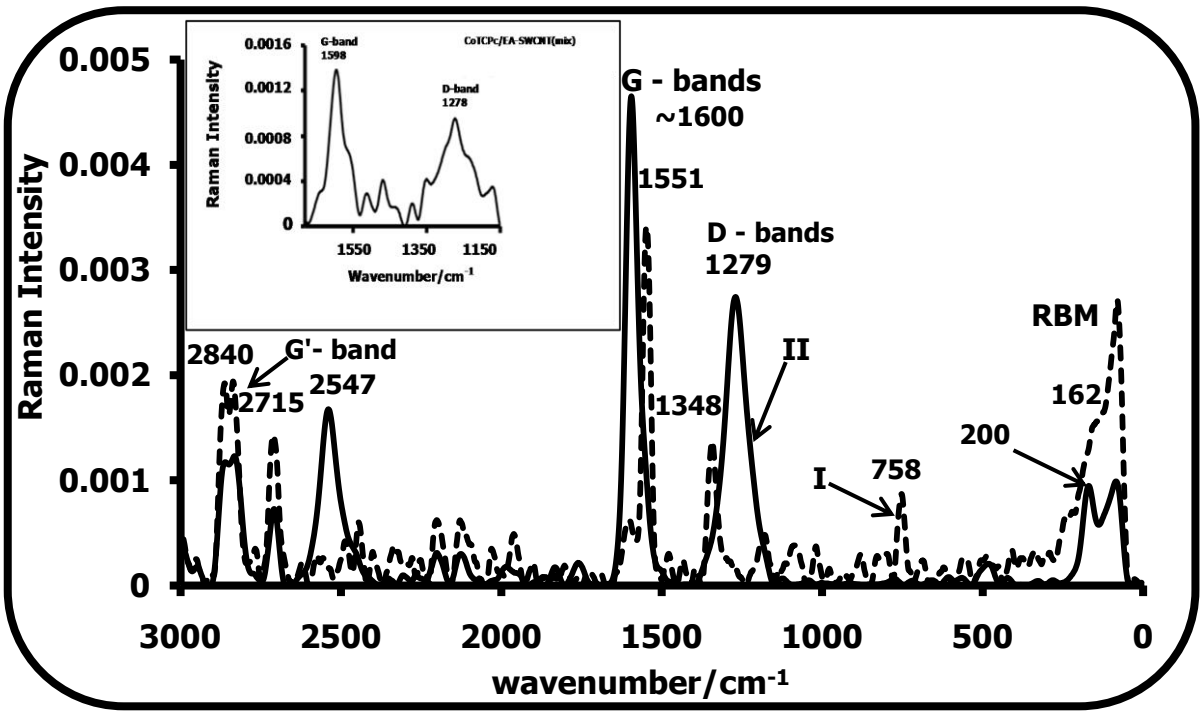

Figure 3.30: Raman spectra for (I, dashed line) CoTCPc (8) and (II, solid line) CoTCPc-EA-SWCNT(linked) (18). Inset: Raman spectrum of CoTCPc/EA-SWCNT(mix).

Figure 3.30 (I and II) shows the Raman spectra of for CoTCPc and CoTCPc-EA-SWCNT(linked). The D bands are at 1348 and 1279 cm^{-1} for the CoTCPc (Fig. 3.30(I)) and CoTCPc-EA-SWCNT(linked) (Fig. 3.30(II)), respectively (Table 3.4). For CoTCPc/EA-SWCNT(mix), the D band at 1278 cm^{-1}, Fig. 3.30 (inset), is close to that of CoTCPc-EA-SWCNT(linked) **(18)**. The G bands are at 1551, 1598 and 1600 cm^{-1} for CoTCPc, CoTCPc-EA-SWCNT(linked) and CoTCPc/EA-SWCNT(mix), respectively (Table 3.4). Both the CoTCPc **(8)** and CoTCPc-EA-SWCNT(linked) **(18)** have a dispersive double resonance G′ band around 2715 cm^{-1} and a non-dispersive phonon

mode around 2547 cm^{-1} (the latter for CoTCPc-EA-SWCNT(linked) only) as observed elsewhere [177]. The D and G bands of CoTCPc/EA-SWCNT(mix) and CoTCPc-EA-SWCNT(linked) are more refined for the latter possibly due to chemical coordination.

3.6.6 Thermogravimetric analyses (TGA)

This technique also discussed only EA-SWCNT since the thermograms are similar to PA-SWCNT.

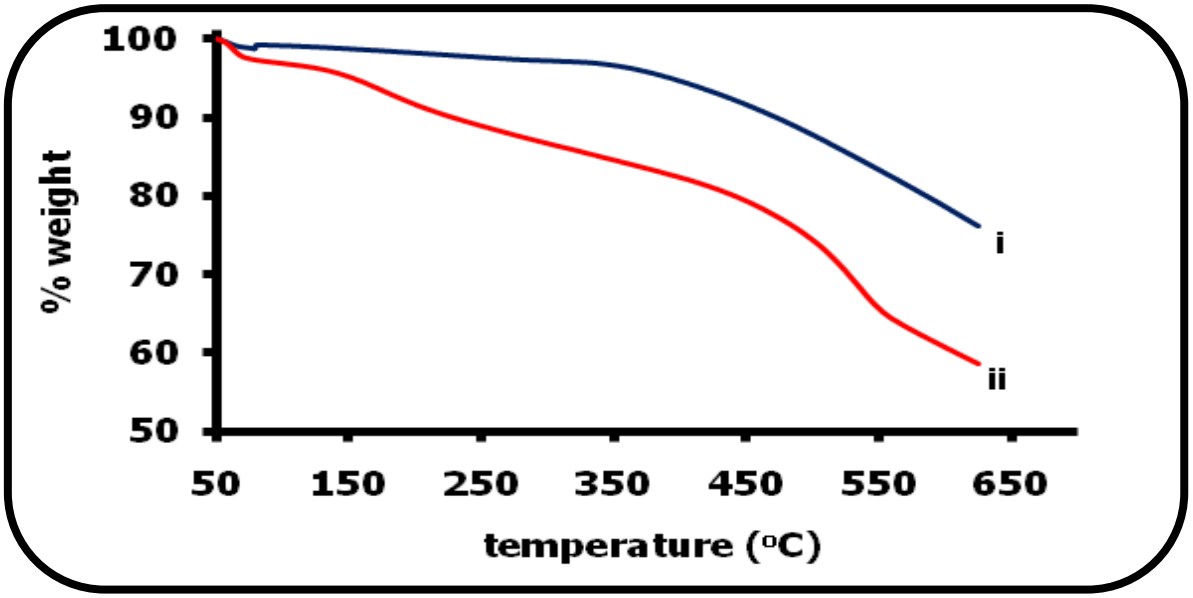

Figure 3.31: Thermogravimetric analysis (TGA) of (i) CoTCPc (8) and (ii) CoTCPc-EA-SWCNT (18) at 10 ^{0}C/min under nitrogen.

Structural differences between CoTCPc **(8)** and CoTCPc-EA-SWCNT(linked) **(18)** were further confirmed using TGA. Different thermal decay profiles point to structurally different materials, (Fig. 3.31). TGA showed weight loss of 23.8% and 41.7 % for CoTCPc **(8)** and CoTCPc-EA-SWCNT(linked) **(18),** respectively, at 625 °C. The extent of functionalization is expressed as the number of substituents per SWCNT carbon atoms as stated above. The estimated weight loss due to the functionalization on CoTCPc-EA-SWCNT(linked) **(18)** is 21.9 %. Applying the formula reported in the literature [209], this gives about one EA functional group per

239 carbon atoms for CoTCPc-EA-SWCNT(linked) **(18)**, compared to one EA group per 25 carbon atoms for EA-SWCNT calculated above.

3.7 Synthesis and characterization of CoMAPc-SWCNT (19)

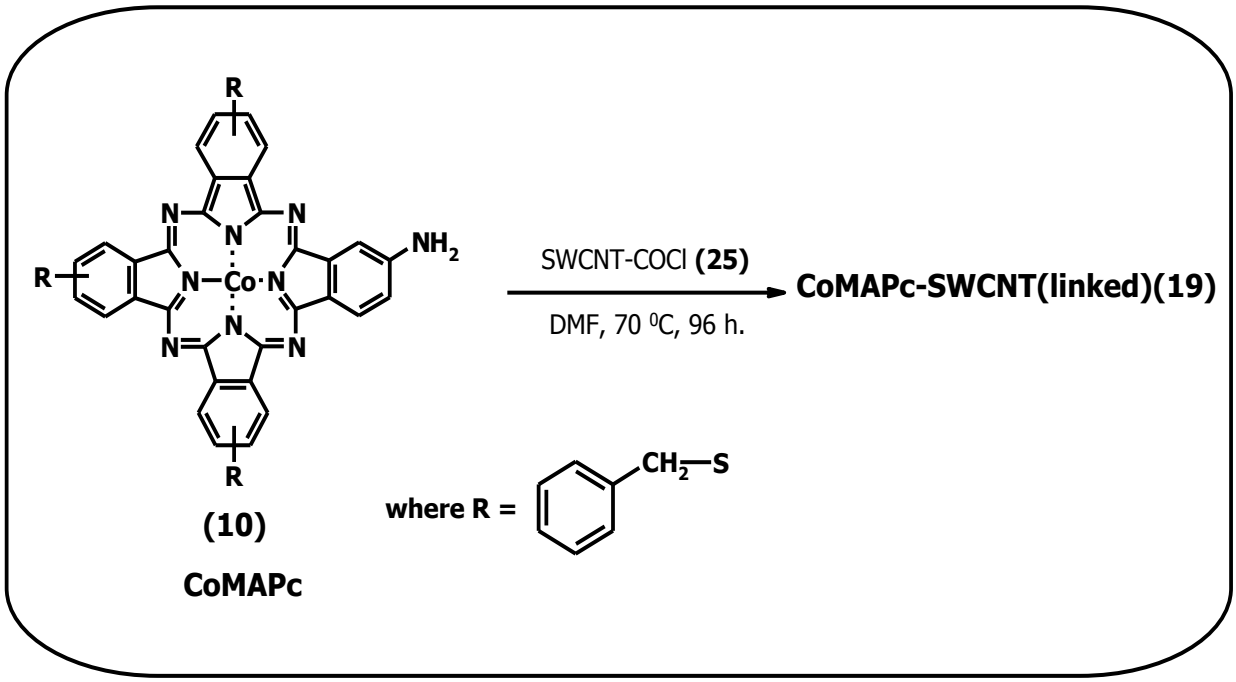

Scheme 3.6: Synthetic route to CoMAPc-SWCNT(linked) (19).

CoMAPc-SWCNT conjugates were synthesized according to Scheme 3.6. $SOCl_2$ was used to convert the COOH groups of SWCNT into the acid chloride derivative (COCl) [278], before reacting with CoMAPc **(9)** to form CoMAPc-SWCNT(linked) **(19)**, which was dried at room temperature under vacuum [163].

3.7.1 Transmission electron microscopy

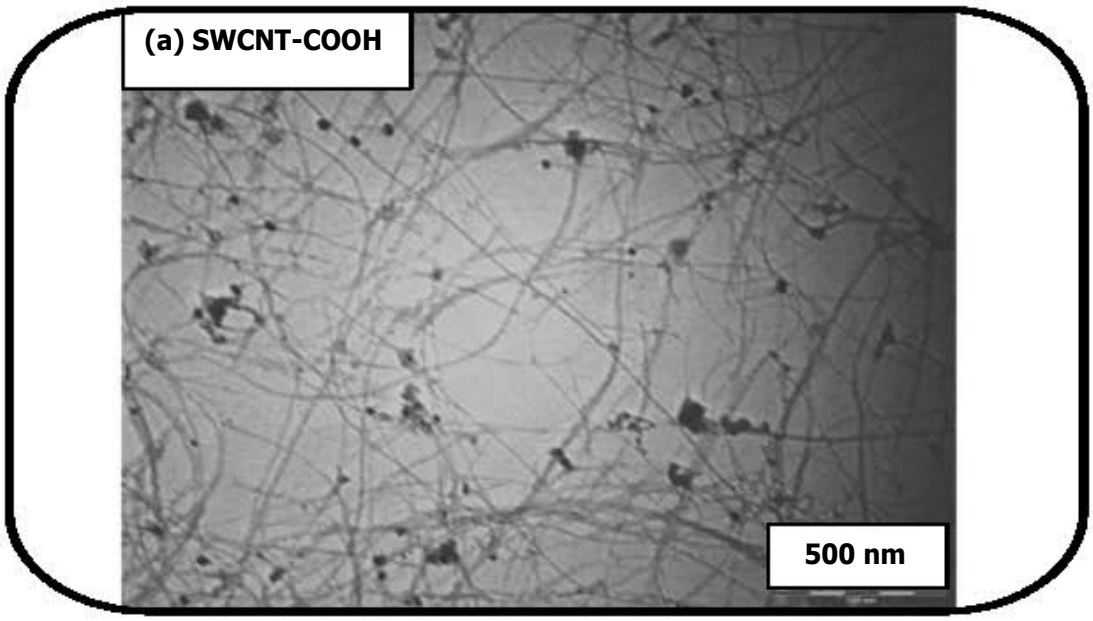

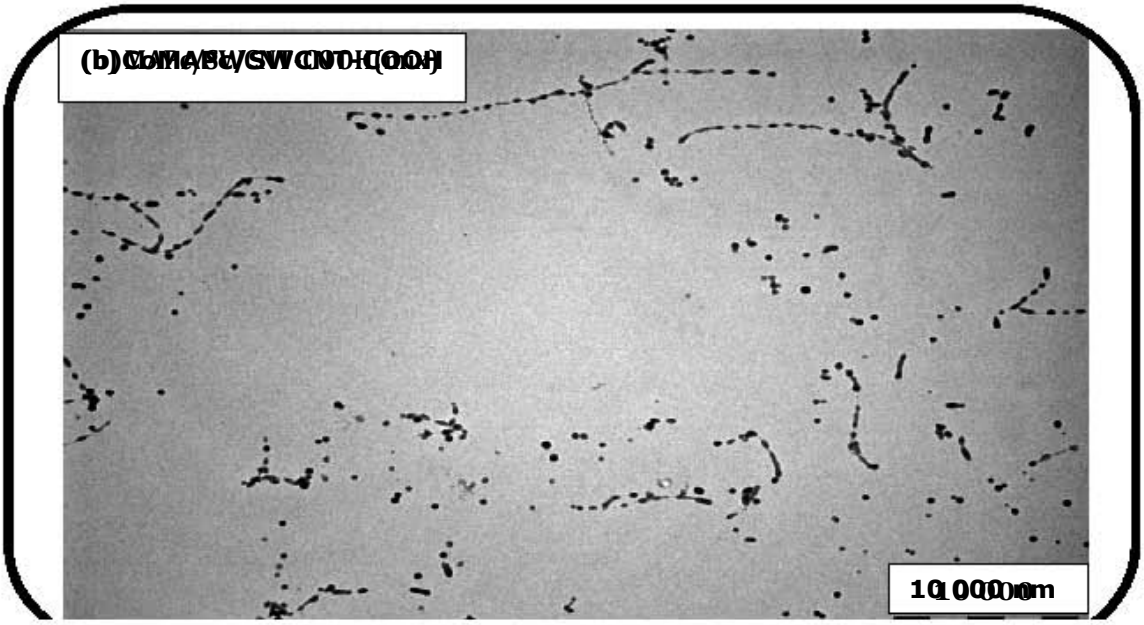

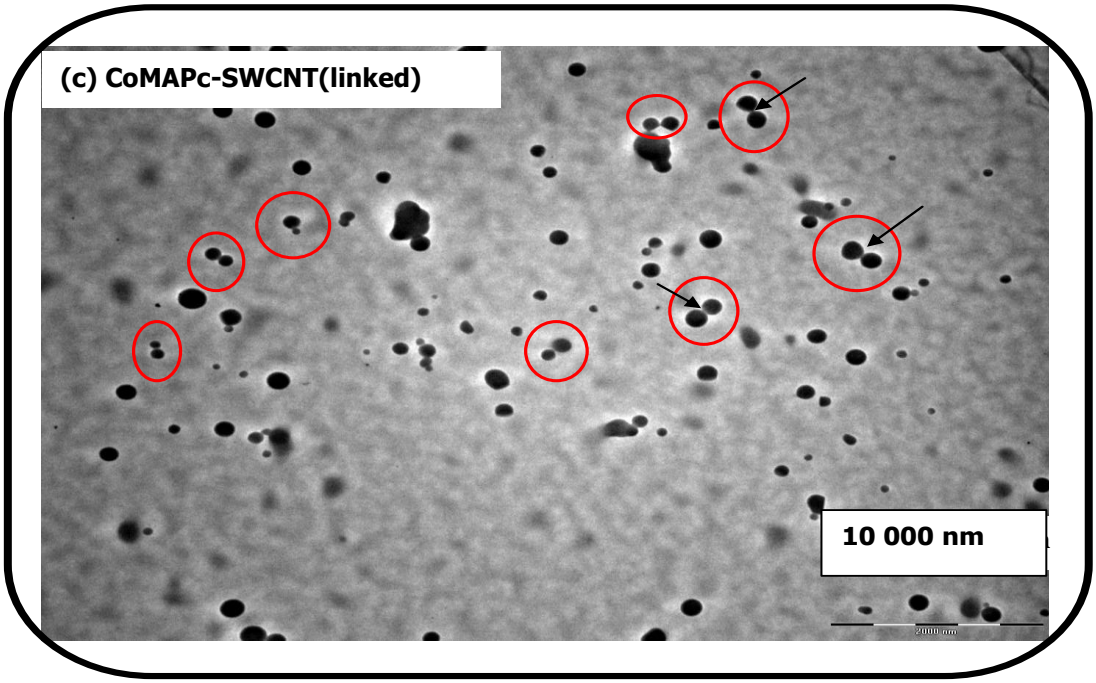

Figure 3.32: TEM pictures of (a) SWCNT-COOH (13), (ii) CoMAPc/SWCNT-COOH(mix) and (iii) CoMAPc-SWCNT(linked), (19), nanorods.

Figure 3.32a-c shows the TEM images of SWCNT-COOH **(13)**, CoMAPc/SWCNT-COOH(mix) and CoMAPc-SWCNT(linked) **(19)** nanorods initially dispersed through ultrasonication in DMF. The TEM image of CoMAPc/SWCNT-COOH(mix) (Fig. 3.32b) shows well dispersed beaded SWCNTs. The beads that are along the SWCNT length are adsorbed phthalocyanine (CoMAPc) aggregates. This shows that CoMAPc **(9)** and SWCNT-COOH are interacting and most probably through their л-system of electrons. The TEM for CoMAPc-SWCNT(linked) nanorods (Fig. 3.32c) show dumb-bell shapes, with the CoMAPc on both sides of the SWCNT, showing that the carboxylic acid groups to which the amino groups are attached are on the terminal ends. The SWCNT are in the middle of the phthalocyanine aggregates (**see arrow**). The lack of continuity in the nature of CoMAPc-SWCNT(linked) nanorods, relative to the SWCNTs (Fig. 3.32a) and the mix (Fig. 3.32b) shows that the nanorods were successfully synthesized. The term nanorod is employed to describe the lack of continuity. The different sizes of rods

observed in Fig. 3.32c could be due to aggregation of MPc or linking of more than one CoMAPc unit to each end of the SWCNT since it is possible that there are more than one carboxylic acid group on each end of the SWCNT.

3.7.2 UV-vis spectroscopy

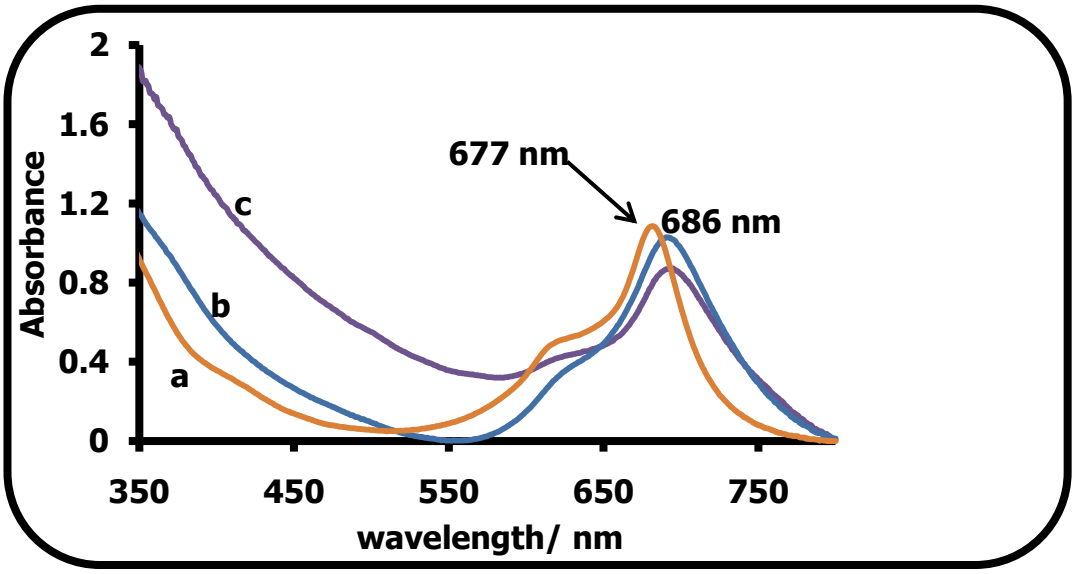

Figure 3.33: (a) UV-vis spectrum of CoMAPc (9), (b) CoMAPc/SWCNT-COOH (mix) and (c) CoMAPc-SWCNT(linked) (19) nanorods. Inset: Structure of CoMAPc. Solvent = DMF. [CoMAPc] = 1 x 10^{-5} M.

Figure 3.33a-c shows the UV-vis spectra for CoMAPc **(9)**, CoMAPc/SWCNT-COOH(mix) and CoMAPc-SWCNT(linked) **(19)** nanorods, respectively, in DMF. The Q-bands for both CoMAPc/SWCNT-COOH(mix) and CoMAPc-SWCNT(linked) are red-shifted at 686 nm, relative to CoMAPc, whose absorption maxima is at 677 nm (Table 3.3). This red shifting is in contrast with the expected blue shifting as observed in MTAPc-SWCNT conjugates. The red shifting in CoMAPc-SWCNT(linked) **(19)** nanorods could be due to the benzyl-mercapto groups that are electron donating and outweigh the electron withdrawing effects induced on CoMAPc by the linked SWCNT-COOH, thereby reducing the HOMO - LUMO gap of the MPc. The same explanation can be offered for the red-shifting observed in

CoMAPc/SWCNT-COOH(mix) as well as the interaction taking place between the CoMAPc and SWCNT-COOH (see TEM pictures, Fig. 3.32b). The sharp rise in absorbance observed for CoMAPc/SWCNT-COOH(mix) and CoMAPc-SWCNT(linked) nanorods from around 550 nm is due to the carbon nanotube absorbance and has been observed in other studies [52].

3.7.3 FTIR spectroscopy

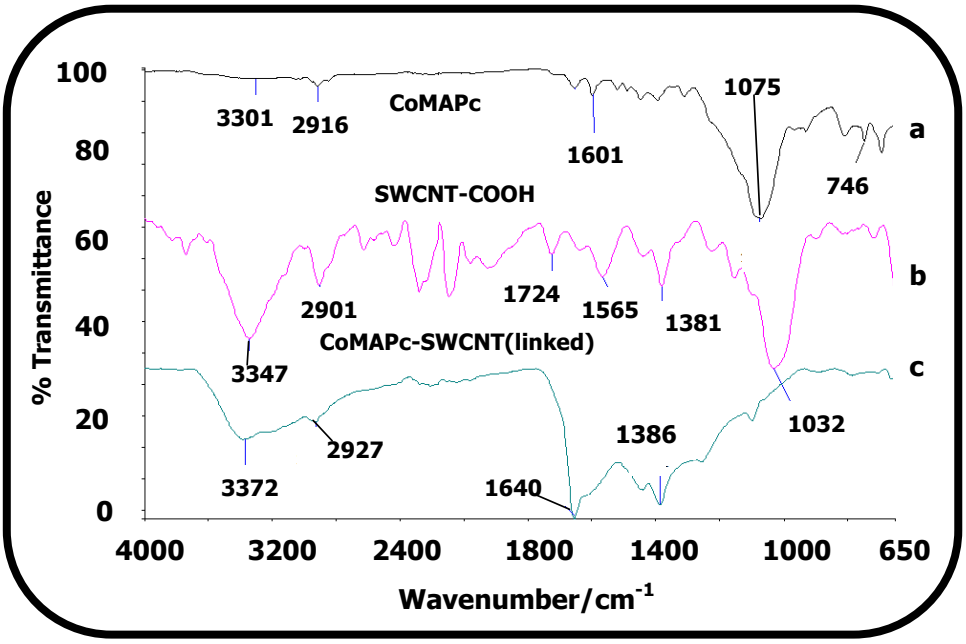

Figure 3.34: FT-IR spectra of (a) CoMAPc (9), (b) SWCNT-COOH (13) and (c) CoMAPc-SWCNT(linked) (19).

Figure 3.34 shows the FTIR spectra for the CoMAPc **(9)**, SWCNT-COOH **(13)** and the CoMAPc-SWCNT(linked) nanorods **(19)**. The spectrum for CoMAPc (Fig. 3.34a) showed a peak at 1601 cm^{-1} as well as a broad (and weak) feature at ~3300 cm^{-1} for the -NH_2 stretching [168] and scissoring modes [168,178,190], respectively. Fig. 3.34c shows the spectrum for the amide linked CoMAPc-SWCNT(linked) nanorods. The nanorods have the –NH stretch of the amide at 3372 cm^{-1}, the C=O strecth of the amide at 1640 cm^{-1}, this is in between the C=O (1724 cm^{-1}) stretch of the carboxylic acid of SWCNT-COOH **(13)** and the –NH_2 stretch of the CoMAPc (1601 cm^{-1}). The

shift of C=O stretch for SWCNT-COOH (1724 cm^{-1}) to 1640 cm^{-1} for CoMAPc-SWCNT(linked) **(19)** nanorods confirms bonding.

3.7.4 XRD spectroscopy

Table 3.7: XRD Parameters for CoMAPc (9), SWCNT-COOH (13) and CoMAPc-SWCNT (19).

ELECTRODE	2θ (in degrees)	d– spacing (Å)
CoMAPc **(9)**	26.5	3.30
SWCNT-COOH **(13)**	17.5; 20.5; 26.0; 44.5; 52.0	5.06; 4.29; 3.36, 2.04; 1.76
CoMAPc-SWCNT(linked) **(19)**	18.0; 22.0; 24.0; 26.5; 30.0; 34.0; 44.5	4.93; 4.08; 3.70; 3.37; 2.92; 2.62; 2.04

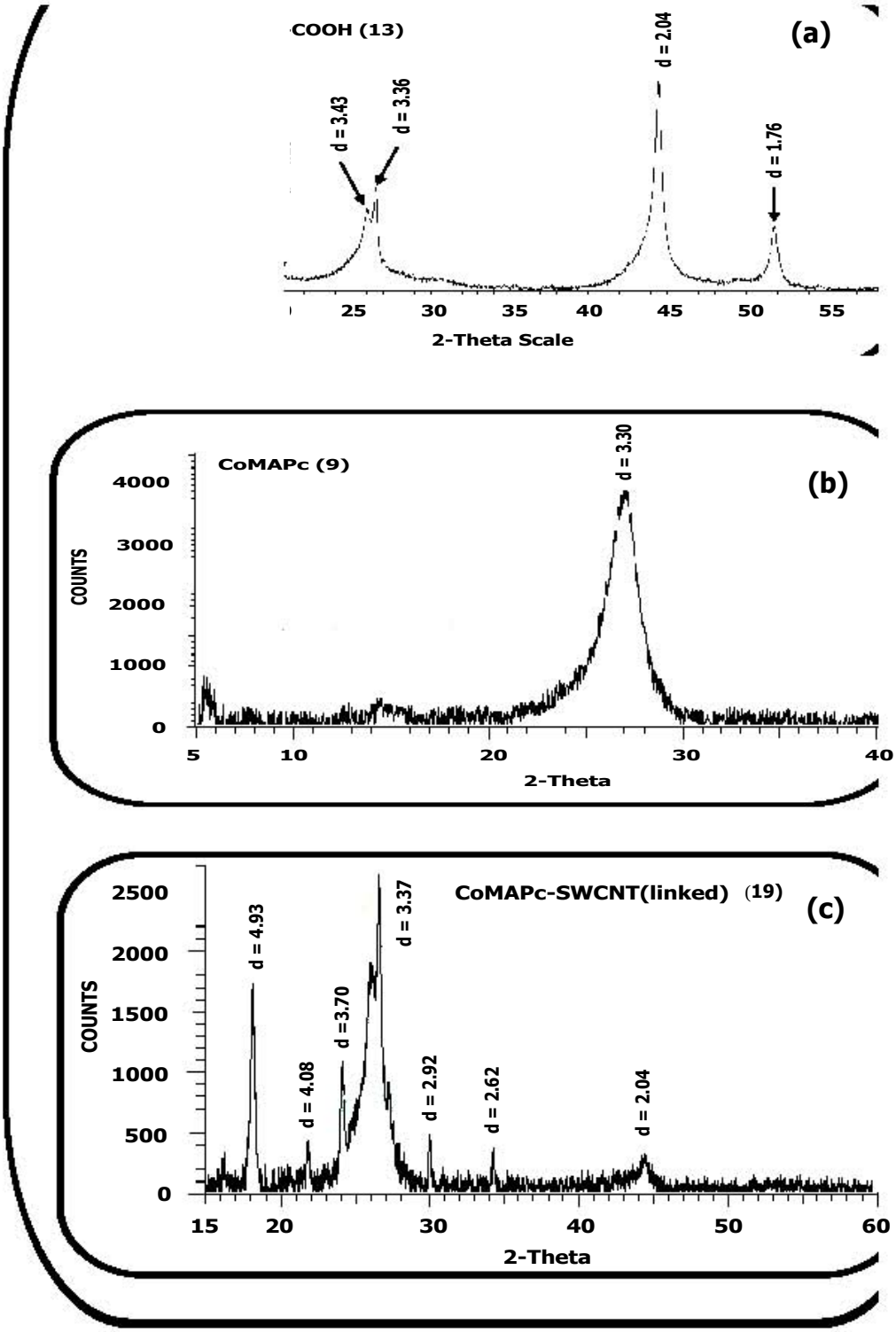

Figure 3.35: XRD spectra for SWCNT-COOH (13), CoMAPc (9) and CoMAPc-SWCNT(linked) (19).

Figures 3.35a-c shows comparative XRD spectrum for SWCNT-COOH **(13)**, CoMAPc **(9)** and CoMAPc-SWCNT(linked) **(19)**, respectively. Table 3.7 gives the 2θ values and d-spacings for SWCNT-COOH, CoMAPc and the CoMAPc-SWCNT(linked).

Apart from the Pc peak at $2\theta = 26.5^0$, the XRD for CoMAPc-SWCNT(linked) show additional peaks at 18.0^0, 22.0^0, 24.0^0, 30.0^0, 34.5^0 and 44.5^0 (Fig. 3.35c). The peak at 44.5^0 is due to the SWCNTs, showing its presence in CoMAPc-SWCNT(linked). The origin of the other peaks in CoMAPc-SWCNT(linked) nanorods XRD spectrum are not yet fully understood. However, it is important to note that the differences in the nature of the XRD spectra for CoMAPc, SWCNT-COOH and the CoMAPc-SWCNT(linked) is an indication of their differences in structural orientations, therefore we can safely conclude that nanorods were successfully synthesized.

3.8 Synthesis and characterization of CoMCPc-PA-SWCNT (20)

PA was chosen over EA for the studies with CoMCPc because of the better solubility of PA-SWCNT over EA-SWCNT in organic solvents.

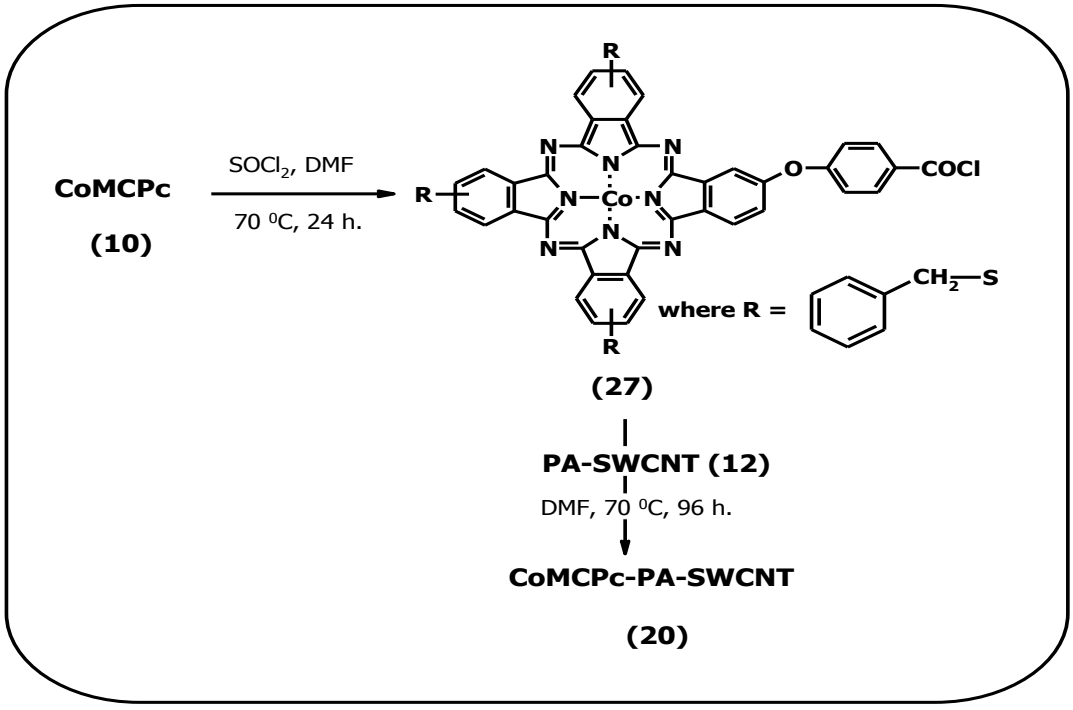

Scheme 3.7: Synthetic route to CoMCPc-PA-SWCNT (20).

CoMCPc-PA-SWCNT(linked) **(20)** conjugates were synthesized according to Scheme 3.7. $SOCl_2$ was used to convert the carboxylic acid group of the CoMCPc **(10)** into the acid chloride as explained for CoTCPc [278] before adding a limiting amount of PA-SWCNT **(12)**, forming CoMCPc-PA-SWCNT(linked) **(20)**.

3.8.1 UV-vis spectroscopy

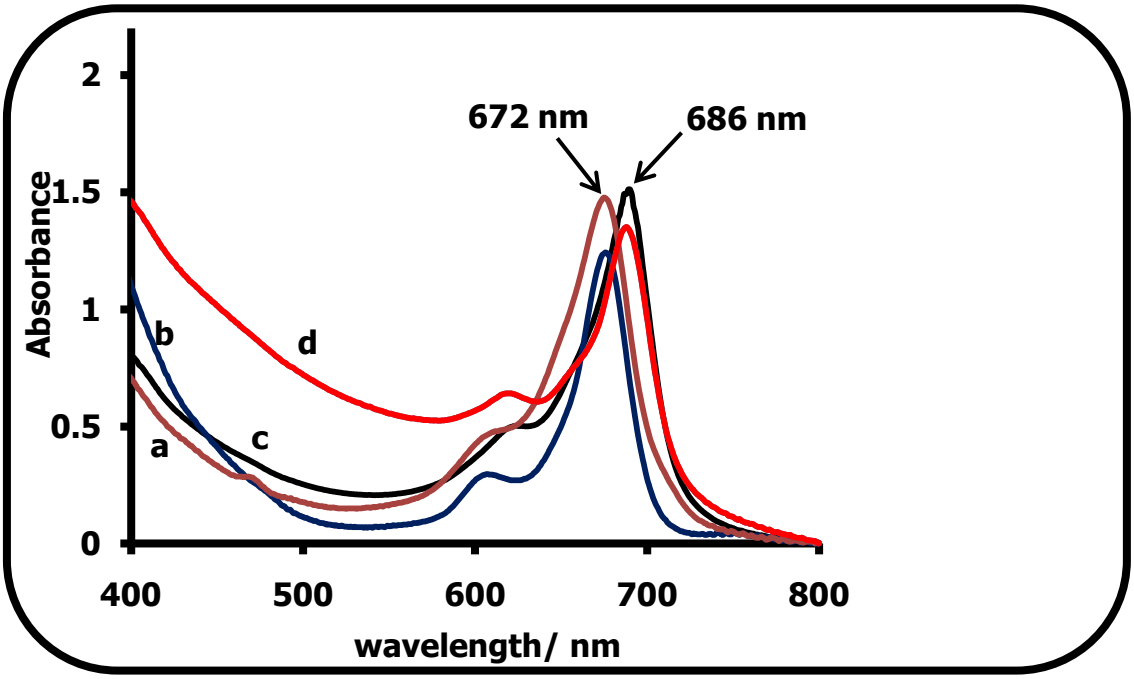

Figure 3.36: UV-vis spectra for: (a) CoMCOClPc, (b) 1 µM CoMCPc (10), (c) CoMCPc/PA-SWCNT(mix) and (d) CoMCPc-PA-SWCNT(linked), 20.

Figure 3.36a-d shows the UV-vis spectra for CoMCOClPc **(27)**, CoMCPc **(10)**, CoMCPc/PA-SWCNT(mix) and CoMCPc-PA-SWCNT(linked) **(20)**, respectively, in DMF. The Q-bands for both CoMCPc and CoMCOClPc are blue-shifted at 672 nm, relative to the CoMCPc/PA-SWCNT(mix) and CoMCPc-PA-SWCNT(linked), whose absorption maxima are at 686 nm (Table 3.3). For CoMCPc-PA-SWCNT(linked) **(20)**, the red shifting is due to the combined effects of the presence of the π-electron rich CNTs and the phenyl-amine groups that donate electrons into the Pc ring, resulting in the reduction of the HOMO - LUMO gap.

The red-shifting observed for the CoMCPc/PA-SWCNT(mix) indicates some form of interaction taking place between the CoMCPc **(10)** and PA-SWCNT **(12)** which also result in the reduction of the HOMO-LUMO gap. This red shifting was also observed in CoMAPc-SWCNT(linked) due to the electron donating benzyl-mercapto groups, as stated before. Although to a lower extend, this red shifting is also observed for CoTCPc-EA-SWCNT(linked), CoTCPc/PA-SWCNT(mix) and CoTCPc-PA-SWCNT(linked) discussed above. This indicates that the benzyl-mercapto groups in CoMCPc have a stronger influence in the reduction of the HOMO-LUMO gap relative to EA or PA carrying SWCNTs. The sharp rise in absorbance for CoMCPc-PA-SWCNT(linked) **(20)** from around 570 nm is due to the carbon nanotube absorbance and has been observed elsewhere [52].

3.8.2 IR spectroscopy

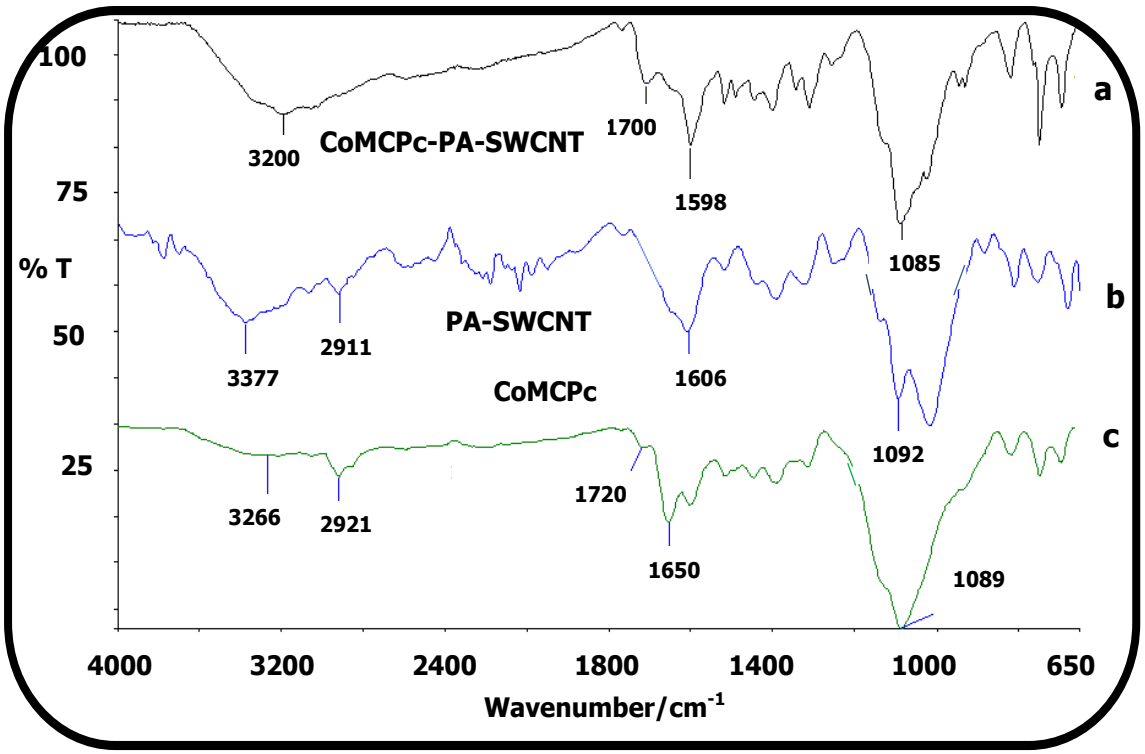

Figure 3.37: FT-IR spectra of: (a) CoMCPc-PA-SWCNT(linked) (20) (b) PA-SWCNT (12) and (c) CoMCPc (10).

Figure 3.37 shows the FT-IR spectra for CoMCPc **(10)**, PA-SWCNT **(12)** and CoMCPc-PA-SWCNT(linked) **(20)**. The spectrum for the CoMCPc (Fig. 3.37c) showed peaks at 1650 and a weak one at 1720 cm^{-1} for the C=O, 3266 cm^{-1} (O-H, broad) and 2921 cm^{-1} (C-H) [201]. PA-SWCNT, Fig. 3.37b, has peaks at 3377 and 1606 cm^{-1} for the $-NH_2$ stretching [168] and scissoring modes [168,178,190], respectively. Fig. 3.37a shows the spectrum for CoMCPc-PA-SWCNT(linked), with peaks at 3200 and 1598 cm^{-1} for the –NH amide stretch. The C=O strecth of the amide at 1700 cm^{-1} falls in between the C=O (1720 cm^{-1}) stretch of the carboxylic acid group of CoMCPc and the $-NH_2$ stretch of the PA-SWCNT at 1606 cm^{-1}. The change in position of the C=O group confirms chemical linking between CoMCPc and PA-SWCNT.

3.8.3 XRD spectroscopy

Table 3.8: XRD parameters for CoMCPc (10), PA-SWCNT (12) and CoMCPc-PA-SWCNT(linked) (20).

ELECTRODE	2θ (in degrees)	d – spacing (Å)
CoMCPc **(10)**	27.0	3.35
PA-SWCNT **(12)**	10.8; 17.6; 20. 6; 26.6; 44.5; 51.5	8.17; 5.04; 4.31; 3.35; 2.03; 1.76
CoMCPc-PA-SWCNT(linked) **(20)**	20.8; 22.2; 26.3; 44.5	4.29; 4.19; 3.30; 2.04

Table 3.8 summarizes the 2θ values and the d-spacings for CoMCPc **(10)**, PA-SWCNT **(12)** and CoMCPc-PA-SWCNT(linked) **(20)**. The XRD spectrum for CoMCPc-PA-SWCNT(linked) was weak (spectra not shown) with peaks 20.8^0, 22.2^0, 26.3^0 and 44.5^0 (Table 3.8). The peak expected around 52.0^0 for the SWCNTs was not very clear in CoMCPc-PA-SWCNT(linked). The peak at 26.3^0 in CoMCPc-PA-SWCNT is due to the overlap of both the CoMCPc and PA-SWCNT bands, while the one at 44.5^0 is due to the PA-SWCNT (Table 3.8). This is an indication of the linking between PA-SWCNT and CoMCPc. The source of the peaks at 2θ values of 10.8^0, 17.6^0 and $20.\ 6^0$ for PA-SWCNT and at 20.8^0 and 22.2^0 for CoMCPc-PA-

SWCNT(linked) are not known. The 2θ values for CoTCPc-PA-SWCNT(linked) (Table 3.6) and those for CoMCPc-PA-SWCNT(linked) (Table 3.8) are different, indicating that these two complexes have different crystalline structures.

3.8.4 Atomic force microscopy (AFM)

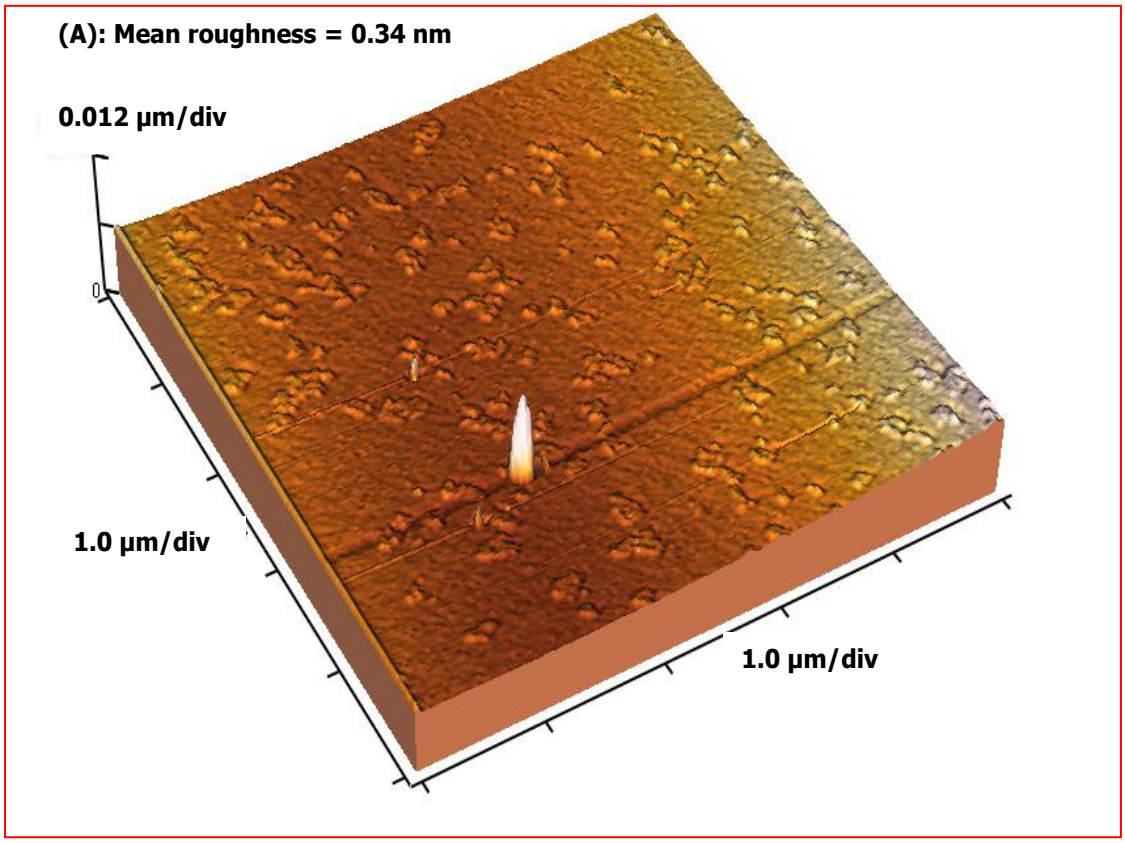

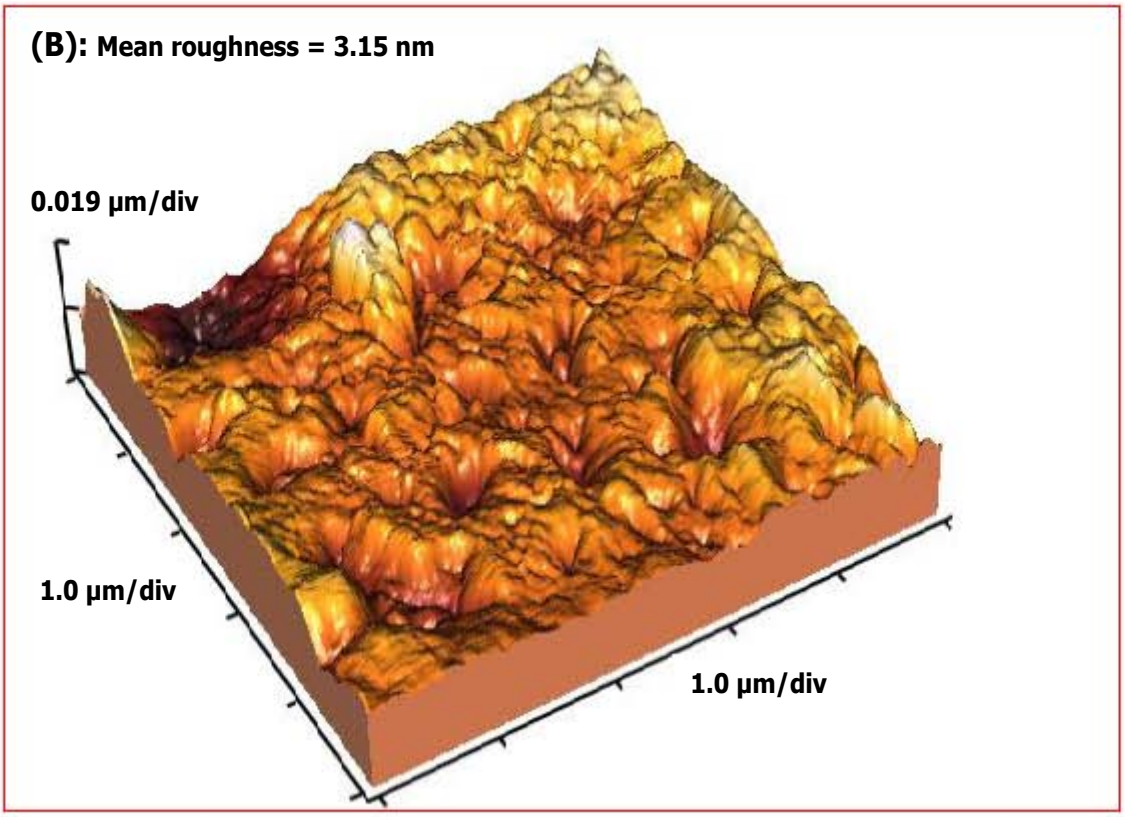
(B): Mean roughness = 3.15 nm
0.019 µm/div
1.0 µm/div
1.0 µm/div

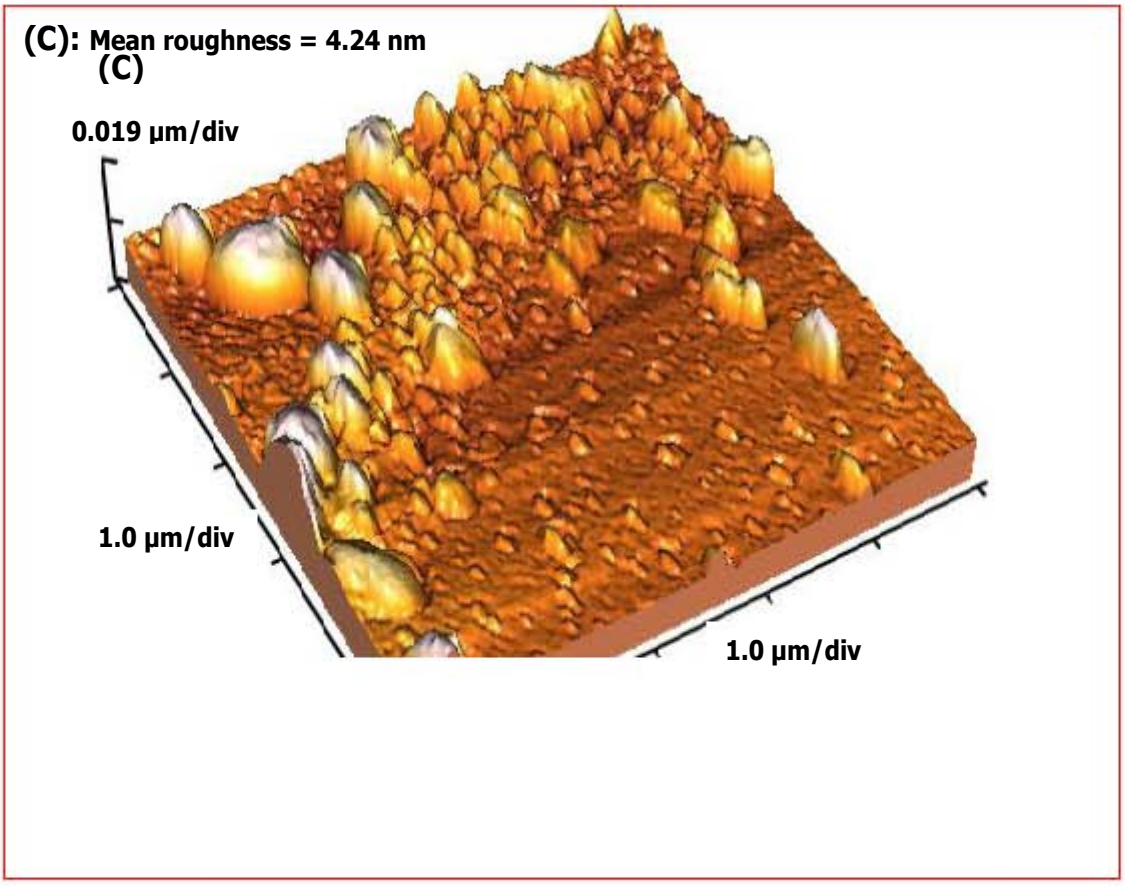
(C): Mean roughness = 4.24 nm
(C)
0.019 µm/div
1.0 µm/div
1.0 µm/div

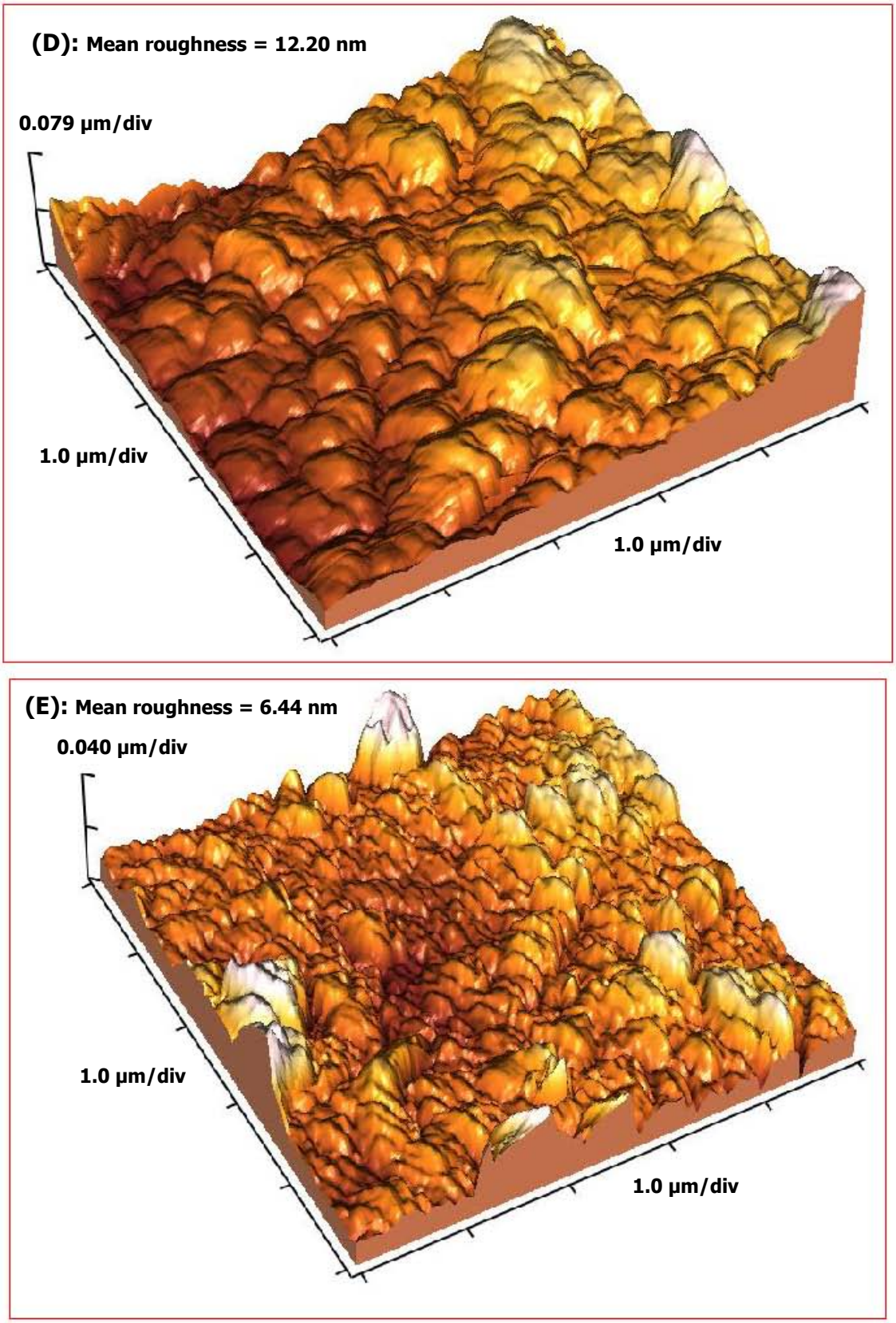

Figure 3.38: AFM pictures of (A) bare GCE, (B) CoMCPc (10), (C) CoMCPc/PA-SWCNT(mix), (D) PA-SWCNT (12) and (E) CoMCPc-PA-SWCNT(linked) (20).

Figure 3.38A-E shows the atomic force microscopy (AFM) images for the following electrodes (A) bare GCE, (B) CoMCPc-GCE **(10)**, (C) CoMCPc/PA-SWCNT(mix)-GCE, (D) PA-SWCNT-GCE **(12)** and (E) CoMCPc-PA-SWCNT(linked)-GCE **(20).** The bare GCE has a mean roughness of 0.34 nm. The sharp spike for the bare GCE (Fig. 3.38A) could be due to a defect. The modified GCE shows different surface morphologies with the highest mean roughness value of 12.20 nm being observed on the PA-SWCNT electrode (Fig. 3.38D). This could be due to the aggregated nature of the SWCNTs. The CoMCPc electrode has a roughness of 3.15 nm, and this increases to 4.24 nm on addition of SWCNT in the mixture (Fig. 3.38C). Chemically linking PA-SWCNT **(12)** to the CoMCPc **(10)** significantly increased the electrode roughness to 6.44 nm (Fig. 3.38E). These different surface roughness values confirm the different surface topologies of the hybrid electrodes used in this study as has been observed before [230].

3.10 Conclusions

Microscopy and spectroscopy techniques were used to confirm the formation of chemical linkages between SWCNTs and MPcs. UV-vis spectroscopy was used to observe the changes in the positions of the Q-band, as an indication of the interaction between the MPcs and SWCNTs. FTIR spectroscopy monitored the changes in the positions of the C=O vibronic bands as a way of confirming chemical linkages between SWCNTs and MPcs. Raman spectroscopy was used to follow the changes in intensities of the D-band in order to confirm functionalization of SWCNTs. Peak shifts were used to confirm formation of amide linkages. Raman spectroscopy was also used to successfully identify ion marker bands and amide peaks. XRD spectroscopy was used to follow changes in 2θ values, d-spacings and peak intensities as a way of confirming chemical linkages between MPcs and SWCNTs. TEM was used to visually observe formation of chemical linkages, as well as to monitor the differences between the conjugate precursors and mixtures. AFM confirmed the formation of different modifier morphologies on the electrode surface. TGA profiles were used to follow changes that occurred during functionalization of SWCNTs and the formation of chemical linkages between MPcs and SWCNTs. From

the TGA profiles, the degrees of functionalization of SWCNTs by amine and carboxylic acid groups, as well as MPcs were obtained.

CHAPTER 4

ELECTROCHEMICAL CHARACTERIZATION OF MODIFIED GCEs

This chapter looks at the different electrochemical methods that were employed to characterize the modified GCEs. The electrodes were modified by the dip- or drop-dry and electropolymerization methods.

4 Cyclic voltammetric characterizations

4.1 Characterization in pH 4 buffer and surface coverage determination

For CoTAPc and its conjugates, the electrodes were modified by the drop-dry method, while for FeTAPc and NiTAPc, polymerization of these complexes was employed and for their conjugates, the electrodes were modified through the drop-dry approach. Though the drop-dry method for CoTAPc produced reliable results (similar to those obtained through polymerization), the electrode lifespan was very short, hence the shift to modification by electropolymerization (for FeTAPc and NiTAPc) which gave a more stable and durable electrode surface. For NiTAPc, polymerization on the electrode surface further allowed for the easy formation of the oxo-bridges on cyclisation in NaOH. The drop-dry method is based on the formation of л-л interactions with the bare GCE since it is a carbon based electrode and assuming all the conditions are the same reproducibility will be ascertained.

The surface roughness factor and the effective electrode area for the modified electrodes was determined using the $[Fe(CN)_6]^{3-/4-}$ redox system and applying the Randles - Sevcik Eq. 4.1 for reversible system [293].

$$I_p = (2.69 \times 10^5) n^{3/2} A D^{1/2} C v^{1/2} \quad (4.1)$$

where n is the number of electrons transferred, A is the geometric electrode area (cm^2), D is the diffusion coefficient of $[Fe(CN)_6]^{3-}$ = 7.6 x 10^{-6} cm^2 s^{-1} at 25 ^{0}C [294] and C is the bulk concentration of the $[Fe(CN)_6]^{3-}$ (1.0 x 10^{-6} mol cm^{-3}).

Surface coverages were estimated using Eq. 4.2 for complexes with well-defined peaks and Eq. 4.3 for those with peaks that are not clearly defined.

$$\Gamma = \frac{Q}{nFA_{eff}} \quad (4.2)$$

where Q is the charge and F is the Faraday constant.

$$I_{pa} = \frac{n^2F^2}{4RT} \upsilon A_{eff} \Gamma \quad (4.3)$$

where I_p is the peak current, A_{eff} is the effective electrode coating geometric area and Γ is the surface coverage of the redox species. From the slope of plot of I_{pa} versus v surface coverage can be estimated.

For all the electrodes, the *Γ* value is a very crude estimation based on the assumption that the electrode coating film is very compact and totally non-porous.

Table 4.1 Ep of complexes and surface coverages (Γ), pH 4 buffer

Complex	Ep/V	Γ/ mol cm^{-2}
CoTAPc	$Co^{III}Pc^{-1}$/ $Co^{III}Pc^{-2}$ (~0.70)	1.18 x 10^{-10}
CoTAPc-SWCNT(linked)	Not defined	1.25 x 10^{-10}
FeTAPc	$Fe^{III}Pc^{-1}$/ $Fe^{III}Pc^{-2}$ (~0.95)	1.22 x 10^{-10}
FeTAPc-SWCNT(linked)	Not defined	1.43 x 10^{-10}
NiTAPc	Ni^{III}/Ni^{II} (0.4); Pc^{-1}/ Pc^{-2} (0.70)	1.51 x 10^{-10}
NiTAPc-SWCNT(linked)	Ni^{III}/Ni^{II} (0.4); Pc^{-1}/ Pc^{-2} (0.70)	1.34 x 10^{-10}
Poly-Ni(OH)TAPc	Ni^{III}/Ni^{II} (0.45)*	1.14 x 10^{-10}
CoTCPc	$Co^{III}Pc^{-1}$/ $Co^{III}Pc^{-2}$ (~0.91)	3.25 x 10^{-10}
CoTCPc-PA-SWCNT(linked)	$Co^{III}Pc^{-1}$/ $Co^{III}Pc^{-2}$(~0.89)	1.89 x 10^{-10}
CoTCPc	$Co^{III}Pc^{-1}$/ $Co^{III}Pc^{-2}$ (~0.70)	1.47 x 10^{-10}
CoTCPc-EA-SWCNT(linked)	Co^{III}/Co^{II} (~0.55)	1.28 x 10^{-10}
CoMAPc	$Co^{III}Pc^{-1}$/ $Co^{III}Pc^{-2}$ (~0.70)	1.24 x 10^{-10}
CoMAPc-SWCNT(linked)	Not defined	1.65 x 10^{-10}
CoMCPc	$Co^{III}Pc^{-1}$/ $Co^{III}Pc^{-2}$ (~0.70)	1.41 x 10^{-10}
CoMCPc-PA-SWCNT(linked)	Not defined	1.36 x 10^{-10}

*$E_{1/2}$ value

4.1.1 CoTAPc and its conjugates

As stated above, the electrodes were modified by drop/dry or dip/dry method. After modification, each of the following electrodes: SWCNT-COOH-GCE, CoTAPc-GCE, CoTAPc-SWCNT(linked)-GCE and CoTAPc/SWCNT-COOH(mix)-GCE, was cyclised in pH 4 buffer in order to determine the peak behaviours, Fig. 4.1A. The peaks observed at ~0.70 V (versus Ag|AgCl) in Fig. 4.1A appear only for CoTAPc and CoTAPc/SWCNT-COOH(mix)–GCE, but not clear for CoTAPc-SWCNT(linked)-GCE in pH 4 buffer. However these peaks are too broad and appear at very high potentials for the Co^{III}/Co^{II} process, suggesting an overlap with peaks due to the ring, $Co^{III}Pc^{-1}/Co^{III}Pc^{-2}$ [74,251]. The Co^{III}/Co^{II} process is known to be irreversible and notoriously difficult to observe for adsorbed CoPc complexes [100], hence its absence in CoTAPc-SWCNT(linked)-GCE is not surprising. Additionally,

the current for the Co^{III}TAPc/Co^{II}TAPc peak increased with increase in scan rate, Fig. 4.1B, for CoTAPc/SWCNT-COOH(mix)-GCE which is typical of species that are adsorbed on an electrode surface [245].

By using the $[Fe(CN)_6]^{3-/4-}$ redox system and Eq. 4.1 at a scan rate (v) of 0.1 V s^{-1}, the experimentally determined effective electrode area (A_{eff}) was found to be 0.079 cm^2 (for the GCE modified with CoTAPc-SWCNT(linked)) giving a surface roughness factor (experimentally determined area/geometric area (0.071 cm^{-2})) of ~1.11 against ~1.0 for the polished electrode GCE, suggesting improved surface for the former. Using the A_{eff} and Eq. 4.2, the surface coverage calculated for CoTAPc using the Co^{III}/Co^{II} process at 0.70 V was 1.18 x 10^{-10} mol cm^{-2} (Table 4.1) and is close to 1 x 10^{-10} mol cm^{-2} observed for a Pc molecule lying flat, confirming monolayer formation [295]. The surface coverage (1.25 x 10^{-10} mol cm^{-2}) for the linked was estimated using Eq. 4.3 and also at 0.7 V, Table 4.1.

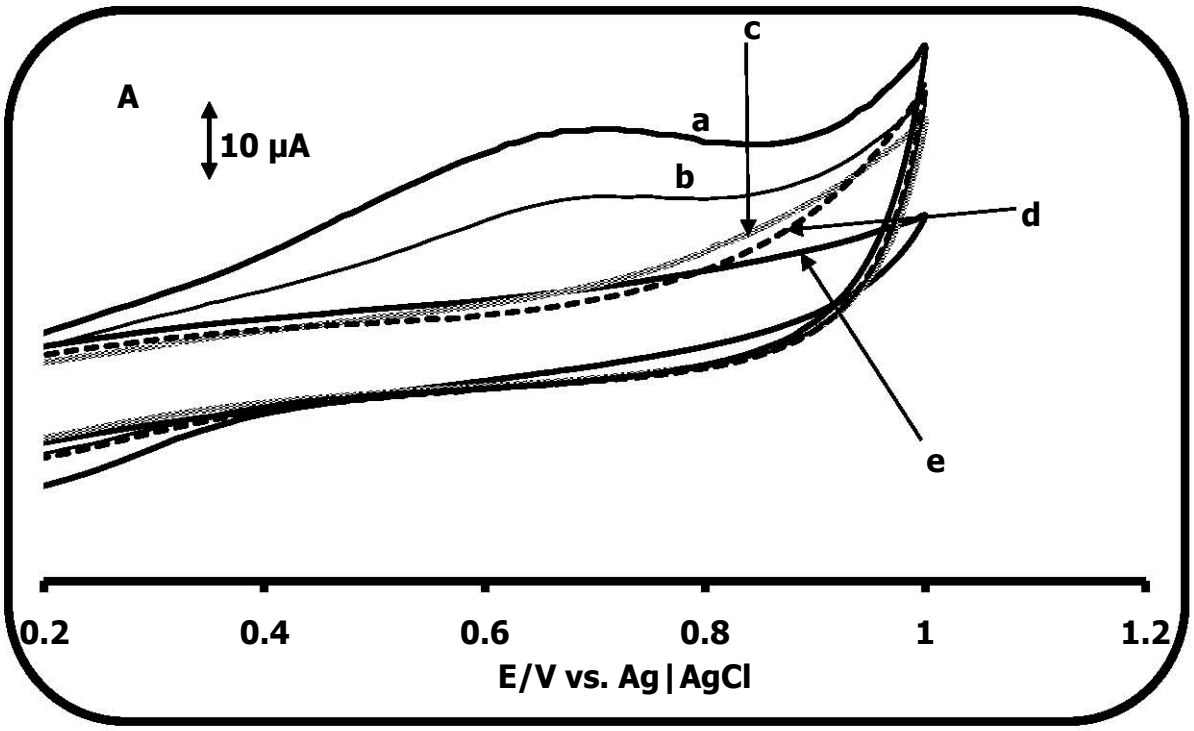

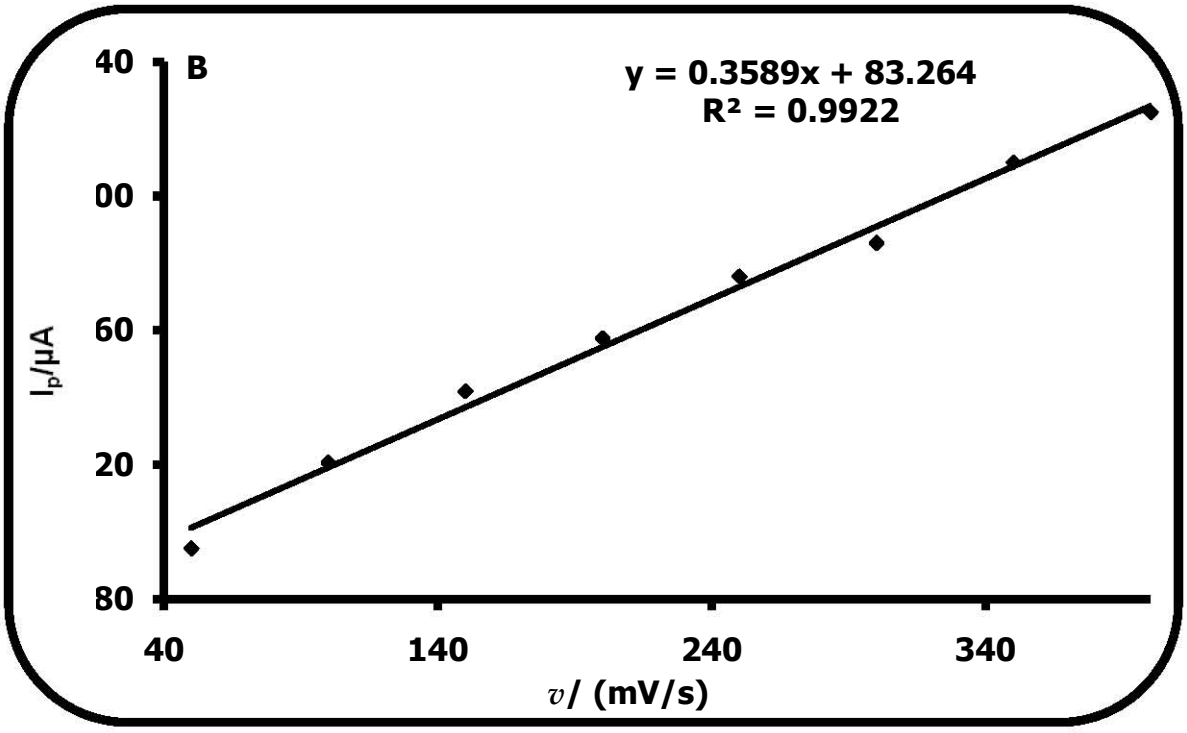

Figure 4.1: (A) Cyclic voltammograms (pH 4 buffer) for (a) CoTAPc/SWCNT-COOH(mix)-GCE (b) CoTAPc-GCE, (c) CoTAPc-SWCNT(linked)-GCE, (d) SWCNT-COOH-GCE and (e) bare GCE. Scan rate = 50 mV/s. B: Variation of Ip with scan rate for CoTAPc/SWCNT(mix)-GCE.

4.1.2 FeTAPc and its conjugates

Initially FeTAPc was electropolymerized onto the GCE. The presence of amino groups on the periphery of the ring results in MPc molecules which can be electro-polymerized onto the electrodes. Amino groups are suitable substituents because they are able to form a network of conjugated bonds and hence polymerize with ease. Electro-polymerization of MTAPc complexes is well-established [103,296].

Fig. 4.2 shows the evolution of *poly*-FeTAPc peaks as the GCE is continuously cyclised in FeTAPc monomer solution in DMSO containing 1 mM $TBABF_4$ between -0.6 and 1.2 V (versus Ag|AgCl). Increase and formation of new peaks is evidence of polymer growth. The redox processes in Fig. 4.2 have been observed elsewhere [76]. The inset in Fig. 4.2 shows the difference between the first and the last scan (cycle 80). The conjugates and SWCNTs were simply adsorbed onto the electrode surface.

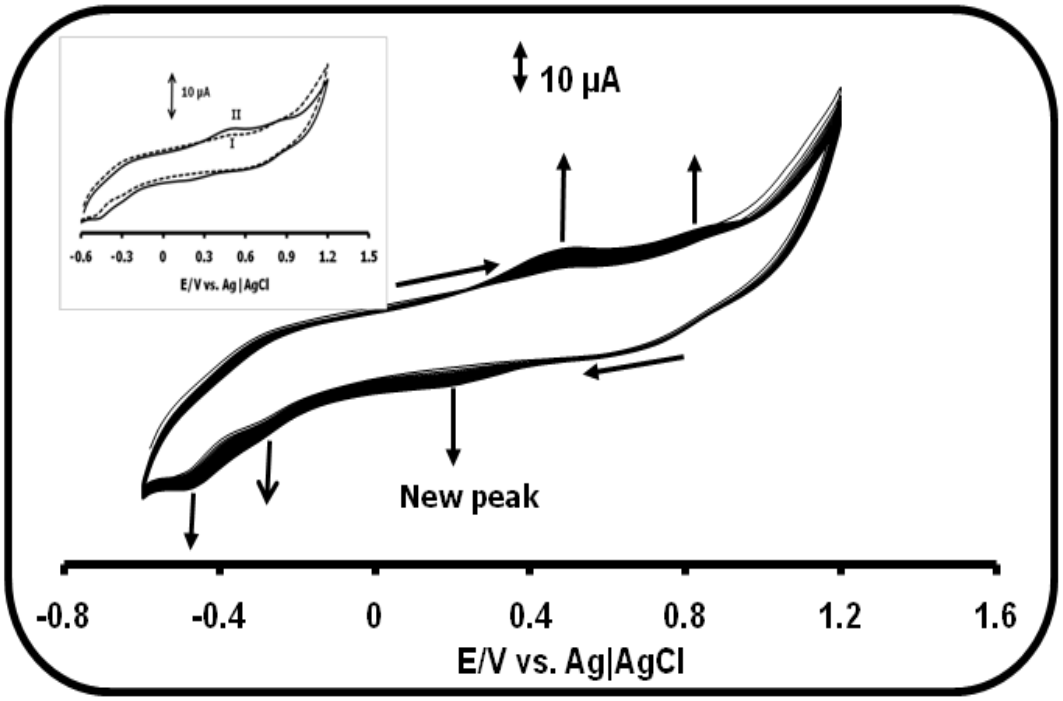

Figure 4.2: Repetitive cyclic voltammetry of 1 x 10^{-3} M FeTAPc on GCE in DMSO containing ~1 x 10^{-3} M $TBABF_4$. Scan rate = 100 mV s^{-1}. Inset: Cycles 1(I) and 80 (II).

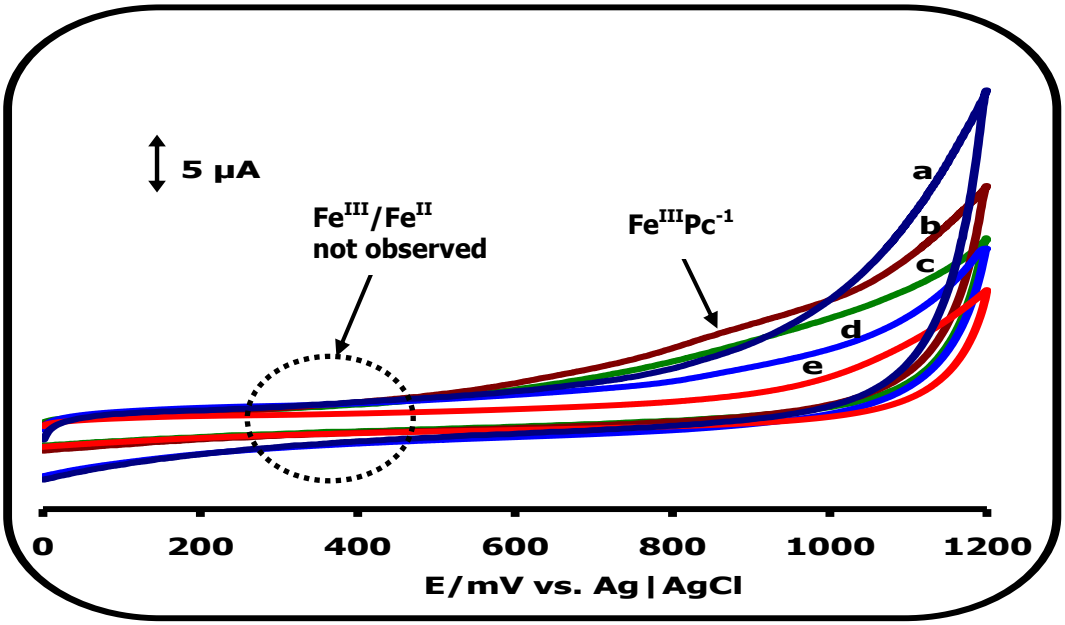

Figure 4.3: Cyclic voltammograms for (a) FeTAPc-SWCNT(linked)-GCE, (b) *poly*-FeTAPc-GCE, (c) SWCNT-COOH-GCE, (d) FeTAPc/SWCNT-COOH(mix)-GCE and (e) bare GCE. pH 4 buffer. Scan rate = 100 mV/s.

Figure 4.3 shows the cyclic voltammograms of FeTAPc-SWCNT(linked)-GCE, FeTAPc/SWCNT(mix)-GCE, *poly*-FeTAPc-GCE and SWCNT-COOH-GCE in pH 4 buffer. The Fe^{III}/Fe^{II} redox peak is not visible in *poly*-FeTAPc-GCE, FeTAPc-SWCNT(linked)-GCE and FeTAPc/SWCNT-COOH(mix)-GCE, Fig. 4.3. In the presence of SWCNTs, the absence of the Fe^{III}/Fe^{II} redox peak (for FeTAPc-SWCNT(linked)-GCE and FeTAPc/SWCNT-COOH(mix)-GCE) could be attributed to an increase in the heterogeneity of the electrode surface which result in the broadening of the Fe^{III}/Fe^{II} peak. The broad peak at 0.95 V versus Ag|AgCl in *poly*-FeTAPc represents the $Fe^{III}Pc^{-1}/Fe^{III}Pc^{-2}$ redox process. Current increased with scan rate showing adsorbed species for FeTAPc-SWCNT(linked) as observed for CoTAPc. Surface coverage were estimated (as described above for CoTAPc and its conjugate) to be 1.22×10^{-10} and 1.43×10^{-10} mol cm^{-2} for FeTAPc and FeTAPc-SWCNT(linked) (Table 4.1), respectively.

4.1.3 NiTAPc and its conjugates

As with FeTAPc, the polymer was formed first by cyclising the GCE in a solution of NiTAPc to form *poly*-NiTAPc (Fig. 4.4).

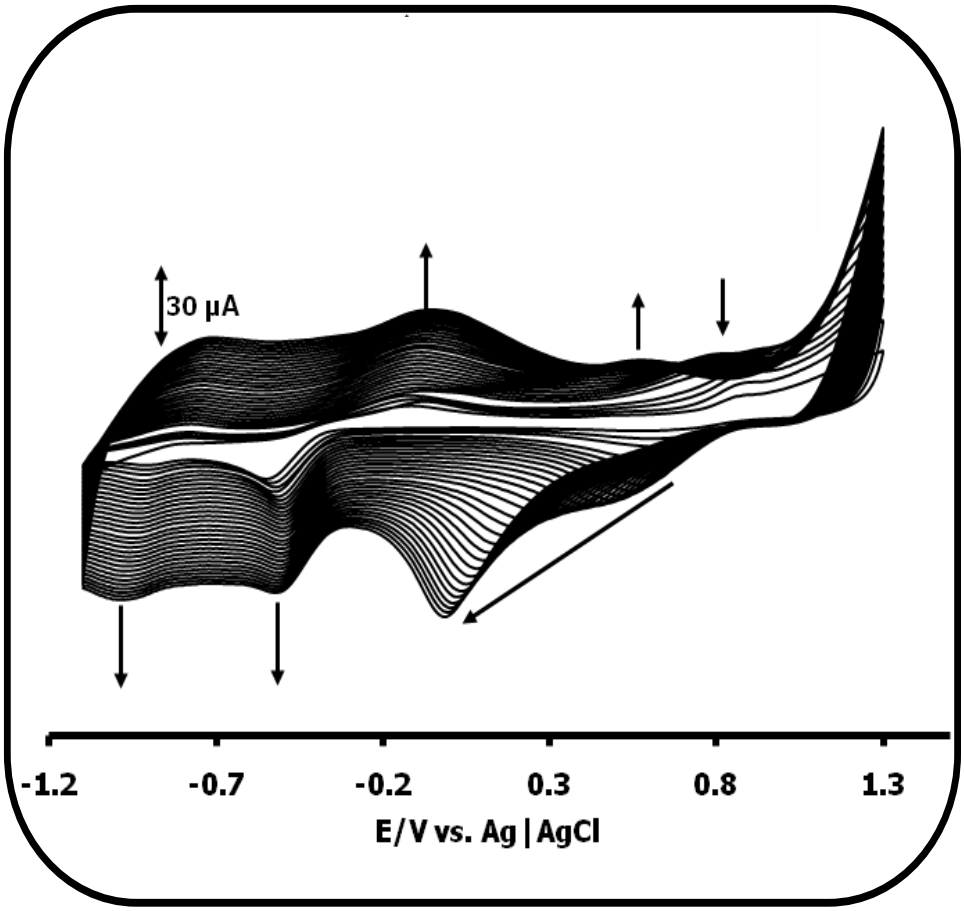

Figure 4.4: Repetitive cyclic voltammetry of 1 x 10^{-3} M NiTAPc on glassy carbon electrode in DMF containing ~1 x 10^{-3} M $TBABF_4$. Scan rate = 100 mV s^{-1}.

Figure 4.4 shows the evolution of cyclic voltammograms during polymerization of NiTAPc monomer in DMF containing $TBABF_4$. The evolution of the polymer in Fig. 4.4 is similar to that observed in literature [296], showing well defined redox processes.

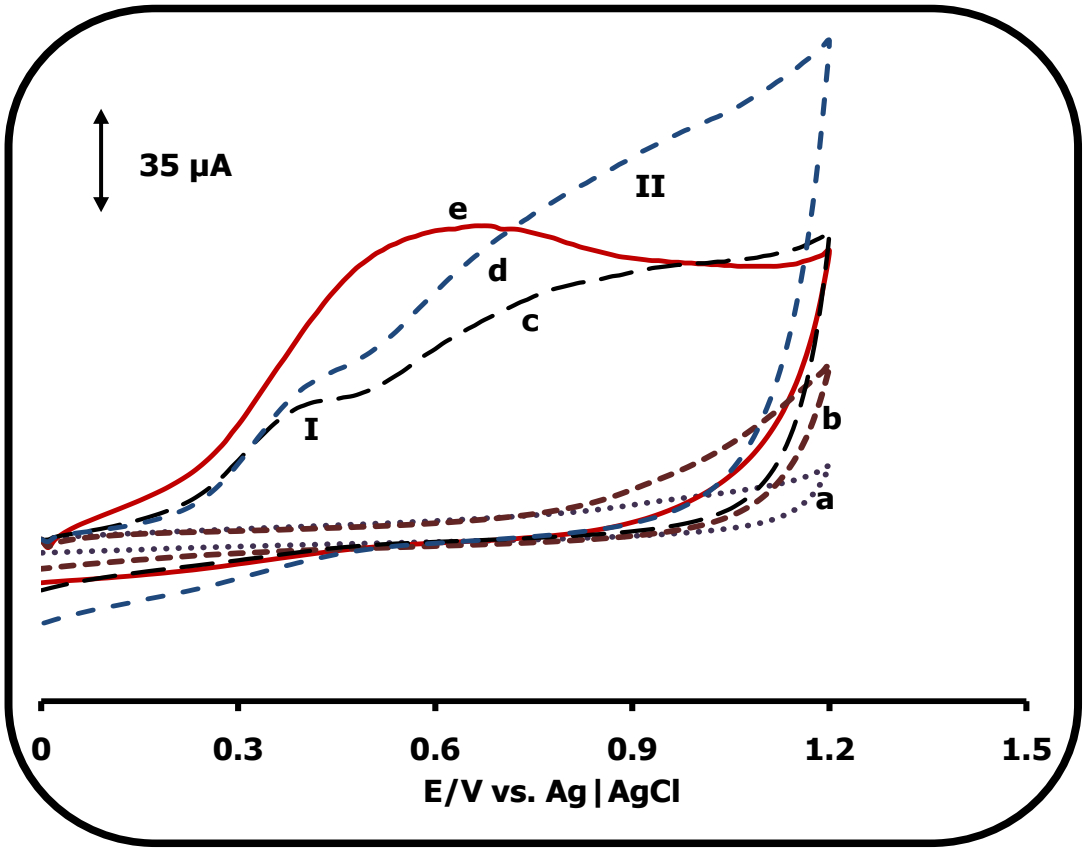

Figure 4.5: Cyclic voltammograms for (a) bare GCE, (b) SWCNT-GCE, (c) *poly*-NiTAPc-GCE, (d) NiTAPc-SWCNT-COOH(mix)-GCE and (e) NiTAPc-SWCNT-GCE(linked), in pH 4 buffer. Scan rate = 100mV/s.

Figure 4.5 compares the cyclic voltammograms of NiTAPc-SWCNT(linked)-GCE, NiTAPc/SWCNT-COOH(mix)-GCE, *poly*-NiTAPc-GCE, SWNT-COOH-GCE and the bare-GCE in pH 4 buffer. Peak **I** represents the Ni^{III}/Ni^{II} oxidation process as observed in other studies [103-106,297]. This peak is very broad for the NiTAPc-SWCNT(linked) and this could be attributed to the increased heterogeneity of the electrode surface as was observed for FeTAPc-SWCNT(linked). Peak **II** represents the first ring oxidation ($Ni^{III}Pc^{-1}/Ni^{III}Pc^{-2}$) and it is probably overlapping with peak **I** in NiTAPc-SWCNT(linked).

Using the methods described for CoTAPc (Eq. 4.1), the effective electrode area of the NiTAPc-SWCNT(linked) (A_{eff} cm^{-2}) was estimated to be 0.480 cm^2. Using peak **I** and Eq. 4.3, the total surface coverage of the NiTAPc-SWCNT(linked) modifier film of

1.34 x 10^{-10} mol cm^{-2} was obtained. Using the same approach (peak **I**), the surface coverage for *poly*-NiTAPc was found to be 1.51 x 10^{-10} mol cm^{-2}, Table 4.1.

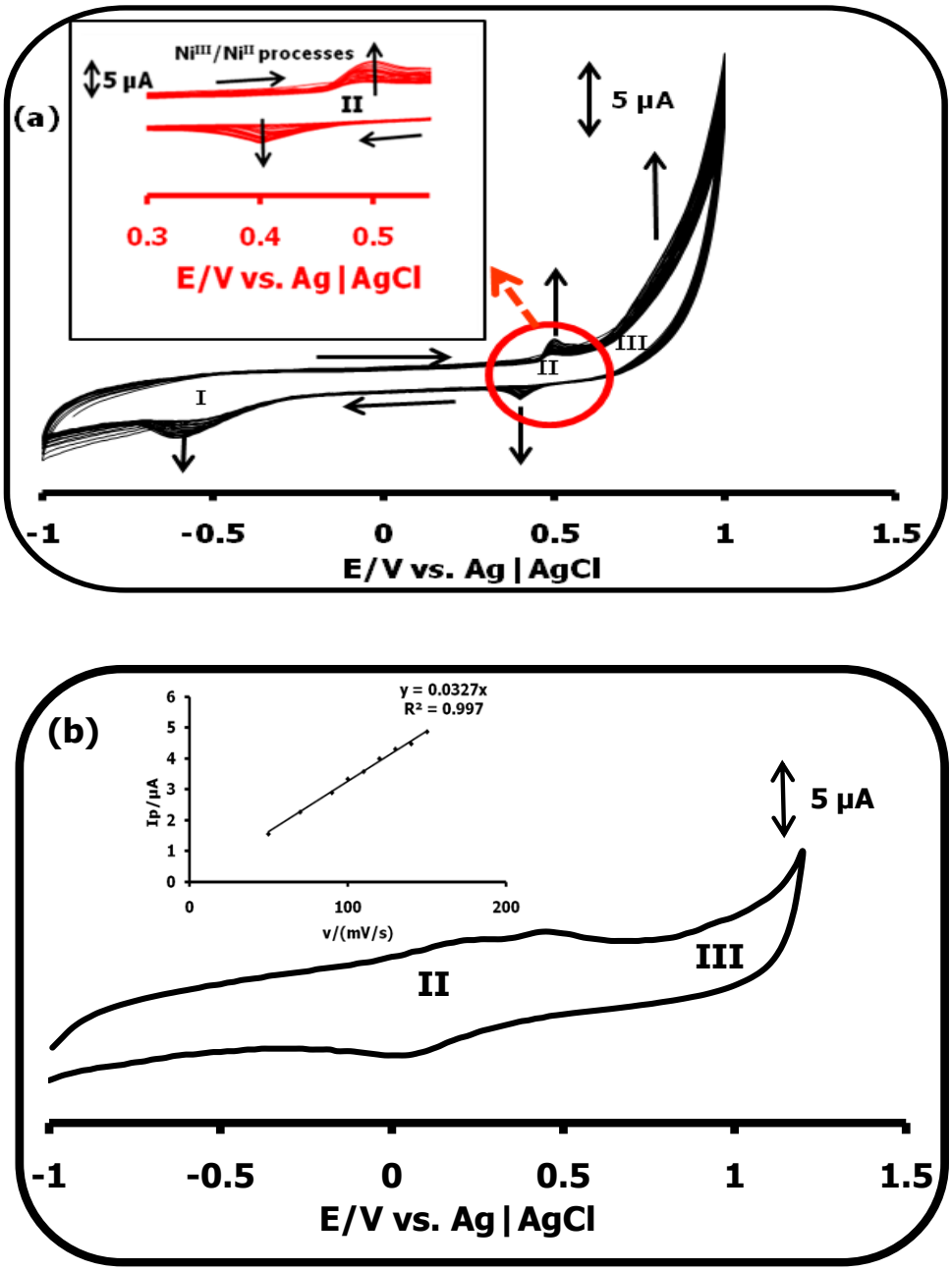

Figure 4.6: (a) 25 repetitive scans of *poly*–NiTAPc-GCE in 0.1 M NaOH (forming *poly*-Ni(OH)TAPc-GCE). Inset: Expanded view showing the Ni^{III}/Ni^{II} processes. (b) Cyclic voltammogram of *poly*-Ni(OH)TAPc-GCE in pH 4 acetate buffer. Inset: Plot of peak current versus sweep rate for *poly*-Ni(OH)TAPc-GCE in pH 4 acetate buffer. The reduction process of couple II in Fig. 4.16b used. Scan rate = 50 mV/s.

It is known that Ni-O-Ni is more catalytic than *poly*-NiTAPc [79], hence *poly*-NiTAPc was transformed into *poly*–Ni(OH)TAPc through repetitive cycling in 0.1 M NaOH in the potential window -1.0 to +1.4 V versus Ag|AgCl at a scan rate of 0.05 V/s for 25 cycles (Fig. 4.6a). Fig. 4.6a (inset) shows expanded view of successive increases in peak currents for the Ni^{III}/Ni^{II} processes (couple **II)**. These processes have been observed in other studies [233,298]. The large increases in currents beyond + 0.6 V have been attributed to the electro-oxidation of OH^- ions to O_2 with $OH^\bullet$ radicals as intermediates [298]. Peak **I** (Fig. 4.6a) represents the first ring reduction of NiTAPc. Figure 4.6b shows the *poly*–Ni(OH)TAPc-GCE in pH 4 buffer with the Ni^{III}/Ni^{II} (process **II**) being shifted to less positive values compared to NaOH solution in Fig. 4.6a. Process **III** in Fig. 4.6b is due to ring based process ($Ni^{III}Pc^{-1}$) of adsorbed *poly*–Ni(OH)TAPc.

Figure 4.6b (inset) shows the plot of the anodic background corrected peak current versus sweep rate, using process **II** in Fig. 4.6b. The linear relationship of the plot of scan rate versus current at these low scan rates is characteristic of surface-immobilized redox species as discussed above. The effective electrode area calculated using Eq. 4.1 and the evolved cyclic voltammograms of $[Fe(CN)_6]^{4-/3-}$ in 0.1 M of KCl [299]. The surface coverage of the redox active *poly*-Ni(OH)TAPc film was estimated from the plot of background corrected peak current versus scan rate, according to Eq. 4.3 [231]. The Γ_{MPc} value of 1.14×10^{-10} mol cm^{-2} (Table 4.1) was obtained for *poly*-Ni(OH)TAPc film formed using 25 cycles and the Ni^{III}/Ni^{II} peaks in Fig. 4.6a inset.

4.1.4 CoTCPc and its conjugates

4.1.4.1 PA-SWCNT

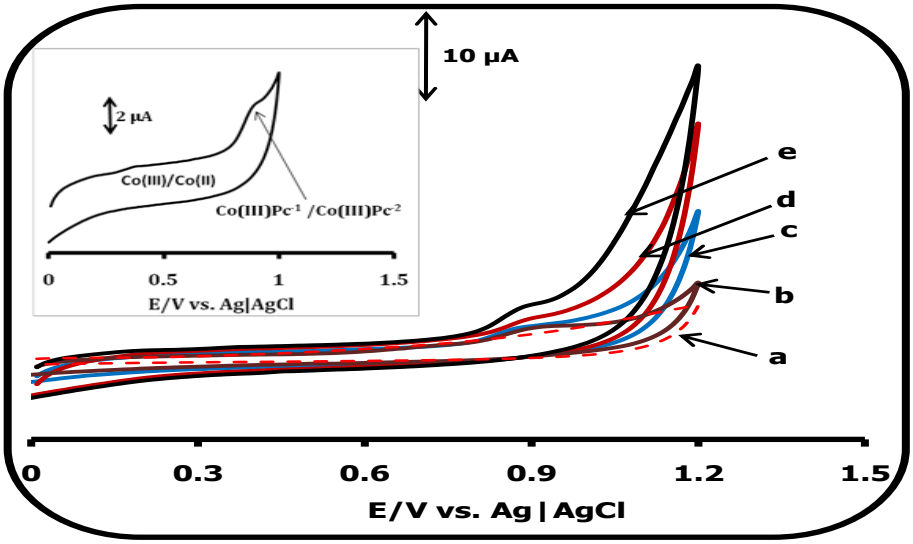

Figure 4.7: Cyclic voltammograms for the bare and modified electrodes in pH 4 buffer: (a) bare GCE, (b) CoTCPc (8), (c) PA-SWCNT (12), (d) CoTCPc/PA-SWCNT(mix) and (e) CoTCPc-PA-SWCNT(linked) (17). Inset: Cyclic voltammogram for CoTCPc-PA-SWCNT(linked) in the potential range 0.0 V – 1.0 V (vs. Ag|AgCl). Scan rate = 100 mV/s.

Figure 4.7 shows the voltammograms for bare GCE (a), CoTCPc-GCE (b), PA-SWCNT-GCE (c), CoTCPc/PA-SWCNT(mix)-GCE (d) and CoTCPc-PA-SWCNT(linked)-GCE (e), all in pH 4 buffer. Figures 4.7e has a peak at around 0.4 V which is associated with Co^{III}/Co^{II} process (see inset) in comparison with literature [75]. All other electrodes, with the exception of the bare GCE show peaks in the potential range 0.89 - 0.91 V (versus Ag|AgCl). For CoTCPc **(8)**, CoTCPc/PA-SWCNT(mix) and CoTCPc-PA-SWCNT(linked), these peaks are due to the first ring oxidation of the phthalocyanine ($Co^{III}Pc^{-1}/Co^{III}Pc^{-2}$). The peak observed on the PA-SWCNT is due to the oxidation of the phenyl-amine group that is attached on the SWCNT wall [300,301]. The CV of phenyl-amine alone showed a peak at around 0.7 V (Fig. 4.8a).

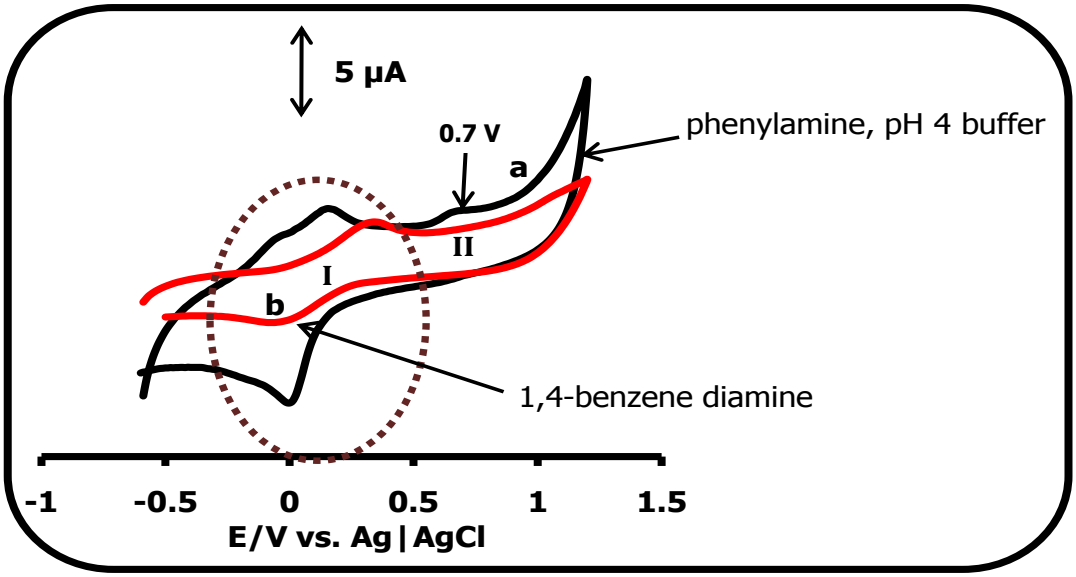

Figure 4.8: Cyclic voltammograms for (a) phenyl-amine and (b) 1,4-benzene diamine in pH 4 buffer.

Couple **I** (Fig. 4.8 a and b) is common to both phenyl-amine and 1,4-benzene diamine (BDA), while peak **II** is a characteristic oxidation peak for phenyl-amine and is absent in BDA. The reversible peak is due to the quinone-diimine units which constitute the structure of *poly*-phenyl-amine, i.e. the electro-oxidation product of phenyl-amine, Scheme 4.1.

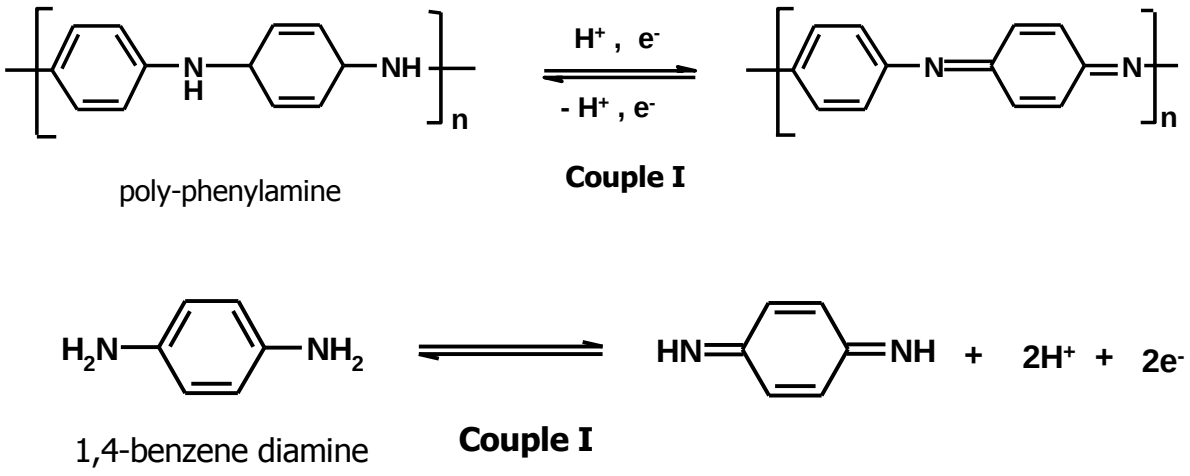

Scheme 4.1: Representative equations for couple I processes.

Couple **I** is absent in Fig. 4.7c, implying that both *poly*-phenyl-amine and quinone-diimine are absent in PA-SWCNT **(12)**. Only peak **II** at around 0.7 V is observed, showing that the phenyl-amine group is anchored on the SWCNT wall. This peak is observed at around 0.9 V on PA-SWCNTs (Fig. 4.7c).

By using the $[Fe(CN)_6]^{3-/4-}$ redox probe and applying the Randles–Sevcik Eq. 4.1, the roughness factor for CoTCPc–PA-SWCNT(linked)-GCE was found to be 5.69 (ratio of I_{pa} experimental/I_{pa} theoretical), corresponding to a real electrode area of 0.40 cm^2 (roughness factor × theoretical surface area = 0.071 cm^2). There is increased roughness for CoTCPc–PA-SWCNT(linked)-GCE relative to the bare electrode. Using Eq. 4.3, linear plots of background corrected current versus sweep rate were observed for CoTCPc, as is typical of surface-immobilized species. The surface coverage was found to be 3.25 x 10^{-10} mol cm^{-2} for CoTCPc alone. This is slightly higher than a monolayer surface coverage [295]. A value of 1.89 x 10^{-10} mol cm^{-2} was obtained for CoTCPc–PA-SWCNT(linked), Table 4.1.

4.1.4.2 EA-SWCNT

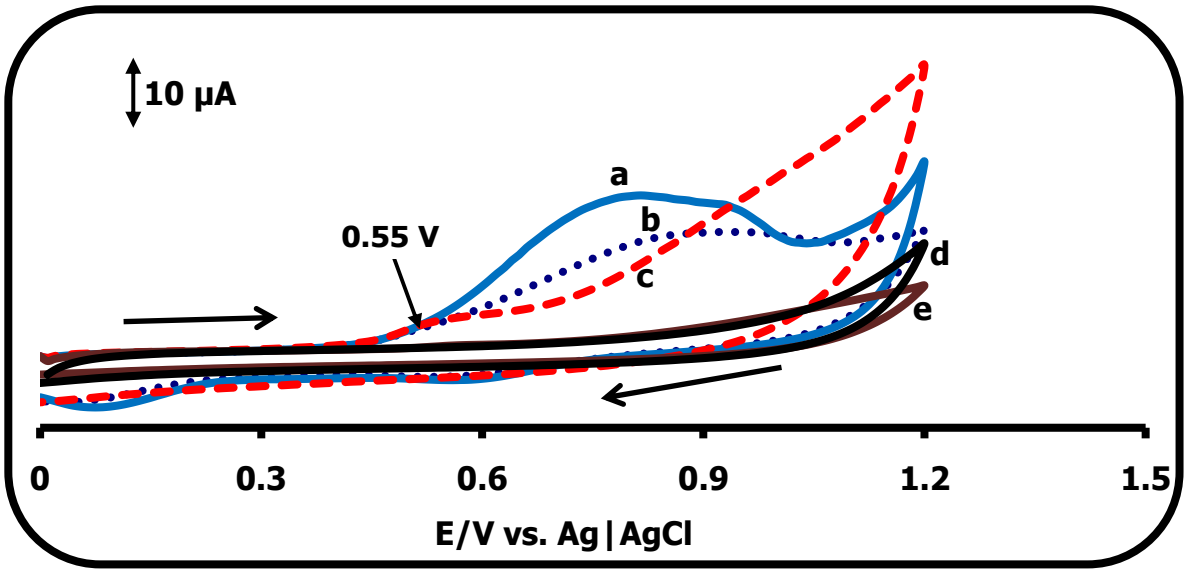

Figure 4.9: Comparative cyclic voltammograms (pH 4 buffer) for (a) CoTCPc/EA-SWCNT(mix)-GCE, (b) CoTCPc-GCE, (c) CoTCPc-EA-SWCNT(linked)-GCE and (d) EA-SWCNT-GCE and (e) bare GCE. Scan rate = 100 mV/s.

Figure 4.9 shows the cyclic voltammograms for CoTCPc/EA-SWCNT(mix)-GCE (a), CoTCPc-GCE (b), CoTCPc-EA-SWCNT(linked)-GCE (c), EA-SWCNT-GCE (d), and bare GCE (e), all in pH 4 buffer. Fig. 4.9c (for CoTCPc-EA-SWCNT(linked)) clearly shows a peak at 0.55 V which is associated with Co^{III}/Co^{II} process in comparison with literature [75]. The Co^{III}/Co^{II} oxidation peak is conspicuous because EA-SWCNT donates electrons into the Pc ring and ultimately the cobalt centre, making the oxidation of cobalt much easier compared to CoTCPc-PA-SWCNT conjugates. This peak is not very clear for CoTCPc/EA-SWCNT(mix) and CoTCPc and this can be attributed to the electron withdrawing effect of the carboxylic acid groups which makes the oxidation of cobalt very difficult. The broad peaks observed near 0.8 V are due to the ring based processes ($Co^{III}Pc^{-1}/Co^{III}Pc^{-2}$). The surface coverages for CoTCPc and CoTCPc-EA-SWCNT(linked) were estimated to be 1.47 x 10^{-10} and 1.28 x 10^{-10} mol cm^{-2} (Table 4.1), respectively, using Eq. 4.3.

4.1.5 CoMAPc and its conjugates

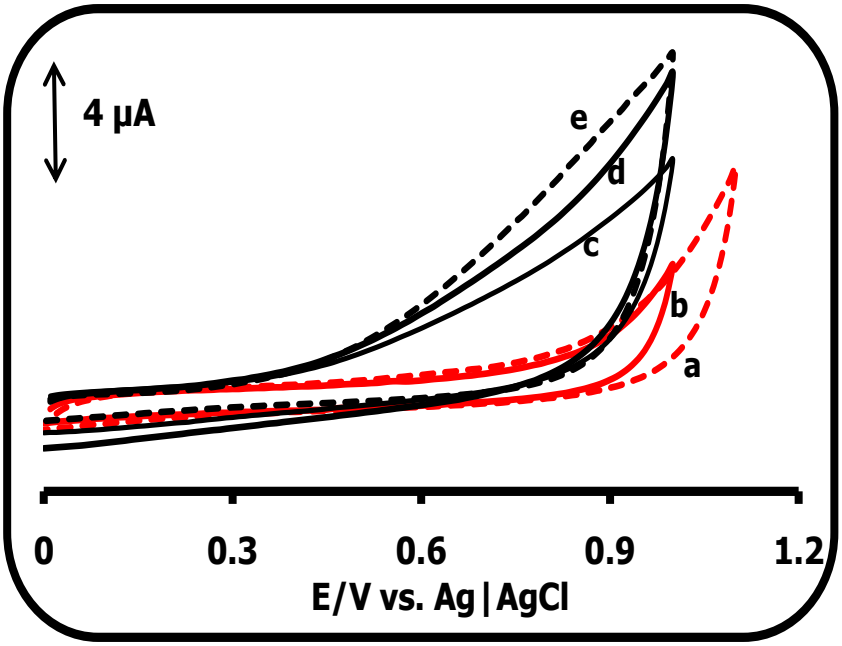

Figure 4.10: Comparative cyclic voltammograms in pH 4 buffer on: (a) bare GCE, (b) SWCNT-COOH-GCE, (c) CoMAPc-GCE, (d) CoMAPc/SWCNT-COOH(mix)-GCE and (e) CoMAPc-SWCNT(linked)-GCE. Scan rate = 100 mV/s.

Figure 4.10 shows the cyclic voltammograms for the bare GCE (a), the SWCNT-COOH-GCE (b), the CoMAPc-GCE (c), the CoMAPc/SWCNT-COOH (mix)-GCE (d) and the CoMAPc-SWCNT(linked)-GCE (e), all in pH 4 buffer. The bare GCE and the SWCNT-COOH-GCE showed no peaks as expected, but CoMAPc-GCE, CoMAPc/SWCNT-COOH(mix)-GCE and CoMAPc-SWCNT(linked)-GCE showed very broad peaks in the region of ~0.4 - ~0.8 V (versus Ag|AgCl) are most probably due to the overlap of the Co^{III}/Co^{II} and $Co^{III}Pc^{-1}/Co^{III}Pc^{-2}$ redox process [74,251]. As explained already the Co^{III}/Co^{II} process is known to be irreversible and notoriously difficult to observe for adsorbed CoPc complexes [53,100], hence its absence in these cobalt-carrying species is not surprising. However this (Co^{III}/Co^{II}) peak was clear in CoTCPc above, showing its dependence on substituents. The surface coverages for CoMAPc and CoMAPc-SWCNT(linked) were estimated to be 1.24×10^{-10} and 1.65×10^{-10} mol cm^{-2}, respectively, using Eq. 4.3 at 0.7 V.

4.1.6 CoMCPc and conjugates

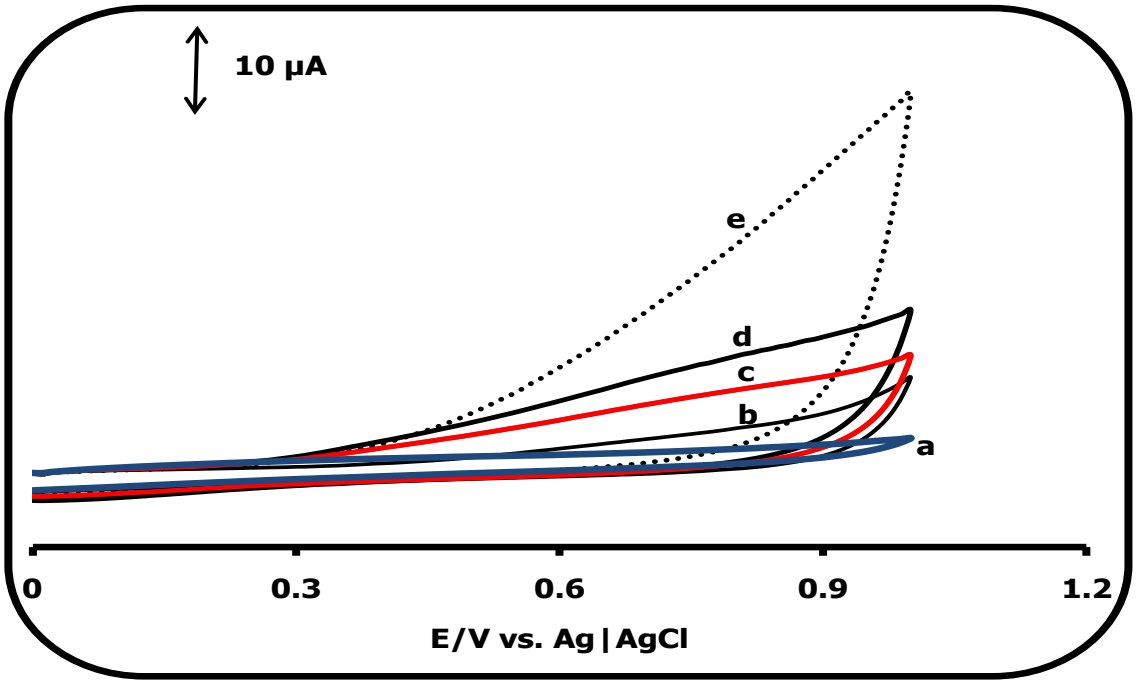

Figure 4.11: Comparative cyclic voltammograms in pH 4 buffer on: (a) bare GCE, (b) PA-SWCNT -GCE, (c) CoMCPc-GCE, (d) CoMCPc/PA-SWCNT(mix)-GCE and (e) CoMCPc-PA-SWCNT(linked)-GCE. Scan rate = 100 mV/s.

Figure 4.11 shows the cyclic voltammograms evolved on the following electrodes in pH 4 buffer: bare GCE (a), PA-SWCNT-GCE (b), CoMCPc-GCE (c), CoMCPc/PA-SWCNT(mix)-GCE (d) and the CoMCPc-PA-SWCNT(linked)-GCE (e). The bare GCE showed no peaks as expected, but as for CoMCPc-GCE, CoMCPc/PA-SWCNT(mix)-GCE and PA-SWCNT-GCE showed broad features beyond 0.6 V (versus Ag|AgCl). These broad peaks are due to the Co^{III}/Co^{II} [74,251] and a combination of Co^{III}/Co^{II} [74,251] and PA-SWCNT [300,301] peaks, for the CoMCPc and CoMCPc/PA-SWCNT(mix) electrodes, respectively. As described earlier the peak observed around these potentials on the PA-SWCNT electrode is due to the oxidation of the phenyl-amine group that is attached on the SWCNT wall [300,301]. As already discussed the Co^{III}/Co^{II} process is known to be irreversible and very difficult to observe for adsorbed CoPc complexes [53,100], hence its absence in complexes such as CoTAPc, CoMAPc and CoMCPc does not surprise. The CoMCPc-PA-SWCNT(linked) gives a broad peak which rises sharply from the rest of the voltammograms. This may be due to the presence of SWCNTs that increase the heterogeneity of the electrode surface, as stated before. The surface coverage for CoMCPc was found to be 1.41×10^{-10} mol cm^{-2}, using Eq. 4.3 at 0.8 V. As for CoMCPc, the surface coverage for CoMCPc-PA-SWCNT(linked) was estimated to be 1.36×10^{-10} mol cm^{-2}, Table 4.1.

4.2 Characterization using $[Fe(CN)_6]^{3-/4-}$ redox probe

4.2.1 CoTAPc and its conjugates

The effects of changes in scan rate on the magnitude of the cathodic to anodic peak potential separations (ΔEp) were studied for CoTAPc and its conjugates. The trends in the behaviour of the MTAPcs and their conjugates in the presence of the $[Fe(CN)_6]^{3-/4-}$ redox probe were similar, hence information on FeTAPc and NiTAPc is not shown in this thesis.

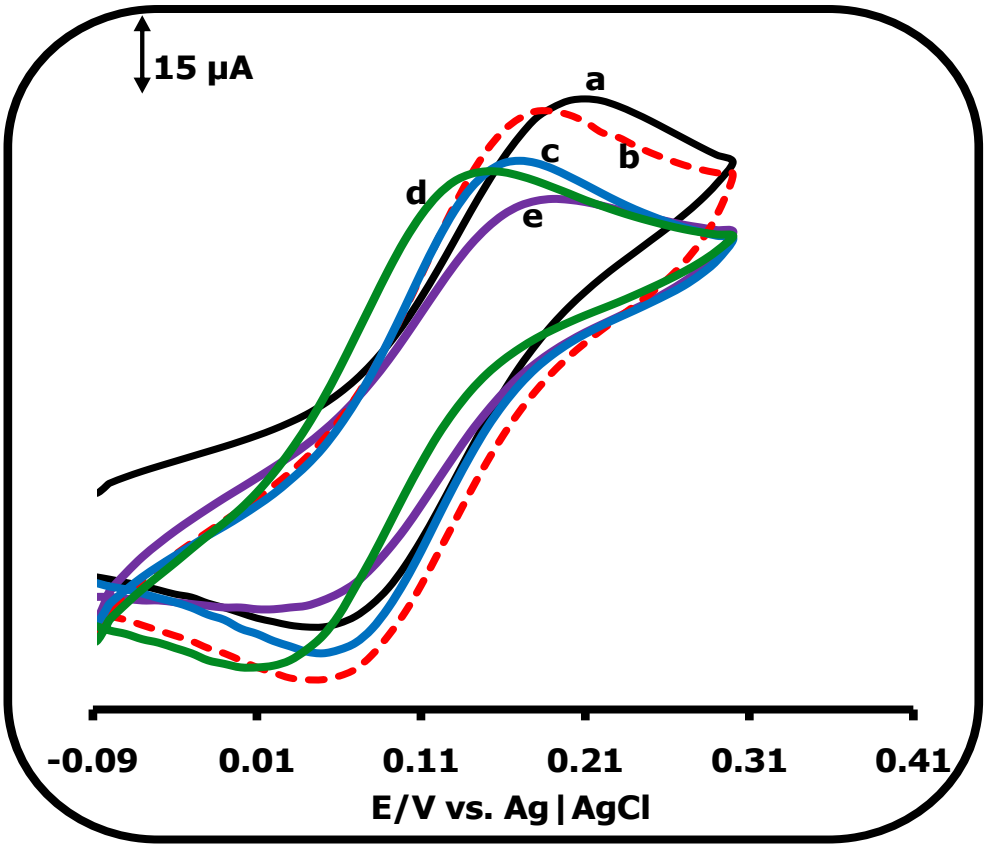

Figure 4.12: Comparative cyclic voltammetric profiles of 1 mM of $[Fe(CN)_6]^{3-/4-}$ in 0.1 M of KCl by using (a) SWCNT-COOH (13), (b) CoTAPc (7a), (c) CoTAPc/SWCNT-COOH(mix), (d) CoTAPc-SWCNT(linked) (14), and (e) bare GCE. Scan rate = 100 mVsec^{-1}.

Figure 4.12 shows comparative CVs for the modified glassy carbon electrodes used in this work in the presence of the $[Fe(CN)_6]^{3-/4-}$ redox couple. The cathodic to anodic peak potential separation (ΔE_p) of the various surface modifications (a) SWCNT-COOH-GCE, (b) CoTAPc-GCE, (c) CoTAPc/SWCNT-COOH(mix)-GCE, (d) CoTAPc-SWCNT(linked)-GCE and (e) bare GCE are 160, 140, 130, 110 and 170 mV (versus Ag|AgCl), respectively, at a scan rate of 100 mV/s. The ΔE_p values ranged from 65 mV (for bare GCE) to 130 mV (SWCNT-COOH) at a lower scan rate of 20 mV/s. Thus at 20 mV/s scan rate, the ΔE_p value for the bare GCE is close to the Nernstian value of 59 mV for a one electron transfer reversible system and for the modified electrodes the processes are quasi-reversible. Of the modified electrodes, CoTAPc-SWCNT(linked) showed the lowest ΔE_p value (110 mV at 100 mV/s)

confirming its improved electron transfer kinetics compared with the rest of the modified electrodes. Irrespective of the changes in scan rate it was observed that the order of electron transfer remained the same.

4.2.2 CoTCPc and its conjugates

4.2.2.1 PA-SWCNT

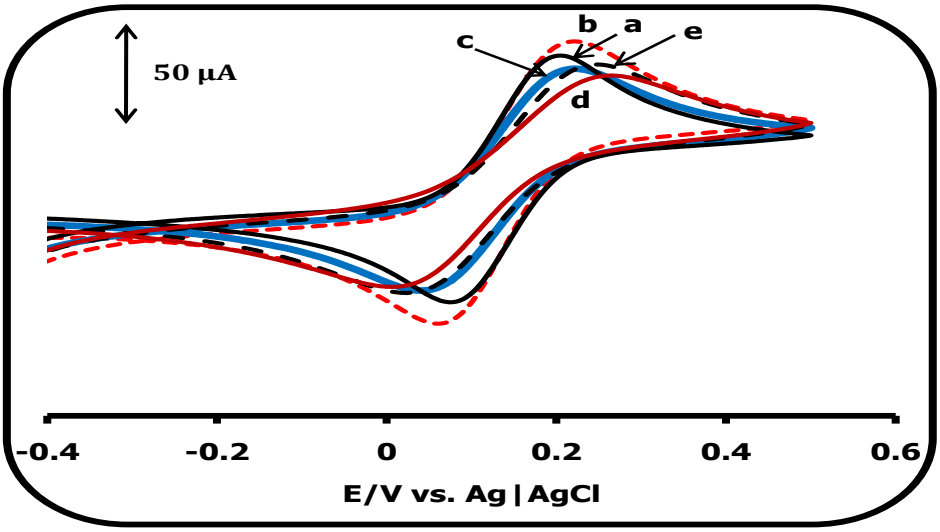

Figure 4.13: Comparative cyclic voltammetric evolutions of 1 mM of $[Fe(CN)_6]^{3-/4-}$ in 0.1 M of KCl using bare GCE (a), CoTCPc–PA-SWCNT(linked)-GCE (b), CoTCPc/PA-SWCNT(mix)-GCE (c), PA-SWCNT-GCE (d) and CoTCPc-GCE (e). Scan rate = 100 mV/s.

Figure 4.13 shows comparative cyclic voltammograms for the modified glassy carbon electrodes used in this work in the presence of the $[Fe(CN)_6]^{3-/4-}$ redox probe. The ΔE_p for bare GCE (a), CoTCPc–PA-SWCNT(linked)-GCE (b), CoTCPc/PA-SWCNT(mix)-GCE (c), PA-SWCNT (d) and CoTCPc-GCE (e) are 128 mV, 156 mV, 180 mV, 250 mV and 216 mV (versus Ag | AgCl), respectively, at a scan rate of 100 mV/s. In terms of electron transfer efficiency, the order is as follows: bare GCE > CoTCPc–PA-SWCNT(linked)-GCE > CoTCPc/PA-SWCNT(mix)-GCE > CoTCPc-GCE > PA-SWCNT-GCE. This confirms the good electron transfer kinetics for the conjugate compared to the rest of the modified electrodes, as observed for CoTAPc with the exception of the bare GCE.

4.2.2.2 EA-SWCNT

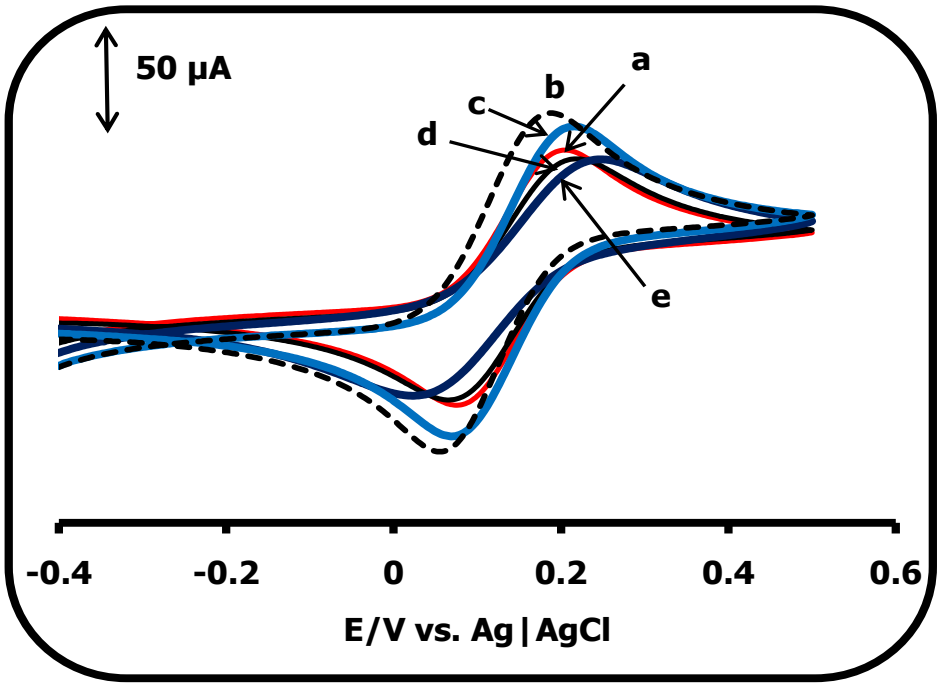

Figure 4.14: Comparative cyclic voltammetric evolutions of 1 mM of $[Fe(CN)_6]^{3-/4-}$ in 0.1 M of KCl using bare GCE (a), CoTCPc–EA-SWCNT(linked)-GCE (b), CoTCPc/EA-SWCNT(mix)-GCE (c), EA-SWCNT-GCE (d) and CoTCPc-GCE (e), Scan rate = 100 mV/s.

Figure 4.14 shows comparative CVs for the modified glassy carbon electrodes used in this work in the presence of the $[Fe(CN)_6]^{3-/4-}$ redox probe. The ΔE_p for bare GCE (a), CoTCPc–EA-SWCNT(linked)-GCE (b), CoTCPc/EA-SWCNT(mix)-GCE (c), EA-SWCNT (d) and CoTCPc-GCE (e) are 128 mV, 124 mV, 146 mV, 150 mV and 216 mV (versus Ag|AgCl), respectively, at a scan rate of 100 mV/s. The order in terms of electron transfer efficiency, is therefore CoTCPc–EA-SWCNT(linked)-GCE > bare GCE > CoTCPc/EA-SWCNT(mix)-GCE > EA-SWCNT-GCE > CoTCPc-GCE, confirming the good electron transfer kinetics for the linked complex compared to the rest of the modified electrodes, including the bare GCE. As was the case with PA, the formal potential for CoTCPc–EA-SWCNT(linked)-GCE is more negative than the other modifiers possibly due to the presence of linkages between the MPc and the SWCNTs which makes electron exchange between the redox probe and electrode modifier much faster.

4.2.3 CoMAPc and its conjugates

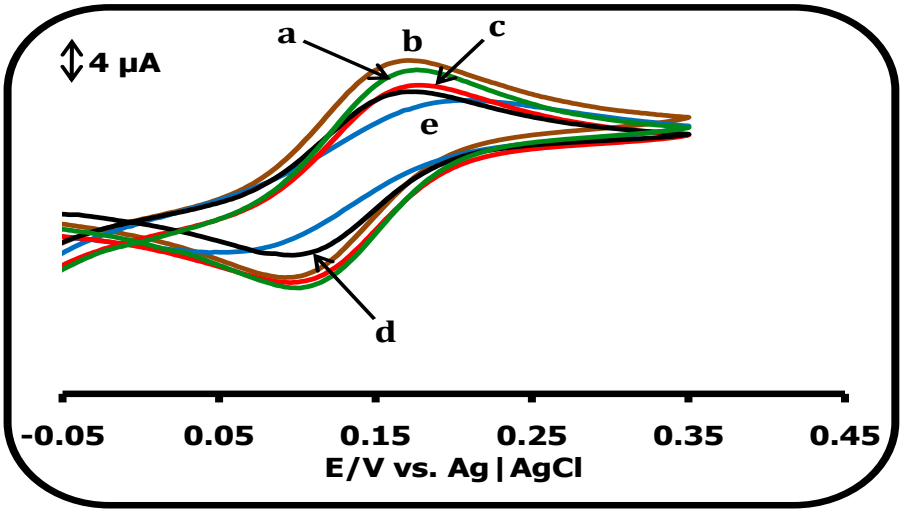

Figure 4.15: Comparative cyclic voltammetric evolutions of 1 mM of $[Fe(CN)_6]^{3-/4-}$ in 0.1 M of KCl using bare GCE (a), CoMAPc-SWCNT(linked)-GCE (b), CoMAPc-GCE (c), SWCNT-COOH-GCE (d) and CoMAPc/SWCNT-COOH(mix)-GCE (e), Scan rate = 20 mV/s.

Figure 4.15 shows comparative cyclic voltammograms for the modified glassy carbon electrodes used in this work in the presence of the $[Fe(CN)_6]^{3-/4-}$ redox probe. The ΔEp for bare GCE (a), CoMAPc-SWCNT(linked)-GCE (b), CoMAPc-GCE (c), SWCNT-COOH-GCE (d) and CoMAPc/SWCNT-COOH(mix)-GCE (e) are 66 mV, 68 mV, 74 mV, 70 mV and 116 mV (versus Ag|AgCl), respectively, at a scan rate of 20 mV/s. ΔEp value for CoMAPc-SWCNT(linked)-GCE is close to the Nernstian value of 58 mV for a one-electron process [235] and similar to that of the bare GCE, confirming their good electron transfer kinetics. The lower ΔEp for CoMAPc-SWCNT(linked)-GCE (compared to the rest of the modified electrodes) is possibly due to the presence of linkages between the CoMAPc **(9)** and SWCNT-COOH **(13)** as well as their good alignment on the electrode surface since they are monosubstituted, which makes electron exchange between the redox probe and electrode modifier much faster.

4.2.4 CoMCPc and its conjugates

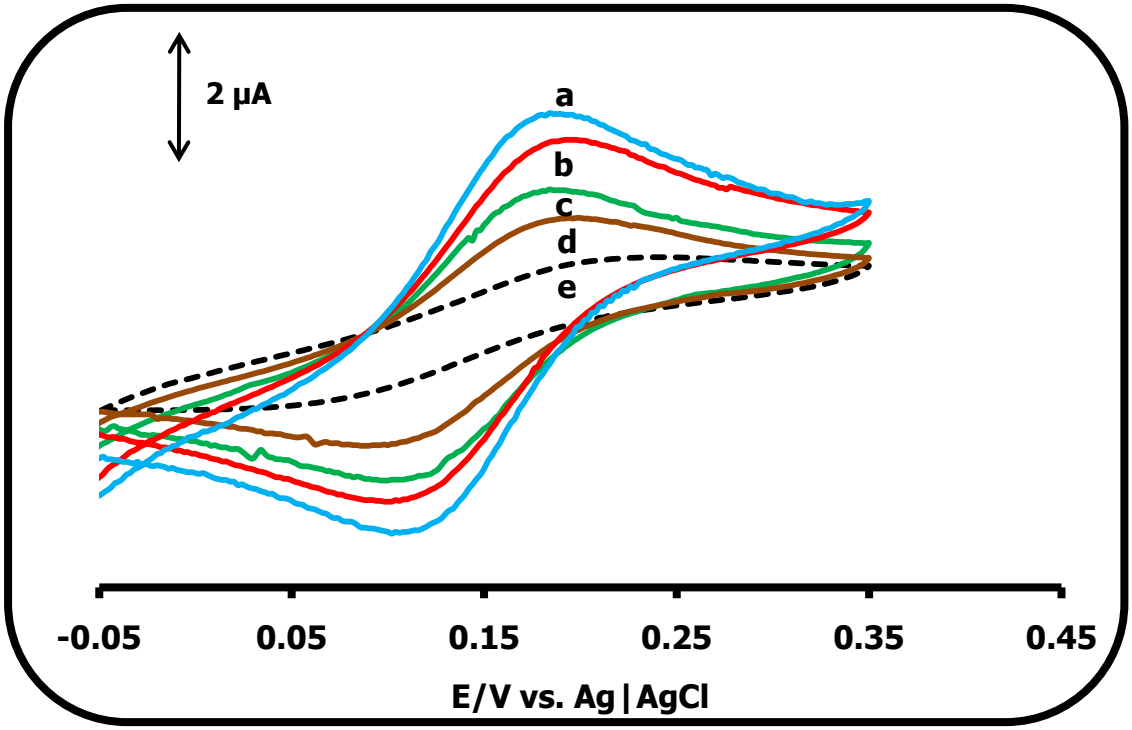

Figure 4.16: Comparative cyclic voltammetric evolutions of 1 mM of $[Fe(CN)_6]^{3-/4-}$ in 0.1 M of KCl using bare GCE (a), PA-SWCNT-GCE (b) CoMCPc-PA-SWCNT(linked)-GCE (c), CoMCPc/PA-SWCNT(mix)-GCE (d) and CoMCPc-GCE (e). Scan rate = 20 mV/s.

Figure 4.16 shows the cyclic voltammograms which evolved on the various modified GCEs using 1 mM $[Fe(CN)_6]^{3-/4-}$ in 0.1 M KCl as a redox probe. The ΔEp for bare GCE (a), PA-SWCNT-GCE (b), CoMCPc-PA-SWCNT(linked)-GCE (c), CoMCPc/PA-SWCNT(mix)-GCE (d) and CoMCPc-GCE (e), are 54 mV, 66 mV, 60 mV, 78 mV and 172 mV (versus Ag|AgCl), respectively, at a scan rate of 20 mV/s. ΔEp values for the CoMCPc-PA-SWCNT(linked), bare GCE and PA-SWCNT are close to the Nernstian value of 58 mV for a one-electron process [235], confirming their good electron transfer kinetics. The order in terms of the electron transfer kinetics is as follows: bare GCE > CoMCPc-PA-SWCNT(linked)-GCE > PA-SWCNT-GCE > CoMCPc/PA-SWCNT(mix)-GCE » CoMCPc-GCE. The large ΔEp for CoMCPc-GCE implies that on its own, it has poor electron transfer properties.

However, when coupled with SWCNTs, its catalytic properties are activated, as evidenced by the good electron kinetics shown by the CoMCPc-PA-SWCNT conjugate (Fig. 4.16). This is explained in terms of the electron donating nature of the PA-SWCNTs (which reduce the redox potentials for the metal centre) as well as the good electron transfer properties of the SWCNTs and encouraged by the presence of the amide bridge. The bridge facilitates the easy flow of electrons to and from the linked CoMCPc molecule. Improved electron transfer kinetics is also a result of the nanostructured sizes of the conjugates which enables them to provide a larger surface area for the transfer of electrons, also monosubstituted as for CoMAPc.

4.9 Conclusion

Cyclic voltammetry showed the differences in behaviour of the modified electrodes in pH 4 buffer solutions. By monitoring peak behaviours with changes in scan rate, the electrode surface coverages of the modifiers were calculated. Through the use of the $Fe(CN)_6^{3-/4-}$ redox probe, the different electron transfer abilities of the modified electrodes were observed. CoTCPc **(8)** and CoMCPc **(10)** showed very poor electron transfer properties, as evidenced by their large ΔEp values. The $Fe(CN)_6^{3-/4-}$ redox probe was also used to obtain the surface areas and surface roughness factors for the modified electrodes. The presence of SWCNTs in conjugates caused broadening of peaks.

CHAPTER 5

ELECTROCATALYSIS

This chapter deals with the electrochemical behaviours of the MPcs, SWCNTs, MPc/SWCNT(mix) and MPc-SWCNT(linked) modified electrodes towards 2-ME, amitrole and diuron.

Preamble

CoTAPc-SWCNT(linked) and FeTAPc-SWCNT(linked) were employed as modifiers for all analytes, thus allowing for the study of the effect of the central metal on catalysis and for comparison of all analytes on one electrode. Since the analysis of 2-ME on CoPc modified electrodes is well documented, it was not studied further with the rest of the electrodes containing CoPc derivatives (i.e. CoTCPc, CoMAPc and CoMCPc). However it was studied on NiTAPc-SWCNT(linked), since 2-ME has never been studied on NiPc derivatives. *Poly*-Ni(OH)TAPc was used as a modifier without SWCNTs on diuron only, with the aim of testing the role of the Ni-O-Ni bridges on an analyte which is quite different from what it has been employed for before (mainly phenols and 2-ME).

Cyclic voltammetry (CV) was employed on all the electrodes used in this study, while chronoamperometry (CA) was used on all electrodes except for the CoTAPc-SWCNT(linked). CV was employed for Tafel slopes and electron transfer coefficient (**α**) and in some cases these parameters were obtained from RDE for comparison. RDE was also employed for rate constants *(k)* for comparison with results from CA in some cases. CA was also used in the determination of diffusion coefficients *(D,* for amitrole and diuron only*)* and limits of detection for the analytes. In some cases electrochemical impedance spectroscopy (EIS) was employed to determine the efficiency of charge transfer on electrode surfaces in the presence of an analyte.

Table 5.1: Electrodes employed for analyses

Electrode	Amitrole	Diuron	2-ME
Poly-NiTAPc	NO	YES	NO
Poly-Ni(OH)TAPc	NO	YES	NO
CoTAPc-SWCNT(linked)	YES	YES	YES
FeTAPc-SWCNT(linked)	YES	YES	YES
NiTAPc-SWCNT(linked)	NO	YES	YES
CoTCPc-PA-SWCNT(linked)	YES	YES	NO
CoTCPc-EA-SWCNT(linked)	YES	YES	NO
CoMAPc-SWCNT(linked)	YES	YES	NO
CoMCPc-PA-SWCNT(linked)	YES	YES	NO

Table 5.2: Parameters for amitrole, diuron and 2-ME on different electrodes

Complex	Analyte	Ep/V vs. Ag|AgCl	Tafel slope	α	k/M^{-1} s^{-1}	LOD /μM	Sensitivity/ A mol^{-1} L cm^{-2}	Stability (as % drop from cycle 1 to 2)
Poly-NiTAPc	Diuron	1.14	-	-	-	-	-	36
Poly-Ni(OH)TAPc	Diuron	1.08	192	0.69	5.91×10^2	0.33	12.90	6
CoTAPc-SWCNT(linked)	Amitrole	0.98	174	0.66	2.50×10^4	0.12	0.78	20
FeTAPc-SWCNT(linked)	Amitrole	0.88	243	0.76	4.55×10^3 **(5.41×10^3)**	0.22	9.30	8
	Diuron	0.92	199	0.70	1.79×10^4 **(4.38×10^4)**	0.26	9.40	6
CoTCPc-PA-SWCNT (linked)	Amitrole	0.82	197 **(183)**	0.70 **(0.68)**	3.58×10^3	0.14	0.51	44
	Diuron	0.87	166	0.65	4.40×10^3	0.18	0.42	46
CoTCPc-EA-SWCNT (linked)	Amitrole	0.83	237 **(238)**	0.75 **(0.75)**	1.20×10^3	0.10	0.75	10
	Diuron	0.85	226	0.74	5.88×10^4	0.16	0.82	9
CoMAPc-SWCNT(linked)	Amitrole	0.78	230 **(239)**	0.74 **(0.75)**	1.09×10^5 **(1.62×10^5)**	0.10	6.76	21
	Diuron	0.82	237 **(228)**	0.75 **(0.74)**	1.43×10^5 **(2.11×10^5)**	0.13	5.63	25
CoMCPc-PA-SWCNT (linked)	Amitrole	0.79	200	0.71	1.83×10^6	0.14	5.10	18
	Diuron	0.85	180	0.67	1.99×10^6	0.20	3.70	37
CoTAPc-SWCNT(linked)	2-ME	0.60	37 **(43)**	0.40 **(0.63)**	3.80×10^3	0.12	2.82	6
FeTAPc-SWCNT(linked)	2-ME	0.95	93	0.37	3.28×10^3	0.11	2.12	12
NiTAPc-SWCNT(linked)	2-ME	0.95	86	0.31	2.95×10^3 **(2.06×10^3)**	0.15	2.53	15

values in **bold** obtained from RDE studies

5.1 *Poly*-Ni(OH)TAPc and *poly*-NiTAPc

5.1.1 CV studies

Table 5.1 shows that these electrodes were used only for diuron. CV and CA were employed for this study. Figure 5.1 compares cyclic voltammograms of 1 x 10^{-3} M diuron (in pH 4 acetate buffer) on (a) the bare GCE, (b) *poly*–NiTAPc-GCE and (c) *poly*–Ni(OH)TAPc-GCE. Electro-catalysis is evidenced by a lowering of potential and increase in currents. A large increase in current is observed on *poly*–Ni(OH)TAPc-GCE compared to the bare GCE and the *poly*-NiTAPc-GCE. In turn *poly*-NiTAPc-GCE shows higher currents compared to bare GCE, Fig. 5.1a. The oxidation potential of diuron on *poly*-Ni(OH)TAPc-GCE occurred at 1.08 V relative to 1.14 V (Table 5.2) on the *poly*–NiTAPc-GCE, an over-potential difference of 60 mV. The bare GCE had lower currents for diuron detection, but at about the same potential as *poly*-Ni(OH)TAPc, Fig. 5.1. Thus in terms of catalytic currents the trend for the oxidation of diuron is as follows: *poly*–Ni(OH)TAPc-GCE > *poly*–NiTAPc-GCE > bare GCE. In terms of potential the order is: *poly*–Ni(OH)TAPc-GCE ~ bare GCE < *poly*–NiTAPc-GCE. However, the onset of the diuron peak on *poly*–Ni(OH)TAPc-GCE occurs at a lower potential (Fig. 5.1) compared to bare GCE and *poly*–NiTAPc-GCE, confirming to effectiveness of the former for diuron oxidation.

Peak **I** (0.5 V) on the *poly*–NiTAPc-GCE, Fig. 5.1 (see also Fig. 4.5c), is due to redox processes on the Pc ring. Peak **III** for *poly*-Ni(OH)TAPc is due to Ni^{III}TAPc reduction process as observed in other studies [79]. The absence of the anodic peak of the Ni^{III}/Ni^{II} processes for *poly*-Ni(OH)TAPc on the forward scan suggests that the formed Ni^{III} species are involved in the initial oxidation of diuron. The fact that there is a return peak (cathodic) for detection shows that diuron is incapable of reducing the entire Ni^{III} species [236] or diuron could be reversibly bound to the Ni^{III} metal centre during the first scan. Oxidation of diuron (peak **II** in Fig. 5.1) occurs at the same potential as the first ring oxidation (process **III** in Fig. 4.6b), indicating that it is the $Ni^{III}(OH)TAPc^{-1}$ species that are involved in the catalytic oxidation of diuron. Having established the superiority of the *poly*-Ni(OH)TAPc, it was employed for the rest of the studies in this section.

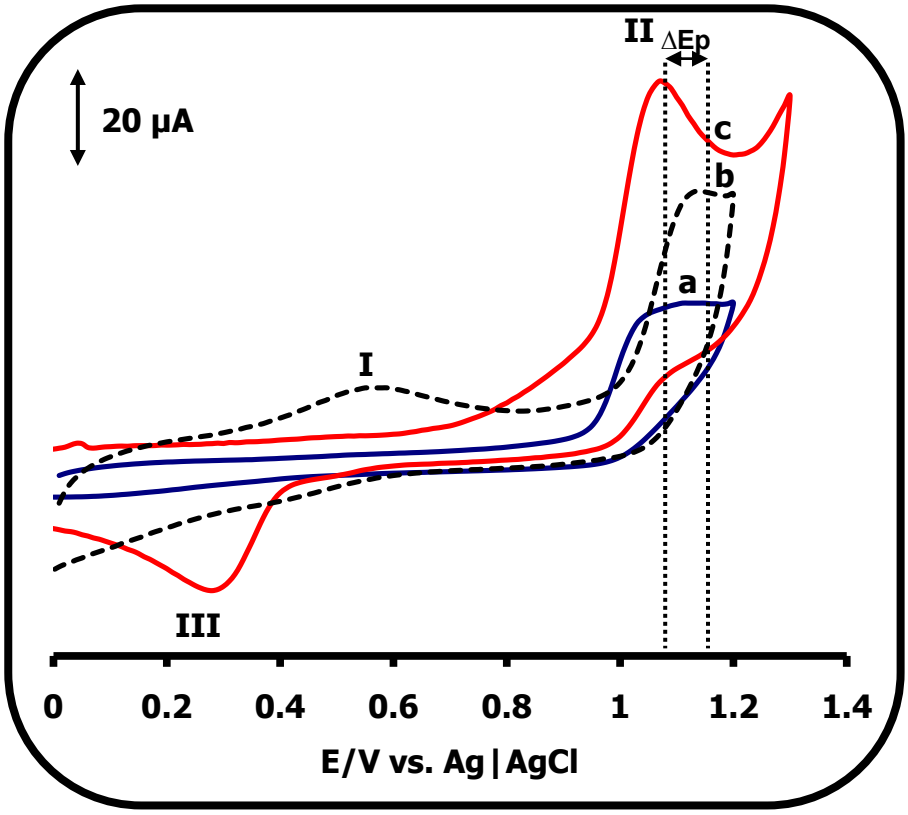

Figure 5.1: Cyclic voltammograms of (a) bare GCE, (b) *poly*-NiTAPc-GCE, and (c) *poly*-Ni(OH)TAPc-GCE in 1 x 10^{-3} M diuron (pH 4 acetate buffer). Scan rate = 100 mV/s.

Figure 5.2 shows the effect of continuous scanning on the cyclic voltammograms for the detection of diuron (only scans 1, 2, 5 and 15 are shown) on *poly*–Ni(OH)TAPc-GCE. While there is no anodic peak for the Ni^{III}/Ni^{II} couple during the first scan, for the reasons provided above, the anodic peak appears on second scan and increases with scan number and stabilizes after cycle 15. The cathodic peak also increases with scan number, but stabilizes after scan number 2. The appearance of the Ni^{III}/Ni^{II} process suggests that this process does not catalyze the oxidation of the products obtained on oxidizing diuron. The cathode component is therefore not much affected by continuous scanning, an observation noted by Berrios et al [302] in their studies with chlorophenols. A new peak is formed at -0.6 V due to the reduction of the oxidation products of diuron. Peak B is due to the oxidation of diuron. The intensity of this peak decreases with the increase in the number of scans, an indication of the passivation of the electrode surface by the

diuron oxidation products. There is also an appearance of a new peak, A', in Fig. 5.2 which is not present during the first scan. This peak is thus associated with the oxidation of diuron oxidation products formed during the first scan. Peak D is in the region of Ni^{II}/Ni^{I} reduction process and it increases during the first scan, and thereafter decreases. Peak E represent the first ring reduction ($Ni^{I}Pc^{-2}$/ $Ni^{I}Pc^{-3}$) and it increases with the number of scans.

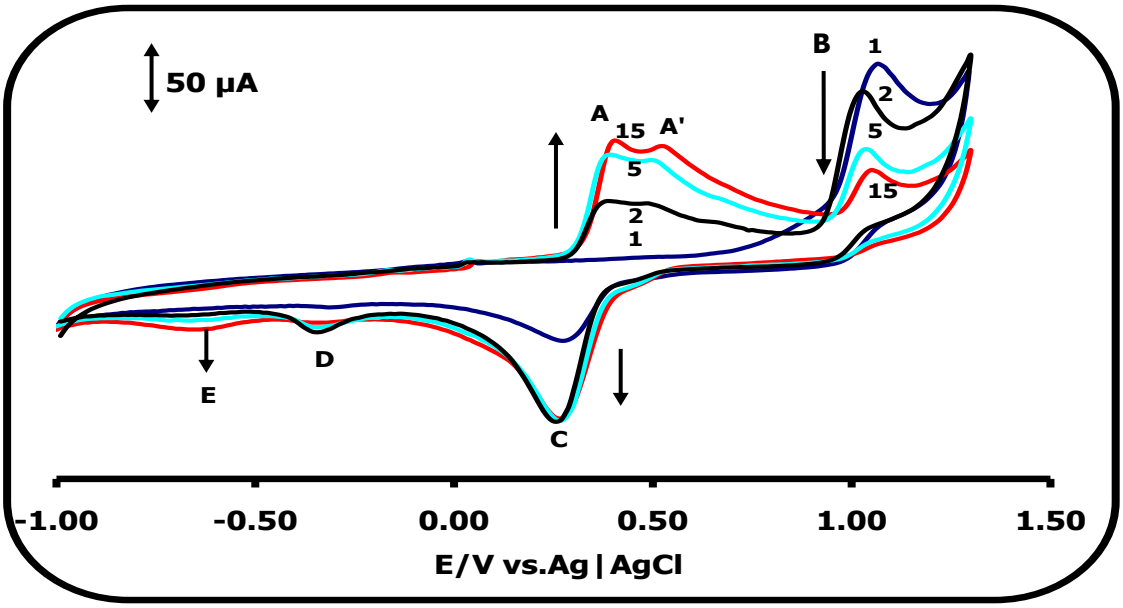

Figure 5.2: Cycles 1, 2, 5 and 15 showing the peak behaviour of *poly*–Ni(OH)TAPc-GCE in 1 x 10^{-3} M diuron (in pH 4 buffer). Scan rate = 100 mV/s.

5.1.2 pH effects

pH influenced the determination of diuron on GCE and on the modified electrodes. There was a shift in peak potentials to negative values with increase in pH, for process **II** (in Fig. 5.1c) as shown in Fig. 5.3. The slope of the plot in Fig. 5.3 is 58.6 mV/pH, indicating a transfer of one electron per proton. Scheme 5.1 represents the proposed one:one electron-proton process [265] leading to the formation of the dimer. The highest oxidation currents were also observed at pH 4, hence this pH was employed for all studies.

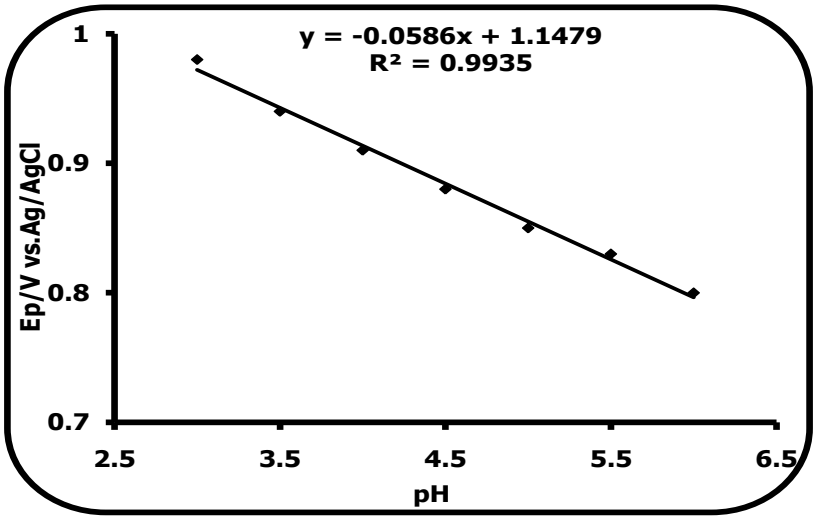

Figure 5.3: Plot of peak potential against pH for the detection of 0.1 x 10^{-3} M diuron on *poly*-Ni(OH)TAPc-GCE.

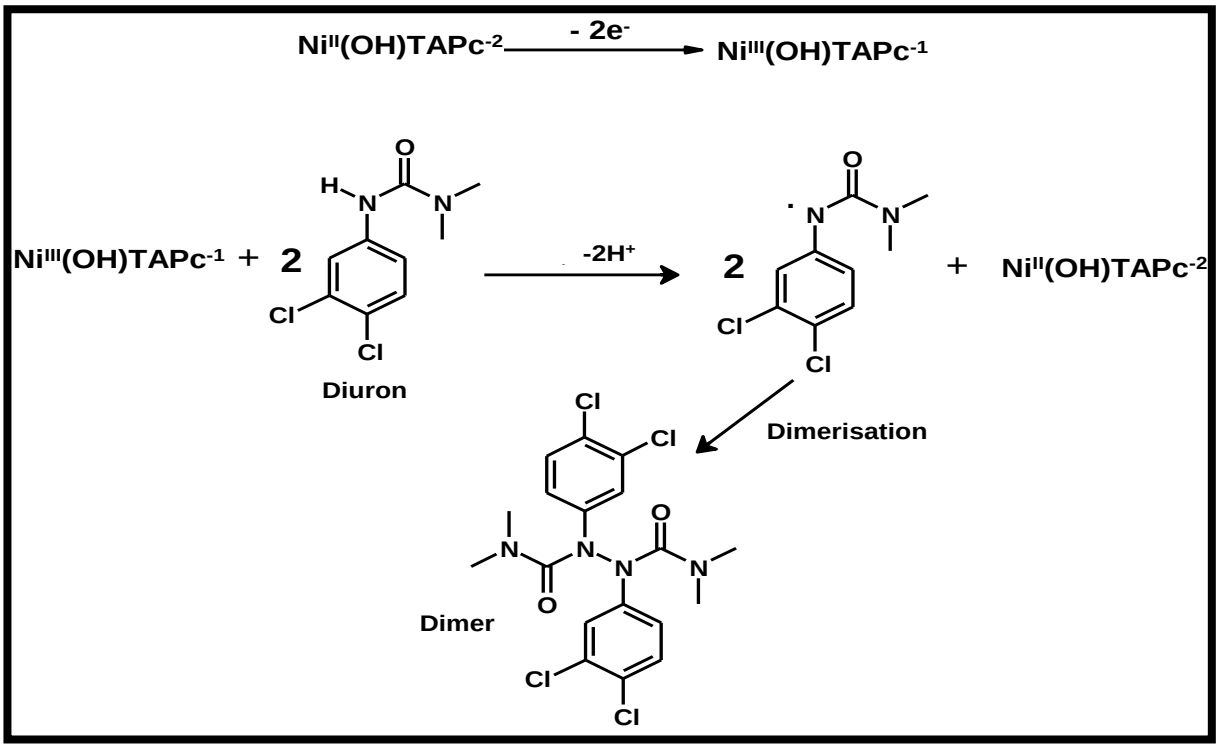

Scheme 5.1: Mechanism for the electrocatalysis of diuron on *poly*-Ni(OH)TAPc-GCE.

5.1.3 Stability

Figure 5.4 shows the change in the peak current of diuron with increase in the number of scans. The currents for *poly*–Ni(OH)TAPc-GCE stabilized at 23% of the

initial current while *poly*–NiTAPc-GCE and bare GCE stabilized at 52% and 63% of their initial currents, respectively. The drop from the first scan to the second scan was 6%, 36% and 43% for *poly*–Ni(OH)TAPc-GCE, poly–NiTAPc-GCE (Table 5.2) and the bare GCE, respectively, an indication that *poly*–Ni(OH)TAPc-GCE is more resistant to passivation due to oxidation products. However, the electrode is easily regenerated completely by rinsing in methanol and continuous cyclisation (using cyclic voltammetry) in pH 4 acetate buffer. The presence of л-л interactions between *poly*-Ni(OH)TAPc and the GCE increases the stability of the electrode. Under continual use, the electrode is stable for up to a period of 3 months if stored in pH 4 acetate buffer.

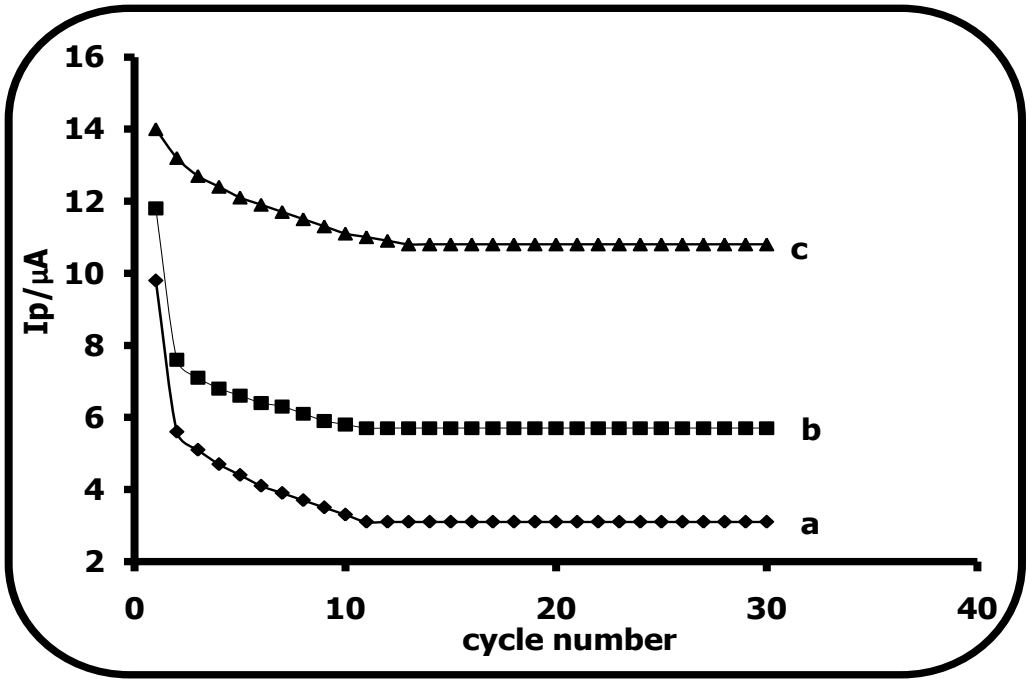

Figure 5.4: Plot of the change in peak current, I_p, versus cycle number for (a) bare GCE, (b) *poly*-NiTAPc-GCE and (c) *poly*-Ni(OH)TAPc-GCE in 80 μM diuron in pH 4 buffer. Scan rate = 100 mV/s.

5.1.4 Tafel slopes

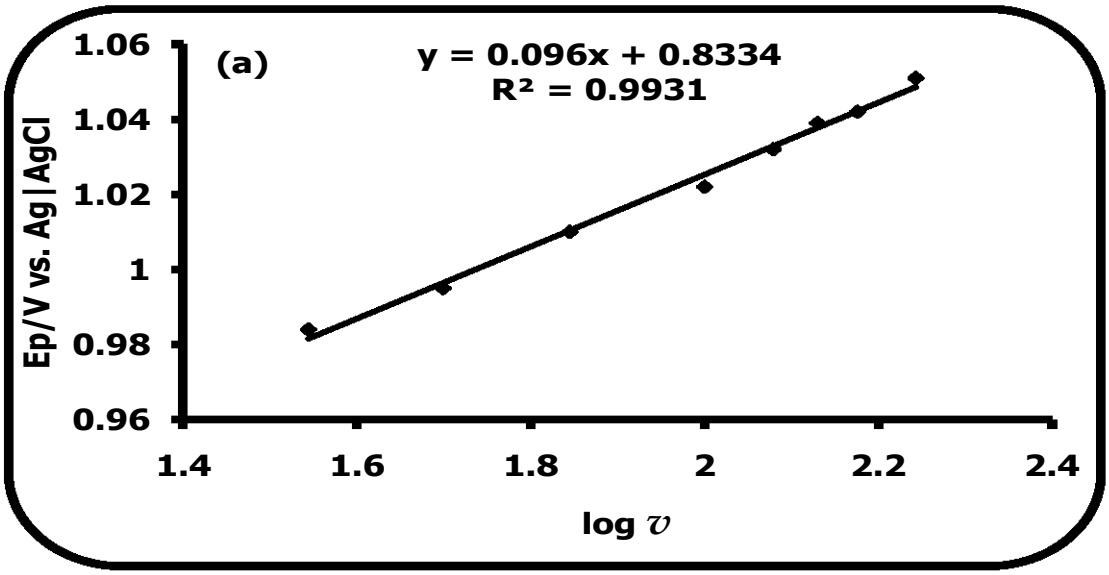

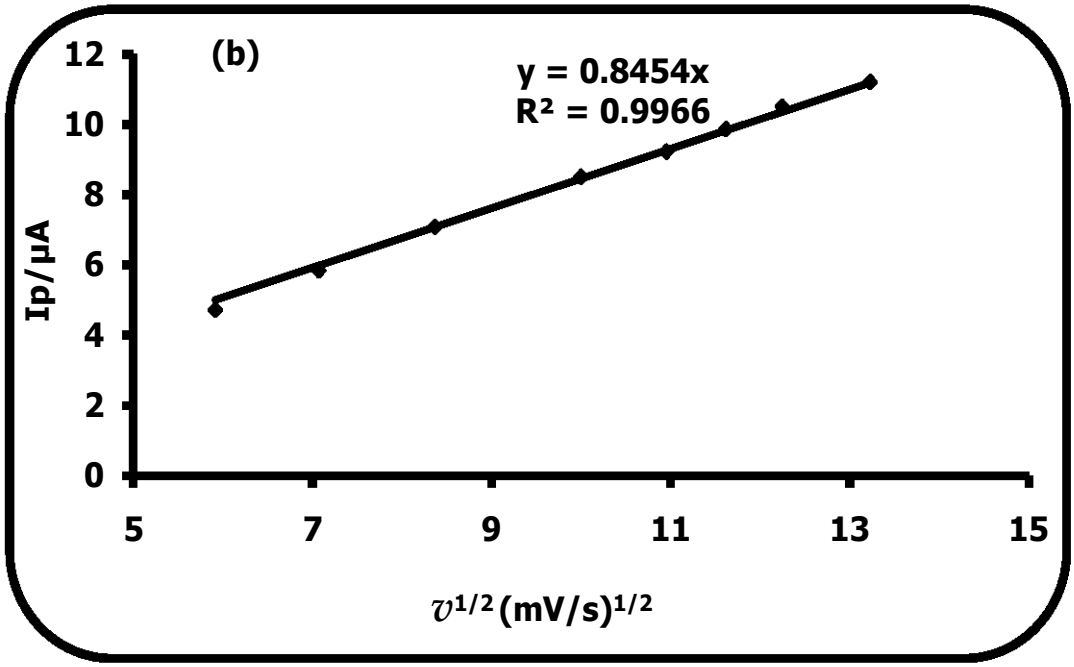

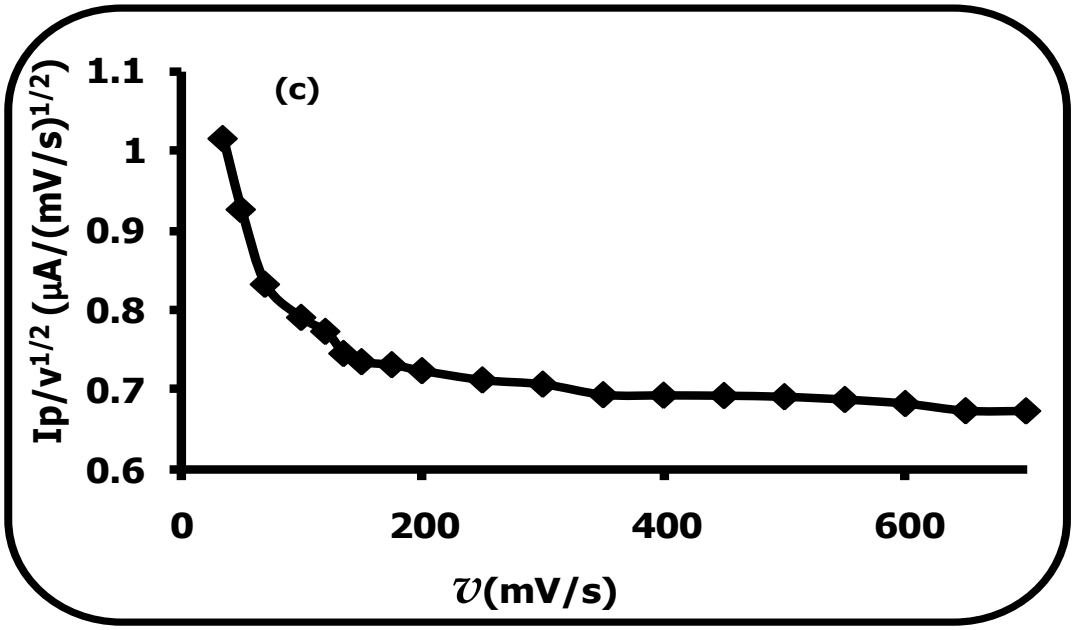

Figure 5.5: Plot of (a) peak potential versus log v, (b) peak current versus square root of sweep rate and (c) sweep rate normalized current versus sweep rate, for 1 x 10^{-3} M diuron in pH 4 buffer.

Figure 5.5a shows that the peak potentials increased with scan rate (log v), thus indicating the chemical irreversibility of the diuron electro-catalytic oxidation process. The Tafel slope for an irreversible diffusion controlled catalytic process was obtained using Eq. 5.1 [245].

$$E_p = \frac{2.303RT}{2(1-\alpha)n_\alpha F}\log v + K \qquad (5.1)$$

where '**α**' is the transfer coefficient, n_α is the number of electrons involved in the rate determining step, v is the scan rate, K is a constant, T is temperature and R is the gas constant. From the plot of E_p versus log v, a Tafel slope of 192 mV/decade was obtained. Tafel slopes this high have no kinetic meaning but could indicate a passivation phenomena occurring on the electrode surface. Tafel slopes much greater (> 240 mV/decade) than the normal 30-120 mV/decade are known [97, 257,303,304] and have been related either to chemical reactions coupled to electrochemical steps [97] or to substrate-catalyst interactions in a reaction intermediate [257,303,304]. Using the slope of the plot of E_p versus log v the value of

'**α**' was estimated to be 0.69, though this value is not too reliable due to the high Tafel slope. Figure 5.5b shows a linear relationship between the peak current and square root of the scan rate, indicating that the diuron electro-catalytic oxidation is diffusion controlled. A plot of sweep-rate normalized current density ($I_p\nu^{-1/2}$) versus the sweep rate (Fig. 5.5c), exhibited a typical shape indicative of a catalytic process with an electrochemical reaction preceding a chemical reaction [305].

5.1.5 Chronoamperometric studies

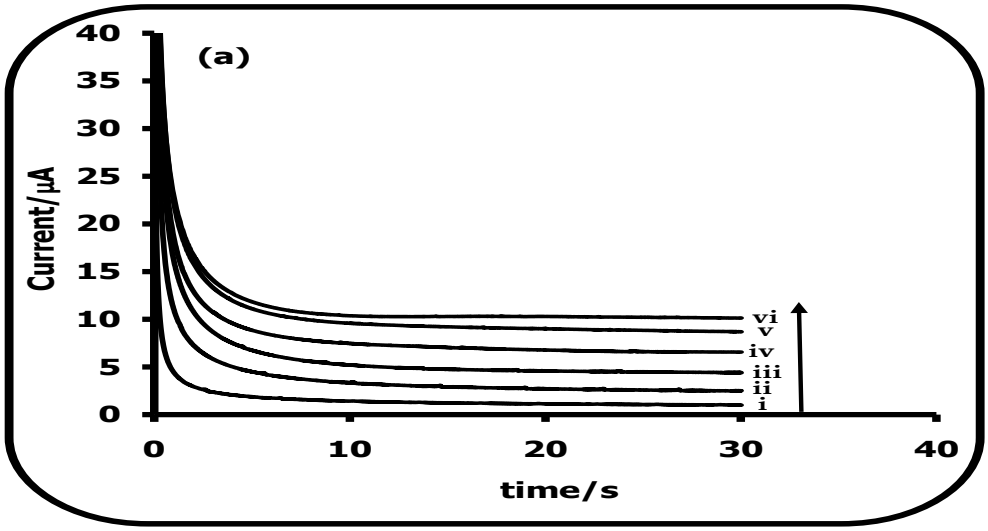

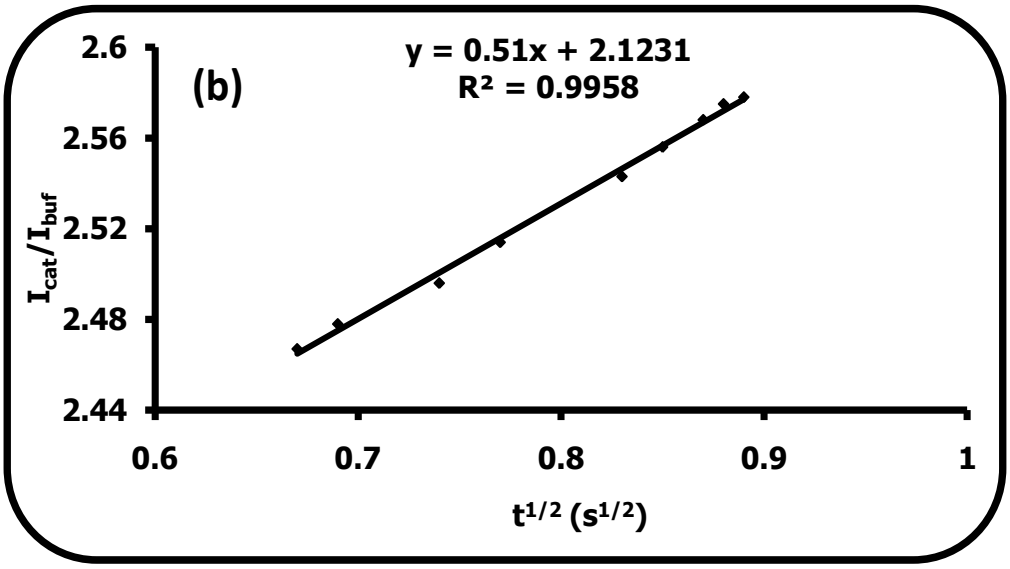

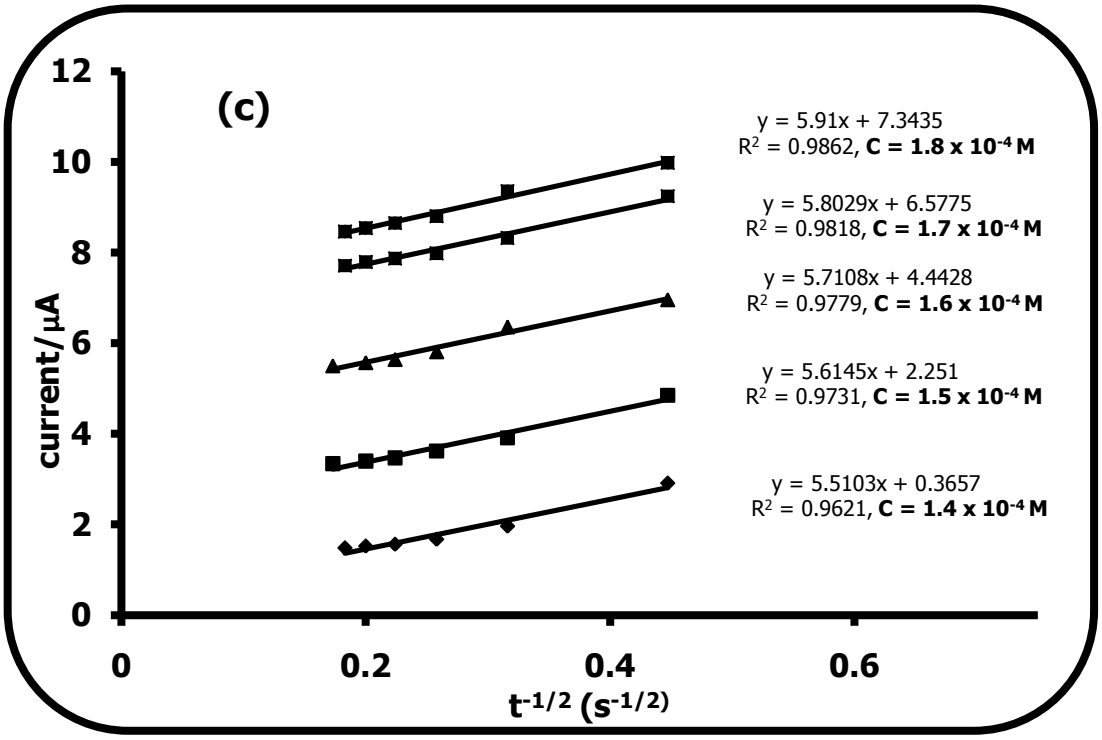
(c)
y = 5.91x + 7.3435
R² = 0.9862, C = 1.8 x 10⁻⁴ M
y = 5.8029x + 6.5775
R² = 0.9818, C = 1.7 x 10⁻⁴ M
y = 5.7108x + 4.4428
R² = 0.9779, C = 1.6 x 10⁻⁴ M
y = 5.6145x + 2.251
R² = 0.9731, C = 1.5 x 10⁻⁴ M
y = 5.5103x + 0.3657
R² = 0.9621, C = 1.4 x 10⁻⁴ M
current/μA
t⁻¹/² (s⁻¹/²)
0
2
4
6
8
10
12
0
0.2
0.4
0.6

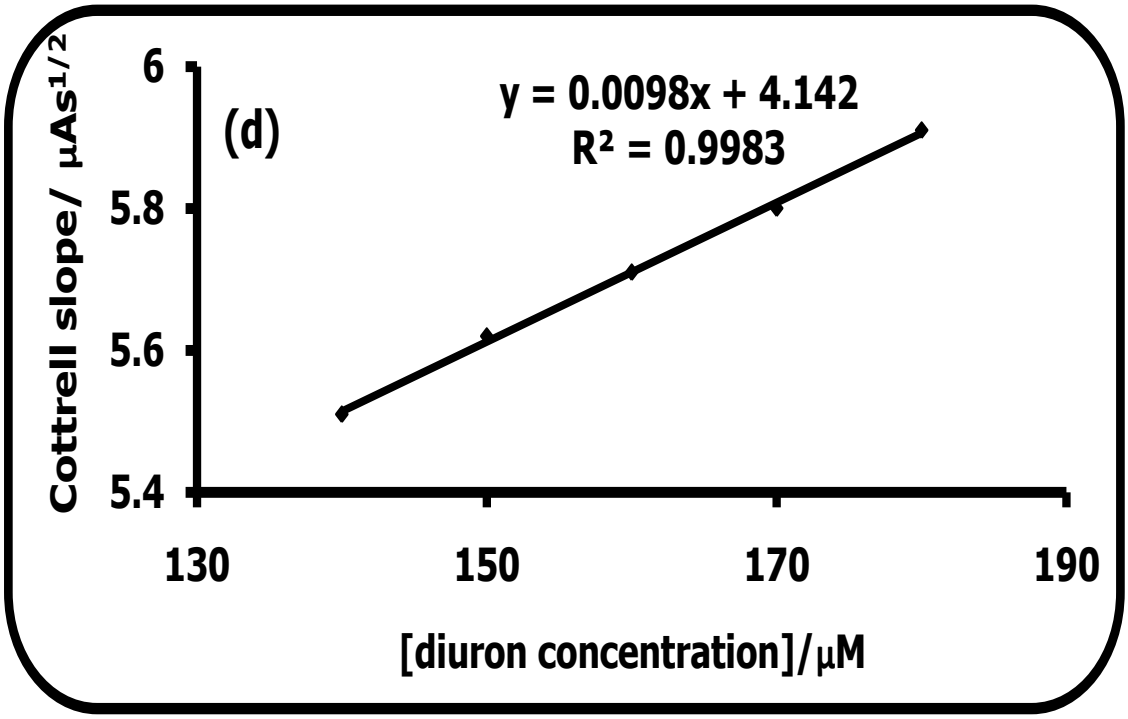
(d)
y = 0.0098x + 4.142
R² = 0.9983
Cottrell slope/ μAs¹/²
[diuron concentration]/μM
5.4
5.6
5.8
6
130
150
170
190

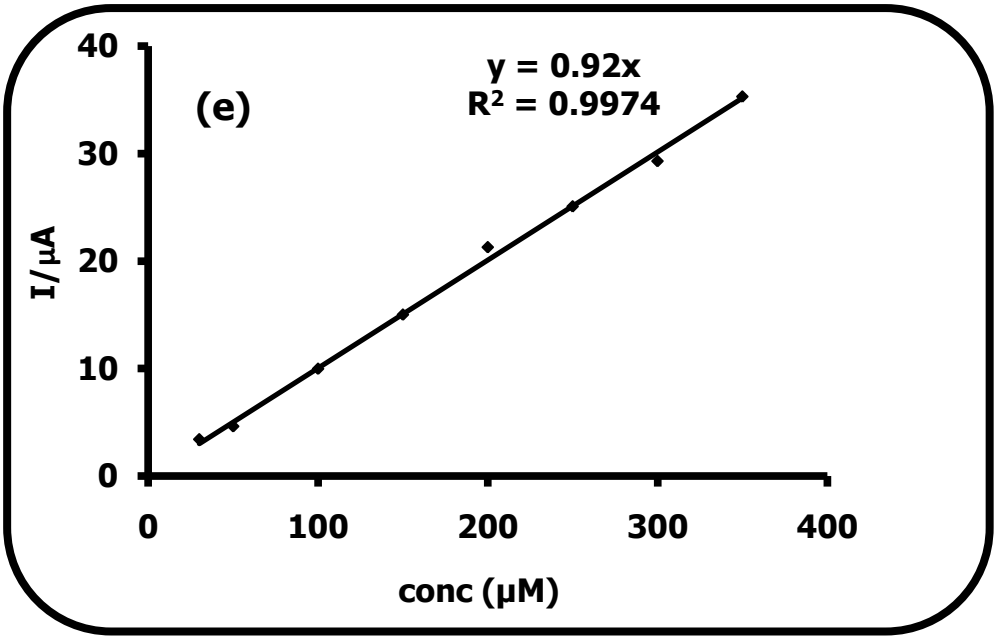

Figure 5.6: (a) Chronoamperograms for the various concentrations of diuron in pH 4 acetate buffer on the *poly*–Ni(OH)TAPc-GCE; (i) pH 4 buffer only; diuron concentrations: (ii) 1.4 x 10^{-4} M, (iii) 1.5 x 10^{-4} M, (iv) 1.6 x 10^{-4} M, (v) 1.7 x 10^{-4} M and (vi) 1.8 x 10^{-4} M. (b) Plot of I_{cat}/I_{buf} versus $t^{1/2}$ for the catalytic oxidation of diuron on *poly*–Ni(OH)TAPc-GCE, (c) Cottrell plots of diuron at different concentrations shown on the plot, (d) Cottrell slopes versus diuron concentrations and (e) Current-concentration plot. Potential = 1.2 V.

Figure 5.6a shows single step chronoamperometric evolutions recorded after polarization of the *poly*–Ni(OH)TAPc-GCE at 1.2 V in different concentrations of diuron (in pH 4 acetate buffer). Chronoamperometry was used for the determination of the catalytic rate constant at intermediate times (the decreasing part of the curve; t = 0.1 – 1 s). The catalytic current, $I_{cat,}$ is dominated by the oxidation of diuron. The rate constant (k) for reaction between diuron and redox sites of the surface-immobilized *poly*-Ni(OH)TAPc is determined according to Eq. 5.2 [247]:

$$\frac{I_{cat}}{I_{buf}} = \gamma^{1/2}\left[\pi^{\frac{1}{2}}\,\mathrm{erf}\left(\gamma^{\frac{1}{2}}\right) + \frac{\exp(-\gamma)}{\gamma^{\frac{1}{2}}}\right] \qquad (5.2)$$

$\gamma = kC_o t$ (C_0 is the bulk concentration of diuron) and erf($\gamma^{½}$) is the argument of the error function. In cases where γ exceeds 2, [247] the error function is almost equal to 1 and Eq. 5.2 reduces to Eq. 5.3:

$$\frac{I_{cat}}{I_{buf}} = \gamma^{1/2}\pi^{1/2} = \pi^{1/2}(kCt)^{1/2} \quad (5.3)$$

where I_{cat} and I_{buf} are currents in the presence and absence of diuron, k is the catalytic rate constant (M^{-1} s^{-1}), C_o is the bulk concentration of diuron (1.4 x 10^{-4} M) and t is the elapsed time in seconds. From the slope of I_{cat}/I_{buf} versus $t^{1/2}$ plot (Fig. 5.6b) for 1.4 x 10^{-4} M diuron, the value of k was found to be 5.91 x 10^2 M^{-1} s^{-1}, Table 5.2. Unfortunately no information could be obtained from the literature on the catalytic rate constants for the electrochemical oxidation of diuron or other phenyl-ureas for comparison.

The diffusion coefficient, D, for diuron was determined from Eq. 5.4 [245]:

$$I = \frac{nFAD^{1/2}C_0}{\pi^{1/2}t^{1/2}} \quad (5.4)$$

where C_0 is the bulk concentration of diuron, F is the Faraday's constant, A is the electrode area, n is the number of electrons and t is the time in seconds. Fig. 5.6c shows the Cottrell plots obtained from the chronoamperograms (ii-vi). From the slopes of Cottrell plots (Fig. 5.6c) for different concentrations of diuron, Fig. 5.6d was obtained, giving an estimated value of D of 6.43 x 10^{-6} cm^2 s^{-1}. Again no information could be obtained from the literature on the catalytic rate constants for the electrochemical oxidation of diuron or other related compounds.

Fig. 5.6e shows a linear plot of current versus the concentration of diuron obtained using chronoamperometry studies. The electrode gave sensitivity of 12.90 A mol^{-1} L cm^{-2} (R^2 = 0.9974) and a limit of detection (LOD) of 3.3 x 10^{-7} M (Table 5.2) using the 3δ/slope ratio notation (where δ is the standard deviation of the plot). An LOD of 6.59 x 10^{-6} M has been reported for diuron using capillary electrophoresis and electrochemical detection [306]. A LOD of 4.7 x 10^{-6} M and 4.0 x 10^{-6} M has been observed for diuron using capillary electrophoresis coupled with UV and electro-chemical detectors, respectively [307]. Thus, the method reported in this thesis using *poly*-Ni(OH)TAPc gives a favorable LOD compared to literature, hence confirming the sensitivity of *poly*–Ni(OH)TAPc-GCE towards the detection of diuron.

The suitability of the developed electrode for electrochemical detection of diuron was done in real samples by confirming known concentrations of the herbicide in tap water and in agricultural soil using chronoamperometry. Overall

average recoveries of 99 ± 0.1 % of the spikes were observed for the water and soil samples. This demonstrated the suitability of the developed method. The repeatability expressed as the relative standard deviation (RSD) was ± 0.102% for tap water and ± 0.105% for soil for the ten samples. The obtained data show the accuracy and precision of the developed method. The electrode showed the same stability as was observed above for the standard diuron detection and the electrode could be renewed similarly.

5.2 FeTAPc-SWCNT(linked)

As stated above (Table 5.1), this electrode was employed for amitrole, diuron and 2-ME, but only amitrole and diuron will be discussed for this electrode. 2-ME will be discussed on CoTAPc-SWCNT(linked) electrode which was also employed for all analytes. CV, CA and RDE were employed in this section. Also note that the CV and CA plots for Tafel and **α** are the same as for section 5.1, except for differences in current and will not be repeated for each section.

5.2.1 Cyclic voltammetry

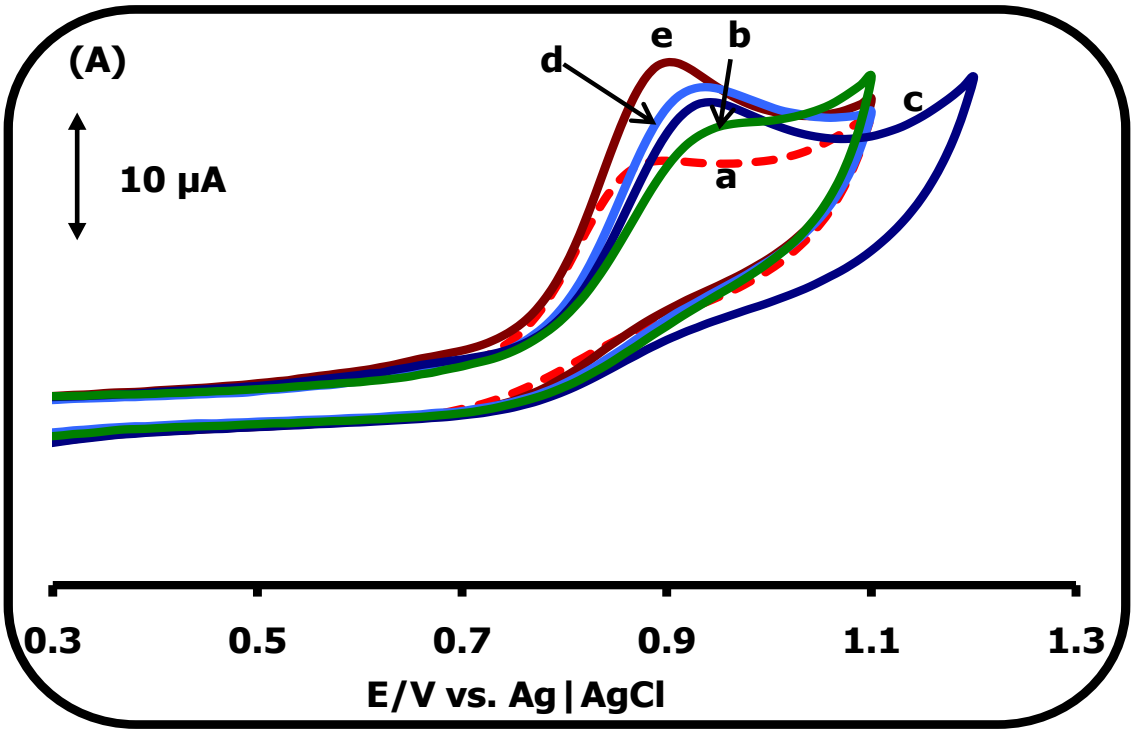

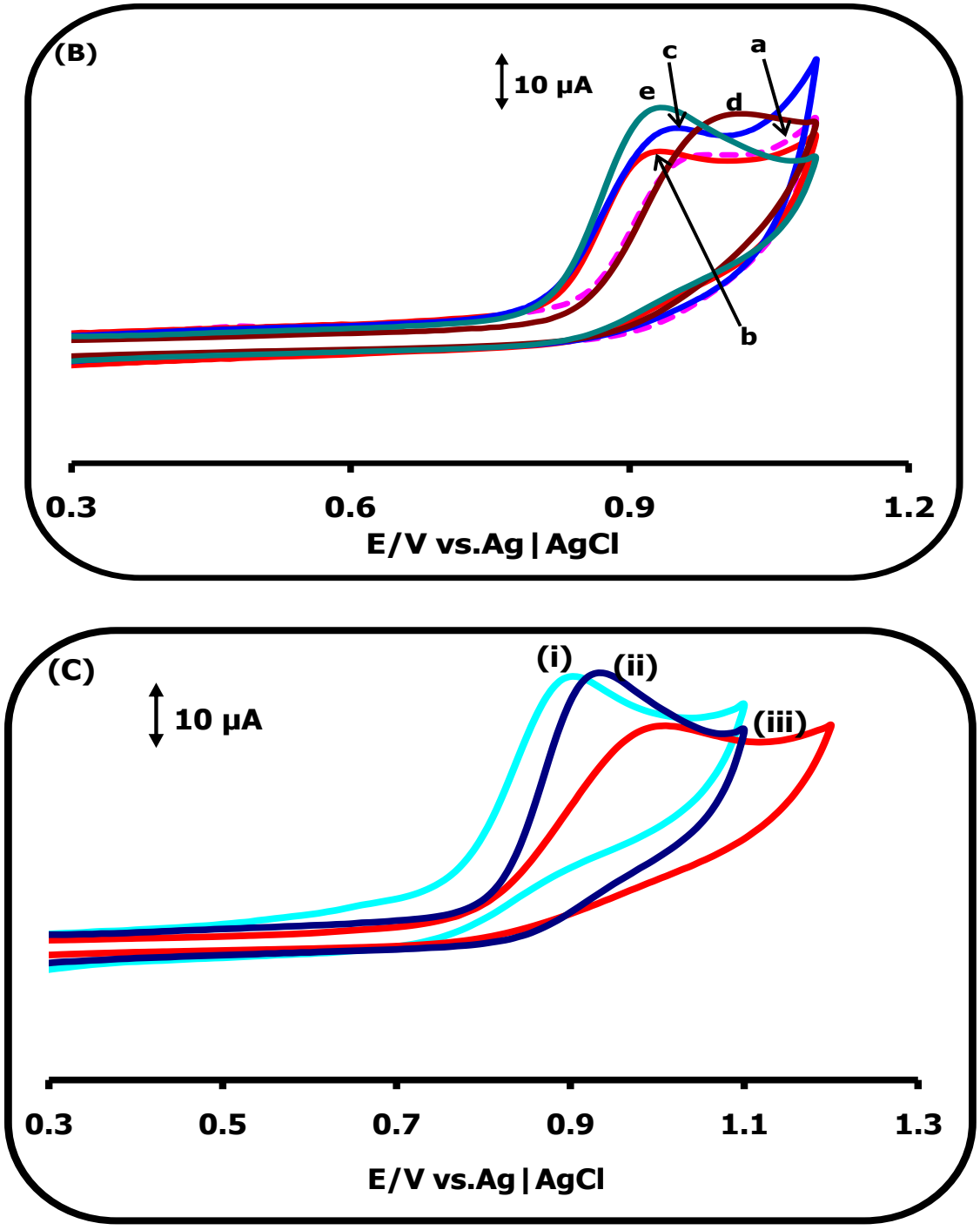

Figure 5.7: Cyclic voltammograms of (A) 0.1 mM amitrole and (B) 0.1 M diuron on bare GCE (a), SWCNT-COOH-GCE (b), *poly*-FeTAPc-GCE (c), FeTAPc/SWCNT-COOH(mix)-GCE (d) and FeTAPc-SWCNT(linked)-GCE (e). (C) Cyclic voltammograms of (i) 0.1 mM amitrole, (ii) 0.1 M diuron and (iii) 1:1 mixture of amitrole to diuron (0.1 mM for both) on FeTAPc-SWCNT(linked)-GCE. pH 4 buffer. Scan rate = 100 mV/s.

Figure 5.7A shows the typical voltammograms for the oxidation of amitrole on the various electrodes. Although the rising part for the oxidation of amitrole on the bare GCE (a) is almost at the same potential as that of FeTAPc-SWCNT(linked)-GCE, there is enhancement in the anodic peak current in the latter, showing its catalytic behaviour. Also compared with the rest of the electrodes, FeTAPc-SWCNT(linked)–GCE (e) showed larger currents for amitrole oxidation. However, the enhancement of currents could be affected by surface coverage, hence it is more reliable to use overpotential lowering in comparing the effectiveness of the electrodes. The order in terms of lowering the oxidation overpotentials for amitrole oxidation is as follows: FeTAPc-SWCNT(linked)-GCE (e) ~ bare GCE (a) > FeTAPc/SWCNT-COOH(mix)-GCE (d) ~ *poly*-FeTAPc- GCE (c) > SWCNT-COOH-GCE (b). In all cases no corresponding cathodic peak was observed, an indication of the irreversibility of the process. The oxidation potential of amitrole is clearly within the oxidation range of $Fe^{III}Pc^{-1}/Fe^{III}Pc^{-2}$ process, indicating that the $Fe^{III}Pc^{-1}$ species is involved in catalysis.

Fig. 5.7B shows the typical voltammograms for the oxidation of diuron on the various electrodes. The oxidation of diuron on the bare GCE (a) occurs at a potential which is 40 mV more positive than its oxidation on the FeTAPc-SWCNT(linked)-GCE (e). This shows clear catalytic behaviour of the linked when compared to the bare GCE. Also compared with the rest of the electrodes, FeTAPc-SWCNT(linked)–GCE showed larger currents for diuron oxidation. The order in terms of lowering diuron oxidation overpotentials is as follows: FeTAPc-SWCNT(linked)-GCE (e) ~ SWCNT-COOH-GCE (b) > *poly*-FeTAPc-GCE (c) > bare GCE (a) > FeTAPc/SWCNT-COOH(mix)-GCE (d). Thus the catalytic activity of FeTAPc is enhanced in the presence of linked SWCNTs. Again in all cases no corresponding cathodic peak was observed, an indication of the irreversibility of the process. The oxidation potential of diuron is also clearly within the oxidation range of $Fe^{III}Pc^{-1}/Fe^{III}Pc^{-2}$ process, indicating that the $Fe^{III}Pc^{-1}$ species is involved in catalysis.

Comparing with poly-Ni(OH)TAPc (1.08 V), diuron is oxidized at a lower potential on FeTAPc-SWCNT (0.92 V), hence showing that the latter to be a better electrode, probably because of SWCNTs and the nature of the central metal.

5.2.2 Interference studies

Fig. 5.7C compares the oxidation peak behaviours of amitrole and diuron on FeTAPc-SWCNT(linked)-GCE surface. Oxidation of diuron occurs at potentials 30 mV more positive than that of amitrole, indicating the difficulty of oxidation of the former. Since diuron and amitrole may be used simultaneously in agriculture, the interference of each other during analysis is of importance. Hence Fig. 5.7C shows the voltammogram of a 1:1 mixture of these two herbicides. The peak for the 1:1 mixture of amitrole:diuron is broad, with the oxidation potential which is more positive than the individual oxidation potentials of amitrole and diuron, an indication that the two analytes interfere with each other.

The interference of diuron on the detection of amitrole was further investigated using the mixed solution method [248]. The value of K_{amp} (where K_{amp} is the amperometric selectivity coefficient) was determined from Eq. 5.5 (using 10^{-4} M diuron as an interferent and 5 x 10^{-5} M amitrole):

$$K_{amp} = \left(\frac{\Delta I_{mixture}}{\Delta I_{analyte}} - 1\right) \frac{[analyte\ ]}{[interferent\ ]} \quad (5.5)$$

where $\Delta I_{mixture}$ and $\Delta I_{amitrole}$ are respectively, the changes in current for the mixture containing amitrole and diuron, and amitrole alone. A K_{amp} value of less than 10^{-3} indicates non-interference while one which falls within the order of 10^{-3} suggests that the species is an interferent but not a strong one. The K_{amp} values of (3.3±0.13) x 10^{-1} was obtained, indicating that diuron is a very strong interferent, thus the electrode cannot be used for the detection of both amitrole and diuron in solution.

5.2.3 Electrode stability

Fig. 5.8a shows a 30 cycle continuous scan voltammogram for FeTAPc-SWCNT (linked)-GCE in 0.1 mM amitrole. There is a drop of 8 % in peak current from cycle 1 to 2 and an overall drop of 39% after 30 cycles, following which, there was stabilization of the currents. The drop in peak currents is an indication of the passivating nature of amitrole. All electrodes were tested for stability towards amitrole (using current drop from scan 1 to 2) and the order was as follows: FeTAPc-SWCNT(linked)-GCE (8%, Table 5.2) > FeTAPc/SWCNT-COOH(mix)-GCE (12%) > *poly*-FeTAPc-GCE (15%) > SWCNT-COOH-GCE (16%) > bare GCE (21%). A 6%

drop in current drop from scan 1 to 2 was observed for diuron. Thus it seems the presence of FeTAPc and SWCNT improves electrode stability. Successful regeneration of FeTAPc-SWCNT(linked)-GCE (Fig. 5.8b) was done by shaking the electrode in methanol and scanning in pH 4 buffer solution. The electrode showed little or no leaching because of the dual combination of strong л-л interactions between the GCE and the FeTAPc and SWCNT components of the conjugate. The stability of *poly*-Ni(OH)TAPc is similar to that of FeTAPc-SWCNT(linked) as shown by the % current drops from scan 1 to 2 (Table 5.2).

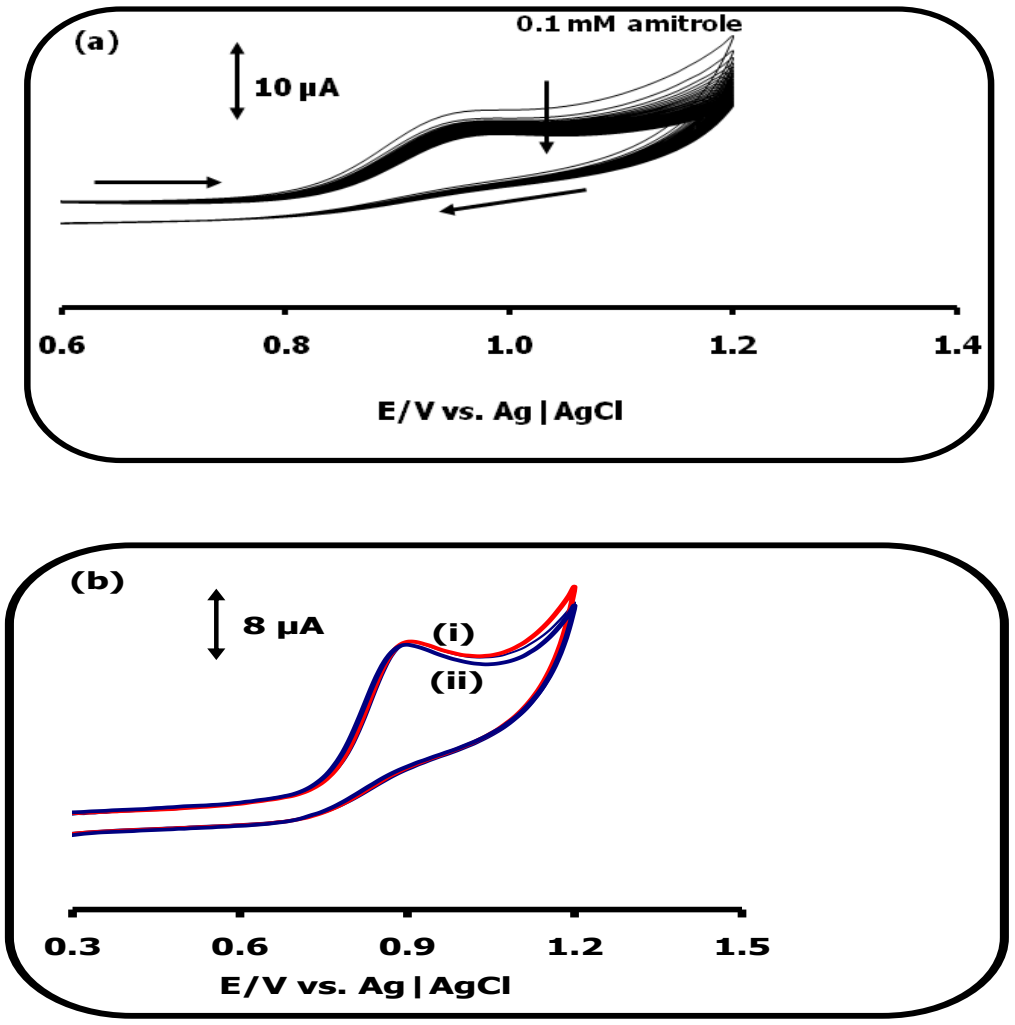

Figure 5.8: (a) Continuous cyclic voltammograms (30) for FeTAPc-SWCNT (linked)-GCE in 0.1 mM amitrole, pH 4 buffer. (b) Regeneration of the FeTAPc-SWCNT(linked)-GCE. (i) 1st scan in 0.1 mM amitrole, (ii) scan after 30 cycles and then rinsing in pH 4 buffer. Scan rate = 100 mV/s.

5.2.4: Tafel slopes

A linear relationship between the peak currents and square roots of the scan rate (plots similar to Fig. 5.5b) indicate that the amitrole and diuron electro-catalytic oxidations are diffusion controlled.

Using Eq. 5.1 and a plot of *E*p versus log *ν,* Tafel slopes of 199 and 243 mV/decade (Table 5.2) were obtained for diuron and amitrole, respectively. As stated above Tafel slopes this high have no kinetic meaning but could indicate a passivation phenomena occurring on the electrode surface. Tafel slopes much greater than the normal 30-120 mV/decade have been related either to chemical reactions coupled to electrochemical steps [97] or to substrate-catalyst interactions in a reaction intermediate [257,303,304], therefore these could still indicate one electron transfer in the rate-determining step [257,308,309]. There is more interaction between amitrole (243 mV/decade) and FeTAPc-SWCNT(linked) than with diuron (199 mV/decade). The extent of interaction of FeTAPc-SWCNT(linked) with diuron is similar to that observed on *poly*-Ni(OH)TAPc (192 mV/decade).

From the slopes of the plots of E_p versus log *v* (similar to Fig. 5.5a), the **α** values for diuron and amitrole were estimated to be 0.70 and 0.76, respectively, indicating higher probability of the activated complex being converted to the product on the reaction coordinate. The electrocatalysis of both amitrole and diuron was found to be first order from a plot of log *I* versus log [concentration] (Fig. 5.9), implying that one analyte molecule interacts with one molecule of FeTAPc-SWCNT(linked).

Using the above arguments, Eqs. 5.6-5.8 represents the proposed mechanism for both amitrole and diuron.

$$Fe(II)TAPc^{-2} \xrightarrow{-e^-} [Fe(III)TAPc^{-2}]^{+1} \quad \textbf{(5.6)}$$

$$[Fe(III)TAPc^{-2}]^{+1} \xrightarrow{-e^-} [Fe(III)TAPc^{-1}]^{+2} \quad \textbf{(5.7)}$$

$$[Fe(III)TAPc^{-1}]^{+2} + \text{amitrole/diuron} \rightleftharpoons Fe(II)TAPc^{-2} + \text{amitrole/diuron oxidation products} \quad \textbf{(5.8)}$$

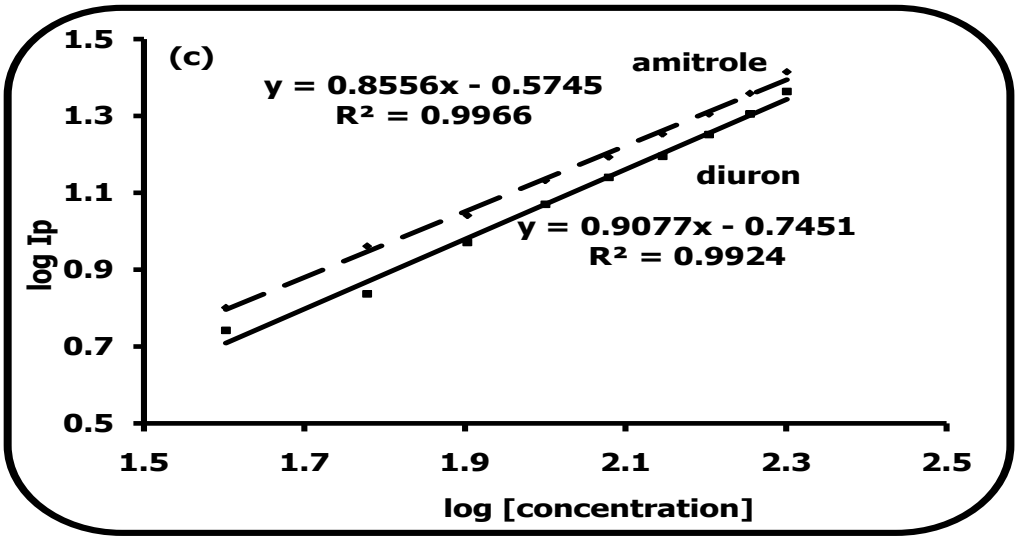

Figure 5.9: Plot of log I_p versus log [concentration] for the oxidation of amitrole and diuron on FeTAPc-SWCNT(linked)-GCE.

5.2.5 Chronoamperometric studies

Chronoamperometry was used in the evaluation of the catalytic rate constants. The chronoamperograms (obtained on linked polarized at 1.0 V) for both amitrole and diuron are similar to Fig. 5.6a except for the differences in current, hence not shown again. From the plots of Eq. 5.3 (I_{cat}/I_{buf} versus $t^{1/2}$) similar to Fig. 5.6b, the values of k for amitrole and diuron (where C_0 = 0.09 mM), were found to be 4.55 x 10^3 $M^{-1}s^{-1}$ and 1.79 x 10^4 $M^{-1}s^{-1}$, Table 5.2, respectively. Unfortunately there is no information that could be obtained from the literature on the rate constants for the electrochemical oxidation of amitrole and diuron. However, the large rate constant for diuron (1.79 x 10^4 $M^{-1}s^{-1}$, Table 5.2) compared to 1.60 × 10^2 M^{-1} s^{-1} for the oxidation of asulum (also a carbamate [310]) on CoPc/MWCNT [75], indicates that the electrochemical oxidation diuron on FeTAPc-SWCNT(linked)-GCE is very fast. Comparing rate constants (*k)* for diuron on FeTAPc-SWCNT(linked) with *poly*-Ni(OH)TAPc shows that *k* is larger for the former, indicating a fast reaction on this electrode.

The diffusion coefficient, *D*, for amitrole was determined using Eq. 5.4. From the slope of the Cottrell plots (I versus $t^{-1/2}$, similar to Fig. 5.6c) and slopes of the Cottrell plots versus concentration (similar to Fig. 5.6d) the *D* value of amitrole was

estimated to be 1.91 x 10^{-4} cm^2 s^{-1}. Once again there is no literature to which to we can compare this D value.

Chronoamperometric studies were done in the linear concentration ranges of 6.3 x 10^{-5} to 1.0 x 10^{-4} M and 5.0 x 10^{-5} to 1.0 x 10^{-4} M for amitrole and diuron, respectively. Sensitivities of 9.30 A mol^{-1} L cm^{-2} and 9.40 A mol^{-1} L cm^{-2} and limits of detection of 2.2 x 10^{-7} M and 2.6 x 10^{-7} M were obtained for amitrole and diuron, respectively (using the 3δ notation). The LOD of amitrole is lower than 0.6 µM obtained from literature [311]. Limits of detection of 4.7 µM and 4.0 µM have been observed for diuron using capillary electrophoresis and electro-chemical detectors, respectively [307]. This is also lower than what was observed on *poly*-Ni(OH)TAPc-GCE, indicating that FeTAPc-SWCNT(linked) is a better electrode for the detection of diuron.

5.2.6 RDE experiments

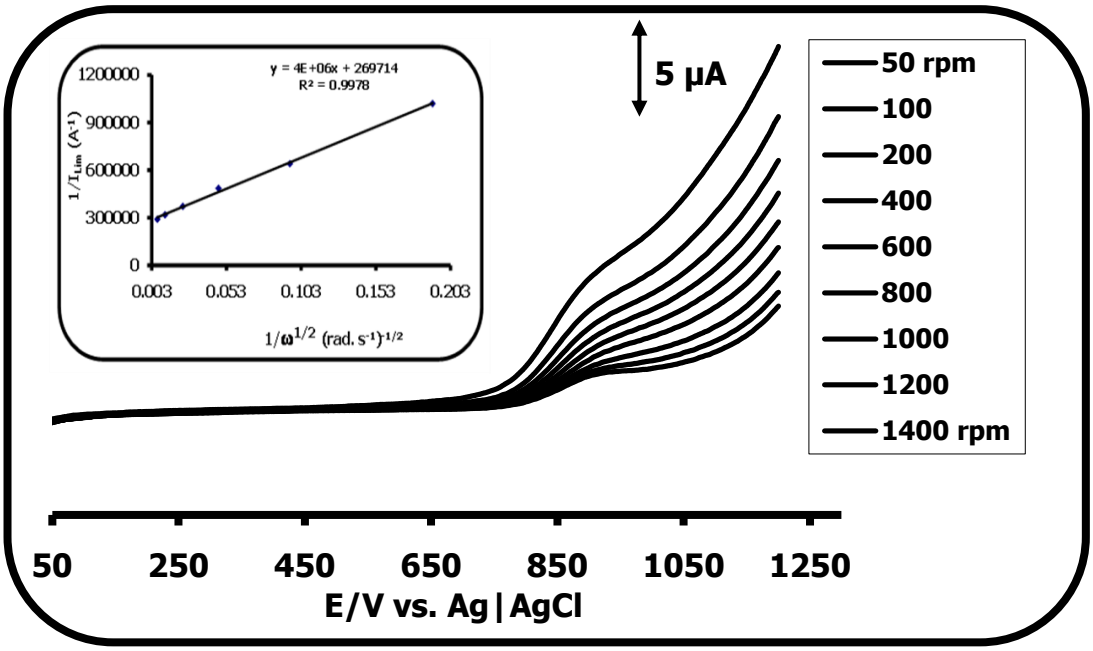

Figure 5.10: Hydrodynamic voltammograms (rotating disk electrode) obtained on FeTAPc-SWCNT(linked)-GCE in 1 mM amitrole (pH 4 acetate buffer). Scan rate = 20 mVs^{-1}. Inset: Koutecky-Levich plot for 1 mM amitrole.

Fig. 5.10 shows the typical RDE responses for amitrole on the FeTAPc-SWCNT(linked)-GCE scanned from 0.0 to 1.2 V at 50, 100, 200, 400, 400, 800, 1000, 1200 and 1400 rpm with a scan rate of 20 mV s^{-1}. Current responses increased with rotational speed, showing that the oxidation process is kinetically controlled.

The Koutecky-Levich (Eq. 5.9) relationship is applicable when the mass transfer processes and the catalytic reactions become dominant [245,247] and is used for kinetic analysis.

$$\frac{1}{I_{lim}} = \frac{1}{nFA\,C_o\,k\Gamma} + \frac{1}{0.62nFA\,D^{2/3}\upsilon^{-1/6}C_0\omega^{1/2}} \qquad (5.9)$$

where n, A, C_o, k, Γ, D, ω and υ are the number of electrons involved, the electrode area (cm^{-2}), the substrate concentration (1 x 10^{-3} M), the catalytic rate constant (M^{-1} s^{-1}), the surface coverage (mol cm^{-2}), the diffusion coefficient (cm^2 s^{-1}), the rotational speed and kinematic viscosity (cm^2 s^{-1}), respectively. The linearity of $1/I_{lim}$ versus $1/\omega^{1/2}$ (Koutecky-Levich plot, Fig. 5.10 inset), implies that the electrocatalytic reaction is faster than the rate of substrate delivery to the electrode surface, so the current is determined by the rate of substrate movement to the modified electrode surface [312]. The values of the rate constants (k) for the catalytic reactions obtained from the intercepts of the Koutecky-Levich plots were found to be 5.41 x 10^3 M^{-1} s^{-1} and 4.38 x 10^4 M^{-1} s^{-1} for amitrole and diuron, Table 5.2, respectively. These values are of the same order of magnitude as those calculated from chronoamperometric studies.

5.3 CoTCPc-EA-SWCNT(linked)

This electrode was employed for amitrole and diuron as shown in Table 5.1. CV, CA, RDE and EIS were employed in this study.

5.3.1 Cyclic voltammetry

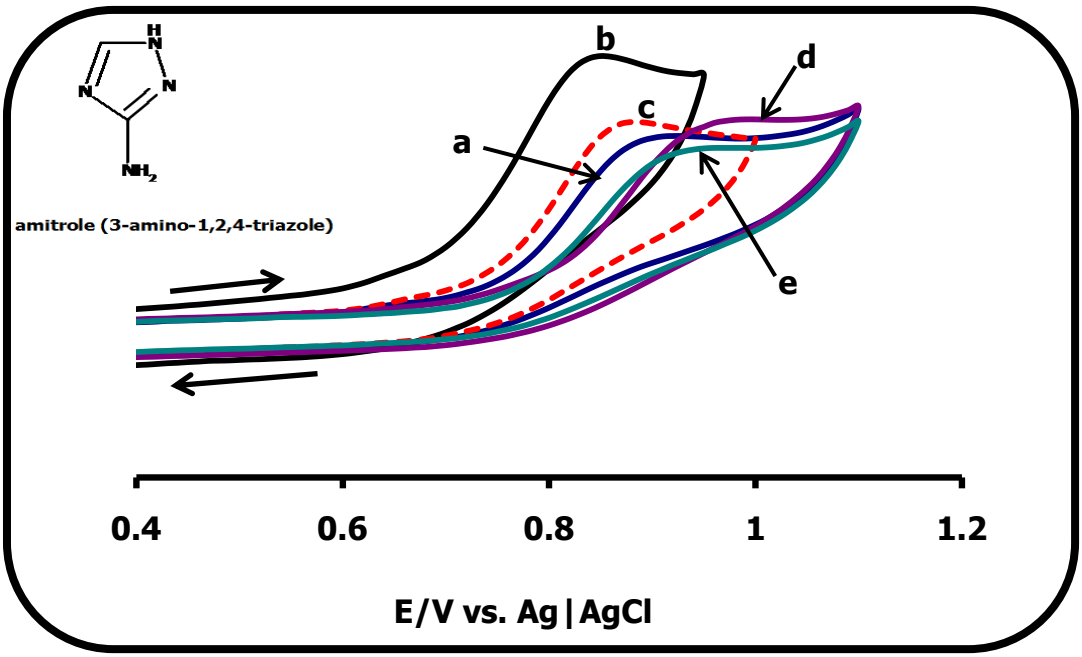

Figure 5.11: Comparative cyclic voltammograms in 0.1 mM amitrole (pH 4 buffer) (a) bare GCE, (b) CoTCPc-EA-SWCNT(linked)-GCE, (c) CoTCPc/EA-SWCNT(mix)-GCE, (d) EA-SWCNT-GCE and (e) CoTCPc-GCE. Scan rate = 100 mV/s. Inset: The molecular structure of amitrole.

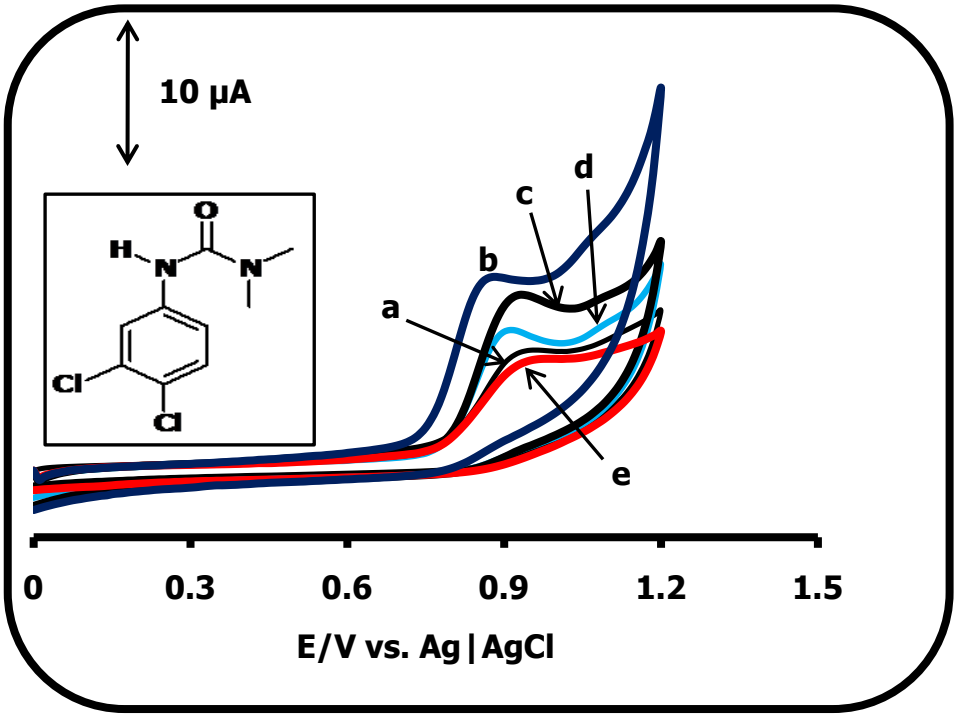

Figure 5.12: Comparative cyclic voltammograms in 0.16 mM diuron (pH 4 buffer) (a) bare GCE, (b) CoTCPc-EA-SWCNT(linked)-GCE, (c) CoTCPc/EA-SWCNT(mix)-GCE, (d) EA-SWCNT-GCE and (e) CoTCPc-GCE. Scan rate = 100 mV/s. Inset: The molecular structure of diuron.

Figures 5.11 and 5.12 shows comparative cyclic voltammetric responses for bare GCE (a), CoTCPc-EA-SWCNT(linked)-GCE (b), CoTCPc/ EA-SWCNT(mix)-GCE (c), EA-SWCNT-GCE (d) and CoTCPc-GCE (e) in 0.1 mM amitrole and 0.16 mM diuron, respectively (pH 4 buffer). The observed peaks in the region 0.8 – 1.0 V are due to the oxidation of amitrole and diuron as observed in other studies [78,306,307,311]. The oxidation potentials for amitrole at 0.92 V, 0.83 V (Table 5.2), 0.87 V, 0.97 V and 0.95 V (versus Ag|AgCl) are for the bare GCE, CoTCPc-EA-SWCNT(linked)-GCE, CoTCPc/EA-SWCNT(mix)-GCE, EA-SWCNT-GCE and CoTCPc-GCE, respectively. The CoTCPc-EA-SWCNT(linked)-GCE (Figs. 5.11b and 5.12b), shows higher oxidation currents at reduced oxidation overpotentials compared to other modified electrodes, a confirmation of better catalytic properties. Oxidation of diuron occurred at 0.85 V (Table 5.2) on CoTCPc-EA-SWCNT(linked)-GCE, compared to 0.94 V, 0.90 V, 0.88 V and 0.94 V (versus Ag|AgCl) for the bare

GCE, CoTCPc/EA-SWCNT(mix)-GCE, EA-SWCNT-GCE and CoTCPc-GCE, respectively. CoTCPc-GCE is not catalytic for both amitrole (Fig. 5.11e) and diuron (Fig. 5.12e), possibly due to the presence of the electron withdrawing carboxy groups which makes the oxidation of the cobalt centre more difficult, rendering it ineffectice as a catalyst. EA-SWCNT-GCE is not catalytic towards amitrole (Fig. 5.11d). The oxidations of amitrole and diuron occurs at potentials for the $Co^{III}Pc^{-1}$ process hence is catalysed by this process. Having confirmed the superiority of CoTCPc-EA-SWCNT electrode over the other electrodes, it was used in the further characterization of amitrole and diuron.

Oxidation of diuron and amitrole on CoTCPc-EA-SWCNT(linked)-GCE occurs at lower potentials (0.85 and 0.83 V, respectively) compared to oxidation on FeTAPc-SWCNT(linked) (0.92 and 0.88 V, respectively), showing the effects of Co as a central metal compared to Fe. However the effects of EA could also contribute to the ease of oxidation of the Co metal centre leading to the better catalysis of CoTCPc-EA-SWCNT(linked).

5.3.2 Electrode stabilities

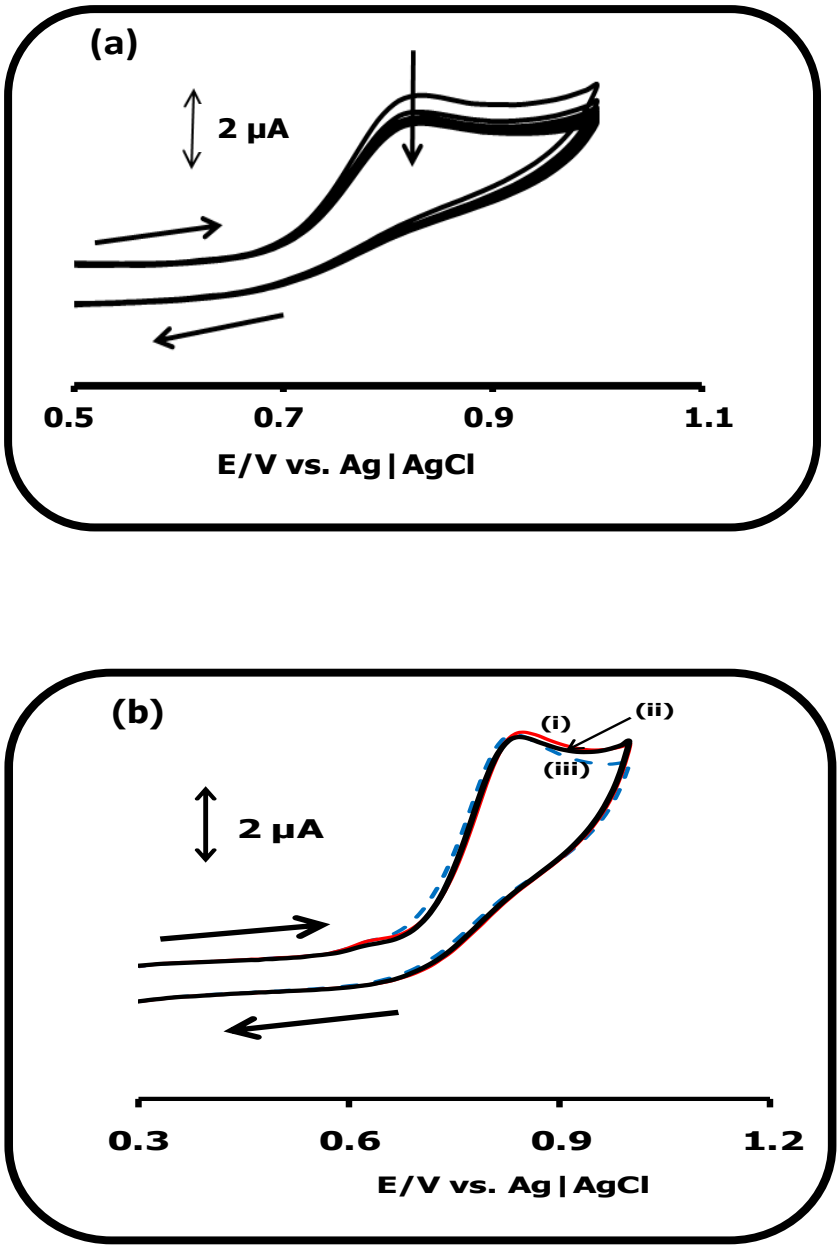

Figure 5.13: (a) Continuous cyclic voltammograms (30) for CoTCPc-EA-SWCNT(linked)-GCE in 0.1 mM amitrole, pH 4 buffer. (b) Regeneration of the CoTCPc-EA-SWCNT(linked)-GCE, (i, red line) 1st scan in 0.1 mM amitrole, (ii, black line) and (iii, blue line) scans after 30 cycles and then rinsing in methanol and scanning in pH 4 buffer. Scan rate = 100 mV/s.

Figure 5.13a shows 30 cycle continuous scan voltammograms for CoTCPc-EA-SWCNT(linked)-GCE in 0.1 mM amitrole. A drop of 10% in peak current from cycle

1 to 2 and an overall drop of 25% after 30 cycles, followed by the stabilization of the currents were observed with amitrole. The extent to which peak currents drop is an indication of the fouling capability of amitrole and the resistance to passivation of the CoTCPc-EA-SWCNT(linked)-GCE. All electrodes were tested for stability after 30 cyclic voltammetry cycles and the order in terms of stability was: CoTCPc-EA-SWCNT(linked)-GCE (25%) > CoTCPc/EA-SWCNT(mix)-GCE (34%) > EA-SWCNT-GCE (41%) > CoTCPc-GCE (46%) > bare GCE (51%). It can be reasonably concluded that the presence of CoTCPc and SWCNT improves electrode stability. The CoTCPc-EA-SWCNT(linked)-GCE showed similar stability towards in 0.16 mM diuron (23% after 30 cycles and 9 % from scan 1 to 2), showing its high resistance to passivation by the oxidation products of the two analytes. Stabilities of other electrodes towards diuron (after 30 cycles) were as follows: CoTCPc/EA-SWCNT(mix)-GCE (28%) > CoTCPc-GCE (31%) > EA-SWCNT-GCE (33%) > bare GCE (51%). The CoTCPc-EA-SWCNT(linked) electrode is more stable towards diuron than amitrole. However, the stability of CoTCPc-EA-SWCNT(linked)-GCE towards both amitrole and diuron is about the same as that for FeTAPc-SWCNT(linked) as shown in Table 5.2. Compared to *poly*-Ni(OH)TAPc, the CoTCPc-EA-SWCNT(linked) electrode has also approximately the same stability towards diuron, as shown in Table 5.2.

Successful regeneration of CoTCPc-EA-SWCNT(linked)-GCE (Fig. 5.13b) was done by shaking the electrode in methanol and scanning in pH 4 buffer solution (through cyclic voltammetry) in the potential window 0.0-1.2 V (versus Ag|AgCl). Methanol cleans the electrode surface by dissolving away all the amitrole and diuron oxidation products while scanning between 0.0-1.2 V in pH 4 buffer is an electrode conditioning process which ensures stable background currents. As shown in Fig. 5.13b, the reproducibility of the voltammograms after shaking in methanol and scanning in pH 4 buffer is a confirmation of little or no leaching at all of the catalyst. This minimum leaching is due to the dual combination of strong л-л interactions between the GCE and the CoTCPc and SWCNT components of CoTCPc-EA-SWCNT unit as discussed above for FeTAPc-SWCNT(linked). Under conditions of continual use and storage in pH 4 buffer, the electrode can have a life span of more than 2 months.

5.3.3: Tafel slopes

Fig. 5.14 shows the plot of current versus scan rate for amitrole oxidation on CoTCPc-EA-SWCNT(linked)-GCE. Peak **I** at ~0.3 V is due to Co^{III}/Co^{II} couple and it is shifted to less positive potential values in the presence of amitrole compared to when it is absent (chapter 4, at 0.55V) and becomes more reversible. The fact that this peak is still observed suggests it is not involved in electrocatalysis. Thus it is the $Co^{III}Pc^{-1}$ which catalyses the oxidation as stated above. Peak **II** represent the oxidation of amitrole. A plot of scan rate normalized current density ($I_p v^{-1/2}$) versus scan rate confirmed the typical behaviour for a catalytic process. Diuron showed similar behaviour to that of amitrole. Linear relationships were observed in the plots of peak currents versus square root of the sweep rates (Fig. 5.14 inset for amitrole), showing that the electrocatalytic oxidations of amitrole and diuron are diffusion controlled.

Plot of E_p versus log v (Eq. 5.1) gave Tafel slopes of 237 and 226 mV $decade^{-1}$ for amitrole and diuron, respectively. Again amitrole interacts more with CoTCPc-EA-SWCNT(linked)-GCE than diuron as observed for FeTAPc-SWCNT(linked)-GCE. As already stated, high Tafel slopes have no kinetic meaning but could indicate a passivation phenomena occurring on the electrode surface. The **α**-values for amitrole and diuron were 0.75 and 0.74, respectively, Table 5.2. The oxidation of amitrole and diuron proceed via a similar mechanism.

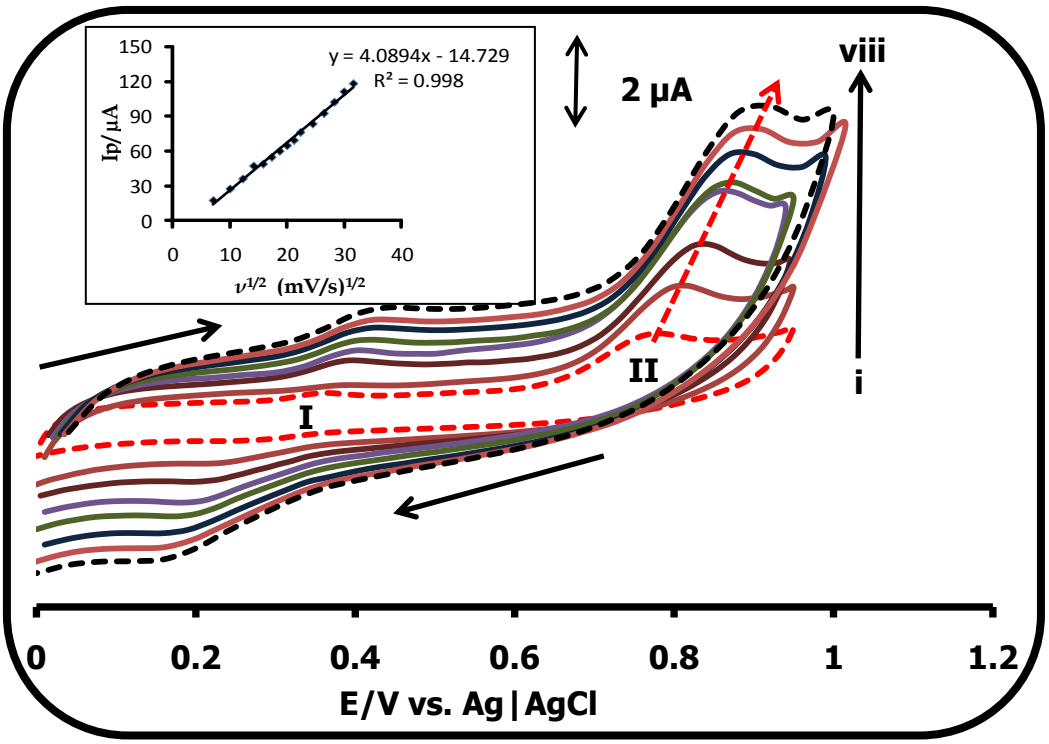

Figure 5.14: Effect of scan rate on peak potentials and currents (i) 50 mV/s, (ii) 100 mV/s, (iii) 150 mV/s, (iv) 200 mV/s, (v) 250 mV/s, (vi) 300 mV/s, (vii) 350 mV/s and (viii) 400 mV/s on CoTCPc-EA-SWCNT(linked) for amitrole oxidation. [Amitrole] = 0.1 mM. Inset: Plot of peak current versus root of sweep rate.

5.3.4 Chronoamperometric studies

The CA for amitrole obtained by polarizing the CoTCPc-EA-SWCNT(linked) at 0.85 V (versus Ag|AgCl) are similar to those in Fig. 5.6a, except for the currents. Using plots similar to Figs. 5.6d and 5.6e the values of *k* were found to be 1.20 x 10^3 and 5.88 x 10^4 M^{-1} s^{-1} for amitrole and diuron, respectively. The *k* value obtained for amitrole less than (but with the same order of magnitude) 4.55 x 10^3 M^{-1} s^{-1} obtained on FeTAPc-SWCNT(linked)-GCE. However, the *k* value for diuron is higher than 1.79 x 10^4 M^{-1} s^{-1} obtained on FeTAPc-SWCNT(linked), but with the same magnitude. These results show that the oxidation of amitrole is faster on FeTAPc-SWCNT(linked) modified electrode than on CoTCPc-EA-SWCNT(linked)-GCE, while the opposite is true for diuron. However, the *k* value of diuron on *poly*-Ni(OH)TAPc (5.91 x 10^2 M^{-1} s^{-1}) is the lowest and therefore the large rate constants observed for FeTAPc-SWCNT(linked) and CoTCPc-EA-SWCNT(linked) complexes

could be attributed to the presence of SWCNTs. Using chronoamperometric information, the plot of log I versus log [concentration] showed that electrocatalysis of amitrole is first order. This implies that one analyte molecule interacts with one molecule of CoTCPc-EA-SWCNT(linked). From the above stated arguments and also that the ring is implicated in the catalysis, the proposed mechanism for the catalytic oxidation of amitrole is represented by Eqs. 5.10 – 5.12:

$$Co(II)TCPc^{-2} \xrightarrow{-e^-} [Co(III)TCPc^{-2}]^{+1} \quad (5.10)$$

$$[Co(III)TCPc^{-2}]^{+1} \xrightarrow{-e^-} [Co(III)TCPc^{-1}]^{+2} \quad (5.11)$$

$$[Co(III)TCPc^{-1}]^{+2} + \text{Amitrole/diuron} \rightleftharpoons Co(II)TCPc^{-2} + \text{amitrole/diuron oxidation products} \quad (5.12)$$

Eqs. 5.10 and 5.12 are proposed since the oxidation of amitrole and diuron occurs in the stability range of the $Co^{III}TCPc^{-1}$ species, hence the latter is involved in the mediation process. Eq. 5.12 shows the oxidation of amitrole/diuron and regeneration of the CoTCPc electrocatalyst. The involvement of two electrons is justified since the oxidation of amitrole is known to be a two electron process [257].

5.3.5 RDE studies

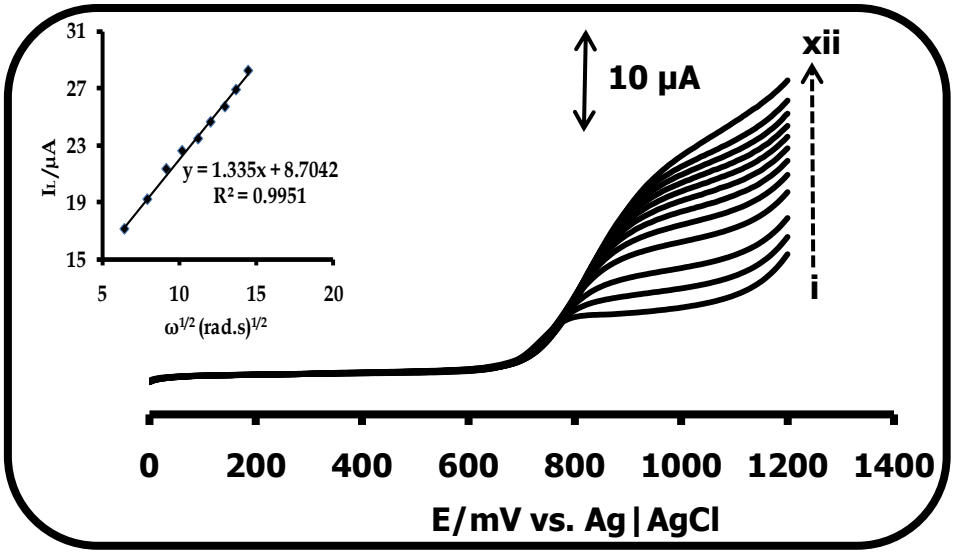

Figure 5.15: RDE evolutions for 160 μM amitrole at the CoTCPc-EA-SWCNT(linked)-GCE at rotational speeds (i) 50, (ii) 100, (iii) 200, (iv) 400, (v) 600, (vi) 800, (vii) 1000, (viii) 1200, (ix) 1400, (x) 1600, (xi) 1800 and (xii) 2000 rpm, with a sensitivity of 10 μA/V. Scan rate = 20 mV/s. Inset: Levich plot.

Fig. 5.15 shows the RDE voltammograms for CoTCPc-EA-SWCNT(linked) in amitrole. Using this data and the Levich theory (Eq. 5.13), a linear relationship was observed between I_{lim} and $\omega^{1/2}$ (Fig. 5.15 inset) showing that the oxidation of amitrole in solution is governed by its mass transfer to the electrode surface [245]. A similar relationship was observed for diuron.

$$I_{lim} = I_{Lev} = 0.62nFAD^{2/3}\upsilon^{-1/6}\omega^{1/2}C_0 \quad (5.13)$$

where D, υ, ω and C_o are the diffusion coefficient, the kinematic viscosity, the rotational speed and the bulk concentration of the reactant in the solution, respectively, with all other parameters having their usual meanings.

A corresponding Tafel slope value for amitrole (not done for diuron since the aim was to compare Tafel slopes obtained using the two methods) was obtained from the plot of E_p vs. log I_k (Fig. 5.16) where $I_k = (I_d \times I_L)/ (I_d - I_L)$. I_L is the limiting current (plateau in RDE voltammogram) and I_d is measured current and it has to be less than 5% of I_L. For plots at 1800 and 2000 rpm on CoTCPc-EA-SWCNT(linked), Fig. 5.16, Tafel slopes of 232 mV decade^{-1} and 243 mV decade^{-1} were obtained, respectively, whose average is 238 mV dacade^{-1} ($\boldsymbol{\alpha}$ = 0.75) and is in agreement with what was obtained from the plot of E_p versus log υ, Table 5.2.

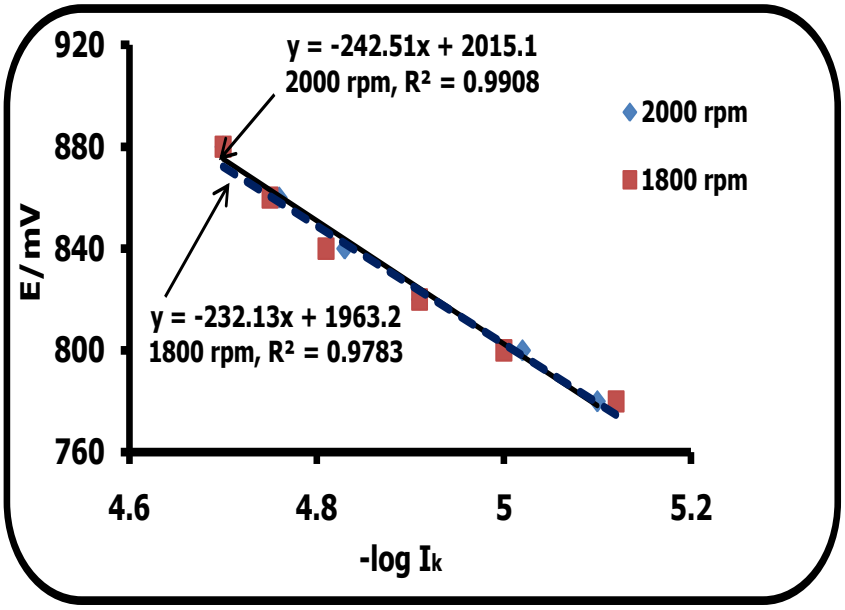

Figure 5.16: Plot of potential versus log I_k for 0.1 mM amitrole in pH 4 buffer (for 1800 and 2000 rpm).

5.3.6 Selectivity and sensitivity

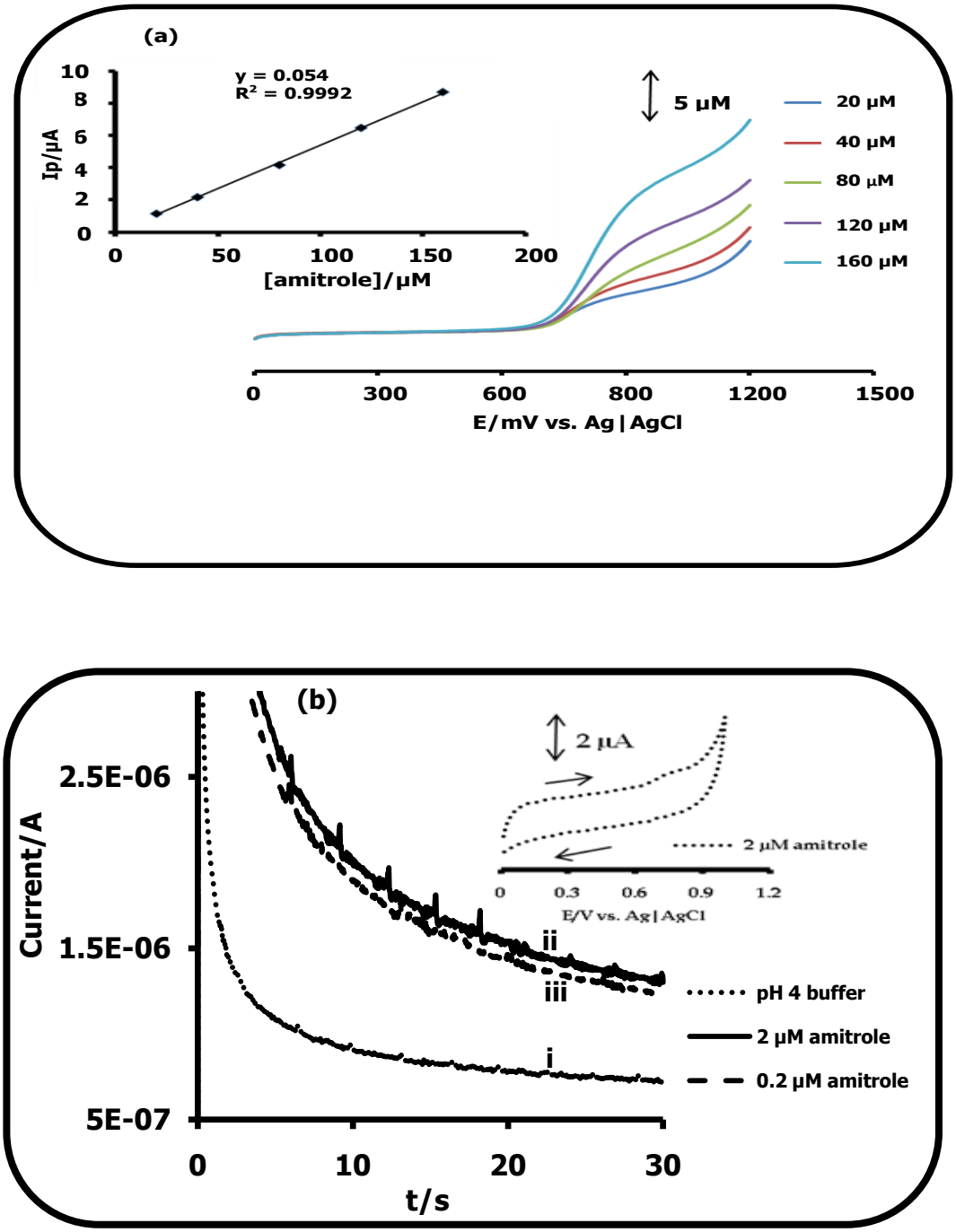

Figure 5.17: (a) RDE evolutions for different concentrations of amitrole at 1000 rpm at a CoTCPc-EA-SWCNT(linked)-GCE at a sensitivity of 10 µA/V. Scan rate = 20 mV/s. (b) Chronoamperograms for (i) pH 4 buffer, (ii) 2 µM amitrole (pH 4 buffer) and (iii) 0.2 µM amitrole (pH 4 buffer). Inset: Cyclic voltammogram for the 2 µM amitrole in pH 4 buffer.

Rotating disk electrode voltammetry (RDE) and chronoamperometry were used to deduce the sensitivity of CoTCPc-EA-SWCNT(linked)-GCE towards amitrole (Fig. 5.17). The linear dynamic range was from 1 x 10^{-5} M – 1.6 x 10^{-4} M with the sensitivities for RDE voltammetry and chronoamperometry being 0.76 A mol^{-1} L cm^{-2} and 0.75 A mol^{-1} L cm^{-2}, (the latter in Table 5.2) respectively. The similarities of these sensitivities indicate the reliability of these two techniques as analytical tools in the determination of amitrole. The limit of detection of amitrole was found to be 0. 10 μM using the 3δ notation, which is lower than what has been observed elsewhere [78,257,311] and also lower than what was on FeTAPc-SWCNT(linked)-GCE, Table 5.2. For diuron, the limit of detection was 0.16 μM with a sensitivity of 0.82 A mol^{-1} L cm^{-2}, Table 5.2.

Fig. 5.17b, shows the chronoamperograms obtained for CoTCPc-EA-SWCNT(linked)-GCE in pH 4 buffer, 2 μM amitrole (pH 4 buffer) and 0.2 μM amitrole (pH 4 buffer). Using chronoamperometry, levels below 0.2 μM amitrole could be detected. The inset in Fig. 5.17b shows a cyclic voltammogram for 2 μM amitrole, an indication that very low concentrations of amitrole could be detected at CoTCPc-EA-SWCNT(linked)-GCE.

Zen and co-workers observed a relatively low detection of 0.15 ng/20 μL of sample for amitrole using a flow injection method [257]. Chicharro and co-workers got a higher detection limit than obtained in this study [78] using a flow injection technique. From these observations we can conclude that it is the nature of the electrode and not necessarily the technique which is important in the detection of amitrole. Therefore the lower detection limits observed on CoTCPc-EA-SWCNT(linked)-GCE makes it a good electrode for the electrochemical detection of amitrole.

The selectivity of CoTCPc-EA-SWCNT(linked)-GCE for amitrole was done in the presence of diuron (whose oxidation potential is close to that of amitrole) using the mixed solution method [248]. The value of K_{amp} was determined from Eq. (5.5) (using 1×10^{-4} M for both diuron (interferent) and amitrole). For an equimolar solution of amitrole and diuron, the K_{amp} values of $(2.2 \pm 0.10) \times 10^{-1}$ were obtained, indicating that diuron is a very strong interferent, thus the electrode cannot be used

for the detection of both amitrole and diuron as already observed for FeTAPc-SWCNT(linked) above. Non-selectivity was further confirmed using cyclic voltammetry. In the presence of diuron, only one oxidation peak was observed, at a more positive potential than that for the oxidation of amitrole but less than that for the oxidation of diuron. In a suspected mixture of amitrole and diuron we would recommend HPLC separation to precede the determination.

5.3.7 Electrochemical impedance spectroscopy (EIS)

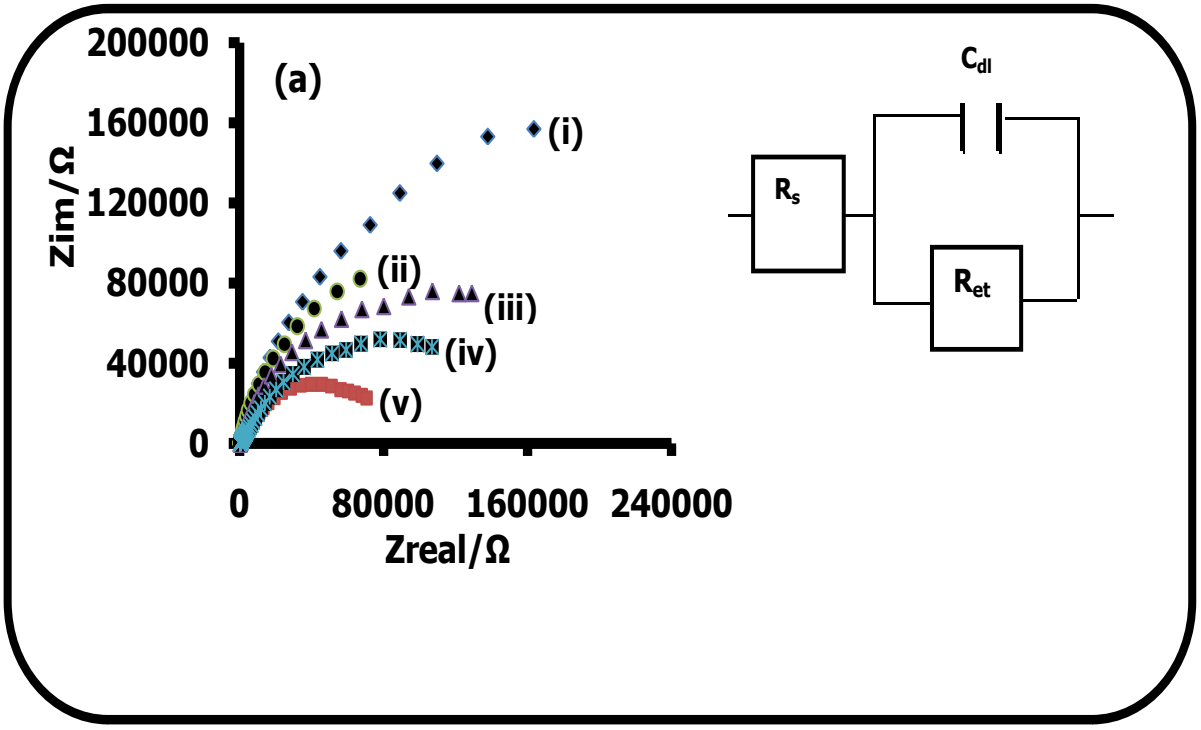

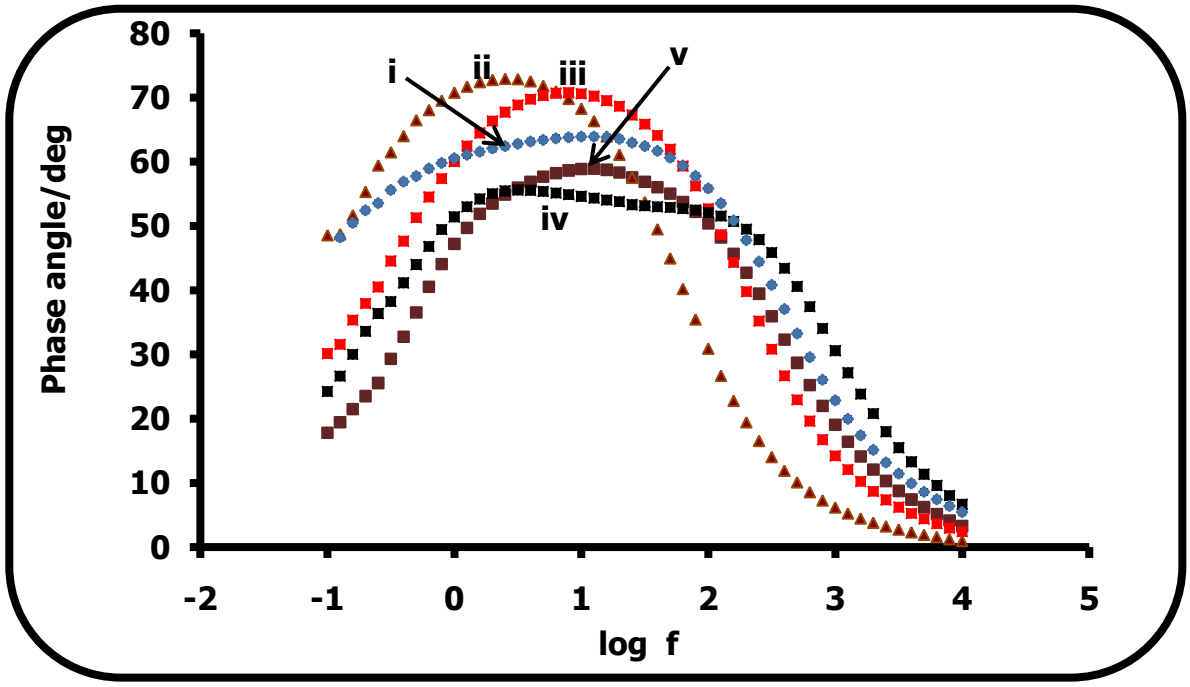

Figure 5.18: (a) Nyquist and (b) Bode (phase angle versus log f) plots obtained for (i) bare GCE, (ii) CoTCPc/EA-SWCNT(mix), (iii) CoTCPc, (iv) EA-SWCNT and (v) CoTCPc-EA-SWCNT(linked) in 0.1 mM amitrole (pH 4 buffer). Inset: Suggested Randle equivalent circuit model for the impedance spectra.

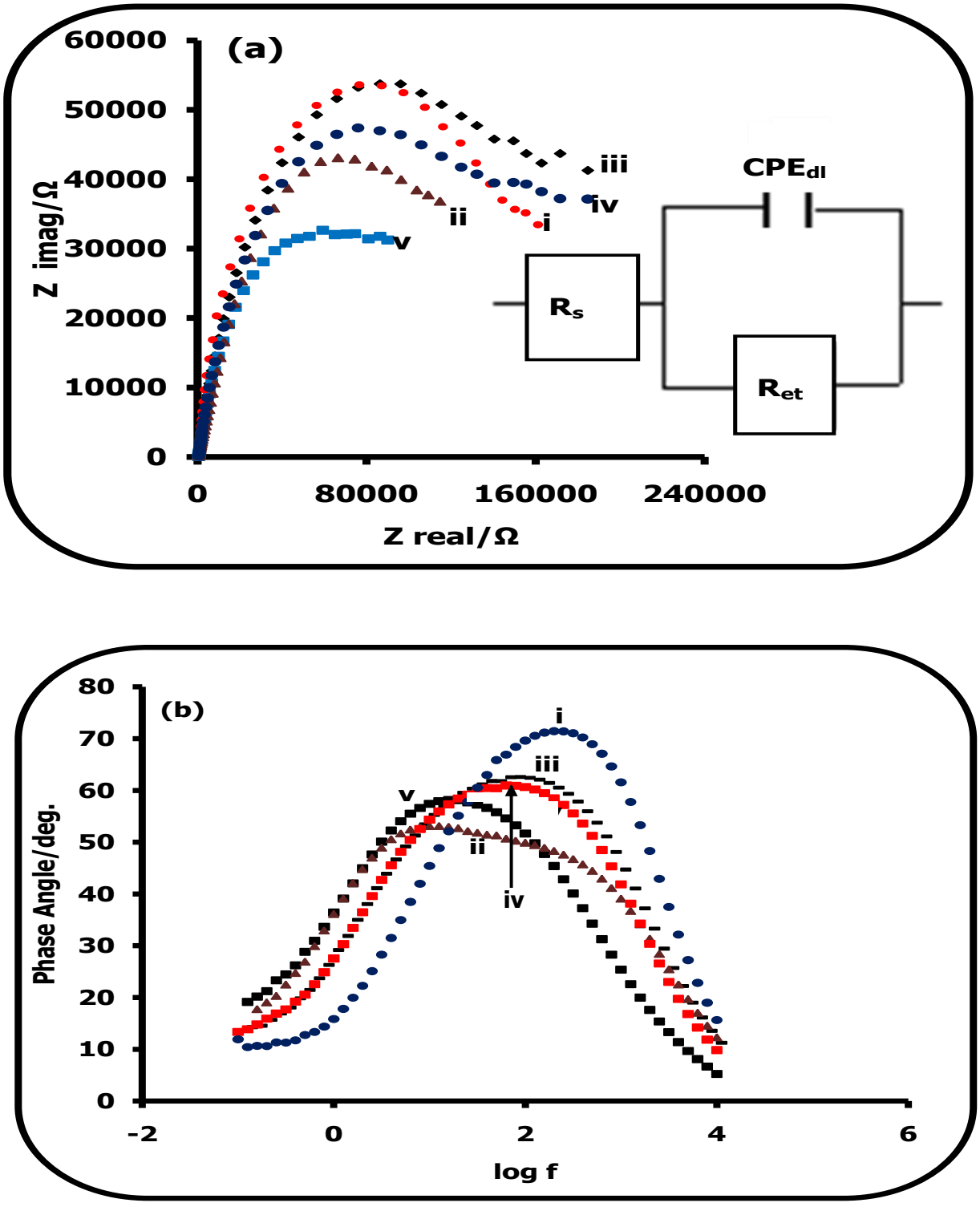

Figure 5.19: (a) Nyquist and (b) Bode (phase angle versus log f) plots obtained for (i) bare GCE, (ii) CoTCPc/EA-SWCNT(mix), (iii) CoTCPc, (iv) EA-SWCNT and (v) CoTCPc-EA-SWCNT(linked) in 0.16 mM diuron (pH 4 buffer). Inset: Suggested Randle equivalent circuit model for the impedance spectra.

Table 5.3: Estimated EIS parameters obtained for the different electrodes.

Electrode	Analyte	R_{et} (kΩ)	n	k_{app} (cm s^{-1})
Bare GCE	Amitrole	402.0	0.85	6.62×10^{-6}
	Diuron	160.8	0.86	1.03×10^{-6}
CoTCPc-GCE	Amitrole	181.6	0.85	1.47×10^{-5}
	Diuron	171.3	0.78	9.71×10^{-6}
EA-SWCNT-GCE	Amitrole	175.4	0.70	1.50×10^{-5}
	Diuron	150.5	0.80	1.11×10^{-5}
CoTCPc/EA-SWCNT(mix)-GCE	Amitrole	161.8	0.88	1.64×10^{-5}
	Diuron	155.4	0.68	1.10×10^{-5}
CoTCPc-EA-SWCNT(linked)-GCE	Amitrole	87.6	0.76	3.00×10^{-5}
	Diuron	105.3	0.75	1.58×10^{-5}

Electrochemical impedance spectroscopy (EIS) was used to probe the redox and structural features of a surface confined species [245] in the presence of analytes. Figs. 5.18a and 5.19a displays the Nyquist plots obtained in 0.1 mM and 0.16 mM of amitrole and diuron, respectively. The bare GCE, CoTCPc-GCE, CoTCPc-EA-SWCNT(linked)-GCE, CoTCPc/EA-SWCNT(mix) and EA-SWCNT-GCE displayed identical semi-circular Nyquist plots. These semi-circles represent a combination of charge-transfer resistance and the double layer capacitance of the electrode modifiers [236] and are in agreement with kinetically controlled movement of electrons [68]. The origin of the semi-circles in Nyquist plots has been attributed to microscopic roughness, which brings heterogeneity in solution resistance and the double layer capacitance [237]. A very large semi-circle at higher frequencies was observed for the bare GC electrode in the presence of amitrole (highest charge transfer resistance), followed by CoTCPc-GCE, EA-SWCNT-GCE, CoTCPc/EA-SWCNT(mix) and the CoTCPc-EA-SWCNT(linked)-GCE in that order (Fig. 5.18a). On diuron the charge transfer resistance for bare GCE is approximately equal to that of CoTCPc-GCE and the order is as follows: CoTCPc-GCE ~ bare GCE > CoTCPc/EA-SWCNT(mix) > EA-SWCNT-GCE > CoTCPc-EA-SWCNT(linked)-GCE (Table 5.3). The circuit compatible with these electrodes from the given Nyquist plots

is shown in Figs. 5.18a and 5.19a, as insets. R_s, CPE_{dl} and R_{et} represent solution resistance, a constant phase element (corresponding to the double layer capacitance) and the charge-transfer resistance, respectively. At the frequency region of the impedance under study, the charge-transfer resistance (R_{et}) decreased (except for CoTCPc on diuron) due to facilitation of the electron transfer by the electrode modifiers, Table 5.3, an indication that films form high electron conduction pathways between the electrode and electrolyte/analyte as observed elsewhere [238]. The Nyquist plots of CoTCPc-EA-SWCNT(linked)-GCE have the lowest charge-transfer resistances (smallest diameters) with values of 87.6 and 105.3 kΩ for amitrole and diuron, respectively (Table 5.3) and hence the highest oxidation currents observed on both amitrole and diuron, respectively, at reduced overpotentials (Figs. 5.11 and 5.12). These charge transfer resistance data proves that amitrole is oxidized at lower potentials than diuron, which is in agreement with cyclic voltammetry, Figs. 5.11 and 5.12.

The n – values are in the range 0.68 – 0.88 which is < 1, confirming the non-capacitative nature of the electrode modifiers.

The apparent electron transfer rate constants, k_{app}, were obtained using Eq. 5.14 [239].

$$k_{app} = RT/F^2 R_{et} C \quad (5.14)$$

where C is the concentration ((amitrole, 1.0 x 10^{-7} mol cm^{-3}) and (diuron, 1.6 x 10^{-7} mol cm^{-3})), with R, T and F having their usual meanings. As reflected in its k_{app} and R_{et} values, CoTAPc-EA-SWCNT(linked)-GCE exhibited fastest electron transfer processes towards both amitrole and diuron compared to other electrodes investigated in this work, Table 5.3. Generally the presence of an electrocatalyst facilitates electron transfer at the electrode|analyte interface as shown by increases in the values of k_{app}, Table 5.3.

The Bode plots (plot of phase-shift (θ) versus the log *frequency*), Figs. 5.17b and 5.18b, were used to obtain frequency related information, which cannot be obtained from their Nyquist plots. The nature of the Bode plots confirmed the structural differences of the GCE modified electrodes and the bare GCE. The bare GCE showed unsymmetrical peak with a maximum value of ~63.9^0 at 12.59 Hz (Fig.

5.18i) corresponding to the relaxation process of the GCE|amitrole interface. After modification of GC electrodes with CoTCPc, EA-SWCNT, CoTCPc-EA-SWCNT(linked) and CoTCPc/EA-SWCNT(mix), all the peaks shifted towards lower frequencies for the relaxation processes of the modifier-GCE|amitrole interfaces, with the EA-SWCNT spectrum showing a broad band which stretches from lower frequencies to higher frequencies. The relaxation process of the CoTCPc-EA-SWCNT-GCE|amitrole interface was at a phase angle of 58.8^0 and a frequency of 15.8 Hz (Fig. 5.18v). The relaxation process for diuron on CoTCPc-EA-SWCNT electrode occurred at the same frequency as that for amitrole but a slightly lower phase angle (57.3^0), Fig. 5.19v. This confirms that oxidations of amitrole and diuron occur at slightly different potentials as shown by cyclic voltammetry (Figs. 5.11 and 5.12, Table 5.2). Changes in phase angles and frequencies confirmed that the oxidation of both amitrole and diuron was taking place at modified platform rather than on the bare GCE surface. Both the Nyquist and the Bode plots confirmed the poor electron transfer kinetics for the CoTCPc-GCE for both amitrole and diuron (Figs. 5.18 and 5.19, Table 5.3).

5.4 CoTCPc-PA-SWCNT(linked)

As with CoTCPc-EA-SWCNT(linked), the electrode was used for amitrole and diuron, Table 5.1. CV, CA, RDE and EIS were employed.

5.4.1 Cyclic voltammetry

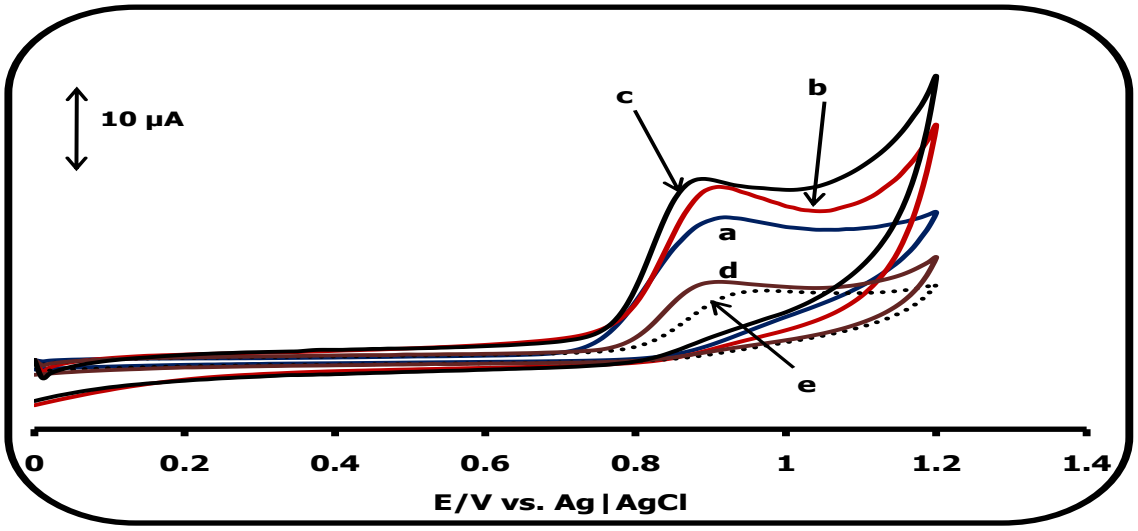

Figure 5.20: Cyclic voltammograms for the bare GCE and the modified electrodes for 0.2 mM diuron in pH 4 buffer: (a) bare GCE, (b) CoTCPc/PA-SWCNT(mix)-GCE, (c) CoTCPc-PA-SWCNT(linked)-GCE, (d) PA-SWCNT-GCE and (e) CoTCPc-GCE. Scan rate = 100 mV/s.

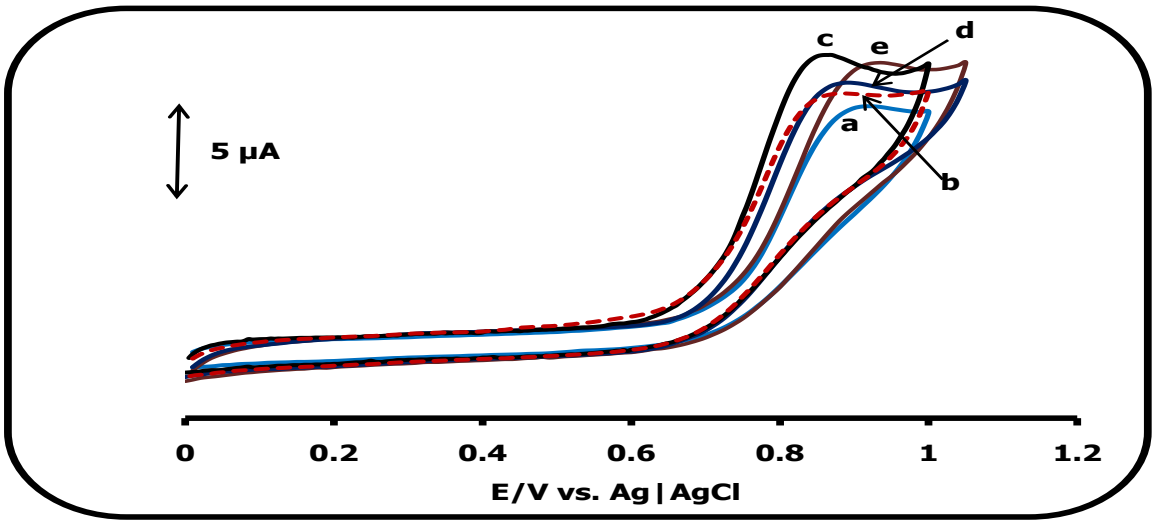

Figure 5.21: Cyclic voltammograms for the bare GCE and the modified electrodes for 0.16 mM amitrole in pH 4 buffer: (a) bare GCE, (b) CoTCPc/PA-SWCNT(mix)-GCE, (c) CoTCPc-PA-SWCNT(linked)-GCE, (d) PA-SWCNT-GCE and (e) CoTCPc-GCE. Scan rate = 100 mV/s.

The comparative cyclic voltammetric responses for diuron and amitrole on bare GCE (a), CoTCPc/ PA-SWCNT(mix)-GCE (b), CoTCPc-PA-SWCNT(linked)-GCE (c), PA-SWCNT-GCE (d) and CoTCPc-GCE (e) are shown in Figs. 5.20 and 5.21, respectively. Peaks in the region 0.8 – 1.0 V are due to the oxidation of amitrole and diuron as observed elsewhere [78,306,307,311]. The oxidation potentials for diuron at bare GCE, CoTCPc-PA-SWCNT(linked)-GCE, CoTCPc/PA-SWCNT(mix)-GCE, PA-SWCNT-GCE and CoTCPc-GCE are 0.92 V, 0.87 V (Table 5.2), 0.90 V, 0.92 V and 0.97 V (versus Ag|AgCl), respectively. For amitrole the potentials for the bare GCE, CoTCPc-PA-SWCNT(linked)-GCE, CoTCPc/PA-SWCNT(mix)-GCE, PA-SWCNT-GCE and CoTCPc-GCE are 0.90 V, 0.82 V (Table 5.2), 0.86 V, 0.89 V and 0.95 V, respectively. The CoTCPc-PA-SWCNT(linked)-GCE (Figs. 5.20c and 5.21c), shows higher oxidation currents (though not too different from the CoTCPc/PA-SWCNT(mix)-GCE for diuron) at reduced oxidation overpotentials compared to other modified electrodes, confirming better catalytic properties. The sharper rise in current for CoTCPc-PA-SWCNT(linked)-GCE on both amitrole and diuron shows its good catalytic activity. The oxidation potentials of both amitrole and diuron coincide with $Co^{III}Pc^{-1}/Co^{III}Pc^{-2}$ process of the phthalocyanine (see Fig. 4.7e), therefore the $Co^{III}Pc^{-1}$ species are involved in the catalysis. In short the involvement of SWCNTs and MPcs in the oxidation of both amitrole (Figs. 5.21b and c) and diuron (Figs. 5.20b and c) is accompanied by reduced oxidation overpotentials and high catalytic currents. For CoTCPc and PA-SWCNT modified GCE, there is no catalytic activity for diuron (as judged by the lower currents compared to the bare GCE), while CoTCPc-GCE is not catalytic towards amitrole because of its more positive oxidation potential relative to the bare GCE. Compared to CoTCPc-EA-SWCNT(linked), the oxidation of amitrole and diuron on CoTCPc-PA-SWCNT(linked) occur at about the same potential, showing little or no effect of EA or PA. The potentials were also compared with those of CoTAPc-SWCNT(linked), Table 5.2, not discussed in detail in this work. In both CoTCPc-PA-SWCNT(linked) and CoTCPc-EA-SWCNT(linked), the CoTCPc is chemically linked to SWCNTs carrying amino groups, while in CoTAPc-SWCNT(linked) the SWCNTs are carrying the carboxylic acid groups. The amino group is electron donating, while the

carboxylic group is electron withdrawing. The amino groups lower the oxidation potential of Co, while electron withdrawing groups have an opposite effect. As a result both PA-SWCNTs and EA-SWCNTs reduced the amitrole oxidation potentials more than SWCNT-COOH. Amitrole was oxidized at 0.83 V, 0.82 V and 0.98 V (versus Ag|AgCl) on CoTCPc-EA-SWCNT(linked)-GCE, CoTCPc-PA-SWCNT(linked)-GCE and CoTAPc-SWCNT(linked)-GCE, respectively, Table 5.2. Such large differences in potential (>120 mV) indicate that both CoTCPc-EA-SWCNT(linked) and CoTCPc-PA-SWCNT(linked) have better electro-catalytic properties compared to CoTAPc-SWCNT(linked). The potentials for CoTCPc-EA-SWCNT(linked) and CoTCPc-EA-SWCNT(linked) are slightly improved compared to FeTAPc-SWCNT(linked) and there is a very high improvement compared to *poly*-Ni(OH)TAPc (for diuron). The poor catalytic activity of CoTCPc has been reported before [229].

5.4.2 Electrode stability

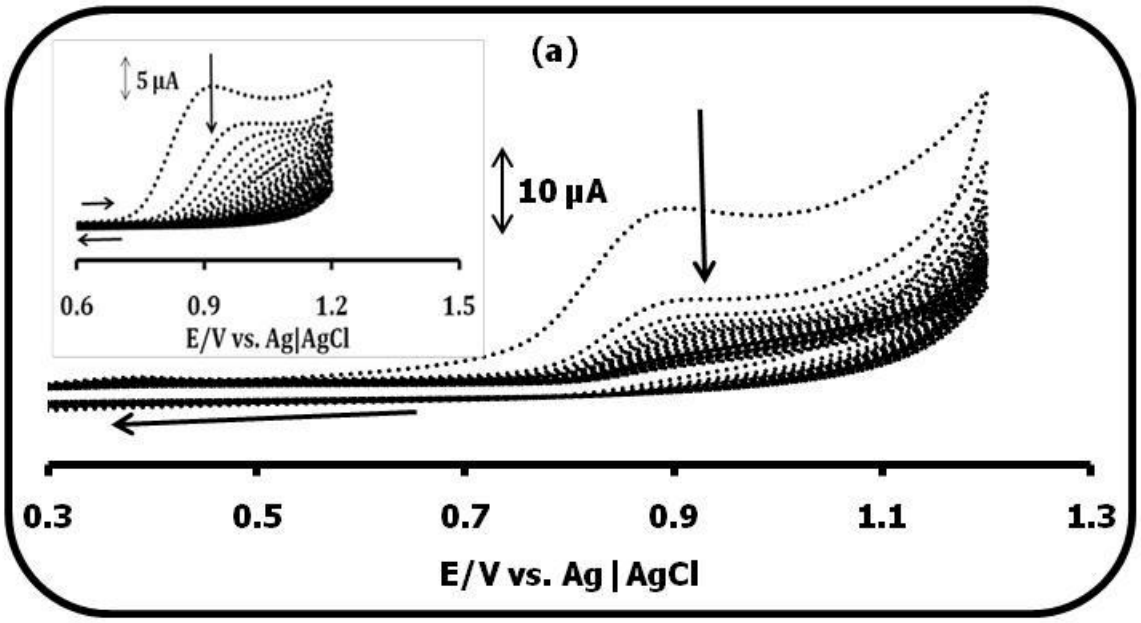

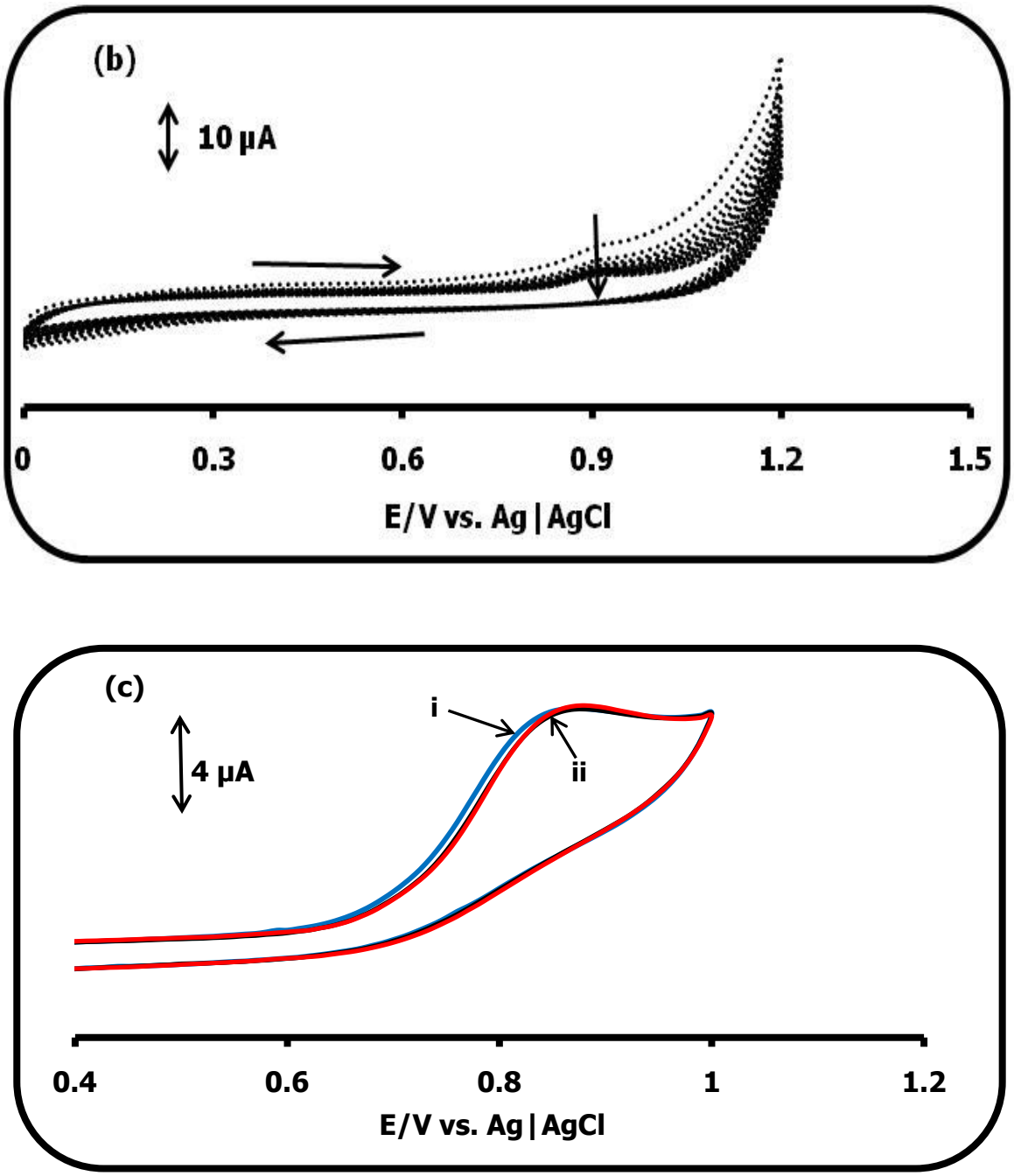

Figure 5.22: (a) Cyclic voltammograms showing the behaviour of the CoTCPc-PA-SWCNT(linked) electrode on continuous cyclisation in 0.2 mM diuron (pH 4 buffer). Inset: Behaviour of bare GCE in 0.2 mM diuron. (b) Cyclic voltammograms obtained during the conditioning of the CoTCPc-PA-SWCNT(linked)-GCE through continuous cyclisation in pH 4 buffer and (c) CoTCPc-PA-SWCNT(linked) regeneration voltammograms (in 0.16 mM amitrole) after conditioning. Scan rate = 100 mV/s.

Figure 5.22a shows 30 cycle continuous scan voltammograms for CoTCPc-PA-SWCNT(linked)-GCE in 0.2 mM diuron. A drop of 46% in peak current from cycle 1 to 2, followed by the stabilization of the currents was observed. The large drop in peak current shows the high passivating nature of the diuron oxidation products on CoTCPc-PA-SWCNT(linked). Figure 5.21a, inset, shows the behaviour of the bare GCE on continual cyclisation in 0.2 mM diuron. A drop of 54% from cycle 1 to 2 and a shift in peak potentials towards the positive values was observed on the bare GCE. Thus in terms of the initial passivation CoTCPc-PA-SWCNT(linked) is not too different from the bare GCE, however no shifts in peak potential were observed for the former during continuous scanning. This is an indication that CoTCPc-PA-SWCNT(linked)-GCE is a better electrode than the bare GCE. Resistance to passivation (due to diuron oxidation products) was measured as % current drop from scan 1 to 2, and the order was as follows: CoTCPc (32%) > PA-SWCNT (43%) > CoTCPc/PA-SWCNT(mix)-GCE (45%) ≅ CoTCPc-PA-SWCNT(linked)-GCE (46%) > bare GCE (54%). However, CoTCPc and PA-SWCNT are not catalytic. The trend in resistance to passivation for amitrole (from scan 1 to 2) is as follows: PA-SWCNT (24%) > CoTCPc (26%) > bare GCE (29%) > CoTCPc/PA-SWCNT(mix)-GCE (31%) > CoTCPc-PA-SWCNT(linked)-GCE (44%). Thus for amitrole, CoTCPc-PA-SWCNT(linked) is the least stable, but shows approximately the same stability as for diuron. The differences in stability could be due to the differences in the extents of interaction between the electrodes and the oxidation products. After use the electrode was conditioned by scanning it in pH 4 buffer solution (after cleaning by shaking in methanol) through cyclic voltammetry in the potential window 0.0-1.2 V (versus Ag|AgCl) until stable currents were observed (Fig. 5.22b). The success of the regeneration was monitored by re-running the electrode in the analyte (Fig. 5.22c regenerated for amitrole). On continual use and storage in pH 4 buffer, the electrode has a life span of more than 2 months for both.

5.4.3 Tafel slopes

Plots of peak current versus the root of scan rate (similar to Fig. 5.5b) for the oxidation of amitrole and diuron on CoTCPc-PA-SWCNT(linked)-GCE, were linear

confirming that their oxidations are governed by the rate at which they diffuse towards the CoTCPc-PA-SWCNT(linked)-GCE|solution interface from the bulk solution.

Using Eq. 5.1 and plots of Ep versus log v (similar to Fig. 5.5a), Tafel slopes of 166 and 197 mV decade^{-1} were obtained for diuron and amitrole, respectively., suggesting a one electron transfer during the rate determining step. As stated before Tafel slopes higher that 30-120 mV/decade have been observed either for chemical reactions coupled to electrochemical steps [97] or to substrate-catalyst interactions in a reaction intermediate [257,303,304]. The lower Tafel slopes on CoTCPc-PA-SWCNT(linked) compared to CoTCPc-EA-SWCNT(linked) suggest less interaction between the analytes and the electrode for the former. The electron transfer coefficients (**α**) for amitrole and diuron were found to be 0.70 and 0.65 (Table 5.2), respectively, indicating higher probabilities of the activated complexes being converted to the products. From a plots of log I_p versus log [diuron] (similar to Fig. 5.9), the electro-catalysis of amitrole and diuron were found to be approximately first order, implying that one analyte molecule interacts with one molecule of CoTCPc-PA-SWCNT(linked). Using the above information, the proposed mechanism is as given in Scheme 5.2 (using diuron as an example), which is similar to Scheme 5.1 except for CoTCPc instead of Ni(OH)TAPc.

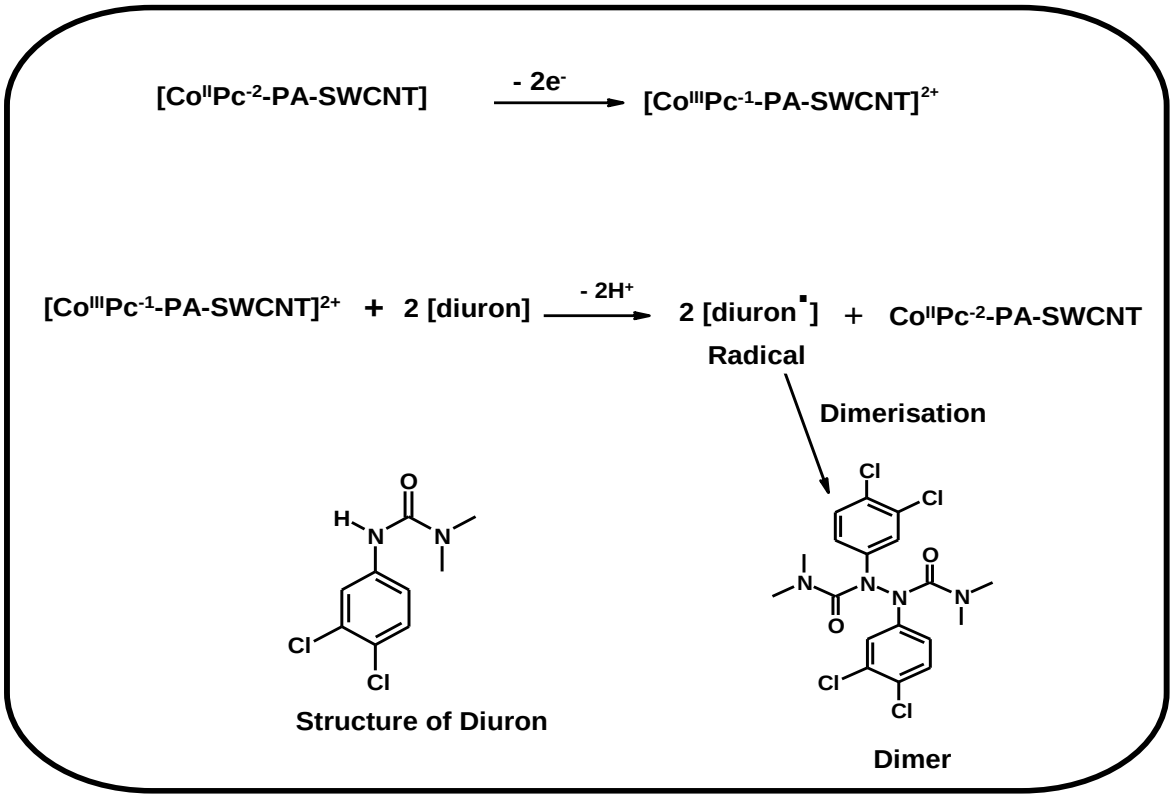

Scheme 5.2: Mechanism for the CoTCPc-PA-SWCNT(linked) mediated oxidation of diuron.

5.4.4 Chronoamperometric studies

Using plots similar to Fig. 5.6 but for CoTCPc-PA-SWCNT(linked) and Eq. 5.3, *k* values of 4.4 x 10^3 and 3.58 x 10^3 M^{-1} s^{-1} were obtained for diuron and amitrole, respectively, Table 5.2. These values are smaller than 1.79 x 10^4 and 5.88 x 10^4 M^{-1} s^{-1} obtained on FeTAPc-SWCNT(linked) and CoTCPc-EA-SWCNT(linked) for diuron, respectively. The rate of oxidation of diuron on CoTCPc-PA-SWCNT(linked)-GCE is therefore slower than on both FeTAPc-SWCNT(linked) and CoTCPc-EA-SWCNT(linked) electrodes. These values obtained on CoTCPc-EA-SWCNT(linked) are however larger than that obtained on *poly*-Ni(OH)TAPc for diuron, Table 5.2, possibly due to the presence of SWCNTs. Rate of oxidation of amitrole is lower on CoTCPc-EA-SWCNT(linked)-GCE relative to CoTCPc-PA-SWCNT(linked)-GCE and FeTAPc-SWCNT(linked)-GCE

Chronoamperometry was used to deduce the sensitivities of CoTCPc-PA-SWCNT(linked)-GCE towards amitrole and diuron. The linear dynamic range was

from 1 x 10^{-5} M – 2.0 x 10^{-4} M (for both), with a sensitivities of 0.42 and 0.51 A mol^{-1} L cm^{-2} and the limits of detection of 0.18 and 0.14 μM (using the 3δ notation) for diuron and amitrole, respectively. For diuron this LOD is lower than what has been observed elsewhere [307]. These LODs are lower (for both amitrole and diuron) than what was observed on FeTAPc-SWCNT(linked)-GCE or 0.33 μM for *poly*-Ni(OH)TAPc (for diuron), Table 5.2, but slightly higher than for CoTCPc-EA-SWCNT(linked).

5.4.5 RDE studies

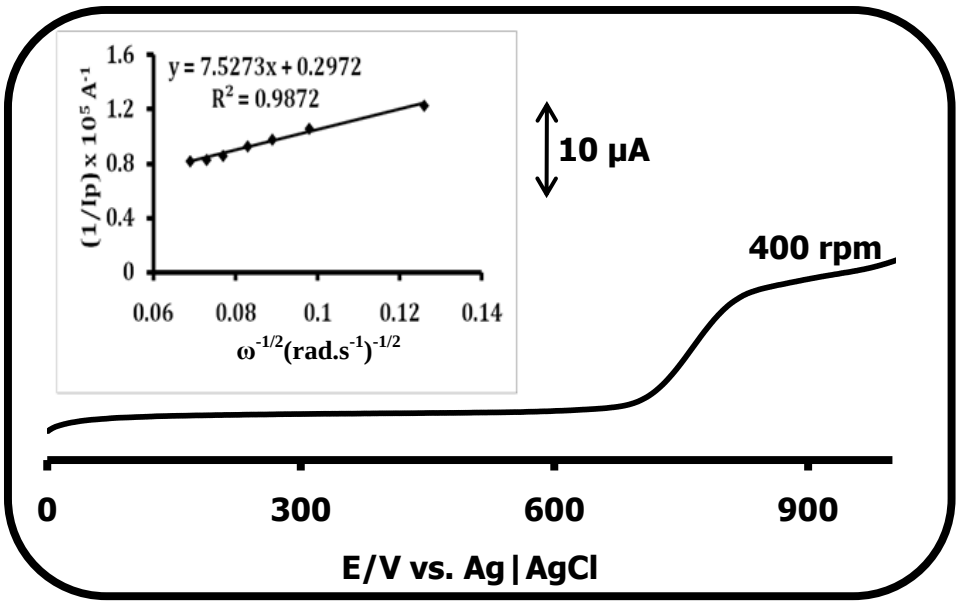

Figure 5.23: Rotating disc electrode linear voltammetry evolution (400 rpm) for 1.6 x 10^{-4} M diuron in pH 4 buffer at the CoTCPc-PA-SWCNT(linked)-GCE with a sensitivity of 10 μA/s. Inset: Koutecky-Levich plot. Scan rate = 20 mV/s.

Figure 5.23 shows the RDE linear voltammogram evolved for 1.6 x 10^{-4} M diuron in pH 4 buffer, at a rotational speed of 400 rpm on the CoTCPc-PA-SWCNT(linked)-GCE. Using the Koutecky-Levich theory (Eq. 5.9), a linear relationship between the inverse of catalytic current and $\omega^{-1/2}$ with a positive intercept (Fig. 5.23, inset) confirms that the oxidation of diuron is controlled more by kinetics than diffusion [313]. Similar observations were made for amitrole.

From a plot of potential versus log I_k at 2000 rpm (similar to Fig. 5.16), a Tafel slope of 183 mV decade^{-1} ($\boldsymbol{\alpha}$ = 0.68) was obtained for amitrole, which is close to 197 mV decade^{-1} ($\boldsymbol{\alpha}$ = 0.70) obtained using cyclic voltammetry data. A rotational speed of 2000 rpm was used because beyond this speed, the limiting current became independent of rotational speed of the electrode. This suggests a one electron transfer during the rate determining step preceding a chemical step and thus confirms a similar mechanism to the one given in Scheme 5.2 for diuron.

5.4.6 Electrochemical impedance spectroscopy

The impedance spectra are only shown for diuron, since they are similar to those for amitrole. The data for both amitrole and diuron is also given in Table 5.4.

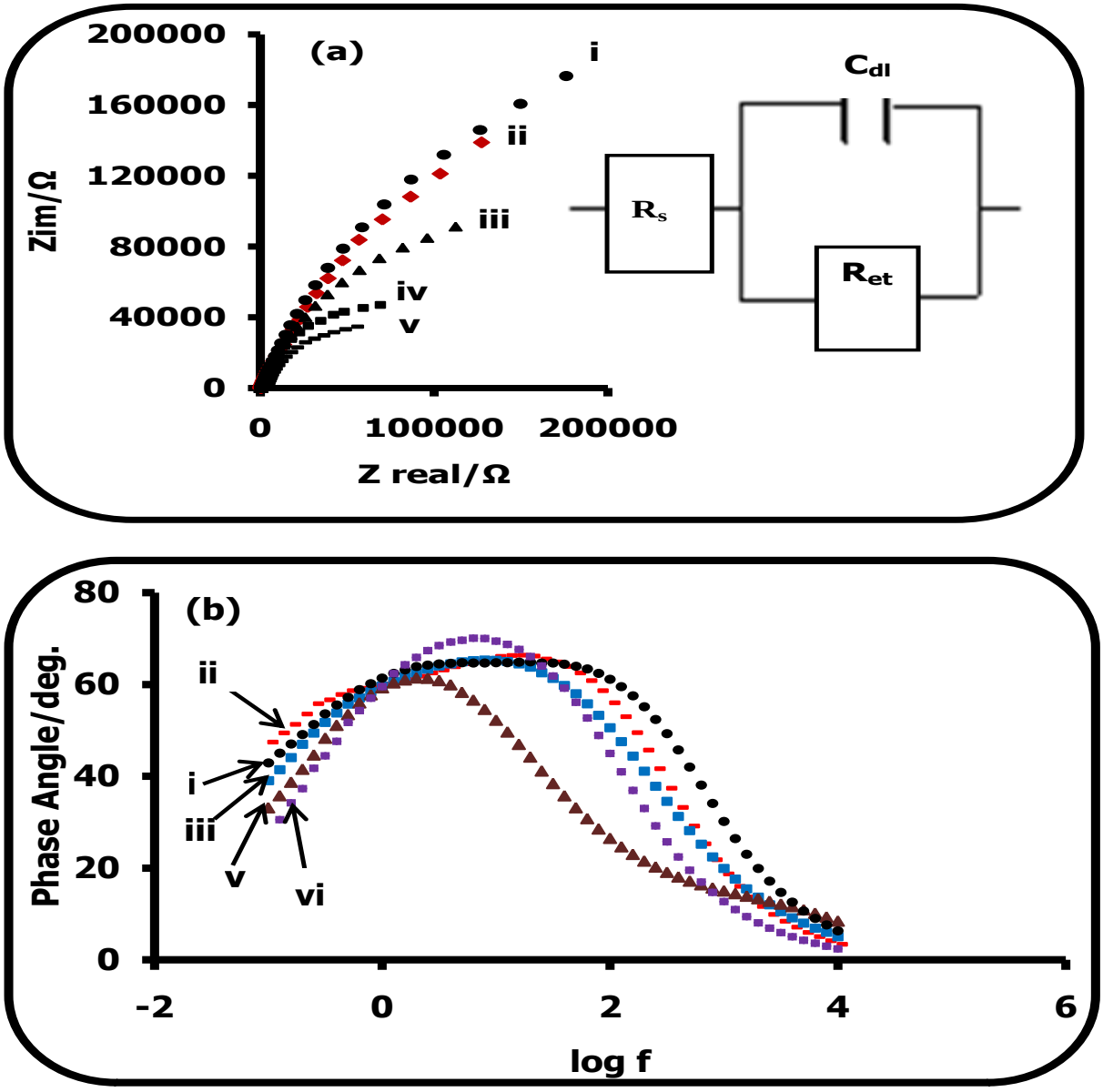

Figure 5.24: (a) Nyquist and (b) Bode (Phase angle versus log f) plots for (i) CoTCPc-GCE, (ii) bare GCE, (iii) PA-SWCNT-GCE, (iv) CoTCPc/PA-SWCNT(mix)-GCE and (v) CoTCPc-PA-SWCNT(linked)-GCE. Inset: Suggested Randle equivalent circuit model for the impedance spectra.

Table 5.4: Estimated EIS parameters obtained for the different electrodes.

Electrode	Analyte	R_{et}(kΩ)	n	k_{app} (cm s^{-1})
Bare GCE	Diuron	360	0.79	6.16×10^{-6}
	Amitrole	389	0.76	4.28×10^{-6}
CoTCPc-GCE	Diuron	518	0.79	4.28×10^{-6}
	Amitrole	398	0.83	4.18×10^{-6}
PA-SWCNT-GCE	Diuron	245	0.78	9.05×10^{-6}
	Amitrole	185	0.80	9.00×10^{-6}
CoTCPc/ PA-SWCNT(mix)-GCE	Diuron	130	0.84	17.1×10^{-6}
	Amitrole	116	0.85	1.43×10^{-5}
CoTCPc-PA-SWCNT(linked)-GCE	Diuron	120	0.73	18.5×10^{-6}
	Amitrole	105	0.78	1.58×10^{-5}

Figure 5.24a displays the EIS (Nyquist plots) obtained in 0.1 mM diuron. The bare GCE, CoTCPc-GCE, CoTCPc-PA-SWCNT(linked)-GCE and PA-SWCNT-GCE displayed identical semi-circular Nyquist plots, with CoTCPc-GCE showing a very large semi-circle at higher frequencies (highest charge-transfer resistance). The order in terms of charge-transfer resistance is as follows: CoTCPc-GCE > bare GCE > PA-SWCNT-GCE > CoTCPc/PA-SWCNT(mix)-GCE > CoTCPc-PA-SWCNT(linked)-GCE. As had been observed from RDE studies, EIS also confirmed that catalysis of amitrole and diuron are kinetically controlled. The absence of a straight portion (for diffusion process) in the Nyquist plot, shows that the overall impedance is dominated by the charge-transfer process (kinetics). The suggested Randle equivalent circuit model for the impedance spectra is given as an inset in Fig. 5.24a. R_s, CPE_{dl} and R_{et} represent solution resistance, a constant phase element (corresponding to the double layer capacitance) and the charge-transfer resistance, respectively. With the exception of CoTCPc-GCE, generally the charge-transfer resistance (R_{et}) decreased due to facilitation of the electron transfer by the electrode modifiers, Table 5.2, an indication that films form high electron conduction

pathways between the electrode and electrolyte/analyte as stated before. The poor electron transfer properties of CoTCPc that have been confirmed through impedance were also observed through cyclic voltammetry, Figs. 5.20e and 5.21e, for diuron and amitrole, respectively. The Nyquist plot of CoTCPc-PA-SWCNT(linked)-GCE has the lowest charge-transfer resistance (smallest diameter) with a value of 120 kΩ for diuron and 105 kΩ for amitrole (Table 5.4), hence the highest oxidation currents of diuron and amitrole at reduced overpotentials as shown in Figs. 5.20c and 5.21c, respectively.

All the n – values were less than 1, Table 5.4, confirming the non-capacitative nature of the electrode modifiers.

The apparent electron transfer rate constants, k_{app}, were obtained using Eq. (5.14) [239], with the concentrations (C) of 1.0 x 10^{-7} and 1.6 x 10^{-7} mol cm^{-3} for diuron and amitrole, respectively. As reflected in its k_{app} and R_{et} values (Table 5.4), CoTCPc-PA-SWCNT-GCE exhibited fastest electron transfer processes towards both amitrole and diuron compared to other electrodes investigated in this section. This has also been confirmed by cyclic voltammetry (Figs. 5.20 and 5.21). However the rate of oxidation of amitrole on CoTCPc-PA-SWCNT(linked) is faster than that of diuron, as shown by the k_{app} values, Table 5.4. Similar observations were made for the oxidation of amitrole on CoTCPc-EA-SWCNT(linked) electrode, Table 5.3. Just like cyclic voltammetry, EIS studies showed that the CoTCPc-EA-SWCNT(linked) is a better electrode for the oxidation of both amitrole and diuron, Tables 5.3 and 5.4.

Fig. 5.24b shows the Bode plot for diuron on CoTCPc-PA-SWCNT(linked)-GCE. The nature of these Bode plots confirms the structural differences of the GCE modified electrodes and the bare GCE. The bare GCE showed unsymmetrical peak with a maximum value of ~64^0 at 50.1 Hz corresponding to the relaxation process of the GCE|diuron interface. PA-SWCNT-GCE, CoTCPc-PA-SWCNT(linked)-GCE and CoTCPc/PA-SWCNT(mix)-GCE have their peaks shifted towards lower frequencies (compared to GCE) for the relaxation processes of the modifier-GCE|diuron interfaces, with the CoTCPc-PA-SWCNT(linked)-GCE showing greatest shift. CoTCPc shows a broad peak. Increase in the phase angles relative to the bare GCE were noted for CoTCPc/PA-SWCNT(mix)-GCE (70^0) and a decrease for CoTCPc-PA-

SWCNT(linked)-GCE at 62^0, with the rest of the electrodes remaining at almost the same phase angles though at lower frequencies. Similar Bode plots were obtained for amitrole. The changes in phase angles and frequencies confirmed that the oxidation processes were taking place at modified surfaces rather than on the bare GCE surface.

5.5 CoMAPc-SWCNT(linked)

This electrode was used for both amitrole and diuron, Table 5.1. CV, CA and RDE were employed in these studies. EIS studies were not done since the effect of linking MPcs to SWCNTs on the rate of electron transfer was elucidated using CoTCPc-PA-SWCNT(linked) and CoTCPc-EA-SWCNT(linked) on these analytes.

5.5.1 Cyclic voltammetry

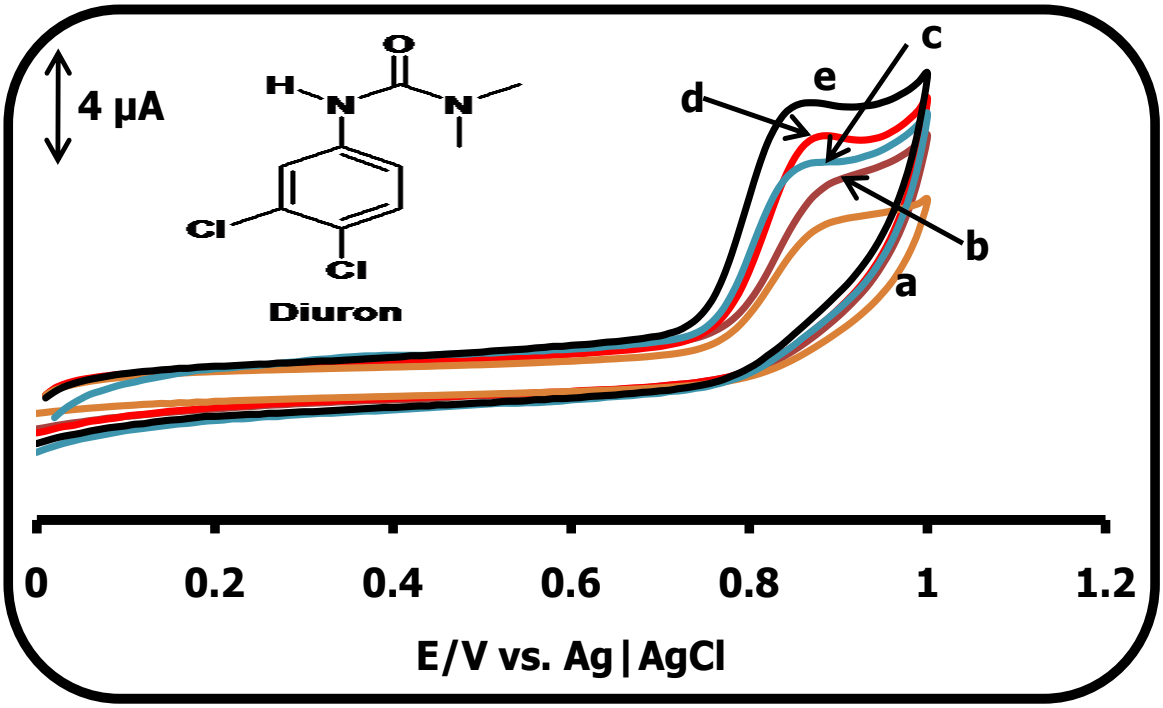

Figure 5.25: Comparative cyclic voltammograms for 10 µM diuron on: (a) bare GCE, (b) CoMAPc-GCE, (c) SWCNT-COOH-GCE, (d) CoMAPc/SWCNT-COOH(mix)-GCE and (e) CoMAPc-SWCNT(linked)-GCE. Inset: Structure of diuron. Scan rate = 100 mV/s. pH 4 buffer.

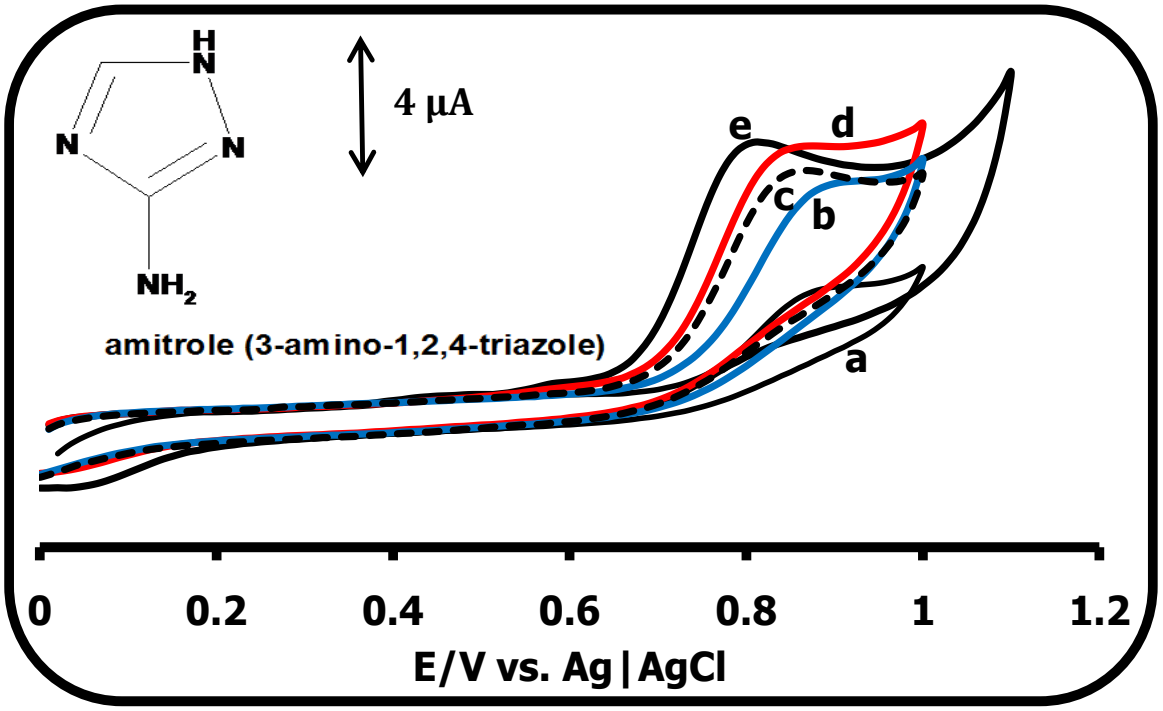

Figure 5.26: Comparative cyclic voltammograms for 10 µM amitrole on: (a) bare GCE, (b) CoMAPc-GCE, (c) SWCNT-COOH-GCE, (d) CoMAPc/SWCNT-COOH(mix)-GCE and (e) CoMAPc-SWCNT(linked)-GCE. Inset: Structure of amitrole. Scan rate = 100 mV/s. pH 4 buffer.

Table 5.5: Electrochemical parameters for amitrole and diuron.

Electrode	E_P (V)		Electrode Stability (as % current drop from cycle 1 to 2)	
	Diuron	Amitrole	Diuron	Amitrole
Bare GCE	0.88	0.90	38	24
SWCNT-COOH-GCE	0.87	0.92	26	24
CoMAPc-GCE	0.90	0.83	28	24
CoMAPc/SWCNT-COOH(mix)-GCE	0.87	0.85	22	21
CoMAPc-SWCNT(linked)-GCE	0.82	0.78	25	21

Figure 5.25 compares the cyclic voltammetric responses for the bare GCE (a), CoMAPc-GCE (b), SWCNT-COOH-GCE (c), CoMAPc/SWCNT-COOH(mix)-GCE (d) and CoMAPc-SWCNT(linked)-GCE (e), all in the presence of 10 μM diuron (in pH 4 buffer). Figure 5.26 shows the comparative voltammetric evolutions of these electrodes in 10 μM amitrole (in pH 4 buffer). The oxidation peak for amitrole was found at 0.78 V, while the one for diuron was observed at 0.82 V (versus Ag|AgCl), Tables 5.2 and 5.5. The oxidation potentials for diuron were at 0.88 V, 0.90 V, 0.87 V, 0.87 V and 0.82 V (versus Ag|AgCl) for the bare GCE (a), CoMAPc-GCE (b), SWCNT-COOH-GCE (c), CoMAPc/SWCNT-COOH(mix)-GCE (d) and CoMAPc-SWCNT(linked)-GCE(e), respectively, Table 5.5. The oxidation of diuron on the bare GCE (Table 5.5, also Table 5.2 for CoMAPc-SWCNT(linked)) occurs at a potential which is ~ 60 mV more positive than on the CoMAPc-SWCNT(linked) modified electrode (Fig. 5.25e). The sharper rise in current for the oxidation of diuron on CoMAPc-SWCNT(linked)-GCE is an indication of good catalytic activity. The oxidation of diuron is initiated at a more negative potential (foot of the oxidation wave) on the CoMAPc-SWCNT(linked) electrode relative to the other electrodes, and this confirms that it is a good electrocatalyst. Amitrole showed oxidation peaks at 0.90 V, 0.83 V, 0.92 V, 0.85 V and 0.78 V for the bare GCE (a), the CoMAPc-GCE (b), the SWCNT-COOH-GCE (c), the CoMAPc/SWCNT-COOH(mix)-GCE (d) and the CoMAPc-SWCNT(linked)-GCE (e), respectively (Fig. 5.26, Table 5.5). CoMAPc-SWCNT(linked)-GCE (Fig. 5.26e), shows higher oxidation current at reduced oxidation overpotentials compared to other modified electrodes, confirming its good electrocatalytic properties. Oxidation of amitrole occurs at a potential 120 mV more positive on the bare GCE relative to the CoMAPc-SWCNT(linked) modified GCE. The oxidation potentials for both amitrole and diuron on CoMAPc-SWCNT(linked) have improved compared to CoTCPc-EA-SWCNT(linked), CoTCPc-PA-SWCNT(linked) and FeTAPc-SWCNT(linked), possibly due the presence of the electron donating aryl-thio groups that lower the cobalt oxidation potential, thereby improving catalysis. The CoMAPc-SWCNT(linked) electrode showed the best catalytic performance towards both amitrole and diuron compared to the rest of the electrodes given in Table 5.2. The oxidation potentials of amitrole and diuron occur

in the potential range for the $Co^{III}Pc^{-1}$/ $Co^{III}Pc^{-2}$ redox process, hence they are catalysed by these species. Having confirmed the superiority of CoMAPc-SWCNT(linked)-GCE over the other electrodes, it was used in the further characterizations of amitrole and diuron.

5.5.2 Electrode stability

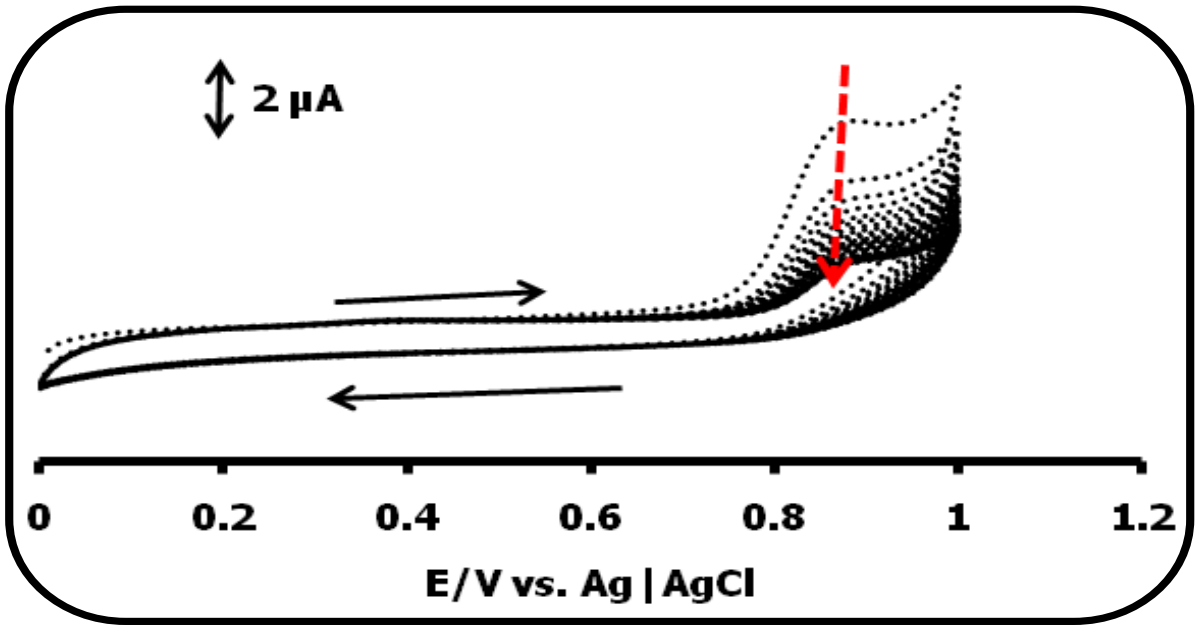

Figure 5.27: Thirty continuous cyclic voltammetric evolutions for 10 µM diuron generated on GCE modified with CoMAPc-SWCNT(linked) nanorods. Scan rate = 100 mV/s. pH 4 buffer.

Figure 5.27 shows 30 cycle continuous scan voltammograms for CoMAPc-SWCNT(linked) nanorods in 10 µM diuron. A drop of 25% in peak current from cycle 1 to 2 and an overall drop of 56% after 30 cycles were observed for diuron, followed by the stabilization of the currents thereafter. All electrodes were tested for stability (as % current drop from cycle 1 to 2) and the order was as follows for diuron: CoMAPc/SWCNT-COOH(mix)-GCE (22%) > SWCNT-COOH-GCE (26%) > CoMAPc-GCE (28%) > CoMAPc-SWCNT(linked)-GCE (25%, Table 5.2) > bare GCE (38%). Amitrole showed a drop of 21% from cycle 1 to 2 and 32% after 30 cycles. The

order of stability for amitrole (as % current drop from cycle 1 to 2) was as follows: CoMAPc-SWCNT(linked)-GCE (21%, Table 5.2) = CoMAPc/SWCNT-COOH(mix)-GCE (21%) > SWCNT-COOH-GCE (24%) ~ CoMAPc-GCE (24%) ~ bare GCE (24%). Drop in current is a passivation phenomena and the rate at which the current drops is a measure of resistance to passivation of the electrode towards that analyte/how much the analyte passivates the electrode. The CoMAPc-SWCNT(linked) electrode showed similar stability for both diuron and amitrole and was successfully regenerated by shaking it in methanol and scanning in pH 4 buffer solution (through cyclic voltammetry) in the potential window 0.0-1.0 V (versus Ag|AgCl). The reproducibility of the voltammograms after shaking in methanol and scanning in pH 4 buffer confirmed little or no leaching at all of the catalyst. As discussed above, this minimum leaching is due to the dual combination of strong л-л interactions between the GCE and the CoMAPc-SWCNT(linked) nanorods. Under conditions of continual use and storage in pH 4 buffer, the electrode has a life span of more than 2 months.

5.5.3 Tafel slopes

Linear relationships were observed from plots of current versus $v^{1/2}$ for both amitrole and diuron, confirming that their oxidation processes are diffusion controlled. Plots of E_p versus log v gave linear relationships as represented by Eq. 5.1. Tafel slopes of 230 and 237 mV decade^{-1} (Table 5.2) were obtained for amitrole and diuron, respectively. Tafel slopes of this magnitude have no kinetic meaning but could indicate a passivation phenomena occurring on the electrode surface as already discussed. The electron transfer coefficients were estimated to be 0.74 and 0.75, Table 5.2, for amitrole and diuron, respectively.

5.5.4 Chronoamperometric studies

Figure 5.28a (similar to Fig. 5.6 for *poly*-Ni(OH)TAPc) shows chronoamperometric evolutions for (i) 1 μM, (ii) 2 μM, (iii) 4 μM, (iv) 6 μM, (v) 8 μM and (vi) 10 μM diuron, produced on polarized CoMAPc-SWCNT(linked)-GCE (0.85 V versus Ag|AgCl)), all in pH 4 buffer. At this potential the rate of electro-catalyzed

oxidation of both amitrole and diuron exceed their diffusion from the bulk solution to the electrode|solution interface [243] and this gives a diffusion controlled current.

Using Eq. 5.3 and Fig. 5.28b, the catalytic rate constants for amitrole and diuron were found to be $1.09 \times 10^5\ M^{-1}\ s^{-1}$ and $1.43 \times 10^5\ M^{-1}\ s^{-1}$, respectively, Table 5.2. These rate constants are higher than what was observed on all the electrodes in Table 5.2, except for CoMCPc-PA-SWCNT(linked), an indication that the oxidation reactions occur very fast at this electrode. This could be due to its higher surface to volume ratios which gives it larger surface coverages on the electrode surface and in turn higher catalytic rate constants. From the plot of log I versus log [concentration of diuron or amitrole], Fig. 5.28c, the electrocatalysis of both amitrole and diuron is approximately first order, as is the case for others above. This implies that one analyte molecule interacts with one molecule of CoMAPc-SWCNT(linked). Considering the above stated arguments and also that the $Co^{III}Pc^{-1}$ species are implicated in the catalysis, the proposed mechanism for the catalytic oxidation of amitrole or diuron is given by Eqs. 5.15 and 5.16:

$$Co^{II}Pc^{-2} \underset{}{\overset{-2e^-}{\rightleftharpoons}} [Co^{III}Pc^{-1}]^{+2} \qquad (5.15)$$

$$[Co^{III}Pc^{-1}]^{+2} + \text{amitrole/diuron} \longrightarrow Co^{II}Pc^{-2} + \text{amitrole/diuron oxidation products} \qquad (5.16)$$

Eqs. 5.15 and 5.16 are proposed since the oxidation of amitrole and diuron occurs in the stability range of the $Co^{III}Pc^{-1}$ species, hence the latter is involved in the mediation process. Eq. 5.16 shows the oxidation of amitrole and diuron and the regeneration of the $Co^{II}Pc^{-2}$ electrocatalyst.

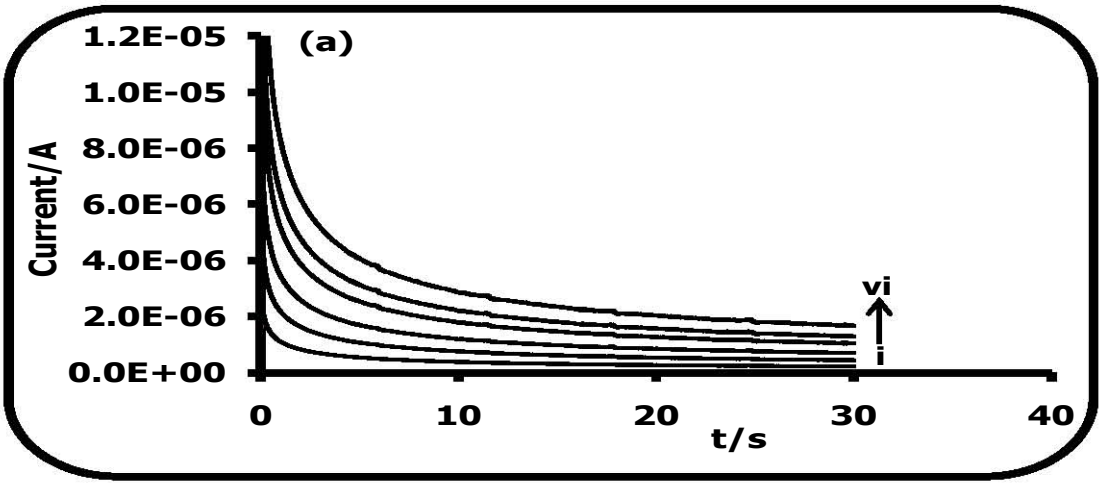

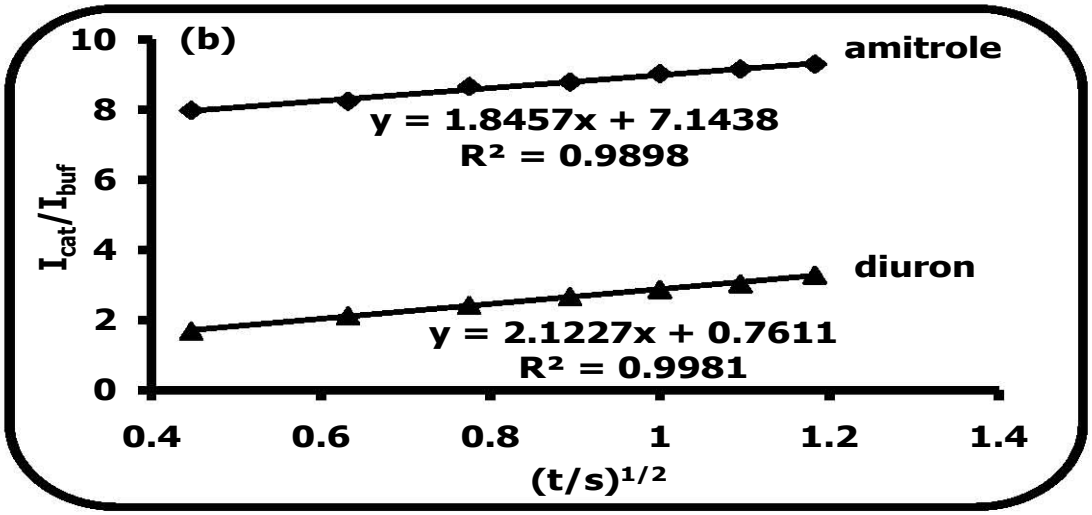

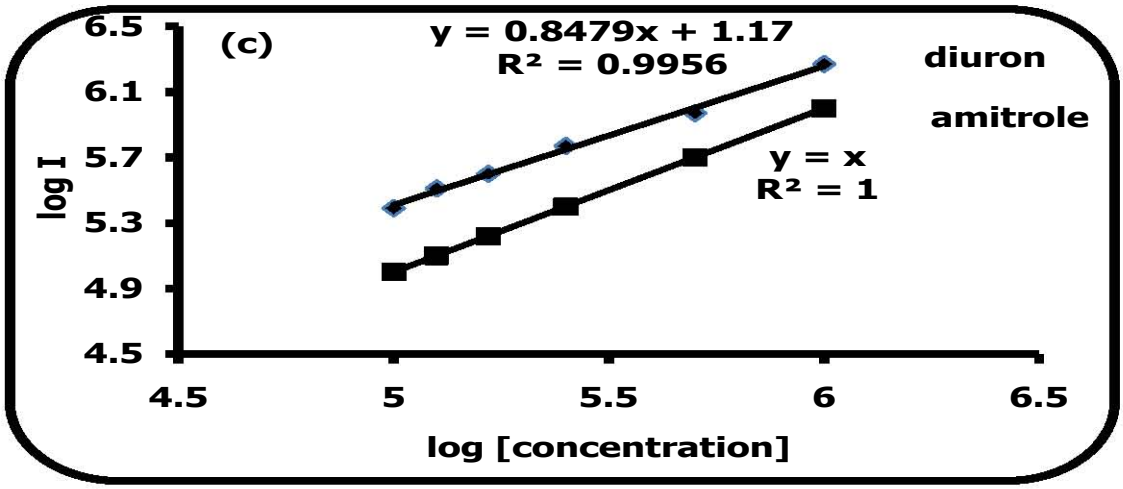

Figure 5.28: (a) Chronoamperometric evolutions on CoMAPc-SWCNT(linked)-GCE for (i) 1 µM, (ii) 2 µM, (iii) 4 µM, (iv) 6 µM, (v) 8 µM and (vi) 10 µM diuron, all in pH 4 buffer, (b) plot of I_{cat}/I_{buf} versus $t^{1/2}$ and (c) plot of log I versus log [concentration], for both amitrole and diuron. Potential = 0.85 V.

The linear dynamic range was from 1 x 10^{-6} M – 1.2 x 10^{-4} M in both cases, with the sensitivities of 6.76 A mol^{-1} L cm^{-2} and 5.63 A mol^{-1} L cm^{-2} (Table 5.2) for amitrole and diuron, respectively. The CoMAPc-SWCNT(linked) electrode shows higher sensitivities towards amitrole than diuron. The sensitivity of this electrode is also higher than that for CoTCPc-EA-SWCNT(linked) and CoTCPc-PA-SWCNT(linked) for both amitrole and diuron, Table 5.2. However these sensitivities are lower than those observed on *poly*-Ni(OH)TAPc (for diuron only) and FeTAPc-SWCNT(linked) (for both amitrole and diuron), Table 5.2. The limits of detection were estimated on the basis of signal-to-noise characteristics (S/N = 3), to be 0.1 μM and 0.13 μM for amitrole and diuron (Table 5.2), respectively and are lower than what has been observed elsewhere [78,257,306] using flow injection techniques and capillary electrophoresis. The LODs for amitrole and diuron on CoMAPc-SWCNT(linked) are the lowest (the LOD for amitrole is the same as for CoTCPc-EA-SWCNT(linked)) compared to all other electrodes in Table 5.2.

5.5.5 Interference studies

The effect of diuron on the detection of amitrole was studied. Fig. 5.29 shows cyclic voltammetric and chronoamperometric evolutions observed to show the interference of diuron on the detection of amitrole. The oxidation peak of amitrole is at 0.78 V and that of diuron is at 0.82 V, Table 5.2, on CoMAPc-SWCNT(linked)-GCE. However, in an equimolar mixture of amitrole and diuron only a single peak with higher current is observed at more positive potentials (at 0.9 V versus Ag|AgCl) than those of amitrole and diuron, as was observed with FeTAPc-SWCNT(linked), except for the lower current in the latter. Higher current for the mixture could indicate the oxidation of both amitrole and diuron. Chronoamperometric studies (Fig. 5.29 inset) also showed the same increase in current for the mixture, an indication that diuron could also be contributing towards the total current. The mixed solution method [248] was then used to check the selectivity of CoMAPc-SWCNT(linked)-GCE for amitrole in the presence of diuron, since the two have very close oxidation potentials. The value of K_{amp} was determined from Eq. 5.5 (using 1×10^{-5} M for both diuron (interferent) and amitrole).

As stated before a K_{amp} value of less than 10^{-3} indicates non-interference while one which falls within the order of 10^{-3} suggests that the species is an interferent but not a strong one. For an equimolar solution of amitrole and diuron, K_{amp} values of (6.6 ± 0.12) × 10^{-1} was obtained, indicating that diuron is a very strong interferent, thus the electrode cannot be used for the detection of both amitrole and diuron, as already discussed for the other electrodes above.

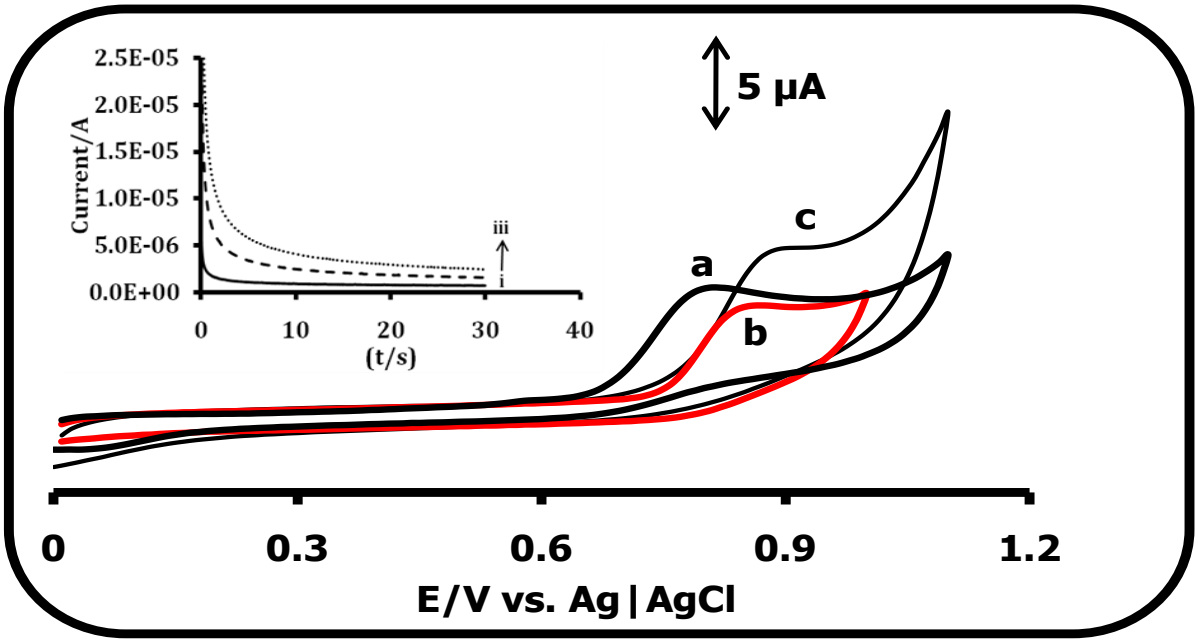

Figure 5.29: Cyclic voltammograms for (a) amitrole, (b) diuron and (c) amitrole: diuron mixture (1:1). Scan rate = 100 mV/s. Inset: Chronoamperometric evolutions for (i) pH 4 buffer, (ii) 10 µM amitrole and (iii) 1:1 amitrole to diuron on CoMAPc-SWCNT(linked)-GCE polarized at 0.9 V (versus Ag|AgCl).

5.5.6 RDE studies

Fig. 5.30 shows the rotating disk electrode linear voltammetry evolutions for 1 mM diuron in pH 4 buffer. Fig. 5.30, inset, shows the linear relationship between the current and the electrode rotational speed, confirming that in solution the oxidation of diuron at the CoMAPc-SWCNT(linked)-GCE is governed by mass transfer. A similar relationship was observed for amitrole. From RDE, the catalytic rate constants for amitrole and diuron were found to be 1.62 x 10^5 and 2.11 x 10^5 M^{-1} s^{-1}, respectively. Though these rate constants are higher than those observed from

chronoamperometry, their magnitude is the same. Using plots of potential versus log I_k (similar to Fig. 5.16), Tafel slopes of 239 and 228 mV/decade were obtained for amitrole and diuron, respectively, and are quite similar to those obtained through cyclic voltammetry. The **α**-values were 0.75 and 0.74 for amitrole and diuron, respectively, Table 5.2.

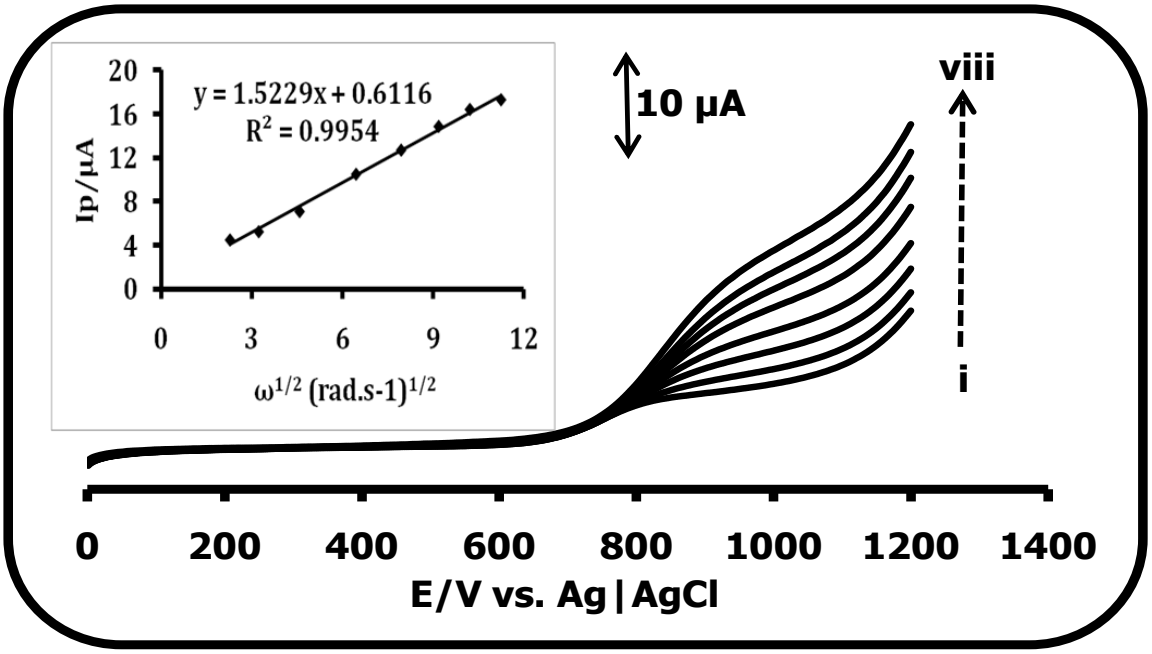

Figure 5.30: (a) RDE evolutions for 1 mM diuron at the CoMAPc-SWCNT(linked)-GCE at rotational speeds (i) 50, (ii) 100, (iii) 200, (iv) 400, (v) 800, (vi) 1200, (vii) 1600, (viii) 2000 rpm, with a sensitivity of 10 µA/V. Scan rate = 20 mV/s. Inset: Levich plot. pH 4 buffer.

5.6 CoMCPc-PA-SWCNT(linked)

This electrode was used on amitrole and diuron, Table 5.1. CV and CA were employed in their analysis. RDE was not done since the Tafel slopes and rate constants were obtained from CA, as was the case with CoMAPc-SWCNT(linked). EIS was employed since the effect of conjugation on electron transfer has already been reported.

5.6.1 Cyclic voltammetry

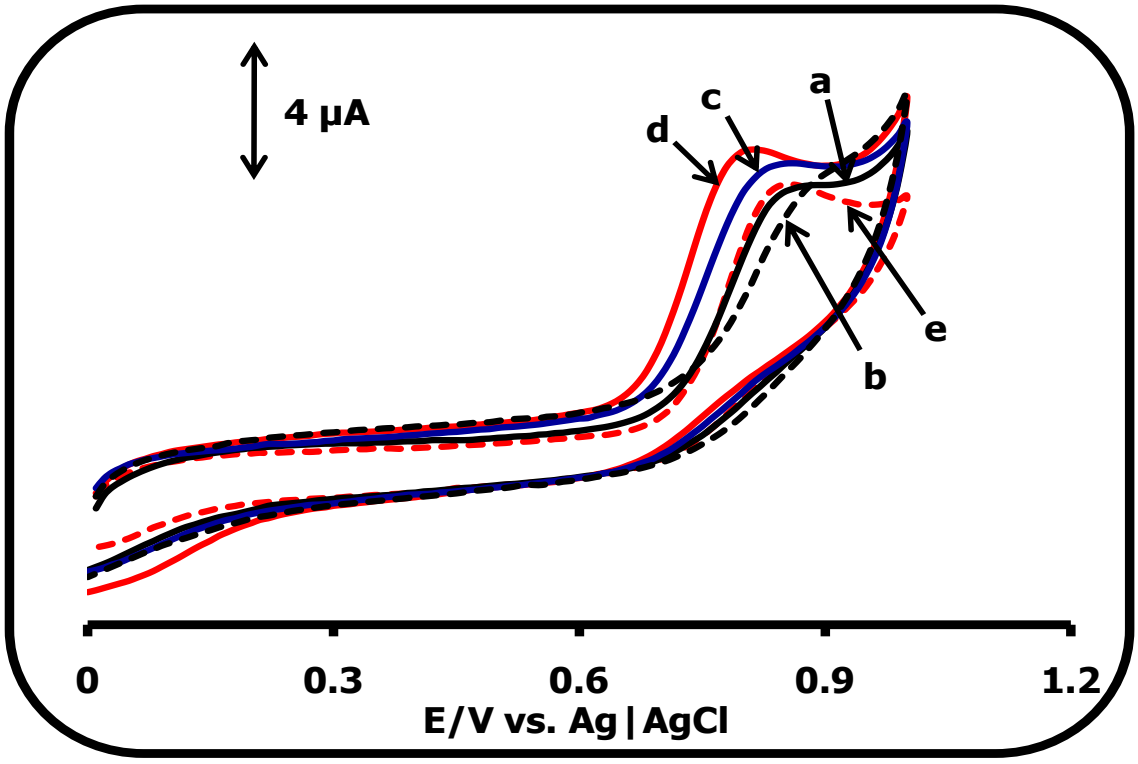

Figure 5.31: Comparative cyclic voltammograms for 10 µM amitrole on: (a) bare GCE, (b) CoMCPc-GCE, (c) PA-SWCNT-GCE, (d) CoMCPc-PA-SWCNT(linked)-GCE and (e) CoMCPc/PA-SWCNT(mix)-GCE. Scan rate = 100 mV/s. pH 4 buffer.

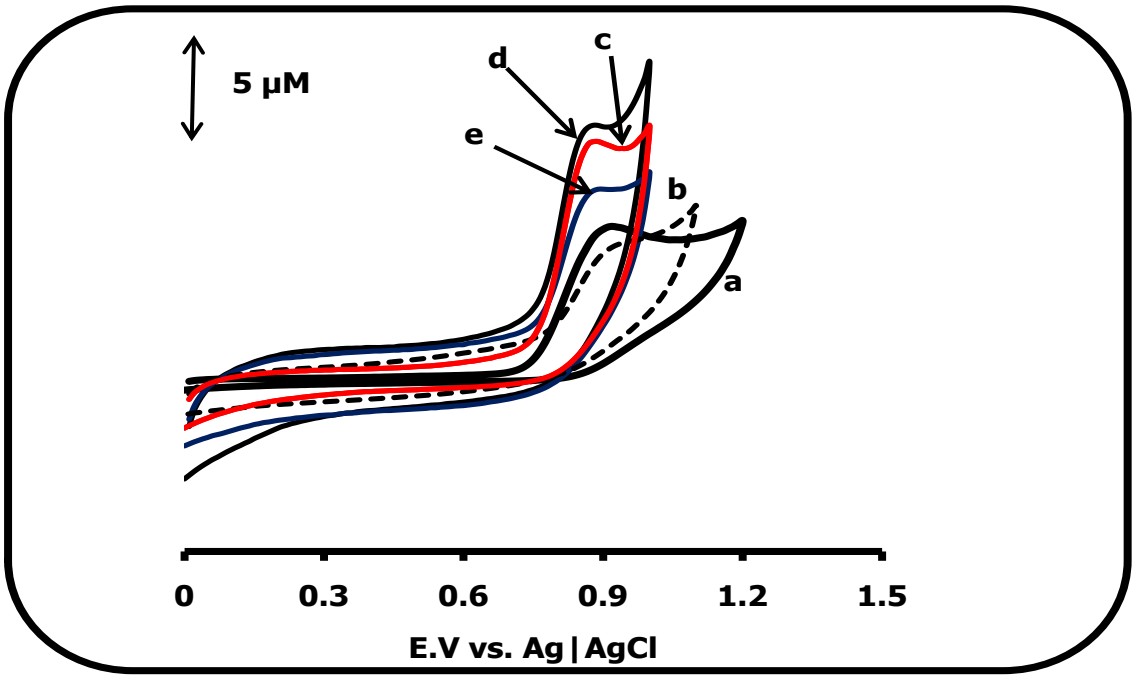

Figure 5.32: Comparative cyclic voltammograms for 10 µM diuron on: (a) bare GCE, (b) CoMCPc-GCE, (c) PA-SWCNT-GCE, (d) CoMCPc-PA-SWCNT(linked)-GCE and (e) CoMCPc/PA-SWCNT(mix)-GCE. Scan rate = 100 mV/s. pH 4 buffer.

Table 5.6: Electrochemical parameters for amitrole and diuron.

Electrode	ΔE (mV) vs Ag|AgCl $[Fe(CN)_6]^{3-/4-}$ (0.1 M KCl)	E_P (V)		Electrode Stability (as % current drop from cycle 1 to 2)	
		Diuron	Amitrole	Diuron	Amitrole
Bare GCE	54	0.90	0.87	32.5	19.7
PA-SWCNT-GCE	66	0.87	0.81	25.0	24.7
CoMCPc-GCE	172	0.94	0.91	29.7	29.4
CoMCPc/PA-SWCNT(mix)-GCE	78	0.86	0.83	24.2	24.4
CoMCPc-PA-SWCNT(linked)-GCE	60	0.85	0.79	37.1	17.8

The effectiveness of the CoMCPc-PA-SWCNT(linked) was explored through comparative cyclic voltammetry as shown in Figs. 5.31 and 5.32, for amitrole (10 µM) and diuron (10 µM), respectively. The order of peak potential for the oxidation of

amitrole on various modified electrodes is as follows: CoMCPc-PA-SWCNT(linked)-GCE (0.79 V, Table 5.2) > PA-SWCNT-GCE (0.81 V) > CoMCPc/PA-SWCNT(mix)-GCE (0.83 V) > bare GCE (0.87 V) > CoMCPc-GCE (0.91 V), Table 5.6. The trend for the oxidation of diuron is as follows: CoMCPc-PA-SWCNT(linked)-GCE (0.85 V, Table 5.2) ~ CoMCPc/PA-SWCNT(mix)-GCE (0.86 V) ~ PA-SWCNT-GCE (0.87 V) > bare GCE (0.90 V) > CoMCPc-GCE (0.94 V), Table 5.6. It is important to note that diuron is more resistant to oxidation on all the electrodes (compared to amitrole), even though these trends show that the CoMCPc (without PA-SWCNT) is not catalytic towards both amitrole and diuron. This is not the case with CoMAPc, Table 5.5. However, when CoMCPc is chemically linked to PA-SWCNTs, its catalytic properties are activated (Figs. 5.31d and 5.32d). This is due to the electron donating effect of the phenyl-amine group, which lowers the redox potentials for the Co^{III}/Co^{II} process, thereby initiating catalysis at lower potentials for the CoMCPc-PA-SWCNT conjugate. The effect of chemical linking is more pronounced in the catalysis of amitrole than diuron, as judged by the large decrease in potential for CoMCPc-PA-SWCNT(linked) compared to CoMCPc/PA-SWCNT(mix)-GCE. PA-SWCNT alone shows good catalytic activity, as judged by the sharp increase in current for both amitrole and diuron oxidation and also lower potentials compared to the bare GCE. Thus it is the PA-SWCNT which is actually catalyzing and not the CoMCPc. Whereas when CoTCPc was linked to PA-SWCNT, there was clear catalysis by CoTCPc in the presence of PA-SWCNT. This could be attributed to the electron donating nature of PA-SWCNTs.

The good catalytic property of the conjugate is in agreement with its good electron transfer efficiency, i.e. a smaller ΔEp value relative to the other modified electrodes (Table 5.6). In both cases, the catalytic oxidations of diuron and amitrole were initiated at more negative potentials and accompanied by sharp rises in currents in comparison to other electrodes used in this study, confirming catalysis of the two by CoMCPc-PA-SWCNT(linked). It is also important to note than the presence of SWCNTs does improve catalysis, though it becomes more defined in the conjugate (see peak oxidation potentials, Table 5.6). The oxidation peak potentials of amitrole occurred at approximately the same potential on CoMAPc-SWCNT(linked)

and CoMCPc-PA-SWCNT(linked), Table 5.2. This may be due to the electron donating nature of the benzyl-mercapto groups, whose effects far outweigh the electron withdrawing effects of the phenoxycarboxy group in CoMCPc-PA-SWCNT conjugates, hence the similarities in the oxidation potentials of both amitrole and diuron. In terms of oxidation potentials for both amitrole and diuron, CoMAPc-SWCNT(linked) and CoMCPc-PA-SWCNT(linked) are relatively better electrodes compared to the rest, Table 5.2. The oxidation peak potentials for both amitrole and diuron occur in the region for the $Co^{III}Pc^{-1}$/ $Co^{III}Pc^{-2}$ redox processes, hence they are catalysed by these species.

5.6.2 Electrode stability

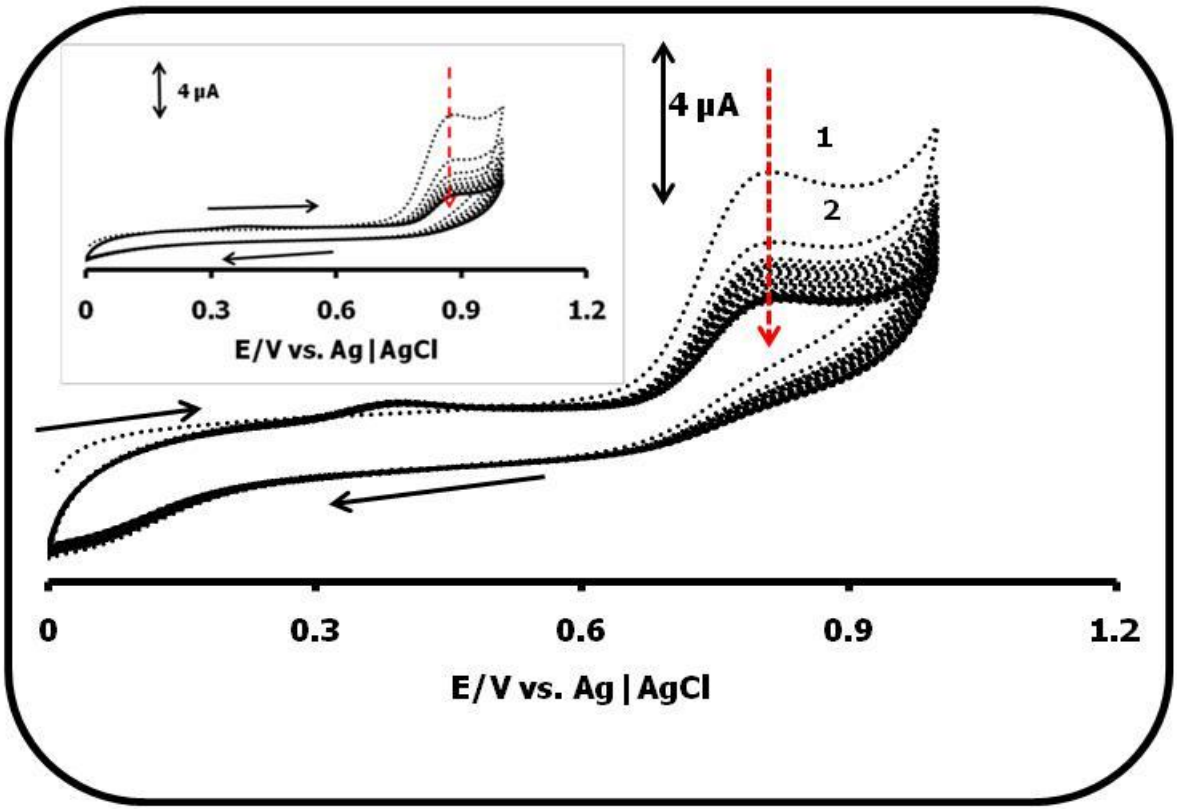

Figure 5.33: 30 continuous cyclic voltammetric evolutions for 10 µM amitrole generated on GCE modified with CoMCPc-PA-SWCNT(linked). Inset: Cyclic voltammograms for 10 µM diuron on the same electrode. Scan rate = 100 mV/s. pH 4 buffer.

Figure 5.33 shows the cyclic voltammograms (30 for each) evolved in 10 μM solutions of amitrole and diuron (Fig. 5.33 inset). The stabilities of the modified electrodes were confirmed by noting the drop in current from scan 1 to 2. The order of passivation of the electrodes by amitrole oxidation products is as follows: CoMCPc-GCE (29%) > PA-SWCNT-GCE (25%) ~ CoMCPc/PA-SWCNT(mix)-GCE (24%) > bare GCE (20%) > CoMCPc-PA-SWCNT(linked)-GCE (18%), Table 5.6. Therefore the CoMCPc-PA-SWCNT(linked) electrode is the most stable i.e. more resistant to passivation by the amitrole oxidation products. The resistance to passivation due to diuron oxidation products is as follows: CoMCPc/PA-SWCNT(mix)-GCE (24%) > PA-SWCNT-GCE(25%) > CoMCPc-GCE (30%) > bare GCE (33%) > CoMCPc-PA-SWCNT(linked)-GCE (37%). Thus for diuron oxidation, CoMCPc-PA-SWCNT(linked) is passivated most and hence the least stable, Table 5.6. This was also observed on CoTCPc-PA-SWCNT(linked), showing that the presence of PA increases passivation from diuron oxidation products, possibly due to increased л-л interactions. However the CoMCPc-PA-SWCNT(linked) electrode was successfully regenerated by shaking it in methanol and scanning in pH 4 buffer solution. Good reproducibility of the voltammograms confirmed little or no leaching of the CoMCPc-PA-SWCNT(linked) electrode. As discussed above, the strong л-л interactions between the GCE and the CoMCPc-PA-SWCNT(linked) could be responsible for the limited leaching. Under conditions of continual use and storage in pH 4 buffer, the electrode has a life span of more than 2 months.

5.6.3 Tafel slopes

Plots of current versus the square root of sweep rate for both amitrole and diuron gave linear relationships confirming diffusion controlled oxidation processes for both amitrole and diuron on the CoMCPc-PA-SWCNT(linked) electrode. From the relationship of peak potential and log scan rate for an irreversible diffusion-controlled process (Eq. (5.1)) [245], Tafel slopes of 200 and 180 mV/decade were obtained for amitrole and diuron, respectively. Though these slopes could be of not much significance, they however highlight the issue of electrode passivation since they are higher than the 30-120 mV/decade expected for a one-electron rate

determining step. The **α**-values for amitrole and diuron were 0.71 and 0.67, respectively, Table 5.2.

5.6.4 Chronoamperometric studies

Chronoamperometry was run for concentrations from 12.5 μM to 20 μM for both amitrole and diuron. Using plots similar to Fig. 5.28 but on CoMCPc-PA-SWCNT(linked), the rate constants for the chemical reaction between amitrole and diuron and the redox sites of surface confined CoMCPc-PA-SWCNT(linked)-GCE were determined according to Eq. 5.3 [247] and found to be $1.83 \times 10^6\ M^{-1}\ s^{-1}$ and $1.99 \times 10^6\ M^{-1}\ s^{-1}$, respectively. These values represent very fast oxidation processes on the electrode surface. This electrode gave the highest catalytic rate constants for both amitrole and diuron compared to all other electrodes in Table 5.2.

From the current-concentration plots, sensitivities of 5.10 and 3.70 A mol^{-1} L cm^{-2} were obtained for amitrole and diuron, respectively. The CoMCPc-PA-SWCNT(linked) electrode shows a higher sensitivity towards amitrole than diuron as observed with CoMAPc-SWCNT(linked). The limits of detection were estimated to be 0.14 μM and 0.20 μM for amitrole and diuron, respectively, using the 3δ notation. These values are quite reasonable considering what has been obtained in other studies [78,257,306]. However the sensitivities for both amitrole and diuron are lower than those observed on CoMAPc-SWCNT(linked), but higher than the rest of the electrodes except FeTAPc-SWCNT(linked) and *poly*-Ni(OH)TAPc (for diuron), Table 5.2. The limits of detection for both amitrole and diuron are higher than those for CoMAPc-SWCNT(linked), Table 5.2.

Plots of log I versus log [concentration], for both amitrole and diuron showed that the electrocatalysis of both amitrole and diuron is approximately first order, indicating that one analyte molecule interacts with one molecule of CoMCPc-PA-SWCNT(linked), as with the rest of the electrodes. From the above stated arguments and also that the $Co^{III}Pc^{-1}$ species are implicated in the catalysis, the proposed mechanism for the catalytic oxidation of amitrole or diuron is similar to the one shown by Eqs. 5.15-5.16 for CoMAPc-SWCNT(linked).

5.6.5 Interference studies

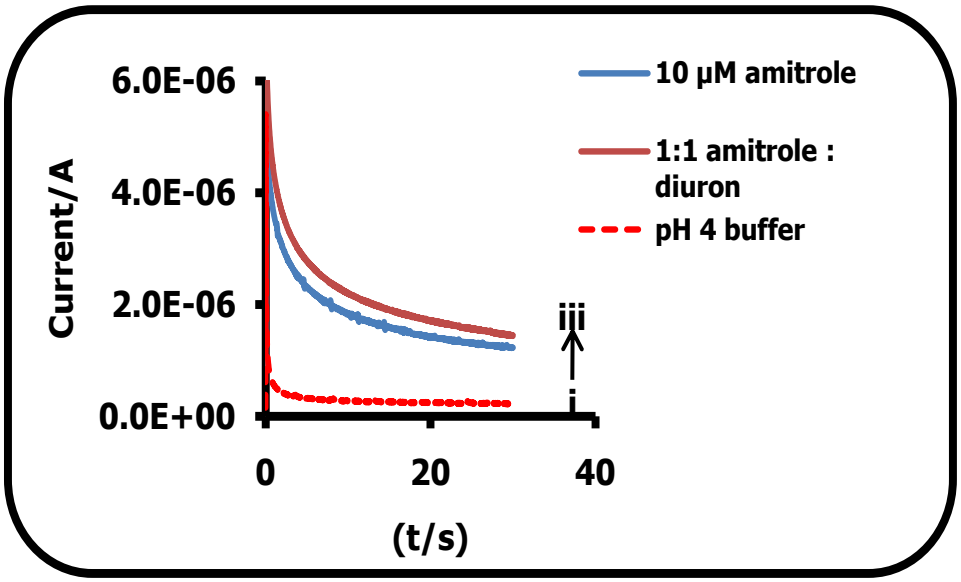

Figure 5.34: Chronoamperometric evolutions for (i) pH 4 buffer, (ii) 10 µM amitrole and (iii) 1:1 amitrole to diuron on CoMCPc-PA-SWCNT(linked)-GCE polarized at 0.8 V (versus Ag|AgCl).

The observed chronoamperometric evolutions (Fig. 5.34) show the interference of diuron on the detection of amitrole. Figure 5.34(i) is the current generated by the CoMCPc-PA-SWCNT(linked) electrode in pH 4 buffer in the absence of analyte (background current), while Fig. 5.34(ii) shows oxidation current for both amitrole and the background. Higher current (Fig. 5.34(iii)) is observed in the presence of diuron (mixture), showing that diuron is contributing towards the total current as observed before and is an indication of its interference. The mixed solution method discussed above was used to confirm the interference of diuron in the detection of amitrole on the CoMCPc-PA-SWCNT(linked)-GCE, since these two analytes follow the similar oxidation mechanism and have very close oxidation potentials on this electrode. The value of K_{amp} was determined from Eq. (5.5), using 1×10^{-5} M for both diuron (interferent) and amitrole. As stated above a K_{amp} values less than 10^{-3} indicate non-interference while one which falls within the order of 10^{-3} suggests that the species is an interferent but not a strong one. For an equimolar solution of amitrole and diuron, a K_{amp} value of $(2.8 \pm 0.08) \times 10^{-1}$ was obtained, indicating that diuron interferes with the detection of amitrole. This electrode

therefore cannot be used for the dual determination of amitrole and diuron as already stated for the other electrodes.

5.7. 2-ME catalysis

2-ME has been studied extensively in basic media where it is oxidized at very low potential values. This work represents its oxidation in acid media which is more difficult and less studied.

5.7.1 CoTAPc-SWCNT(linked)

5.7.1.1 Cyclic voltammetry

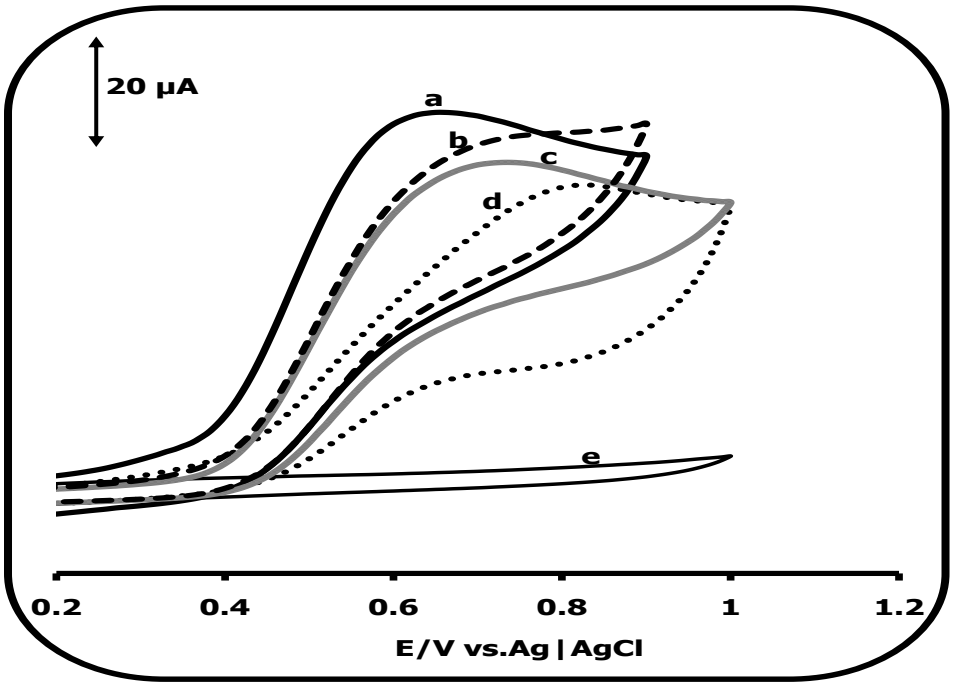

Figure 5.35: Cyclic voltammograms a-d for 1 mM 2-ME buffered at pH 4 (a) CoTAPc-SWCNT(linked)-GCE, (b) CoTAPc/SWCNT-COOH(mix)-GCE, (c) CoTAPc-GCE and (d) SWCNT-COOH-GCE and (e) bare GCE. Scan rate = 50 mV/s.

Cyclic voltammograms of SWCNT-COOH-GCE, CoTAPc-GCE, CoTAPc/SWCNT-COOH(mix)-GCE, CoTAPc-SWCNT(linked)-GCE and bare GCE in 1 mM 2-ME (pH 4) are shown in Fig. 5.35. No peak was observed on the bare

electrode alone for 2-ME (Fig. 5.35e). Larger currents were observed for CoTAPc-SWCNT(linked)-GCE (Fig. 5.35a) compared to the rest of the electrodes, followed by CoTAPc/SWCNT-COOH(mix)-GCE (Fig. 5.35b). The currents for CoTAPc-SWCNT(linked)-GCE are much higher than for CoTAPc/SWCNT-COOH(mix)-GCE, considering the fact that the former did not show currents due to CoTAPc, while the latter did in Fig. 4.1. Thus the CoTAPc-SWCNT complex has proved to be a better catalyst for 2-ME. The oxidation of 2-ME occurred at 0.76 V on CoTAPc-GCE, 0.67 V on CoTAPc/SWCNT-COOH(mix)-GCE and 0.60V on CoTAPc-SWCNT(linked)-GCE (Table 5.2), thus showing that chemical linking enhances the activity of CoTAPc-SWCNT conjugates.

5.7.1.2 Stability of the CoTAPc-SWCNT(linked) (14)

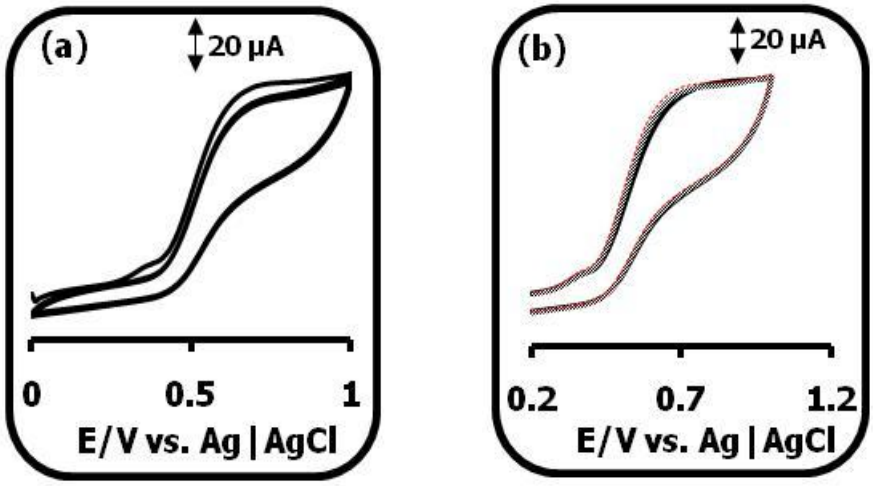

Figure 5.36: Cyclic voltammograms for (a) 30 continuous cycles of CoTAPc-SWCNT(linked)-GCE in 1 mM 2-ME and (b) 3 successive regenerations of CoTAPc-SWCNT(linked)-GCE after rinsing in methanol and running in 1 mM 2-ME (pH 4). Scan rate = 50 mV/s.

Figure 5.36a shows a voltammogram for 30 continuous scans on the conjugate modified electrode in 1 mM 2-ME. The CoTAPc-SWCNT(linked)-GCE showed high stability, an indication of being highly resistant to passivation. A 6% drop in current from the first scan to the second scan was observed for the CoTAPc-SWCNT(linked)-

GCE relative 26% for the CoTAPc/SWCNT-COOH(mix)-GCE. The CoTAPc-SWCNT(linked) modified electrode was very durable and showed minimum/no signs of stripping from the electrode, and was easily recovered by rinsing it in methanol (Fig. 5.36b).

A linear dependence of 2-ME concentration on cyclic voltammetric currents is shown in Fig. 5.37. The linear concentration range was 2 x 10^{-5} to 1.4 x 10^{-4} M and a sensitivity of 2.82 A mol^{-1} L cm^{-2} was obtained. The limit of detection of 1.2 x 10^{-7} M using the 3δ notation which is higher than 1 x 10^{-6} M obtained in other studies was achieved [314].

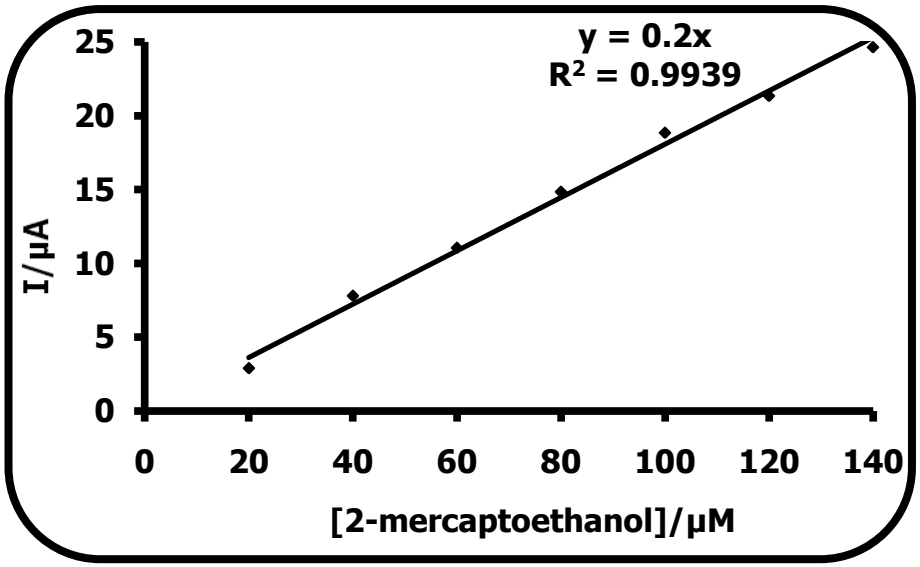

Figure 5.37: Dependence of 2-ME concentration on peak currents.

5.7.1.3 Tafel slopes

The plots of sweep-rate normalised current density ($I_p v^{-1/2}$) versus the sweep rate showed typical behaviour for a catalytic process for CoTAPc-SWCNT(linked)-GCE. A linear relationship was observed between the peak current and square root of the scan rate (Figures similar to Fig. 5.5), indicating that the 2-ME electro-catalytic oxidation is diffusion controlled.

The Tafel slope was determined using Eq. 5.1 and plot of Ep versus log v. A Tafel slope of 37 mV/decade was obtained for CoTAPc-SWCNT(linked)-GCE and is

within the normal 30-120 mV/decade for a one electron transfer rate determining step. An electron transfer coefficient of 0.40 was obtained.

5.7.1.4 RDE studies

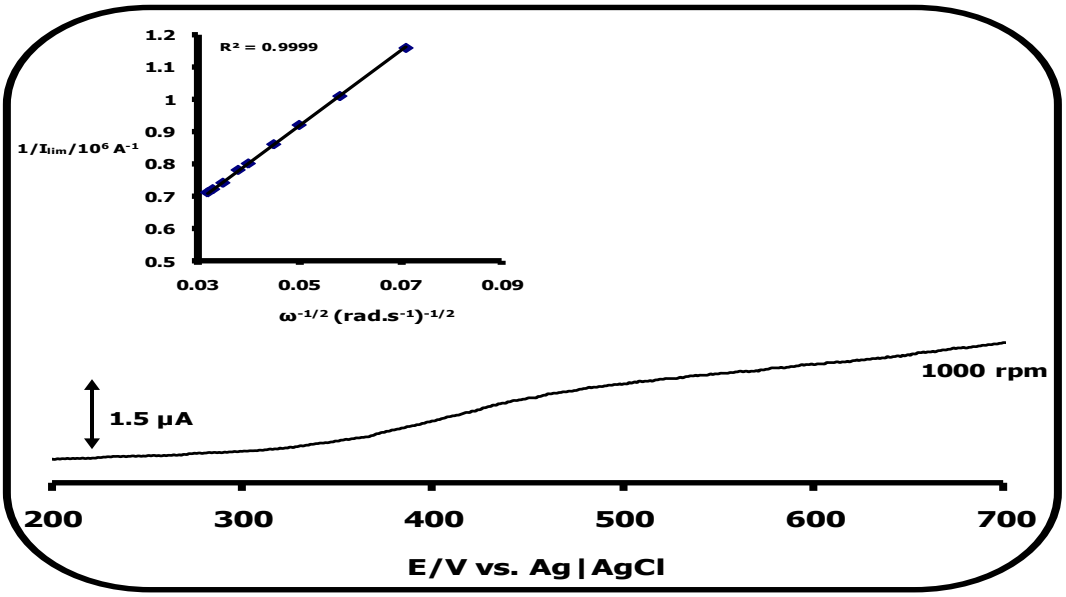

Figure 5.38: Rotating disk voltammogram for 2-ME (1.0×10^{-6} mol cm^{-3}) oxidation on GCE modified with CoTAPc-SWCNT(linked). Rotation rate = 1000 rpm, scan rate = 20 $mV.s^{-1}$. Inset: Koutecky-Levich plot.

Further experiments were performed using a rotating disk electrode (RDE) linear scan voltammetry technique. The RDE voltammetric evolutions were obtained at a constant concentration of 1 mM 2-ME and at different rotating electrode speeds. Fig. 5.38 shows a typical RDE curve obtained for 2-ME oxidation on CoTAPc-SWCNT(linked)-GCE at 1000 rpm. The Koutecky-Levich plot (Fig. 5.38, inset) was obtained from the Koutecky-Levich theory [245]. The results in Fig. 5.38 (inset) show that the inverse of the catalytic currents increased linearly with increasing $\omega^{-1/2}$ with a positive intercept, indicating that the electrode reactions are controlled by both kinetics and the mass transport of 2-ME species at the electrode surfaces, as predicted by Koutecky and Levich, Eq. 5.9. A catalytic rate constant of 3.8×10^3 M^{-1} s^{-1} was obtained. The Tafel slope was found to be 43 mV/decade (α = 0.63), Table 5.2. This is in close agreement with the Tafel slope of 37 mV/decade obtained from cyclic

voltammetry studies. These Tafel slope values are lower than 70 mV/decade that have been obtained elsewhere [100]. The values of the Tafel slopes suggest that the first one electron transfer is rate determining. However the **α** value (0.63) obtained from RDE studies is higher than the one obtained from cyclic voltammetry (**α** = 0.40).

5.7.2 NiTAPc-SWCNT(linked)

5.7.2.1 Cyclic voltammetry

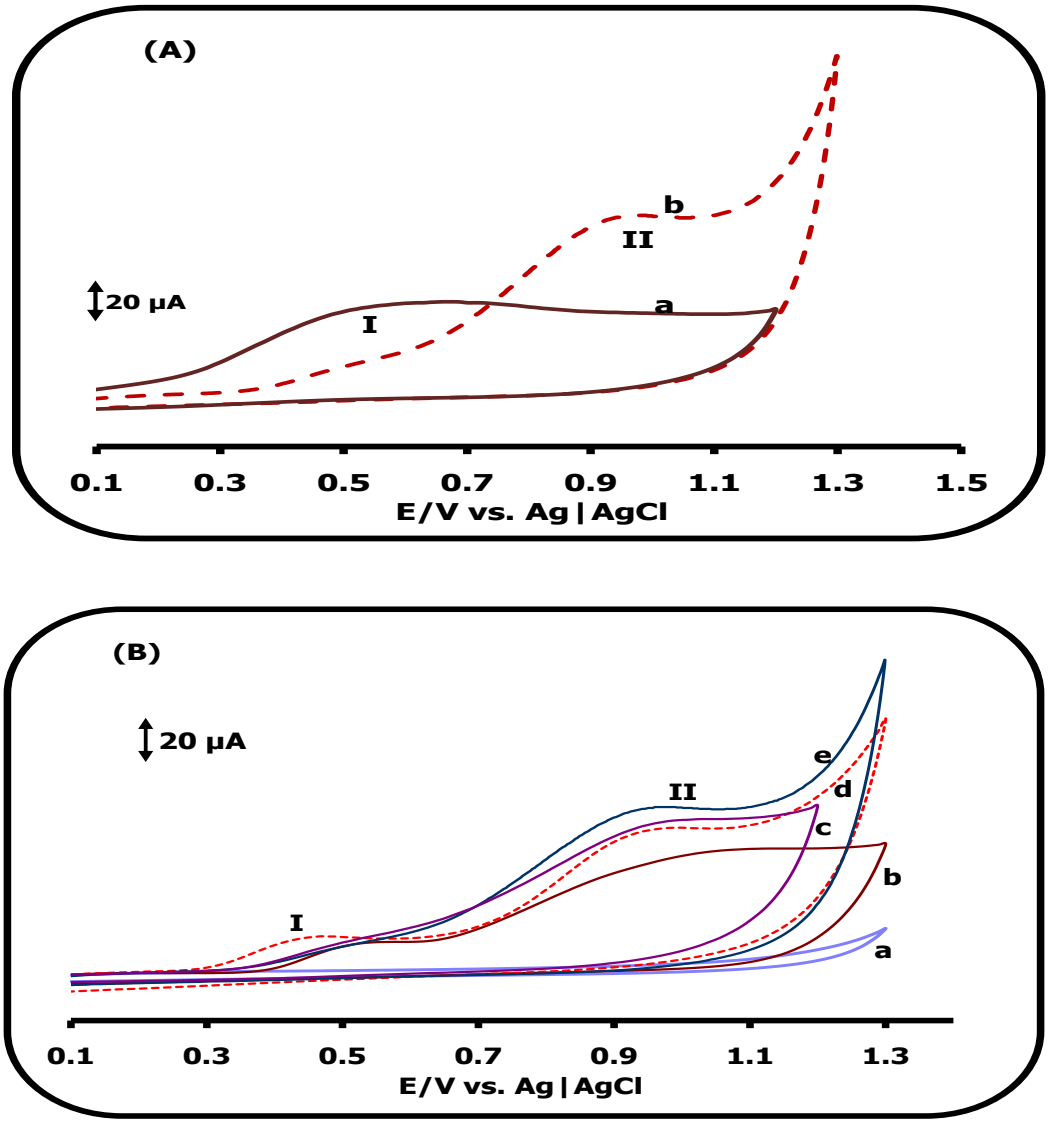

Figure 5.39: Cyclic voltammograms for A: (a) NiTAPc-SWCNT(linked)-GCE in pH 4 buffer and (b) NiTAPc-SWCNT(linked)-GCE (1 mM 2-ME in pH 4 buffer) and B: (a) bare GCE, (b) NiTAPc-GCE, (c) SWCNT-COOH-GCE, (d) NiTAPc/SWCNT-COOH(mix)-GCE, and (e) NiTAPc-SWCNT(linked)-GCE in 1 mM 2-ME (pH 4 buffer). Scan rate = 100 mV/s.

Figure 5.39 shows the voltammograms for the NiTAPc-SWCNT(linked)-GCE in pH 4 buffer (Fig. 5.39A(a)) and in 1 mM 2-ME in pH 4 buffer (Fig. 5.39A(b)). Peak **I** is due to the Ni^{III}/Ni^{II} oxidation process (in both Fig. 5.39A(a) and (b)) [103-106], while peak **II** (0.95 V versus Ag|AgCl) in Fig. 5.39A(b) is due to the oxidation of 2-ME at the electrode surface. The 2-ME oxidation peak has been reported at 0.78 V on electrodes modified with CoPc derivatives and at pH 4 [98], which is a lower potential than reported in this work. CoTAPc-SWCNT(linked) showed a lower oxidation potential for 2-ME compared to NiTAPc-SWCNT(linked). However, this work clearly shows that the linking of SWCNT does improve the catalytic activity of NiTAPc, which is not known to be catalytic unless it has been polymerized in NaOH to form O-Ni-O bridges [315].

Figure 5.39B shows the comparative cyclic voltammograms of NiTAPc-SWCNT(linked)-GCE, NiTAPc/SWCNT-COOH(mix)-GCE, NiTAPc-GCE, SWCNT-COOH-GCE and the bare-GCE in 1 mM 2-ME in pH 4 buffer. Peak **I** around potentials 0.4 V – 0.6 V (versus Ag|AgCl) represent the Ni^{III}/Ni^{II} oxidation process as observed in other studies and stated above [103-106], while peak **II** around 0.95 V (versus Ag|AgCl) is due to the oxidation of 2-ME. Relative to all other electrodes the bare GCE gave no 2-ME signal but on introduction of NiTAPc-SWCNT(linked) as observed for CoTAPc, a 2-ME peak was observed showing that the conjugate catalyses the oxidation of 2-ME. At the potential for catalytic oxidation of 2-ME, the background contribution from the NiTAPc-SWCNT(linked) is the least relative to the other modified electrodes (see Fig. 4.5). The $Ni^{III}Pc^{-1}$ species are implicated in the catalysis of 2-ME. The current response for 2-ME on NiTAPc-SWCNT(linked)-GCE is higher than for all modified electrodes in Fig. 5.39B(e), thus showing improved catalytic activity of the linked NiTAPc-SWCNT. NiTAPc-SWCNT(linked) show higher currents for 2-ME oxidation than for NiTAPc alone or NiTAPc/SWCNT-COOH(mix), showing that the linking of SWCNT to NiTAPc is important for the catalytic oxidation of 2-ME.

5.7.2.2 Electrode stability

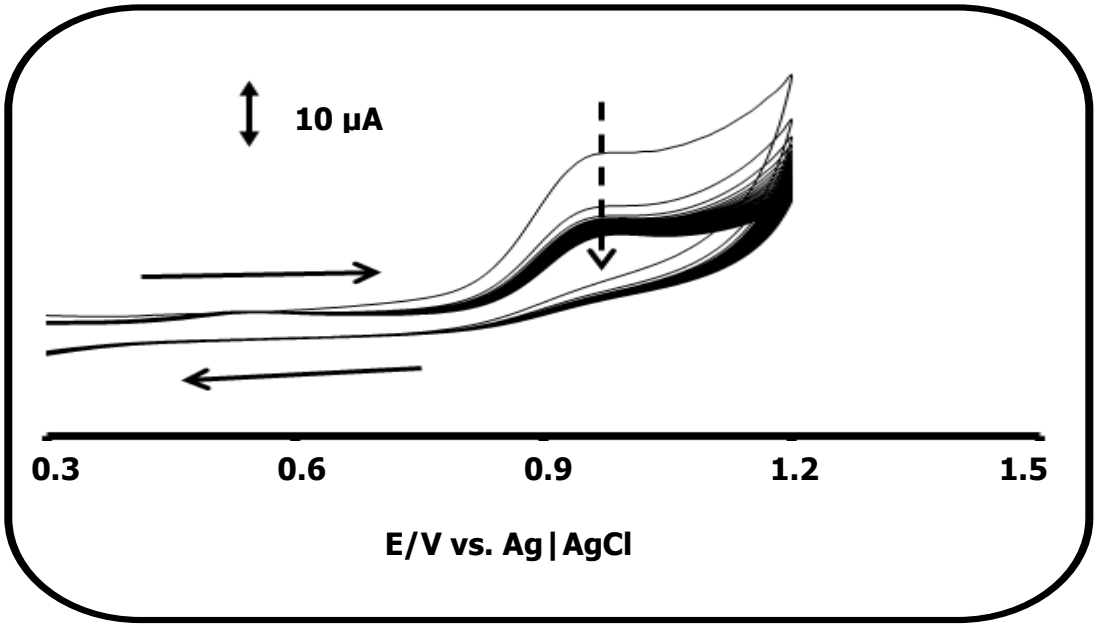

Figure 5.40: Cyclic voltammograms showing the effect of continous cyclisation of NiTAPc-SWCNT(linked)-GCE in 1 mM 2-ME (pH 4 buffer). Scan rate = 100 mV/s.

Figure 5.40 shows the stability of the NiTAPc-SWCNT(linked) modified electrode in 1 mM 2-ME. A drop in current of about 15% from the first scan to the second scan at the oxidation potential of 2-ME was observed. The order of stability is as follows: NiTAPc-SWCNT(linked)-GCE > SWCNT-COOH-GCE > NiTAPc-GCE ≈ NiTAPc/SWCNT-COOH(mix)-GCE. NiTAPc-SWCNT(linked)-GCE is more passivated by 2-ME oxidation products than CoTAPc-SWCNT(linked), Table 5.2. The drop in current is an indication of the passivating nature of the 2-ME oxidation products. However the electrode was easily regenerated by shaking in pH 4 buffer solution. Under conditions of continuous use the electrode is stable for up to 6 weeks if stored in pH 4 buffer.

5.7.2.3 Tafel slopes

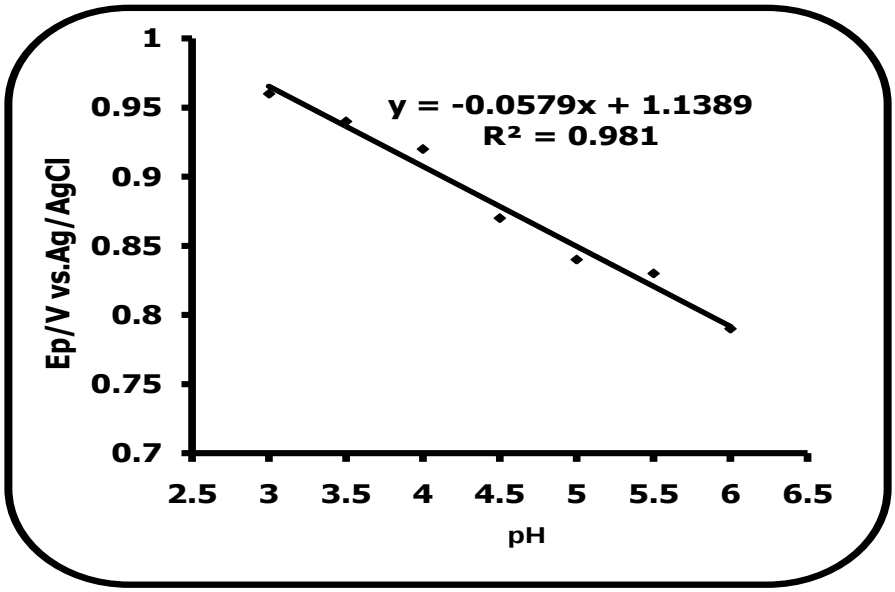

Figure 5.41: Plots of peak potential, E_p, versus pH for 2-ME.

Plot of peak currents versus the square root of the sweep rate gave a linear relationship (similar to Fig. 5.5b), an indication that the oxidation of 2-ME is diffusion controlled. Plot of sweep rate normalized current versus sweep rate gave a curve typical of a catalytic process (similar to Fig. 5.5c).

Plot of E_p versus log v (using Eq. 5.1 for an irreversible process, similar to Fig. 5.5a) gave a linear relationship and a Tafel slope of 86 mV decade^{-1}. This is consistent with a one-electron rate determining step [316], and is in agreement with what has been obtained in other studies [267,268]. The transfer coefficient was found to be 0.37.

The pH dependence of the peak potential (E_p) is shown in Fig. 5.41. It was observed that the peak potentials shifted to more negative values with increase in pH (Fig. 5.41), with slope of 0.0579 V/pH which indicates the involvement of one electron and one proton [265].

5.7.2.4 Chronoamperometry

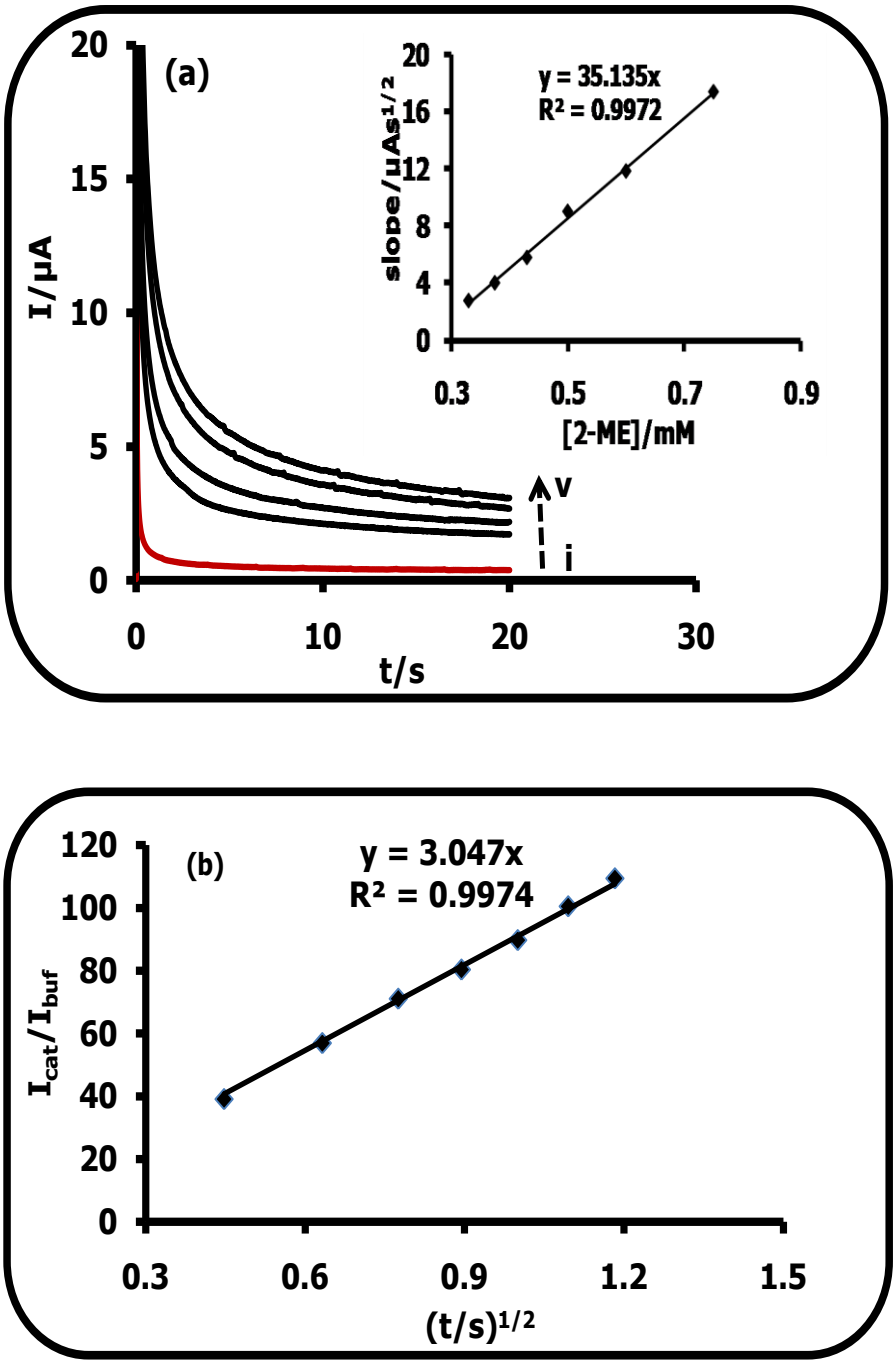

Figure 5.42: (a) Typical chronoamperograms: (i) pH 4 buffer, (ii) 3.75 x 10^{-4} M, (iii) 4.3 x 10^{-4} M, (iv) 5 x 10^{-4} M, and (v) 7.5 x 10^{-4} M for 2-ME in pH 4 buffer. Inset: Plot of different Cottrell slopes at different concentrations of 2-ME vs. concentration. (b) Plot of I_{cat}/I_{buf} vs. $t^{1/2}$ obtained from the chronoamperometric evolutions at the NiTAPc-SWCNT(linked)-GCE in pH 4 buffer on addition of 1 mM 2-ME. Potential = 1.1 V.

Figure 5.42a shows typical single step chronoamperometric evolutions recorded after polarization of the NiTAPc-SWCNT(linked)-GCE at 1.1 V for the buffer and the different concentrations of 2-ME (in pH 4 buffer). Using Fig. 5.42b and Eq. 5.3, the rate constant (*k*) for the reaction between 2-ME and the redox sites of surface confined NiTAPc-SWCNT(linked) was found to be 2.95 x 10^3 M^{-1} s^{-1}. This value is smaller than what was observed on the CoTAPc-SWCNT(linked). Unfortunately there is no information that could be obtained from the literature on the rate constants for the electrochemical oxidation of 2-ME in acid media. These large values indicate that the electrochemical oxidation of 2-ME at NiTAPc-SWCNT(linked)-GCE surface is very fast.

5.7.2.5 Rotating disk electrode experiments

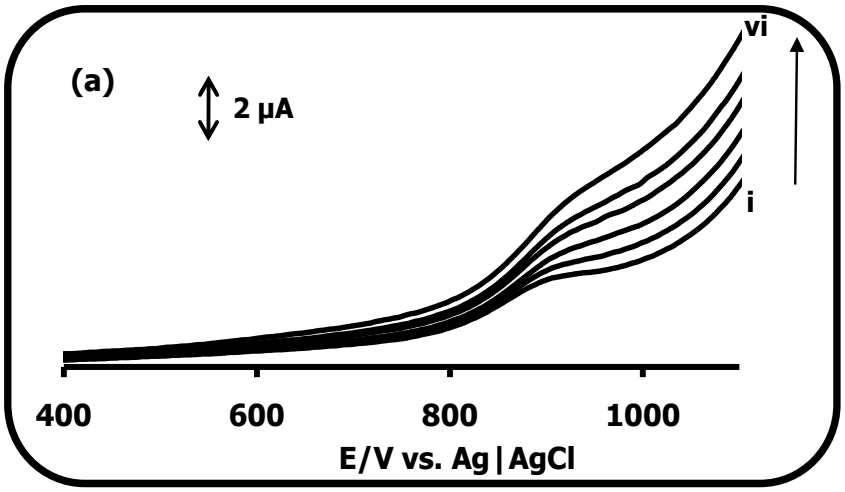

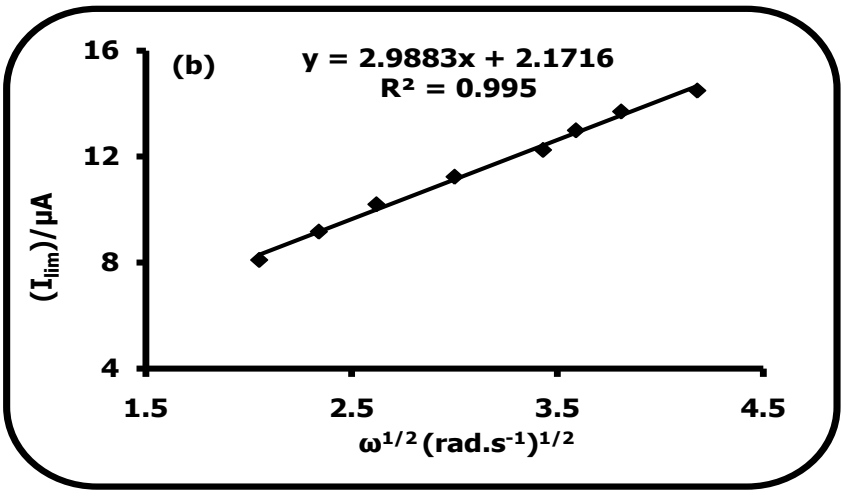

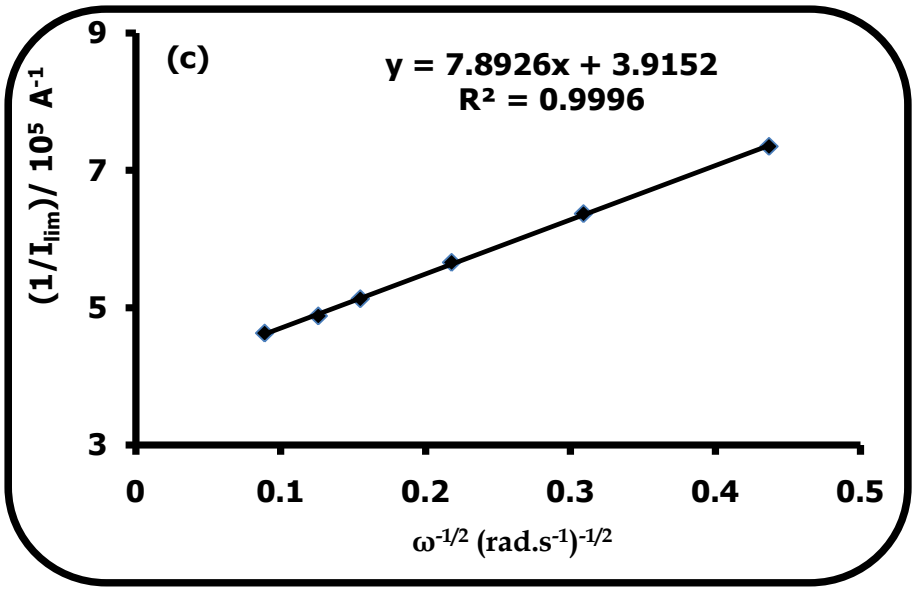

Figure 5.43: (a) Rotating disc electrode voltammograms (rpm): (i) 50, (ii) 100, (iii) 200, (iv) 300, (v) 400, and (vi) 500 for 1 mM 2-ME on NiTAPc-SWCNT(linked)-GCE in pH 4 buffer. Scan rate = 20 mV/s, (b) Levich plot for the variation in oxidation current with increasing rotational speed, (c) Koutecky-Levich plot for 1 mM 2-ME on NiTAPc-SWCNT(linked)-GCE in pH 4 buffer.

Figure 5.43a shows the linear sweep evolutions of the rotating disc electrode experiments obtained at the NiTAPc-SWCNT(linked)-GCE for 0.2 mM 2-ME in pH 4 buffer. The oxidation of 2-ME at a surface modified GCE is governed by mass transfer process in the solution and the relationship between the limiting current and the rotational speed should obey the Levich equation (Eq. 5.13) [245]. Fig. 5.43b shows a linear relationship between the limiting current and the electrode rotational speed, in agreement with Eq. 5.13.

The Koutecky-Levich plot (Fig. 5.43c) was obtained from the conventional Koutecky-Levich theory [105] represented by Eq. 5.9. The observed linear relationship between inverse of catalytic current and $\omega^{-1/2}$ with a positive intercept (Fig. 5.43c) indicate that the electrode reactions were controlled by both kinetics and the mass transport of 2-ME species at the electrode surfaces. From the intercept, the value of k was found to be 2.06 x 10^3 M^{-1} s^{-1}, Table 5.2, which is in close agreement with a value of 2.95 x 10^3 M^{-1} s^{-1} obtained from chronoamperometric studies.

Using chronoamperometry it was observed that the current – concentration plots of 2-ME was linear (equation: peak current (μA) = (0.197 μA/μM)[2-ME] + 8.73) in the concentration range 5 x 10^{-6} – 1 x 10^{-4} M, highlighting the usefulness of this method as an analytical tool. The sensitivity was 2.53 A mol^{-1} L cm^{-2} and the LOD was found to be 0.15 μM using the 3δ-notation and higher than for CoTAPc-SWCNT(linked). This detection limit is lower than what has been reported in other studies [314] and therefore can serve as a good method for the detection of 2-ME.

5.7.3 Effect of the metal centre on catalysis of 2-ME

The cyclic voltammetry data for FeTAPc-SWCNT(linked) on 2-ME is being used in this thesis to only deduce the effect of the metal centre on catalysis, hence was not discussed in detail above.

Figure 5.44 shows the comparative oxidation voltammograms for 2-ME on CoTAPc-SWCNT(linked) (a,**14**), FeTAPc-SWCNT(linked) (b,**15**) and NiTAPc-SWCNT(linked) (c,**16**) conjugates. The 2-ME oxidation peak on the CoTAPc-SWCNT electrode is at 350 mV less positive compared to both FeTAPc-SWCNT and NiTAPc-SWCNT electrodes, Table 5.2. The CoTAPc-SWCNT conjugate is therefore a better electrocatalyst and this is not surprising since the oxidation of thiols is closely related to the Co^{III}/Co^{II} couple of the CoPc species in acid media [251]. Cobalt metal centre enhances the catalytic oxidation of thiols because its orbital energies closely match those of sulphur, enabling easy transfer of electrons from the sulphur orbital to the d_z^2 and d_{xz} orbitals of the metal [25]. The oxidation of thiols proceeds via an inner sphere mechanism [25], with bonding between the sulphur atom and the active metal centre occurring before or during electron transfer [25]. At pH 4, the $Fe^{III}Pc^{-1}$ species are implicated in the catalysis of 2-ME. Though the oxidation peak potential for 2-ME on FeTAPc-SWCNT(linked) **(15)** and NiTAPc-SWCNT(linked) **(16)** electrodes is approximately the same (0.95 V vs. Ag|AgCl), its oxidation is initiated at lower potentials for the latter, an indication of better catalytic properties for conjugate **(16)**. Peak **I** represent the Ni^{III}/Ni^{II} oxidation process [103-106] and is responsible for the early oxidation of amitrole.

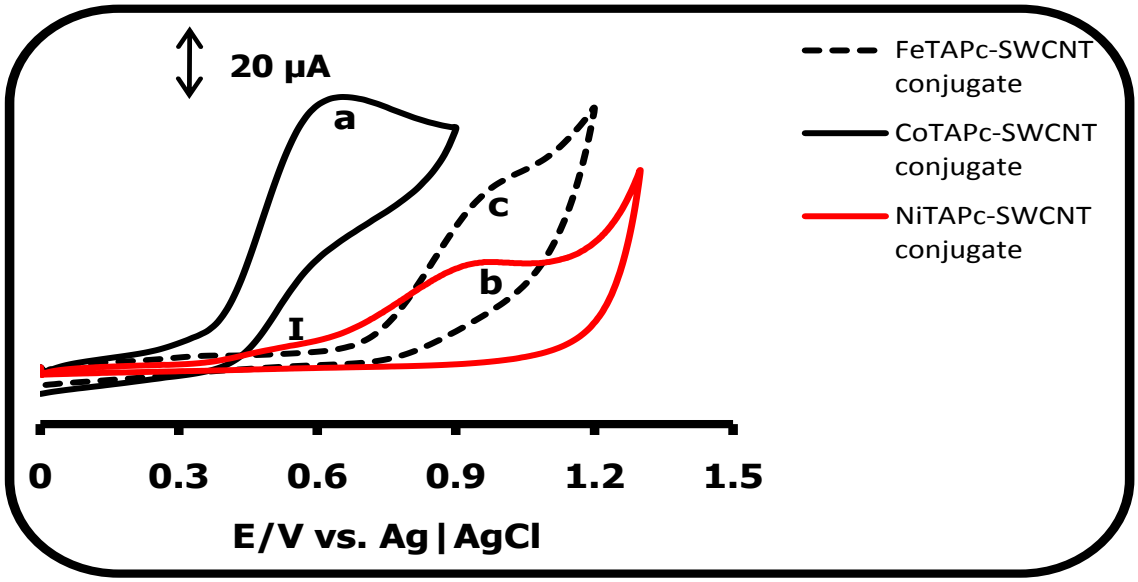

Figure 5.44: Comparative cyclic voltammograms for: (a) CoTAPc-SWCNT(linked) (14), (b) FeTAPc-SWCNT(linked) (15) and NiTAPc-SWCNT(linked) (16) in 1 mM 2-ME (pH 4 buffer). Scan rate = 100 mV/s.

5.4 Conclusions

Most of the MPc modified electrodes used in this study were good electrocatalysts for 2-ME, amitrole or diuron, except for CoTCPc **(8)** and CoMCPc **(10)**. This may be due to the electron withdrawing nature of the carboxylic acid groups, which interfere with the oxidation of the electro-active cobalt centre. Conversion of the *poly*-NiTAPc **(7c)** into *poly*-Ni(OH)TAPc was also accompanied by improved catalytic activity of diuron due to the presence of the activated Ni^{III}/Ni^{II} redox species. Chemically linking amine and carboxylic acid functionalized SWCNTs to MPc improved catalysis. Amine carrying SWCNTs induced good catalytic activity into the electro-inactive carboxy-MPcs (i.e. CoTCPc and CoMCPc). This was more pronounced in CoTCPc **(8)** and less in CoMCPc **(10)**, possibly due to the electron-donating benzyl-mercapto groups and the little electron-withdrawing effect of the phenoxycarboxy group in the later. Impedance studies (Nyquist plots) showed that chemically linking SWCNTs to MPcs produce electrodes with lower resistance to charge transfer, hence the good catalytic properties observed in all the conjugates used in this study. Bode plots showed that catalysis was occurring from modified electrodes rather than the bare GCE surfaces. Tafel slopes observed for 2-

ME on CoTAPc-SWCNT(linked) **(14),** FeTAPc-SWCNT(linked) **(15)** and NiTAPc-SWCNT(linked) **(16)** were within the 30-120 mV/decade expected for a one-electron rate determining step. This also indicated that in the presence of SWCNTs, passivation of the electrode is limited. However, for amitrole and diuron, the Tafel slopes were higher than 120 mV/decade expected of a reaction in which an electrochemical step precede a very fast chemical reaction. This phenomenon has been explained in terms of increased interaction between the catalyst and the substrate, which is convincing in this study because of the dipole-dipole interactions between the л-electrons of the analytes and those of the catalyst. Chronoamperometry and RDE studies showed that the kinetics of analytes on *poly*-Ni(OH)TAPc and MPc-SWCNT(linked) electrodes was much favourable, with catalytic rate constants being higher on the latter. Highest rate constants were observed on CoMCPc-PA-SWCNT(linked) **(20)** electrodes, followed by CoMAPc-SWCNT(linked) **(19)** for both amitrole and diuron. Studies also showed that diuron strongly interferes with the detection of amitrole, and in a suspected mixture HPLC separation is recommended before analysis.

CHAPTER 6

SYNTHESIS AND CHARACTERIZATION OF SINGLE WALLED CARBON NANOTUBES (SWCNTs)

This chapter deals with the synthesis of SWCNTs from the pyrolysis of an iron (II) phthalocyanine (FePc) in the presence of ferric acetate and metal free phthalocyanine (H_2Pc).

6.1 Synthesis of SWCNTs

FePc, metal free phthalocyanine and ferric acetate (Fig. 6.1b1) were mixed together in the ratio of 1:1:2 using a pestle and mortar (Fig. 6.1b4). The powdered mixture was converted into activated tablets in a tablet making attachment (Fig. 6.1b2), to a 300 kN Press (Fig. 6.1a). The activated tablets (Fig. 6.1b3) were ground into powder (Fig. 6.1b5) using a pestle and mortar and placed in a ceramic boat and then inserted into a quartz heating tube. The quartz tube and its contents were placed into a furnace (Fig. 6.1c) and the temperature raised to 1000 ^{0}C in the presence of an argon/hydrogen mixture flowing at a rate of 40 cm^3/min for 1 h, after which the furnace was allowed to cool. The synthesized SWCNTs (raw SWCNTs) were subsequently removed from the furnace. Such SWCNTs normally contain impurities like carbonaceous materials (e.g. amorphous carbon, fullerenes and carbon nanoparticles) and metal catalyst particles.

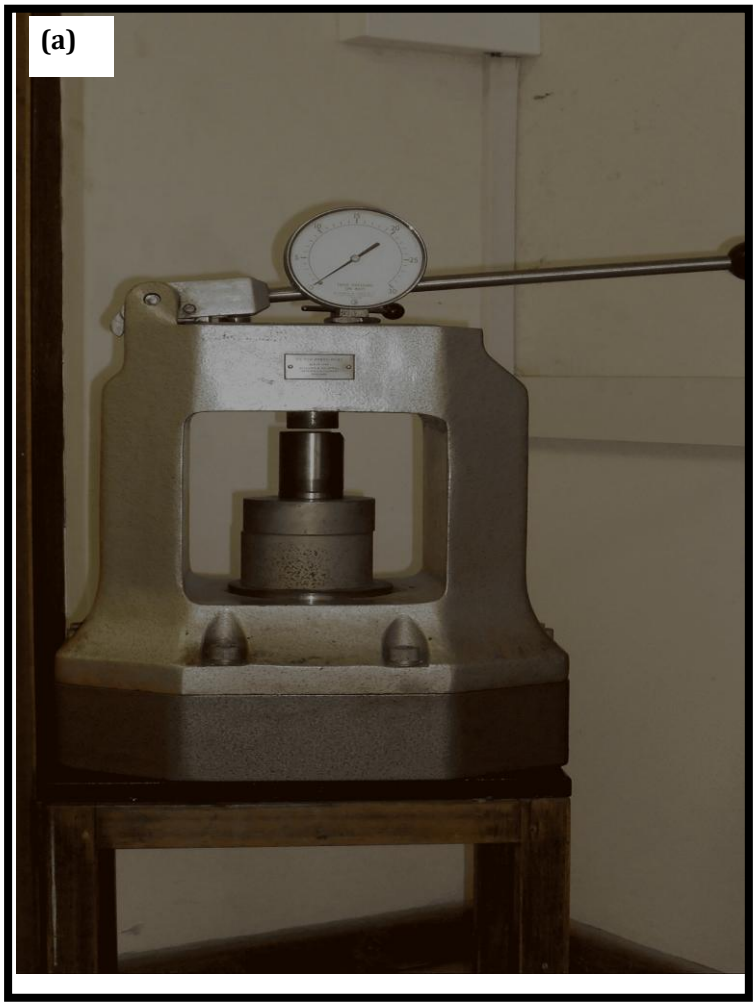

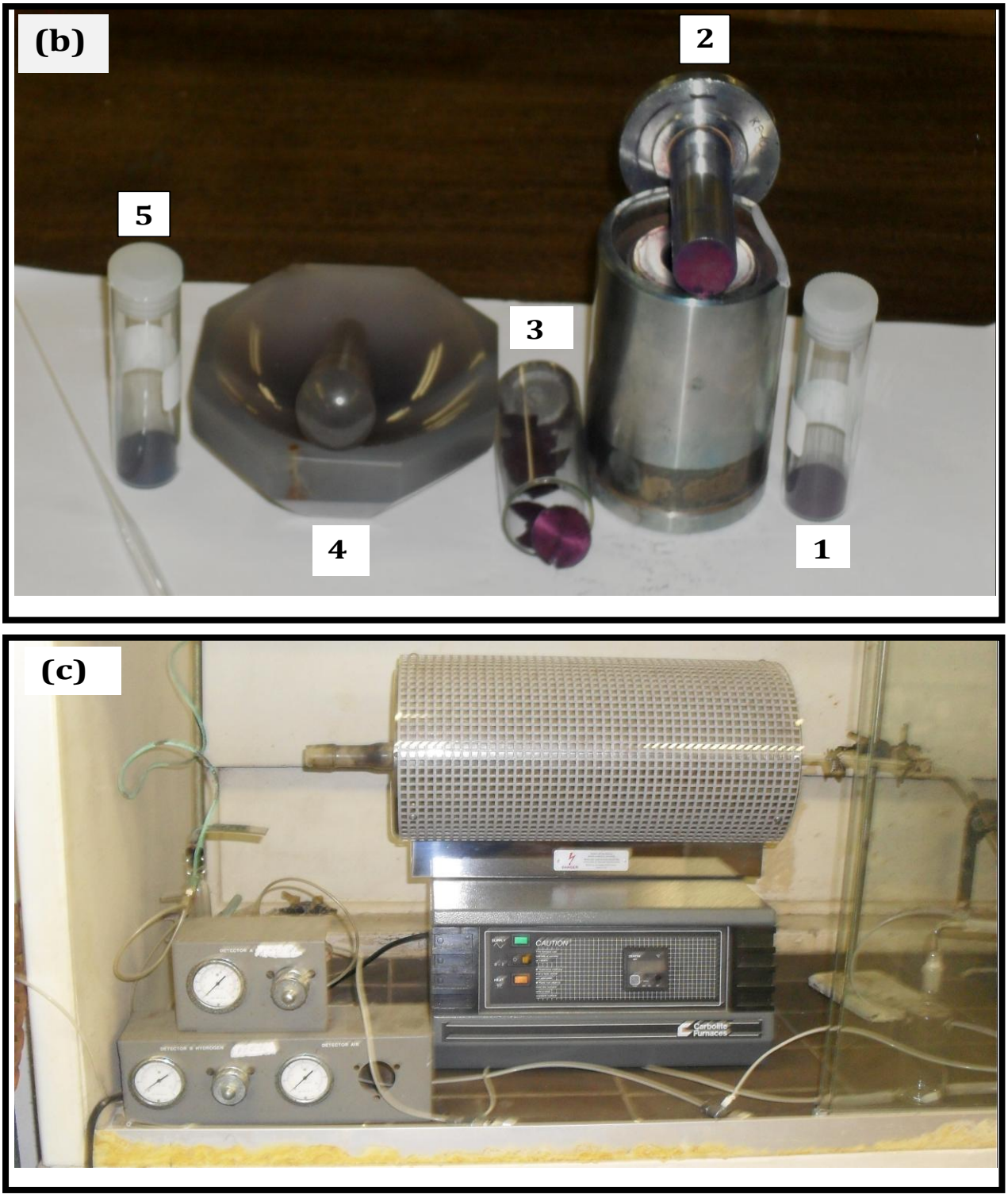

Figure 6.1: (a) 300 kN Press M-30 from the Research and Industrial Instruments Company, England, (b) (1) FePc/metal free Pc/ ferric acetate mixture, (2) Pc tablet making accessory, (3) activated FePc/metal free Pc/ ferric acetate tablet, (4) pestle and mortar and (5) activated FePc/metal free Pc/ ferric acetate powder and (c) Carbolite Furnace, Zenith 681.

6.2 Purification of SWCNTs

The raw SWCNTs were mixed with toluene and the mixture thoroughly stirred for 2 h to remove any fullerenes [107] that may be present. Amorphous carbon and carbon nanoparticles were removed through oxidation of SWCNT in a 3:1 mixture of concentrated H_2SO_4: concentrated HNO_3 for 2 h [154], leaving behind relatively pure SWCNTs [107]. This chemical purification process is selective and removes carbonaceous impurities due to their dangling bonds and structural defects [107] with the only limitation being the opening of the CNT ends and the introduction of oxygenated terminals [155]. These purified SWCNTs were then subjected to low-speed centrifugation in order to remove any unoxidised amorphous carbon, leaving behind SWCNTs and carbon nanoparticles (CNPs), in the sediment. The remaining mixture was then exposed to high-speed centrifugation that settled CNPs leaving SWCNTs suspended in aqueous media [107]. Chemical oxidation of the SWCNTs and centrifugation ensured effective purification. The resulting SWCNTs were centrifuged and washed with millipore water several times until a pH of 5 was attained, giving SWCNT-COOH. The SWCNT-COOH were oven dried at 110 ^{0}C for 12 h [154]. The acid treated SWCNT-COOH were analyzed through different spectroscopic and microscopic techniques.

6.3 Characterization of SWCNTs

6.3.1 Transition Electron Microscopy (TEM)

TEM can provide qualitative information on defects, and on amorphous carbons and fullerenes that are adsorbed onto the CNTs walls [107] with the limitation being its failure to give quantitative information [171]. The TEM in Fig. 6.2 shows the functionalized SWCNT dispersed in DMF. The dark sports observed in Fig. 6.2 could be remnant metallic (iron) clusters after acid treatment [164]. The TEM pictures confirm that it is the SWCNTs that were successfully synthesized since the diameters of SWCNTs are normally within the range of 1-3 nm [317]. CNTs with diameters greater than 3 nm are referred to as large diameter SWCNTs [317]. The use of a catalyst such as Fe usually results in SWCNT, but MWCNT can form depending on the ratio of catalyst to carbon and FePc to metal free Pc [140]. The TEM images

show diameters that are of varied sizes, from 2.56 nm to 10.03 nm and are several nanometers long. This shows that the synthesized CNTs are single walled and the observed larger diameter sizes could be due to aggregated SWCNTs. Normally for the non-activated FePc, the SWCNT bundle diameters are in the range 40 – 100 nm [318], but in this work diameter sizes were reduced to less than 20 nm, showing, additionally, the effectiveness of the activation process.

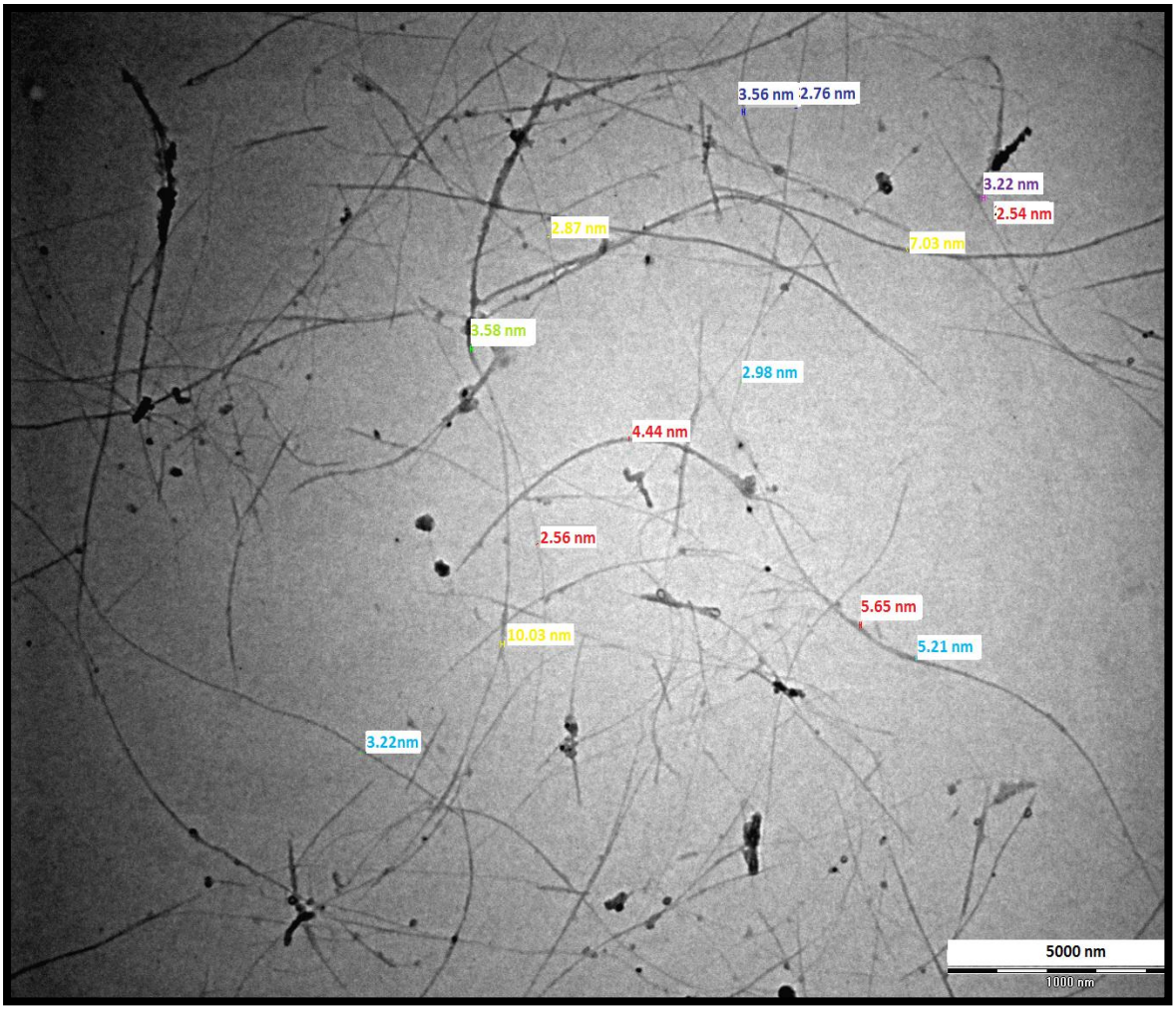

Figure 6.2: TEM image of functionalized SWCNTs dispersed in DMF.

6.3.2 UV-vis Spectroscopy

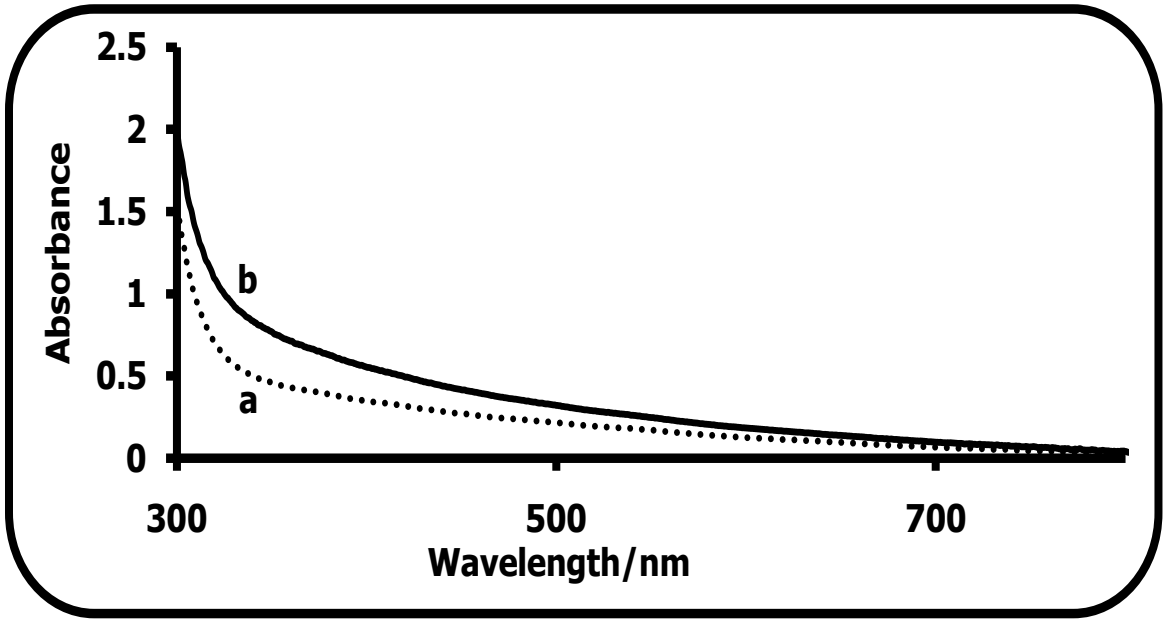

Figure 6.3: UV-vis spectra for (a) raw SWCNTs and (b) SWCNT-COOH dispersed in DMF.

UV–vis spectroscopy is a rapid and convenient qualitative technique to estimate the relative purity of bulk SWCNTs [171]. The absorption spectra for both the raw and the functionalized SWCNTs are relatively smooth with increased absorption for the SWCNT-COOH as shown in Fig. 6.3. Normally raw CNTs absorption spectra are associated with van Hove singularities of metallic and semiconducting nanotubes that are attributed to their band-gap transitions whose widths reflect the overlap of features from CNTs having different diameters and chiral indices [186]. These van Hove singularities are absent in purified SWCNTs [176,187,188].

6.3.3. Infrared Spectroscopy

Figure 6.4 shows the FTIR spectra for the raw SWCNTs and functionalized SWCNTs. Raw SWCNTs show ill-defined absorption bands which improved with functionalization as observed elsewhere [167]. Well defined peaks for SWCNT-COOH at 3448, 2967, 2998, 1740, 1368 and 1214 cm^{-1} are attributed to the O-H, C-H,

C=O, C-N and C-O stretches, respectively, as has been reported before [167]. This confirms the successful synthesis and functionalization of the SWCNTs.

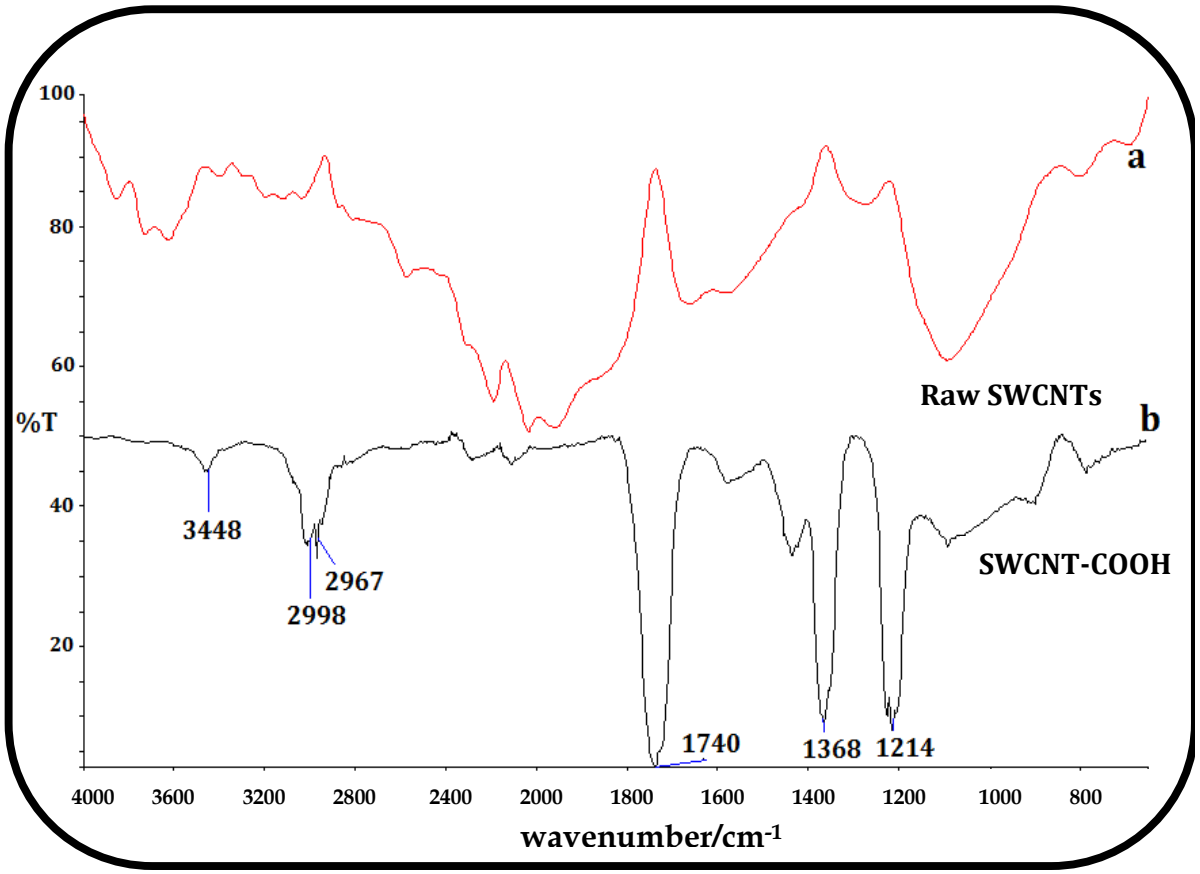

Figure 6.4: FTIR spectra for (a) raw SWCNTs and (b) SWCNT-COOH.

6.3.4 Thermogravimetric analysis

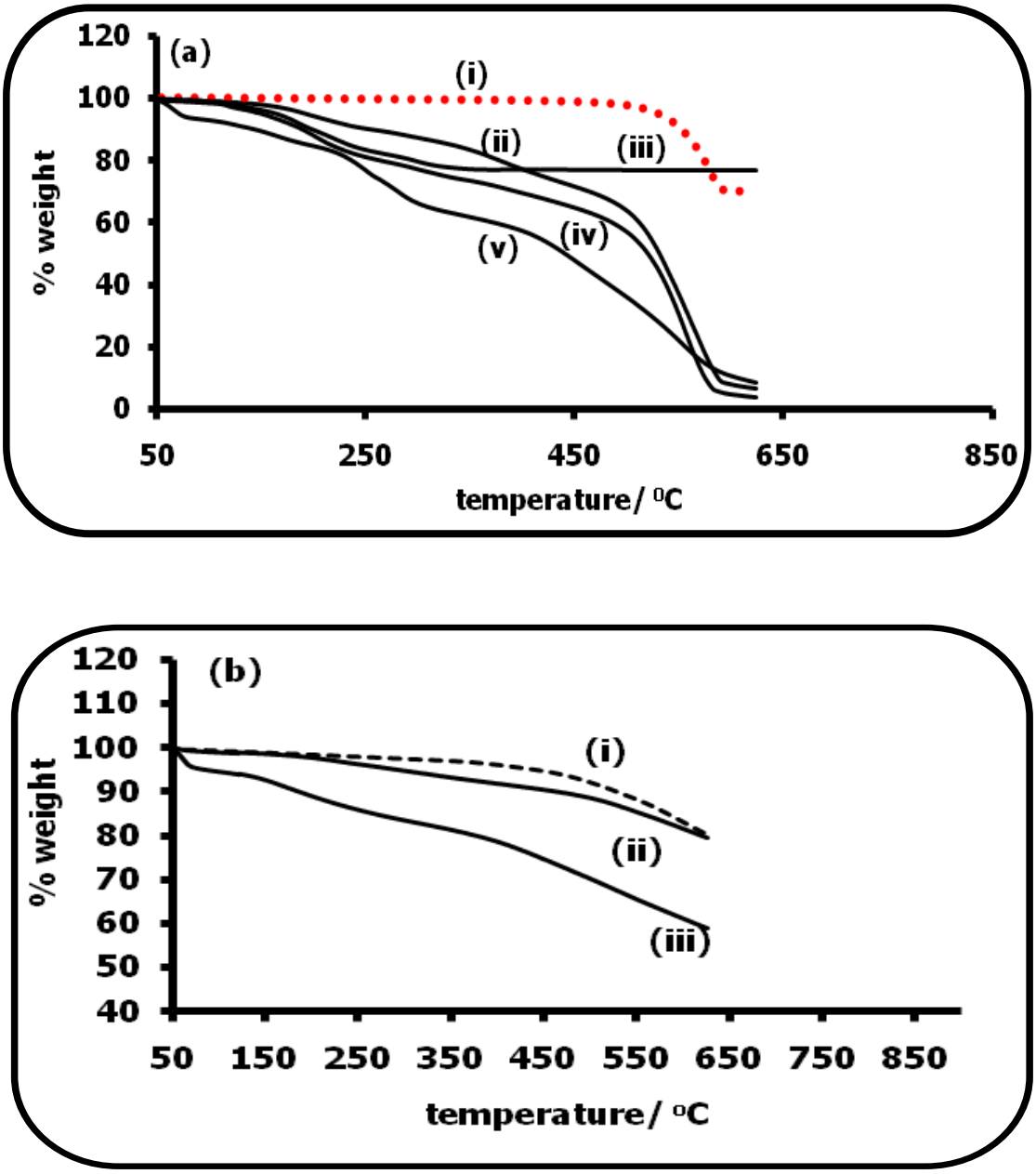

Figure 6.5: TGA of (a) (i) metal free Pc, (ii) non-activated metal free Pc/FePc/ferric acetate mixture, (iii) ferric acetate, (iv) FePc and (v) activated metal free Pc/FePc/ferric acetate mixture. (b) (i) SWCNTs (purchased), (ii) synthesized raw SWCNT and (iii) SWCNT-COOH at a heating rate of 10 ^{0}C/min under nitrogen.

Thermogravimetric analysis (TGA) was used to show quantitative and qualitative structural and behavioral differences between the metal free Pc, FePc, ferric acetate, non-activated and activated (metal free Pc/FePc/ferric acetate)

mixture. Figure 6.5a compares the TGA traces for metal free Pc, FePc, non-activated Pc mixture, activated Pc mixture and ferric acetate. Derivative TGA was used to deduce the initial decomposition temperatures for all the materials under study. Thermal decomposition of the FePc (Fig. 6.5a (iv)) begins at around 230 ^{0}C as observed elsewhere [319], a temperature very close to where ferric acetate starts to decompose (220 ^{0}C), while the decomposition of the metal free Pc begins at around 560 ^{0}C (Fig. 6.5a (i)). In the non-activated metal free Pc/FePc/ferric acetate mixture, the decomposition of ferric acetate and FePc begins in the temperature range 220-230 ^{0}C, in agreement with thermogram (iii) for ferric acetate and (iv) for FePc. The decomposition of the activated mixture is initiated at a lower temperature compared to the non-activated mixture. This was confirmed by derivative TGA, which gave the initial decomposition temperatures for the activated and non-activated mixtures to be 205 ^{0}C and 245 ^{0}C, respectively. It can be conclusively deducted from TGA studies that the compression method of activation is effective in imparting the necessary structural and behavioral changes that are required for the formation of CNTs from the mixture. This leads to the lowering of the decomposition temperatures in the activated mixture (as shown in Fig. 6.5a (v)) which in turn should lead to the lowering of the pyrolysis temperature of the Pcs.

Figure 6.5b shows the thermograms obtained for raw SWCNTs (purchased), raw SWCNTs (synthesized) and SWCNT-COOH (synthesized). Samples of 1.4 mg each of SWCNTs (purchased), raw SWCNTs (synthesized) and SWCNT-COOH were heated under nitrogen from 50 ^{0}C to 625 ^{0}C at a heating rate of 10 ^{0}C/min. The difference in the nature of the TGA profiles is an indication of their structural differences. Weight loss observed for the raw CNTs (purchased and synthesized) may be due to loss of water, but is more likely due to the destruction of the residual amorphous carbon present in the carbon nanotubes [194]. For SWCNT-COOH, further weight loss could be due the decomposition of the carboxylic acid group in addition to the loss of water and maybe some remaining amorphous carbon. TGA traces showed similar weight loss of ~ 17.0 % (at 625 ^{0}C) for both the purchased and synthesized raw SWCNTs and 39.1 % for the functionalized SWCNTs. Similarities in the % weight loss for the purchased and synthesized CNTs signifies approximately

equal amounts of amorphous carbon content. Having considered the weight loss due to adsorbed volatiles (6.1%), the % loss due to amorphous carbon is ~13.1, giving a purity of about 80.8% (as single walled carbon nanotubes) at 625 ^{0}C. Their quality is comparatively good relative to the Aldrich SWCNTs, whose carbon content as single walled carbon nanotube is estimated to be 82.5 % at the same temperature. This is a crude estimation, based on the assumption that all impurities have been eliminated, though CNTs are known to contain some residual metallic clusters, irrespective of the acid washing [131].

The extent of functionalization is expressed as the number of substituents per SWCNT carbon atoms. By applying the formula reported in the literature [209], the estimated weight loss due to the functionalization of SWCNT-COOH was 22.1 % giving on average, one carboxylic group per 13 carbon atoms.

6.3.5 X-ray diffraction spectroscopy

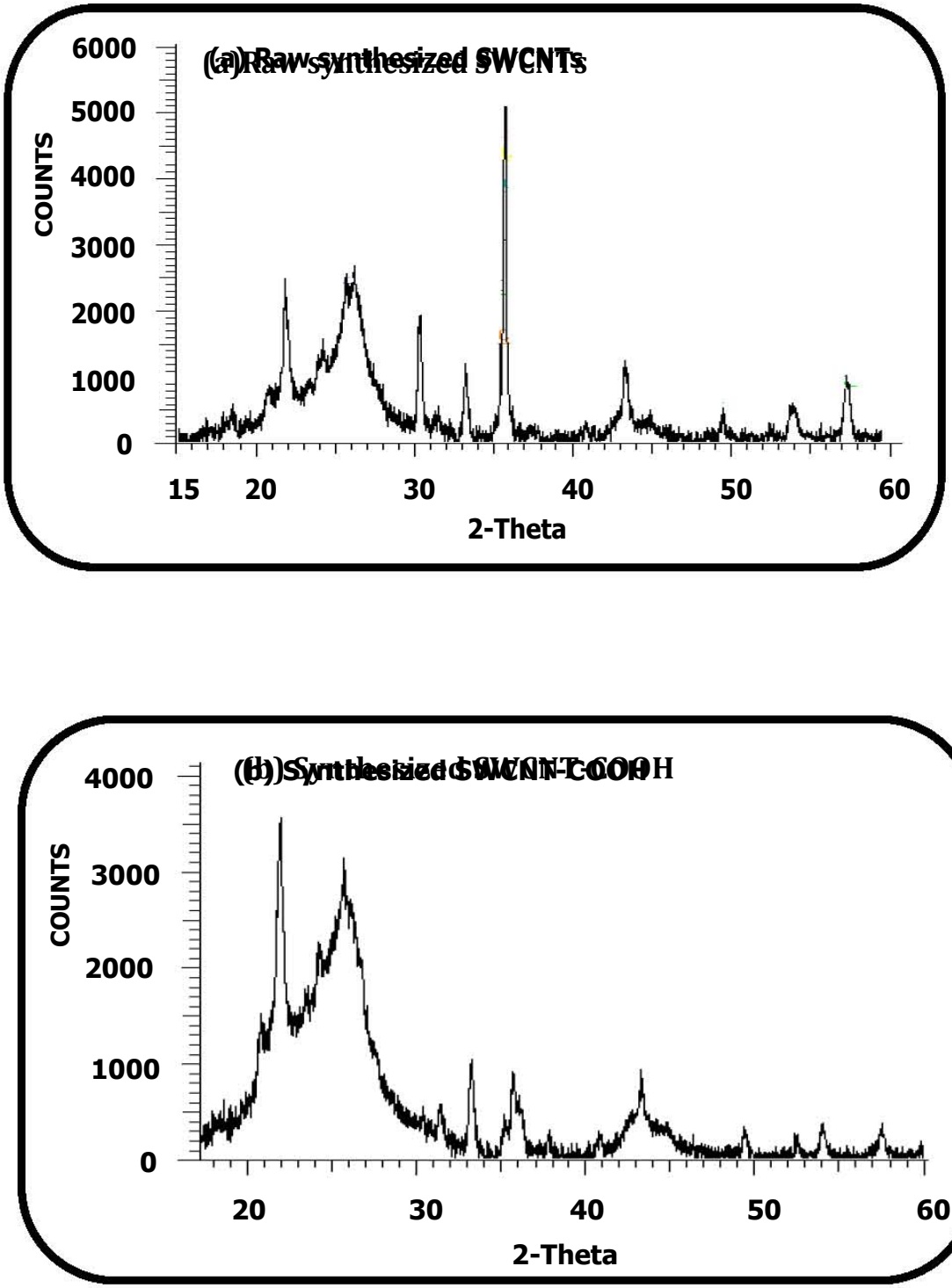

Figure 6.6: XRD spectra for the synthesized (a) raw SWCNTs and (b) SWCNT-COOH.

Table 6.1: 2θ, d-spacings and peak intensities of the synthesized SWCNTs.

2θ	d-spacings	Intensity
Raw SWCNTs		
21.7; 25.8; 30.3; 33.2; 35.7; 43.4; 49.5; 52.5; 54.1; 57.5	4.09; 3.44; 2.95; 2.70; 2.57; 2.09; 1.83; 1.70; 1.61	2527.1; 2610.1; 1946.2; 1275.1; 5235.9; 1480.7; 770.0; 792.0; 920
SWCNT-COOH		
22.0; 25.7, 26.0; 31.4; 33.1; 35.8; 43.4; 49.5; 52.4; 54.0; 57.5	4.05; 3.46; 2.84; 2.70; 2.51; 2.09; 1.84; 1.74; 1.70; 1.60	3590.6; 3160.1; 613.6; 1097.0; 920.6; 980.2; 389.6; 310; 377.21; 381.2

X-ray diffraction spectroscopy was used to explore the structural differences between the raw and the carboxylic acid functionalized SWCNTs (SWCNT-COOH). Figs. 6.6a and b shows the XRD spectra for raw SWCNTs and SWCNT-COOH, respectively. Table 6.1 lists the 2θ-values, d-spacings and the peak intensities for the two forms of SWCNTs. The peaks at 2θ angles of 25.7^0, 43.4^0 and 52.4^0 in Fig. 6.6b SWCNT-COOH) correspond to the graphite (002) d-spacing of the SWCNTs [193-195], the (111) and (200) reflections of carbon [195], respectively. The raw SWCNTs show these peaks at 25.8^0, 43.4^0 and a small peak at 52.5^0, respectively. Functionalization of SWCNTs increased the intensities of the first two peaks while the rest of the peaks decreased in intensities. Decreases and increases in peak intensities could be associated with the oxidizing nature of the H_2SO_4/HNO_3 mixture. Peaks at ~33^0, 36^0 and 57.5^0 have been observed elsewhere and assigned Miller indices but their origin was not explained [194].

6.3.6. Raman spectroscopy

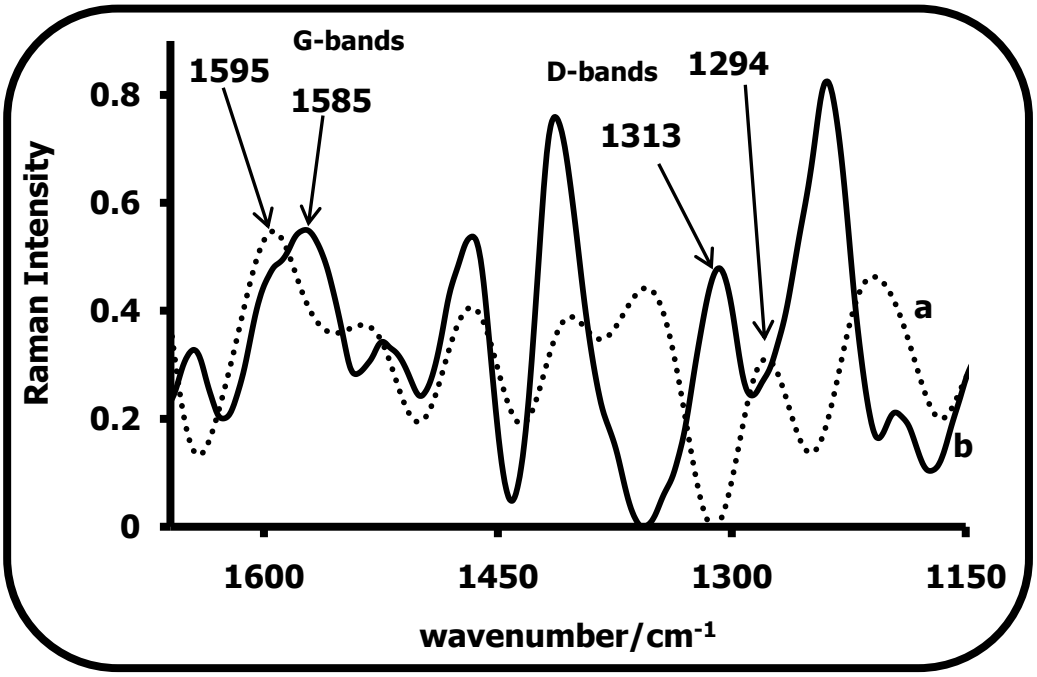

Figure 6.7: Raman spectra for (a) raw SWCNTs and (b) SWCNT-COOH.

Raman spectroscopy is a fast, convenient and non-destructive analytical technique and can be used to some extent to quantify the amount of impurities by using the ratio of D/G bands under fixed laser power intensity [320]. Figure 6.7 shows the Raman spectra of the raw and functionalized SWCNTs. The D and G bands are at 1294 and 1595 cm^{-1} and at 1313 and 1585 cm^{-1} for the raw and functionalized SWCNTs, respectively. The ratios of D/G peak intensities for the raw and functionalized SWCNTs are 0.56 and 0.87, respectively. This significant increase in the D band intensity is an indication of hybridization from sp^2 to sp^3 of the side-wall carbon atoms, as has been reported [164]. The appearance of D and G-bands is an indication of successful synthesis of CNTs.

6.3.7 Electrochemical characterization

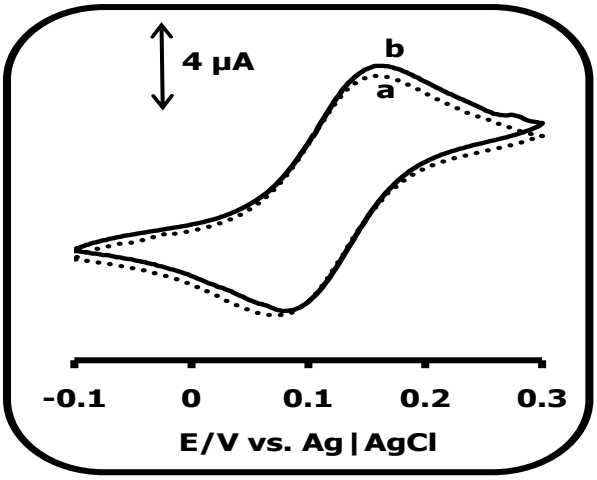

Figure 6.8: Comparative cyclic voltammetric evolutions of 1 mM of $[Fe(CN)_6]^{3-/4-}$ in 0.1 M of KCl using bare GCE (a) and SWCNT-COOH-GCE (b). Scan rate = 20 mV/s.

The performance of purified SWCNTs was evaluated by studying parameters such as peak separations (ΔEp), overpotentials and peak currents of electroactive species. The electrocatalytic behaviour of the SWCNTs was evaluated against the bare electrode. It has been reported that the use of CNTs improves the reversibility of redox processes [246,321] by providing many active sites. Fig. 6.8 shows the cyclic voltammograms of the $[Fe(CN)_6]^{3-/4-}$ redox probe on bare GCE and SWCNT-COOH modified GCE. The SWCNT-COOH-GCE gave a peak-to-peak separation of 60 mV versus 70 mV for the bare electrode (at a scan rate of 20 mV/s), showing that the SWCNT-COOH modified electrode has better electron transfer properties.

The electro-activity of SWCNT based electrodes for the oxidation of amitrole was studied in pH 4 buffer, Fig. 6.9. In general, catalytic activity is evidenced by lowering of overpotential and increased currents. In Fig. 6.9, catalytic activity of the SWCNT-COOH was evidenced by sharper voltammograms [249,250] at reduced reaction overpotentials. The oxidation of amitrole occurred at ~0.81 V on the SWCNT-COOH-GCE versus ~0.92 V observed on the bare GCE, an indication of better electron transfer mediation by the SWCNT-COOH adsorbed on the GCE.

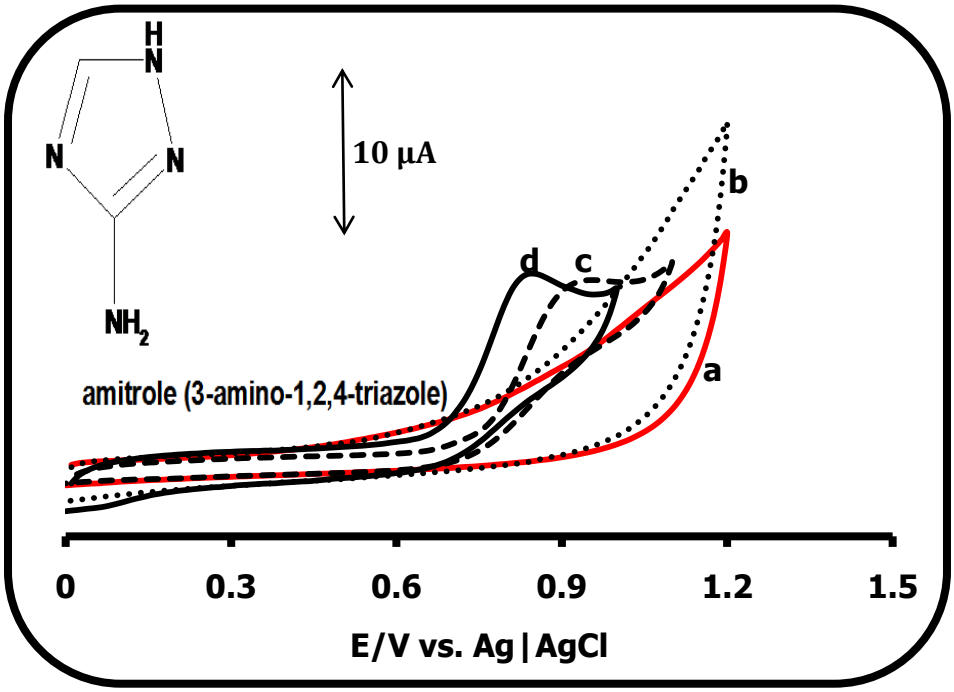

Figure 6.9: Comparative cyclic voltammograms for the bare GCE (a) and SWCNT-COOH-GCE (b) in pH 4 buffer; the bare GCE (c) and SWCNT-COOH-GCE (d) in 0.12 mM amitrole. Scan rate = 100 mV/s. Inset: The molecular structure of amitrole.

6.4 Conclusion

The use of the compression technique to activate the phthalocyanine employed in this work, proved to be very effective, rapid and reduced the time required for the synthesis of CNTs from days to hours. TEM proved to be an essential analytical tool in ascertaining the successful synthesis of SWCNTs. XRD, Uv-vis, FTIR, Raman, TGA and cyclic voltammetry were also used to characterize the in-situ synthesized SWCNTs. Based on the different CNT diameters observed in the synthesized SWCNTs, it proves that the conditions necessary for the control of the diameter sizes of CNTs is still a major challenge.

CHAPTER 7

GENERAL CONCLUSIONS & FUTURE PERSPECTIVES

This chapter summarizes the results obtained for the studies conducted and reported in this thesis and future prospects.

7.1 General conclusions

The synthesis of tetrasubstituted carboxy and amino carrying MPcs (including low symmetry) was successfully achieved. Microscopic, spectroscopic and electrochemical techniques were used in the characterization of the synthesized MPcs and MPc-SWCNT conjugates. Chemically linking MPcs to SWCNTs improves the catalytic properties of phthalocyanines.

Results showed that catalysis of MPcs and MPc-SWCNT conjugates is affected by:

(i) The nature of substituents on the MPc, with the COOH group rendering the Pc molecule non-catalytic. However, chemically linking the carboxy carrying MPc to SWCNTs **(11, 12)**, catalytic activity is induced into the Pc molecule.

(ii) The nature of functional groups introduced onto the SWCNT. Amine carrying SWCNTs enhance catalytic activity more than carboxylic acid functionalized CNTs.

(iii) Presence of a linker, e.g. CoTAPc-SWCNT **(14)** versus CoTCPc-EA-SWCNT **(18)** or CoTCPc-PA-SWCNT **(17)**, the EA and PA greatly enhance catalysis, as confirmed by the reduced oxidation overpotentials in the later.

(iv) The size of the molecule/nature of conjugate. Tetrasubstituted conjugates are less catalytic compared to the nanosized complexes of low symmetry MPcs with SWCNTs **(19,20)**. This could be due to their good alignment on the electrode surface.

(v) In conjugates of low symmetry MPcs with SWCNTs **(19,20)**, amine functionalized SWCNTs produced better catalytic properties relative to SWCNT-COOH **(13)**, as shown by the very high catalytic rate constants. This behaviour has also been observed for the conjugates of tetra- amino and carboxy MPcs with SWCNTs (iii above).

(vi) Conversion of *poly*-NiTAPc into *poly*-Ni(OH)TAPc, improved catalytic properties of the later.

(vii) Application of conjugates to simultaneously determine amitrole and diuron is very difficult due to the non-selectivity of electrodes. It therefore calls for a separation of the two prior to electrochemical analysis.

Although MPcs, especially those carrying electroactive metals and SWCNTs are catalytic, the work described in this thesis shows improved electron transfer properties for the MPcs when they are chemically linked to SWCNTs. This has resulted in high catalytic currents at reduced reaction overpotentials for both amitrole and diuron, relative to the MPcs and SWCNTs alone.

7.2 Future perspectives

Comparative studies should be done between SWCNTs carrying carboxylic acid groups on both the walls and the terminals. This will enable deductions to be made about the solubilities and the catalytic properties of the MPc-SWCNT conjugates. Improved solubility of SWCNTs can also be brought through chemically linking them to MPcs via ester bridges. Thereafter, comparative work can be done on the catalytic efficiencies of ester-bridged versus amide-bridged conjugates. More work can also be done to show the effects of introducing larger alkyl or aryl groups onto the surface of the SWCNTs and how this will affect the electrocatalytic activities of the MPcs. Further electrocatalytic studies can be done on MPcs that are directly linked to the SWCNTs through a carbon-carbon bond (in the absence of an amide linkage).

REFERENCES

1. P. Gregory, J. Porphyrins Phthalocyanines 4 (2000) 432.

2. F. Bedioui, S. Griveau, T. Nyokong, A. J. Appleby, C. A. Caro, M. Gulppi, G. Ochoa, J. H. Zagal, Phys. Chem. Chem. Phys. 9 (2007) 3383.

3. K. R. V. Reddya, J. Keshavayya, Dyes Pigments 53 (2002) 187.

4. G. La Torre, T. Torres, J. Porphyrins Phthalocyanines 1 (1997) 221.

5. R. von Braun, J. Tcherniak, J. Chem. Ber. 40 (1907) 2709.

6. De Diesbach, von der Weid, Helv. Chim. Acta 10 (1927) 886.

7. R. P. Linstead, J. Chem. Soc. (1934) 1016.

8. G. T. Byrne, R.P. Linstead, A. R. Lowe, J. Chem. Soc. (1934) 1017.

9. R. P. Linstead, A. R. Lowe, J. Chem. Soc. (1934) 1022.

10. C. E. Dent, R.P. Linstead, J. Chem. Soc. (1934) 1027.

11. R. P. Linstead, A. R. Lowe, J. Chem. Soc. (1934) 1031.

12. C. E. Dent, R. P. Linstead, A. R. Lowe, J. Chem. Soc. (1934) 1034.

13. J. M. Robertson, J. Chem. Soc. (1935) 615.

14. J. M. Robertson, J. Chem. Soc. (1936) 1195.

15. J. M. Robertson, J. Chem. Soc. (1936) 1736.

16. J. M. Robertson, J. Chem. Soc. (1937) 219.

17. J. M. Robertson, J. Chem. Soc. (1940) 36.

18. Great Britain Patent 322169, ICI, 1928.

19. P. Gregory, J. Porphyrins Phthalocyanines 3 (1999) 468.

20. M. Zabkowska-Waclawek, Z. Ziembik, J. Mater. Scie. 40 (2005) 1465.

21. A. B. P. Lever, J. Porphyrins Phthalocyanines 3 (1999) 488.

22. M. Kimura, Y. Yamaguchi, T. Koyama, K. Hanabusa, H. Shirai, J. Porphyrins Phthalocyanines, 1 (1997) 309.

23. A. B. P. Lever, M. R. Hempstead, C. C. Leznoff, W. Liu, M. Melnik, W. A. Nevin, P. Seymour, Pure App. Chem. 58 (1986) 1467.

24. N. Chebotareva, T. Nyokong, Electrochim. Acta 42 (1997) 3519.

25. J. H. Zagal, Coord. Chem. Rev. 119 (1992) 89.

26. M. Nicolau, B. Del Rey, T. Torres, C. Mingotaud, P. Delhaes, M.J. Cook, S.C. Thorpe, Synth. Met. 102 (1999) 1462.

27. S. Vilakazi, T. Nyokong, Polyhedron 19 (2000) 229.
28. T. Nyokong, J. Porphyrins Phthalocyanines 12 (2008) 1005.
29. M. P. Somashekarappa, J. Keshavayya, S. Sampath, Pure Appl. Chem. 74 (2002) 1609.
30. B. N. Achar, K. S. Lokesh, J. Organomet. Chem. 689 (2004) 3357.
31. M. Jurıcek, P. H. J. Kouwer, J. Rehak, J. Sly, A. E. Rowan, J. Org. Chem. 74 (2009) 21.
32. M. Hanack, J. Mertz, G. Pawlowski, Chem. Ber., 115 (1982) 2836.
33. G. Mbambisa, P. Tau, E. Antunes, T. Nyokong, Polyhedron 26 (2007) 5355.
34. T. Kimura, N. Kanota, K. Matsui, I. Tanaka, T. Tsuboi, Y. Takaguchi, A. Yomogita, T. Wakahara, S. Kuwahara, F. Nagatsugi, T. Akasaka, Inorg. Chem. 47 (2008) 3577.
35. M. J. Cook, A. J. Dunn, S.D. Howe, A. J. Thompson, K. J. Harrison, J. Chem. Soc., Perkin Trans.1 (1988) 2453.
36. A. J. Thompson, K. Murata, D.C.Miller, J. L. Stanton, W. E. Broderick, B. M. Hoffamn, J. A. Ibers, Inorg. Chem. 53 (1983) 2339.
37. N. B. Mckeown, I. Chambrier, M. J. Cook, J. Chem. Soc. Perkin Trans. 1 (1990) 1169.
38. M. Brewis, G. J. Clarkson, P. Humberstone, S. Makhseed, N.B. Mckeown, Chem. Eur. J. 4 (1998) 1633.
39. S. A. Mikhalenko, V. M. Derkacheva, E. A. Lu'yanets, J. Gen. Chem., USSR 51 (1981) 1405.
40. H. Ali, R. Langlois, J. R. Wanger, N. Brasseur, B. Paquette, J.E. van Lier, Photochem. Photobiol. 47 (1988) 713.
41. T. Nyokong, H. Isago, J. Porphyrins Phthalocyanines 8 (2004) 1083.
42. M. Sanchez, E. Fache, D. Bonnet, B. Meunier, J. Porphyrins Phthalocyanines 5 (2001) 867.
43. B. N. Achar, P.K. Jayasree, Synt. Met. 104 (1999) 101.
44. A. Sivanesan, S. A. John, Electrochim. Acta 53 (2008) 6629.
45. J. Obirai, T. Nyokong, Electrochim. Acta 49 (2004) 1417.

46. Y.-H. Tse, P. Janda, H. Lam, J. Zhang, W. J. Pietro, A. B. P. Lever, J. Porphyrins Phthalocyanines 1 (1997) 3.
47. P. Tau, T. Nyokong, J. Electroanal. Chem. 10 (2007) 611.
48. A. Sivanesan, S. A. John, Biosens. Bioelectr. 23 (2007) 708.
49. N. Nombona, P.Tau, N. Sehlotho, T. Nyokong, Electrochim. Acta 53 (2008) 3139.
50. H.-B. Xu, H.-Z. Chen, M.-M. Shi, R. Bai, M. Wang, Mater. Chem. Phys. 94 (2005) 342.
51. N. A. Wiederkehr, J. Braz. Chem. Soc. 1 (1996) 7.
52. W. Chidawanyika, T. Nyokong, Carbon 48 (2010) 2831.
53. G. I. Cardenas-Jiro, M. A. Gulppi, C. A. Caro, R. del Rio, M. Paez, J. H. Zagal, Electrochim. Acta 46 (2001) 3227.
54. S. V. Kudrevich, H. Ali, J. E. van Lier, J. Chem. Soc. Perkin Trans. 1 (1994) 2767.
55. M. Geyer, F. Plenzig, J. Rauschnabel, M. Hanack, B. del Rey, A. Sastre, T. Torres, Synthesis (1996) 1139.
56. N. Kobayashi, R. Kondo, S. Nakajima, T. Osa, J. Am. Chem. Soc. 112 (1990) 9640.
57. S. Dabak, A. Gul, O. Bekaroglu, Chem. Ber. 127 (1994) 2009.
58. A. Weitemeyer, H. Kliesch, D. Wöhrle, J. Org. Chem. 60 (1995) 4900.
59. C. C. Leznoff, T. W. Hall, Tetrahedron Lett. 23 (1982) 3023.
60. C. C. Leznoff, P. Snirskaya, B. Khouw, R.L. Cerny, P. Seymour, A.B.P. Lever, J. Org. Chem. 56 (1991) 82.
61. S.-H. Jung, J.-H. Choi, S.-M. Yang, W.-J. Cho, C.-S. Ha, Mat. Sci. Engineer. B85 (2001) 160.
62. Y. Pan, W. Chen, S. Lu, Y. Zhang, Dyes and Pigments 66 (2005) 115.
63. A. B. Sorokin, S. Mangematin, C. J. Pergrale, Mol. Cat. A. 267 (2002) 182.
64. T. V. Tararykina, V. E. Maizlish, N. E. Galanin, G. P. Shaposhnikov, V. V. Bykova, N. V. Usoltseva, Russ. J. Org. Chem. (43) (2007) 1719.
65. R. P. Feazell, N. Nakayama-Ratchford, H. Dai, S. J. Lippard, J. Am. Chem. Soc. 129 (2007) 8438.
66. W. Yang, P. Thordarson, J. J. Gooding, S. P. Ringer, F. Braet, Nanotech. 18 (2007) 412001.
67. A. Bianco, K. Kostarelos, C. D. Partidos, M. Prato, Chem Commun 5 (2005) 571.

68. K. I. Ozoemena, T. Nyokong, D. Nkosi, I. Chambrier, M. J. Cook. Electrochim Acta 52 (2007) 4132.
69. M. Siswana, K. I. Ozoemena, T. Nyokong, Sensors 8 (2008) 5096.
70. S. Khene, D. A. Geraldo, C. A. Togo, J. Limson, T. Nyokong, Electrochim. Acta 54 (2008) 183.
71. H. Ogata, R. Higashi, N. Kobayashi, J. Porphyrins Phthalocyanines 7 (2003) 551.
72. J. P. Zelina, C. K. Njue, J. F. Rusling, G. N. Kamau, M. Masila, J. Kibugu, J. Porphyrins Phthalocyanines 3(1999) 188.
73. R. D. George, A. W. Snow, J. S. Shirk, W. R. Barger, J. Porphyrins Phthalocyanines, 2 (1998) 1.
74. K. I. Ozoemena, J. Pillay, T. Nyokong, Electrochem. Commun. 8 (2006) 1391.
75. M. P. Siswana, K. I. Ozoemena, T. Nyokong, Electrochim. Acta 52 (2006) 114.
76. P. Ardiles, E. Trollund, M. Isaacs, F. Armijo, J.C. Canales, M.J. Aguirre, M.J. Canales, J. Mol. Catal. A: Chemical 165 (2001) 169.
77. D. Nkosi, K. I. Ozoemena, J. Electroanal. Chem. 621 (2008) 304.
78. M. Chicharro, A. Zapardiel, E. Bermejo, M. Moreno, E. Madrid, Anal. Bioanal. Chem. 373 (2002) 277.
79. B. O. Agboola, K. I. Ozoemena, T. Nyokong, Electrochim. Acta 51 (2006) 6470.
80. A. Koca, H. A. Dincer, M. B. Kocak, A. Gül, Russian J. Electrochem. 42 (2006) 31.
81. A. B. P. Lever, P.C. Minor, Inorg. Chem. 20 (1980) 4015.
82. A. B .P. Lever, Adv. Inorg. Chem. Radiochem. 7 (1965) 27.
83. D. Schlettwein, T. Yoshida, J. Electroanal. Chem. 441 (1998) 139.
84. A. B. P. Lever, S.R. Pickens, P.C. Minor, S. Licoccia, B.S. Ramaswany, K. Magnell, J. Am. Chem. Soc. 103 (1981) 6800.
85. A. B. P. Lever, S. Liccocia, K. Magnell, P. C. Minor, B. S. Ramaswamy, ACS Symp. Ser. 201 (1982) 237.
86. J. Zagal, M. Paez, A. A. Tanaka, J.R. dos Santos, Jr. C.A. Linkous , J. Electroanal. Chem., 339 (1992) 13.
87. C. G. Claessens, W. J. Blau, M. Cook, M. Hanack, R. J. M. Nolte, T. Torres, D. Wohrle, Monatsh. Chem. 132 (2001) 3.
88. D. Wohrle, Macromol. Rapid Commun. 22 (2001) 68.

89. J. H. Zagal, M. A. Gulppi, G. Cardenas-Jiron, Polyhedron 19 (2000) 2255.
90. A. R. Ozkaya, E. Hamuryudan, B. Z. Altuntas, O. Bekaroglu, J. Porphyrins Phthalocyanines 7 (2000) 689.
91. N .M. Alpatova, E. V. Ovsyannikova, L. G. Tomilova, O. V. Korenchenko, Y. V. Kondrashov, Russ. J. Electrochem. 37 (2001) 1012.
92. N. R. Neustroeva, M. I. Bazanov, Y. G. Vorob'ev, Russ. J. Electrochem. 37 (2001) 205.
93. M. Ozer, A. Altındal, A. R. Ozkaya, M. Bulut, O. Bekaroglu, Polyhedron 25 (2006) 3593.
94. K. I. Ozoemena, T. Nyokong, Electrochim. Acta 47 (2002) 4035.
95. Z. Li, M. Lieberman, Langmuir 17 (2001) 4887.
96. J. Obirai, N. Pereira-Rodrigues, F. Bedioui, T. Nyokong, J. Porphyrins Phthalocyanines 7 (2003) 508.
97. C. A. Caro, F. Bedioui, J. H. Zagal, Electrochim. Acta 47 (2002) 1489.
98. N. Sehlotho, T. Nyokong, Electrochim. Acta 51 (2006) 4463.
99. J. Obirai, T. Nyokong, Electrochim. Acta 50 (2005) 5427.
100. S. Griveau, J. Pavez, J.H. Zagal, F. Bedoui, J. Electroanal. Chem. 497 (2001) 75.
101. E. H. Yu, S. Cheng, B.E. Logan, K. Scott, J. Appl. Electrochem 39 (2009) 705.
102. B. Agboola, T. Nyokong, Electrochim. Acta 52 (2007) 5039.
103. Z-H. Wen, T-F. Kang, Talanta 62 (2004) 351.
104. E. F. Perez, L. T. Kubota, A. A. Tanakab, G. D. O. Neto, Electrochim. Acta 43 (1998) 1665.
105. T. F. Kang, G. L. Shen, R.Q. Yu, Anal. Chim. Acta 356 (1997) 245.
106. C. Berríos , M. S. Ureta-Zañartu, C. Gutiérrez, Electrochim. Acta 53 (2007) 792.
107. P.-X. Hou, C. Liu, H.-M. Cheng, Carbon 46 (2008) 2003.
108. S. Iijima, Nature 354 (1991) 56.
109. M. S. Dresselhaus, G. Dresselhaus, M. Hofmann, Vib. Spectrosc. 45 (2007) 71.
110. M. Terrones, Annu. Rev. Mater.Res. 33 (2003) 419.
111. A. Javey, J. Guo, Q. Wang, M. Lundstrom, H. Dai, Nature 424 (2003) 654.
112. S. Latil, S. Roche and J.-C. Charlier, Nano Lett. 5 (2005) 2216.
113. P. Avouris, Acc. Chem. Res. 35 (2002) 1026.

114. J. Bernholc, D. Brenner, M.B. Nardelli, V. Meunier, C. Roland, Ann.Rev. Mater. Res. 32 (2002) 347.
115. Q. Zhao, Z. H. Gan, Q.K. Zhuang, Electroanalysis 14 (2002) 1609.
116. P. J. Britto, K. S. V. Santhanam, P. M. Ajayan, Bielectrochem. Bioenerg. 41 (1996) 121.
117. L. Valentini, C. Cantalini, L. Lozzi, I. Armanetano, J.M. Kenny, S. Santucci, Mater. Sci. Eng. C 23 (2003) 523.
118. P. Qi, O. Vermesh, M. Grecu, A. Javey, Q. Wang, H. Dai, S. Peng, K.J. Cho, Nano Lett. 3 (2003) 347.
119. K. S. Ahn, J. H. Kim, K. N. Lee, C.O. Kim, J. P. Hong, J. Korean Phys. Soc. 45 (2004) 158.
120. K.P. Gong, Y. Dong, S.X. Xiong, Y. Chen, L.Q. Mao, Biosens. Bioelectron. 20 (2004) 253.
121. S.-F. Wang, Q. Xu, Anal. Lett. 38 (2005) 657.
122. C. G. Hun, W. L. Wang, S. X. Wang, W. Zhu, Y. Li, Diamond Relat. Mat. 12 (2003) 1295.
123. R. P. Deo, J. Wang, Electrochem. Commun. 6 (2004) 284.
124. M. Guo, J. Chen, J. Li, B. Tao, S. Yao, Anal. Chem. Acta 532(2005) 71.
125. L. Dai, P. He, S. Li, Nanotech. 14 (2003) 1081.
126. F.L. Cheng, S. Du, B.K. Jin, Chin. J. Chem. 21 (2003) 436.
127. D. S. Bethune, C. H. Kiang, M. S. de Vries, G. Gorman, R. Savoy, J. Vazquez, R. Beyers, Nature 363 (1993) 605.
128. H. J. Li, L. H. Guan, Z. J. Shi, Z. N. Gu, J. Phys. Chem. B 108 (2004) 4573.
129. A. Thess, R. Lee, P. Nikolaev, H. Dai, P. Petit, J. Robert. Xu, Y.H. Lee, S.G. Kim, A.G. Rinzler, D.T. Colbert,G.E. Scuseria, D. Tomanek, J.E. Fischer, R.E. Smalley, Science 273 (1996) 483.
130. P.G.Collins, P. Avouris, Sci Am. 283 (2000) 62.
131. T. Guo, P. Nikolaev, A. G. Rinzler, D.Tomanek, D. T. Colbert, R. E. Smalley, Chem. Phys. Lett. 99 (1995) 10694.
132. S. Huang, L. Dai, A.W.H. Mau, J. Phys. Chem. B 103 (1999) 4223.

133. D.-C. Li, L. Dai, S. Huang, A.W.H. Mau, Z.L. Wang,Chem. Phys. Lett. 316 (2000) 349.
134. S. Huang, L. Dai, J. Phys. Chem. B 106 (2002) 3543.
135. Y. Chen , J. Yu, Carbon 43 (2005) 3181.
136. B. C. Liu, T.J. Lee, S.H. Lee, C.Y. Park, C.J. Lee, Chem. Phys. Lett. 377 (2003) 55.
137. F. L. Deepak, A. Govindaraj, and C. N. R. Rao, Chem. Phys. Lett. 345 (2001) 5.
138. H. Araki, T. Katayama, and K. Yoshino, Appl. Phys. Lett. 79 (2001) 2636.
139. T. Katayama, H. Araki, and K. Yoshino, J. Appl. Phys. 19 (2002) 6675.
140. A. R. Harutyunyan, G. Chen and P. C. Eklund, Appl. Phys. Lett. 82 (2003) 4794.
141. Y. Chen, L. T. Chadderton, J. Mater. Res. 19 (2004) 2791.
142. Y. Chen, M. J. Conway, J. D. F. Gerald, Appl. Phys A Mater. 76 (2003) 633.
143. Y. Chen, M. J. Conway, J. D. F. Gerald, J. S. Williams, L. T. Chadderton, Carbon 42 (2004) 1543.
144. S. Amelinckx, X.B. Zhang, D. Bernaerts, X.F. Zhang, V. Ivanov, J.B. Nagy, Science 265 (1994) 635.
145. J. L. Zimmerman, R. K. Bradley, C.B. Huffman, R. H. Hauge, J.L. Margrave, Chem, Mater. 12 (2000) 1361.
146. I. W.Chiang, B. E. Brinson, R.E. Smalley, J. L. Margrave, R. H. Hauge, J. Phys. Chem. B 105 (2001) 1157.
147. Y. Q. Xu, H. Q. Peng, R. H. Hauge, R. E. Smalley, Nano Lett. 5 (2005) 163.
148. T. Jeong, W.Y.Kim, Y.B. Haha, Chem. Phys. Lett. 344 (2001)18.
149. G.Tobias, L. D. Shao, C. G. Salzmann, Y. Huh, M. L. H. Green, J. Phys. Chem. B 110 (2006) 22318.
150. J. Liu, M. J. Casavant, M. Cox, D. A. Walters, P. Boul, W. Lu, A. J. Rimberg, K. A. Smith, D. T. Colbert, R. E. Smalley, Chem. Phys. Lett. 303 (1999) 125.
151. H. Hu, B. Zhao, M. E. Itkis, R. C. Haddon, J. Phys. Chem. B 107 (2003) 13838.
152. Y. H. Wang, H. W. Shan, R. H. Hauge, M. Pasquali, R. E. Smalley, J. Phys. Chem. B 111 (2007) 1249.
153. J. F. Colomer, P. Piedigrosso, A. Fonseca, J. B. Nagy, Synt. Met. 103 (1999) 2482.
154. J. Liu, A. G. Rinzler, H. Dai, J. H. Hafner, H. Jason, R. K. Bradley, P. J. Boul, A. Lu, T. Iverson, K. Shelimov, H. Konstantin, C. B. Huffman, F. Rodriguez-

Macias, S. Young-Seok, R. T. Randall, D. T. Colbert, T. Daniel, R. E. Smalley, Science 280 (1998) 1253.

155. S. Banerjee, T. Hemraj-Benny, S. S.Wong, Adv. Mater. 17 (2005) 17.
156. A. Hirsch, Angew. Chem. Int. Ed. 41 (2002) 1853.
157. M. Trojanowicz, Trends in Anal. Chem. 25 (2006) 480.
158. M. Alvaro, P. Atienzar, P. de la Cruz, J. L. Delgado, H. Garcia, F. Langa, J. Phys. Chem. B 108 (2004) 12691.
159. W.Wu, S. Wieckowski, G. Pastorin, M. Benincasa; C. Klumpp, J. P. Briand, R. Gennaro, M. Prato, A. Bianco, Angew. Chem. Int. Ed. 44 (2005) 6358.
160. K. A. Williams, P. T. M. Veenhuizen, B. G. de la Torre, R. Eritja, C. Dekker, Nature 420 (2002) 761.
161. T. J. Yim, J. W. Liu, Y. Lu, R. S. Kane, J. S. Dordick, J. Am. Chem. Soc. 127 (2005) 12200.
162. D. Pantarotto, C. D.Partidos, R. Graff, J. Hoebeke, J. P. Briand, M. Prato, A. Bianco, J. Am. Chem. Soc. 125 (2003) 6160.
163. J. Chen, M. A. Hamon, H.Hu, Y. Chen, A. M. Rao, P. C. Eklund and R. C. Haddon, Scie. 282 (1998) 95.
164. B. Ballesteros, G. de la Torre, Ch. Ehli, G. M. A. Rahman, F. Agullo-Rueda, D. M. Guldi, T. Torres, J. Am. Chem. Soc. 129 (2007) 5061.
165. C. Ehli, S. Campidelli, F. G. Brunetti, M. Prato, D. M. Guldi, J. Porphyrins Phthalocyanines 11 (2007) 442.
166. E. Menna, G. Scorrano, M. Maggini, M. Cavallaro, F. D. Negra, M. Battagliarin, R. Bozio, F. Fantinel, M. Meneghetti, ARKIVOC xii (2003) 64.
167. J. L. Stevens, A. Y. Huang, H. Peng, I. W. Chiang, V. N. Khabashesku, J.L. Margrave, Nano Lett. 3 (2003) 331.
168. M. D. Ellison, P. J. Gasda, J. Phys. Chem. C 112 (2008) 738.
169. V. Georgakilas, K. Kordatos, M. Prato, D. M. Guldi, M. Holzinger, A. Hirsch, J. Am. Chem. Soc. 124 (2002) 760.
170. C. W. Bauschlicher, Chem. Phys. Lett. 322 (2000) 237.
171. M. E. Itkis, D. E. Perea, R. Jung, S. Niyogi, R. C. Haddon, J. Am. Chem. Soc. 127 (2005) 3439.

172. S. K. Pillai, S. S. Ray, M. J. Moodley, Nanosci Nanotech. 7 (2007) 3011.

173. A. Jorio, M.A. Pimenta, A.G.S. Filho, R. Saito, G. Dresselhaus, M.S. Dresselhaus, New J. Phys. 5 (2003) 139.

174. S. Banerjee, S. S. Wong, Nano Lett. 4 (2004) 1445.

175. C. Casiraghi, A. Hartschuh, H. Qian, S. Piscanec, C. Georgi,A. Fasoli, K. S. Novoselov, D. M. Basko, A. C. Ferrari, Nano Lett. 9 (2009) 1433.

176. H. Peng, L. B. Alemany, J. L. Margrave, V.N. Khabashesku, J. Am. Chem. Soc. 125 (2003) 15174.

177. M. S. Dresselhaus , G. Dresselhaus, A. Jorio, A. G. S. Filho, R. Saito, Carbon 40 (2002) 2043.

178. A. C. Ferrari, Solid State Commun. 143 (2007) 47.

179. K. E. Hurst, A. C. Dillon, S. Yang, J. H. Lehman, J. Phys. Chem. C 112 (2008) 16296.

180. C. A. Dyke, J. M. Tour, Nano Lett. 3 (2003) 1215.

181. R.R. Bacsa, E. Flahaut, C. Laurent, A. Peigney, S. Aloni, P. Puech, W.S. Bacsa, New J. Phys. 5 (2003) 131.

182. A.M. Rao, E. Richter, S. Bandow, B. Chase, P.C. Eklund, K.A. Williams, S. Fang, K. R. Subbaswamy, M. Menon, A. Thess, R. E. Smalley, G. Dresselhaus, M.S. Dresselhaus, Science 275 (1997) 187.

183. H. Kuzmany, W. Plank, M. Hulman, C. Kramberger, A. Gruneis, T. Pichler, H. Peterlik, H. Kataura, Y. Achiba, Eur. Phys. J. B 22 (2001) 307.

184. S. Osswald, E. Flahaut, H. Ye, Y. Gogotsi, Chem. Phys. Lett. 402 (2005) 422.

185. T. J. Park, S. Banerjee, T. Hemaraj-Benny, S.S. Wong, J. Mater. Chem. 16 (2006) 141.

186. R. K. Saini, I. W. Chiang, H. Peng, R. E. Smalley, W. E. Billups, R. H. Hauge, J. L. Margrave, J. Am. Chem. Soc. 125 (2003) 3617.

187. V. Georgakilas, A. Bourlinos, D. Gournis, T. Tsoufis, C. Trapalis, A. Mateo-Alonso, M. Prato, J. Am. Chem. Soc. 130 (2008) 8733.

188. W. Zhang, T. M. Swager, J. Am. Chem. Soc. 129 (2007) 7714.

189. Z.-L. Yang, H.-Z. Chen, L. Cao, H.-Y. Li, M. Wang, Mater. Scie. Eng.B106 (2004) 73.

190. S. L. A. Maranhao, I. C. Guedes, F. J. Anaissi, H. E. Toma ,I. V. Aoki, Electrochim. Acta 52 (2006) 519.
191. S. Osswald, M. Havel, Y. Gogotsi, J. Raman Spectrosc. 38 (2007) 728.
192. B. N. Achar, K. S. Lokesh, J. Organomet. Chem. 689 (2004) 2601.
193. M. Fujiki, H. Tabei, Langmuir, 4 (1988) 320.
194. Z. Hao, Q. F. Liu, J. B. Wang, J. Composite Mater. 44 (2010) 389.
195. I. Stamatina, A. Morozan, A. Dumitru, V. Ciupina, G. Prodan, J. Niewolski, H. Figiel, Physica E 37 (200 7) 44.
196. Y. Zhang, X. Sun, L. Pan, H. Li, Z. Sun, C. Sun, B. K. Tay, J. Alloys Compd. 480 (2009) L17.
197. S.-K. Cui, D-J. Guo, J. Colloid Interface Science 333 (2009) 300.
198. W. Lu, N. Li, W. Chen, Y. Yao, Carbon 47 (2009) 3337.
199. B. Ballesteros, S. Campidelli, G. de la Torre, C. Ehli, D. M. Guldi, M. Prato, T. Torres, Chem. Commun. (2007) 2950.
200. W. X. Cheng, G. Y. Jin, Y. Z. Zhang, Russian J. Electrochem. 41 (2005) 1061.
201. J. Pillay, K.I. Ozoemena, Electrochim. Acta 52 (2007) 3630.
202. S. A. Mamuru, K. I. Ozoemena, T. Fukuda, N. Kobayashic, T. Nyokong, Electrochim. Acta 55 (2010) 6367.
203. F. C. Moraes, L.H. Mascaro, S. A.S. Machado, C. M. A. Brett, Talanta 79 (2009) 1406.
204. J. Pillay, K. I. Ozoemena, Electrochim. Acta 54 (2009) 5053.
205. K. I. Ozoemena, D. Nkosi, J. Pillay, Electrochim. Acta 53 (2008) 2844.
206. B. O. Agboola, S. L. Vilakazi, K. I. Ozoemena, J Solid State Electrochem 13 (2009) 1367.
207. D. Nkosi, K. I. Ozoemena, Electrochimica Acta 53 (2008) 2782.
208. A. P. Gutierrez, S. Griveau, C. Richard, A. Pailleret, S. G. Granados, F. Bedioui, Electroanalysis 41 (2009) 2303.
209. S. Campidelli, B. Ballesteros, A. Filoramo, D. Dıaz Dıaz, G. de la Torre, T. Torres, G. M. A. Rahman, C. Ehli, D. Kiessling, F. Werner, V. Sgobba, D. M. Guldi, C. Cioffi, M. Prato, J.-P. Bourgoin, J. Am. Chem. Soc. 130 (2008) 11503.

210. T. J. Mafatle, T. Nyokong, J. Electrochem. Anal. 408 (1996) 213.
211. B. J. Hwang, R. Santhanam, Y. W. Chang, Electroanal.14 (2002) 363.
212. M. J. Cook, D. A. Mayes, R. H. Poynter, J. Mater. Chem. 5 (1995) 2233.
213. P. N. Mashazi, K. I. Ozoemena, D. M. Maree, T. Nyokong, Electrochim. Acta 51 (2006) 3489.
214. R. A. Durst, A. J. Bäumner, R.W. Murray, R.P. Buck, C.P. Andrieux, Pure Appl. Chem. 69 (1997) 1317.
215. E. M. Genies, G. Bidan, A. F. Diaz, J. Electroanal. Chem. 149 (1983) 101.
216. M. Gulppi, S. Griveau, J. Pavez, J. H. Zagal, F. Bedioui, Electroanal. 15 (2003) 779.
217. S. Shahrokhian, J. Yazdani, Electrochim. Acta 48 (2003) 4143.
218. A. Deronzier, J. C. Moutet, Acc. Chem. Res. 22 (1989) 249.
219. D. Curran, J. Grimshaw, S. D. Perera, Chem. Soc. Rev., 20 (1991) 391.
220. H. Randriamahazaka, V. Nöel, C. Chevrot, J. Electroanal. Chem. 472 (1999) 103.
221. J. Obirai, T. Nyokong, Electrochimica Acta 49 (2004) 1417.
222. B. Ortiz, S.-M. Park, N. Doddapaneni, J. Electrochem. Soc. 143 (1996) 1800.
223. H. Li, T.F. Guarr, J. Chem. Soc., Chem. Commun. (1989) 832.
224. J. H. Zagal, S. Griveau, J.F. Silva, T. Nyokong, F. Bedioui, Coord. Chem. Rev. (2010), doi:10.1016/j.ccr.2010.05.001.
225. K. I. Ozoemena, Z. Zhao, T. Nyokong, Inorg. Chem. Commun. 9 (2006) 223.
226. G. Liu, S.L. Riechers, M.C. Mellen, Y. Lin, Electrochem. Commun. 7 (2005) 1163.
227. A. Salimi, L. Miranzadeh, R. Hallaj, Talanta 75 (2008) 147.
228. A. Salimi, A. Noorbakhsh, M.Ghadermarzi, Sensors and Actuators B 123 (2007) 530.
229. F. Matemadombo, N. Sehlotho, T. Nyokong, J. Porphyrins Phthalocyanines 13 (2009) 986.
230. D. A. Geraldo, C. A. Togo, J. Limson, T. Nyokong, Electrochim. Acta 53 (2008) 8051.
231. D. Martel, N. Sojic, A. Kuhn, J. Chem. Educ. 79 (2002) 349.
232. J. C. Obirai, T. Nyokong, J. Electroanal. Chem. 600 (2007) 251.
233. J. Obirai, F. Bedioui, T. Nyokong, J. Electroanal. Chem. 576 (2005) 323.

234. J. Obirai, T. Nyokong, J. Electroanal. Chem. 573 (2004) 77.

235. G. A. Mabbott, J.Chem. Educ. 60 (1983) 697.

236. S. Majdi, A. Jabbari, H. Heli, A. A. Moosavi-Movahedi, Electrochim. Acta 52 (2007) 4622.

237. A. Maritan, F. Toigo, Electrochim. Acta 35 (1990) 141.

238. Y. Liu, M. Wang, F. Zhao, Z. Guo, H. Chen, S. Dong, J. Electroanal. Chem. 581 (2005) 1.

239. E. Sabatani, I. Rubinstein, J. Phys. Chem. 91 (1987) 6663.

240. B. J. Palys, G.J. Puppels, D. van den Ham and D. Feil, J. Electroanal. Chem., 326 (1992) 105.

241. S. George, H. K. Lee, Anal. Methods 2 (2010) 326.

242. H. Beitollahi, M. Mazloum-Ardakani, H. Naeimi, B. Ganjipour, J Solid State Electrochem 13 (2009) 353.

243. R. E. Sabzi, J. Braz. Chem. Soc. 16 (2005) 1262.

244. H. R. Zare, N. Nasirizadeh, M. Mazloum-Ardakani, M. Namazian, Sensors and Actuators B 120 (2006) 288.

245. A. J. Bard, L. R. Faulkner, Electrochemical Methods, John Wiley and Sons, New York, 2001.

246. F. Valentini, A. Amine, S. Orlanducci, M.L. Terranova, G. Palleschi, Anal. Chem. 75 (2003) 5413.

247. M. H. Pournaghi-Azar, R. Sabzi, J. Electroanal. Chem. 543 (2003) 115.

248. R. I. Stefan, J.F. van Staden, H.Y. Aboul-Enein, Electrochemical Sensors in Bioanalysis, Marcel Dekker, New York, 2001, p. 66.

249. A. Chou, T. Bocking, N.K. Singh, J.J. Gooding, Chem. Comm. (2005) 842.

250. J. F. Silva, S. Griveau, C. Richard, J. H. Zagal, F. Bedioui, Electrochem. Commun. 9 (2007) 1629.

251. S. Maree, T. Nyokong, J. Electroanal. Chem. 492 (2000) 120.

252. M. J. Aguirre, M. Isaacs, F. Armijo, L. Basa´ez, J.H. Zagal, Electroanalysis 14 (2002) 356.

253. USA EPA, Washington D.C. 20460, Office of prevention, pesticides and toxic substances, amitrole reregistration (1996).

254. F. Mattioli, L. Robbiano and P. Barachhini, Fundam. Appl. Toxicol. 23 (1994) 101.

255. T. Meretoja, U. Gripenberg, D. Bamford, I. Laamanen, M. Sorsa, Mutation Research 40 (1976) 191.

256. European Commission, Directorate-General Health & Consumer Protection, Directorate E - Public, animal and plant health, Unit E1 Legislation relating to crop products and animal nutrition, Amitrole 6839/VI/97 (2001) 1.

257. J.-M. Zen, A. Senthil Kumar, M.-R. Chang, Electrochim. Acta 45 (2000) 1691.

258. M. Siswana, K.I. Ozoemena, T. Nyokong, Talanta 69 (2006) 1136.

259. Environmental Monitoring Branch, Department of Pesticide Regulation (DPR) California, Pesticide Chemistry Database, 2003.

260. L. Guzzella, E. Capri, A. Di Corcia, A. Barra Carracciolo, G. Giuliano, J. Environ.Qual. 35 (2006) 312.

261. K. Abass, P. Reponen, M. Turpeinen, J. Jalonen, O. Pelkonen, Am. Soc. Pharm. Exp. Tech. 35 (2007) 1634.

262. USA EPA, Washington D.C. 20460, Office of prevention, pesticides and toxic substances, diuron reregistration (2003).

263. A. M. Polcaro, M. Mascia, S. Palmas, A. Vacca, Electrochim. Acta 49 (2004) 649.

264. G. Achilli, G. P. Cellerino, G. M. d'Eril, S. Bird, J. Chromatogr. A 697 (1995) 357.

265. K. Macounova, J. Klima, C. Bernard, C. Degrand, J. Electroanal. Chem. 457 (1998) 141.

266. M. Chanda, A. Grinshpun, K.F. O'Driscoll, G.L. Rempel, J. Mol. Catal. 26 (1984) 267.

267. B. A. Retamal, M. E. Vaschetto, J. H. Zagal, J.Electroanal. Chem. 43 (1997) 1.

268. N. Sehlotho, Tebello Nyokong, J. H. Zagal, F. Bedioui, Electrochim. Acta 51 (2006) 5125.

269. A. Napier, J. P. Hart, Electroanalysis 8 (1996) 1006.

270. J. Kulys, A. Drungiliene, Anal. Chim. Acta 243 (1991) 287.

271. D. Worhle, M. Eskes, K. Shigehara, A. Yamada, Synthesis (1993) 194.

272. B. Agboola, K.I. Ozoemena, T. Nyokong, Electrochim. Acta 51 (2006) 4379.

273. A. G. Gurek, O. Bekaroglu, J. Chem. Soc. Dalton Trans. (1994) 1419.

274. J. G. Young, W. Onyebuagu, J. Org. Chem. 55 (1990) 2155.
275. X. Song, Y. She, H. Ji, Y. Zhang, Org. Proc. Res. Dev. 9 (2005) 297.
276. L. Wei, Y. Zang, Nanotech. 18 (2007) 1.
277. R. C. Haddon, C. Jiang**,** United States Patent 633126 **(**2001**).**
278. R. C. Haddon, J. Chen, United States U.S. Patent 6187823 B1 (2001).
279. J. L. Bahr, J.Y. Dmitry, V. Kosynkin, M.J. Bronikowski, R.E. Smalley, J.M. Tour, J. Am. Chem. Soc. 123 (2001) 6536.
280. H.T. Fang, C. G. Liu, C. Liu, F. Li, M. Liu, H. M. Cheng, Chem. Mater. 16 (2004) 5744.
281. A. Govindaraj, C. N. R. Rao, Pure Appl. Chem. 74 (2002) 1571.
282. S. Sapra, D. D. Sarma, Pramana 65 (2005) 565.
283. M. P. Somashekarappa, S. Sampath, Anal. Chim. Acta 503 (2004) 195.
284. X. Y. Yang, Z. F. Liu, J. Mao, S. J. Wang, Y. F. Ma, Y. S. Chen, Chinese Chem. Lett. 18 (2007) 1551.
285. M. J. Stillman, T. Nyokong in: Phthalocyanines: Properties and Applications, C. C.Leznoff, A.B.P. Lever (Eds.), vol. 1 VCH, New York, 1989 (Chapter 3).
286. A. A. İsbir, A.O. Solak, Z. Üstündağ, S. Bilge and Z.Kılıç Anal. Chim. Acta 573-574 (2006) 26.
287. D. R. Tackley, G. Dent, W. E. Smith, Phys. Chem. Chem. Phys. 3 (2001) 1419.
288. C. Thiemann, C. M. A. Brett, Synth. Metals 125 (2002) 445.
289. N. E. Triggs,J. J. Valentini, J. Phys. Chem. 96 (1992) 6922.
290. D. Gani, P. J. Hendra, W.F. Maddams, C. Passingham, I, A. M. Royaud,H. A. Willis, V. Zichy,M. E. A. Cudby, Analyst 115 (1990) 1313.
291. G. Dent, F. Farrell, Spectrochim. Acta: A 53 (1997) 21.
292. C. A. Dyke, J.M. Tour, J. Phys. Chem. A 108 (2004) 11151.
293. S. Dong, Z. Jin, Electrochim. Acta 34 (1989) 963.
294. J. J. Gooding, V. G. Praig, E. A. H. Hall, Anal. Chem. 70 (1998) 2396.
295. S. Griveau, V. Albin, T. Pauporté, J.H. Zagal, F. Bedioui, J. Mater. Chem. 12 (2002) 225.
296. J.-P Fan, X-M Zhang, M Ying, J. Solid State Electrochem 12 (2008) 1143.

297. A.B.P. Lever, E.R. Milaeva, G. Speier in Phthalocyanines: Properties and Applications, C.C. Leznoff, A.B.P. Lever (eds), VCH Publishers, New York Vol. 3 (1993) pg. 1.

298. M. S. Ureta-Zanartu, P. Bustos, M.C. Diez, M.L. Mora, C. Gutierrez, Electrochim. Acta. 2001, 46, 2545.

299. H. O. Finklea, in: Electroanalytical Chemistry. A.J. Bard, I. Rubinstein (Eds.), vol.19, Marcel Dekker, New York (1996).

300. P. Rapta, A.Vargova´ J.Polovkova, A. Gatial, L. Omelka, P. Majzlık, M.Breza,Polymer Degradation and Stability 94 (2009) 1457.

301. A. Volkov, G.Toljrillon, P-C. Lacaze, J-E Dubois, J. Electroanal. Chem. 115 (1980) 279.

302. C. Berríos, J. F. Marco, C. Gutiérrez, M. S. Ureta-Zañartu, Electrochim. Acta 54 (2009) 6417.

303. B. Wermeckes, F. Beck, Electrochim. Acta, 30 (1985) 1491.

304. M. E. G. Lyons, C.A. Fitzgerald, M.R. Smyth, Analyst, 119 (1994) 855.

305. S. M. Golabi, H. R. Zare,J. Electroanal. Chem. 465 (1999) 168.

306. M. Chicharro, E. Bermejo, A. Sanchez, A. Zapardiel,A. Fernandez-Gutierrez, D. Arraez, Anal. Bioanal. Chem. 382 (2005) 519.

307. M. Chicharro, A. Zapardiel, E. Bermejo, A. Sanchez, R. Gonzalez, Electroanalysis 16 (2004) 311.

308. A. Salimi, K. Abdi, Talanta 63 (2004) 475.

309. S. S. Khaloo, M. K. Amini, S. Tangestaninejad, S. Shahrokhian, R. Kia, J. Iranian Chem. Soc. 1 (2004) 128.

310. E. M. Garrido, C. Delerue-Matos, J. L. F. C. Lima, A. M. O. Brett, Anal. Lett. 37 (2004) 1755.

311. M. Chicharro, E. Bermejo, M. Moreno, A, Sanchez, A. Zapardiel, G. Rivas, Electroanalysis 17 (2005) 476.

312. H. Razmi, M. Harasi, Int. J. Electrochem. Sci. 3 (2008) 82.

313. H. R. Zare, N. Nasirizadeh, Electrochim. Acta 52 (2007) 4153.

314. A. M. Kazem, S. Said, T. Shahram, Mohammadpoor-Baltork Iraj, Iran J. Chem. Chem. Eng. 1 (2001) 29.

315. A. Goux, F. Bedioui, L. Robbiola, M. Pontie, Electroanalysis 15 (2003) 696.

316. J. A. Harrison, Z. A. Khan, J. Electroanal. Chem. 28 (1970) 131.

317. J. Ma, J.-N. Wang, C.-J. Tsai, R. Nussinov, B. Ma, Front. Mater. Sci. China 4 (2010) 17.

318. A. S. Milev, N. Tran, G. S. K. Kannangara, M. A. Wilson, I. Avramov, J. Phys. Chem. C 112 (2008) 5339.

319. S. S. Jewur, J. C. Kuriacose, Thermochim. Acta 19 (1977) 195.

320. S. Costa, E. Borowiak-Palen, M. Kruszyńska, A. Bachmatiuk, R. J. Kaleńczuk, Mat. Scie.-Poland, 26 (2008) 433.

321. R. S. Chen, W.H. Huang, H. Tong, Z.-L. Wang, J.-K. Cheng, Anal. Chem. 75 (2003) 634.